2018

Structural Transformations Of Multimetallic Nanoparticles

Guangfang Li
University of South Carolina

STRUCTURAL TRANSFORMATIONS OF MULTIMETALLIC NANOPARTICLES

by

Guangfang Li

Bachelor of Science
Wuhan Institute of Technology, 2009

Master of Science
Wuhan Institute of Technology, 2012

Submitted in Partial Fulfillment of the Requirements

For the Degree of Doctor of Philosophy in

Chemistry

College of Arts and Sciences

University of South Carolina

2018

Accepted by:

Hui Wang, Major Professor

Donna A. Chen, Committee Member

Sheryl L. Wiskur, Committee Member

Kevin Huang, Committee Member

Cheryl L. Addy, Vice Provost and Dean of the Graduate School

DEDICATION

This dissertation is dedicated to my family and friends. Thanks so much for all their love and support.

ACKNOWLEDGEMENTS

The whole journey of completion of my Ph.D. dissertation has been like a marathon which is full of challenge and encouragement. It would not be possible for me to finish this long but fulfilling journey without the support from my advisor, my dear family, and all my friends. To me, the biggest joy of completion of my Ph.D. study is to look over the journey past and appreciate all the unforgettable drips and drops happened during the past years.

First of all, I would like to give my deepest gratitude to my advisor Dr. Hui Wang, for his constructive guidance and continuous support. Hui has beel always a real model for me. I have always been impressed by his scientific attitude and knowledge breath, especially his confidence and enthusiasm in science. He has been investing great amounts of time and efforts in all the projects that I was involved. His creative ideas always inspire me to achieve the desired goals in science. I also would like to acknowledge the entire Wang group, both past and present, Dr. Hao Jing, Dr. Qingfeng Zhang, Dr. Lichao Sun, Esteban Villarreal, Mengqi Sun, Zixin Wang, Dr. Xiaoqi Fu, and Dr. Shiru Le for their selfless friendship and fruitful discussion in both science and daily life. I am also very grateful to all my committee members, Prof. Donna Chen, Prof. Sheryl Wiskur and Prof. Kevin Huang (Mechanical engineering, University of South Carolina) for their professional guidance in my research plan and proposal and comments on my Ph.D. dissertation.

This dissertation is full of TEM and SEM images. So I am also grateful to all

Electron Microscopy Center members at the USC for instrument use and technical assistance, including Ms. Jinbin Zhao, Dr. Soumitra Ghoshroy. Special thanks go to Dr. Doug Blom at Nanocenter USC for his instructive discussion and instrument use of STEM. Besides, I want to give special thanks to Dr. Stefik for the access for the X-ray diffraction facilities at the South Carolina SAXS Collaborative. In addition, I would also like to express my thanks to Dr. Greytak for the use of the heating furnace.

Finally, I would like to express my deepest love to my parent Congfeng Wang and Congjin Li, my brother Guangyuan Li, my sister-in-law Fen Wang, and other family members for their infinite support everything during my Ph.D. study. I would also love to thanks all my dear friends in China and in USA, they always stand by me through pain and joy.

ABSTRACT

Atomic-level understanding of the structural transformations of multimetallic nanoparticles (NPs) triggered by external stimuli is of vital importance to the enhancement of our capabilities to precisely fine-tailor the key structural parameters and thereby to fine-tune the catalytic properties of the NPs. In this work, I firstly show that Au-Cu bimetallic NPs demonstrate stoichiometry-dependent architectural evolutions during chemical dealloying processes and nanoporosity-evolving percolation dealloying only occurs for Au-Cu alloy NPs with Cu atomic fractions above the parting limit. The electrochemically active surface area and the specific activity of the dealloyed nanoframes can be systematically tuned to achieve the optimal electrocatalytic activity. Both the stability and the activity of the dealloyed Au nanoframes could be remarkably enhanced by incorporation of residual Ag into Au nanoframes through percolation dealloying of Au-Ag-Cu ternary alloy NPs. In addition, the catalytic selectivity of dealloyed porous Au NPs could be realized by precise control over of the surface atomic coordination numbers through percolation dealloying of Au-Cu bimetallic alloys with interior compositional gradients. Besides, nanoscale galvanic replacement reaction induced structural evolutions of Au-Cu bimetallic NPs has also been investigated in this dissertation. I have demonstrated the compositional stoichiometry and the structural ordering function as two key factors dictating the resulting architectures. More sophisticated and intriguing nanostructures have been achieved by coupling galvanic replacement with percolation dealloying or co-reduction. The electrocatalytic activity and

the stability of the resulting NPs with controllable geometries have been pushed to a new level. Lastly, I extend the investigation to Au-Ni system with huge lattice mismatch. The success in geometry-controlled syntheses of a series of Au-Ni bimetallic heteronanostructures represents a significant step toward the extension of nanoscale interfacial heteroepitaxy to the ones exhibiting large lattice mismatches and even dissimilar crystalline structures.

In summary, the goal of this dissertation is to gain new insights on structural transformations of multimetallic NPs which serve as a central design principle that guides the development of synthetic approaches to controllably fabricate architecturally sophisticated and compositionally diverse multimetallic nanostructures and build the structure-composition-property relationships and eventually optimize their performances.

Table Of Contents

LIST OF FIGURES

CHAPTER 1

INTRODUCTION

The current increasing interest in Au catalysis could be dated back to the 1980s when it was first reported that oxides supported-nanosized Au particles showed unexpected highly catalytic activity toward low-temperature carbon monoxide (CO) oxidation, which is strikingly contrast to the well-known traditional chemically inert bulk Au.[1,2] Since then, extensive research enthusiasm has been devoted in studying and understanding catalytic mechanisms of Au catalysis followed by sequentially considerable debate and controversy regarding to intrinsic reactivity of Au catalysts.[3-6] During the past decades, it has been consistently showed that only the ultrasmall Au less than 5 nm nanoparticles deposited on high-surface-area supports exhibit highly catalytic activity. It thus has become increasingly evident that undercoordinated surface atoms located on the edges, which become highly abundant when the nanoparticles are in sub-5 nm size regime, serve as the primary active sites for catalyzing a series of interfacial chemical and electrochemical reactions.[7-11] However, this inference remains a limited understanding about the origin of catalytic activity especially when the convoluted intertwining effects among nanoparticles, surfactants, and supports are taken into considerations for the catalytic promotion.[12]

Support-free nanoporous Au materials like Au bulk foams[13] open a unique opportunity and provide an ideal platform to explore the intrinsic catalytic activity of Au catalysis, which have been found to display similar even remarkably enhanced catalytic activities as supported- ultrasmall Au nanoparticles, although they have much larger characteristic lengths far beyond 5 nm both in ligament and pore diameters.[14,15] More importantly, support-free nanoporous Au, which successfully avoid issues associated with nanoparticle aggregation and support detachment of small catalytically active Au

nanoclusters, demonstrates promising advantages of excellent conductivity, highly thermal stability, large surface area, tunable composition, and a high density of various types of undercoordinated surface active atoms that might provide favorable reactive sites for specific reactions, all of which are highly desired for an optimal catalyst. Recently, research interesting in Au catalysis have been extended from macroscopic Au foam to nanoparticulate porous Au catalysts due to their striking distinct features of in terms of architectural uniformity, structural diversity and tunability, compositional flexibility, and easy material processing. Such remarkably advanced architectural accessibility enables us to precisely tailor the physical and chemical properties, then build up structure-composition-activity relationship, and eventually aim to catalytic optimization of porous Au nanocatalysts. In this review, we discuss the mechanistic formation of nanoporous Au and the explanation of their intrinsic reactivity toward a couple of representative chemical and electrochemical reactions. We highly focus on the current progress and especially potential strategies to overcome the challenges in precisely geometric and compositional control of nanoparticulate porous Au structures. More importantly, through systematic bottom-to-up studies, we provide a quantitative understanding of structure-composition-property relationships underpinning the catalytic behaviors of porous Au nanocatalysts and propose a series of approaches toward optimization of their catalytic activity, durability, and selectivity from a specific perspective.

1.1 Fabrication of Nanoporous Au Foam

The percolation dealloying of multimetallic alloy materials, entangling the selective dissolution of electrochemically more active metals accompanied with atomic migration and structural rearrangements of more-noble components in the bulk and at the solid-

electrolyte interfaces, provides a unique and versatile pathway to introduce nanoscale porosity into bulk system. Various of nanoporous metallic Au materials have commonly been obtained through percolation dealloying of Au-containing multimetallic alloy materials, such as Au-Cu,[16] Au-Ag,[17] Au-Sn,[18] and ternary Au-Ag-Pt or Au-Pt-Cu alloys.[19,20] A prototypical system of particular interest has been the percolation dealloying of bulk Au-Ag alloy membranes,[14,17,21] which evolve into sponge-like porous architectures with unique three-dimensional (3D) bicontinuous solid/void structures comprising Au-rich nanoligaments by exposure the alloy to a corrosive environment such as concentrated nitric acid. According to a surface-diffusion continuum model developed by Erlebacher and co-workers,[17] as kinetic Monte Carlo simulations illustrated in Figure 1.1A,[22] the percolation dealloying of Au-Ag alloy is initiated upon the dissolution of a single Ag atom on the flat surface, leaving behind a terrace vacancy coordinated with fewer Ag atoms that are more susceptible to dissolution. As the entire terrace is stripped, the undercoordinated Au atoms left behind undergo rapid surface diffusion and migration to agglomerate into Au-rich islands. Therefore, the surface of the alloy upon initiation of dealloying is composed of Au-rich domains that locally passivate the surface and patches of un-dealloyed material still exposed to the electrolyte. As dealloying further proceeds, the interfacial dissolution of Ag atoms and coarsening of the Au-rich domains continues, leading to formation of pit and porosity and eventual evolving into bicontinuous spongy structures. Figure 1.1B shows the scanning electron micrograph (SEM) of a typical dealloyed nanoporous Au film fabricated by selective dissolution of Ag by immersing Au-Ag alloy in nitric acid under free corrosion conditions. This model demonstrates the nanoporosity-evolving in metals is a consequence of an intrinsic dynamical pattern

formation process, which is well supported by the result of theoretical simulation of alloy dissolution (Figure 1.1C). The entire nanoporosity evolution dealloying process occurs on multi-scales, involving the kinetics of dissolution, surface diffusion, and mass transport through the bulk of both alloy and electrolyte. Erlebacher's model also suggests Au-Ag alloys exhibit bulk-composition-dependent dealloying dynamic behaviors of Ag dissolution. As the both experimental and simulated polarization curves shown in the Figures 1.1D-1.1F for the Au-Ag alloy films of different stoicheomitries, the Ag dissolution current drastically increased once a critical potential was reached, and the critical potential gradually increased with the Au content increase. A successful percolation dealloying for making porous metallic materials is essentially dictated by two parameters: the parting limit and the critical potential,[23,24] both of which are strongly dependent on the compositional stoichiometry of the starting alloy systems. Percolation dealloying occurs only when the content of less-noble element is higher than a threshold value known as the parting limit. In Ag-Au alloys, this parting limit was measured to be ~55 at % Ag,[17] while the critical potential is the electrochemical parameter signifying the onset of percolation dealloying, that is, the transition from a ''passivated'' alloy surface to a bicontinuous porous structure.[23] In addition, the dealloyed porous structures are actually composed of Au-rich nanoligaments with residual less-noble content left over because it is impossible to completely remove all the less-noble components, and the residues might remain alloyed with Au and homogeneously distributed in the ligaments, or locally segregate around the atomic steps and kinks on the topmost surface atomic layer,[25] while the accurate distribution is still a challenge. These dealloyed nanoligament-composed porous Au film exhibits of an unusual bicontinuous porous network with large

specific surface areas, open surface structures, and high density of surface active sites. Furthermore, the feature size including both ligament and pore dimensions could be fine-tailored by controlling the surface diffusion kinetics namely the ligament coarsening which is closely related the starting alloy composition, and dealloying conditions, as well as following treatment. For instance, Ding et al. demonstrated the characteristic length scale of the ligament could be well controlled over a wide range from a few to hundreds of nanometers by annealing treatment at various elevated temperatures,[26] whereas a low-temperature dealloying technique was developed by Chen et al. to generate an ultrafine nanoporous Au structure with thinner nanoligament and small pore size because the interfacial diffusion of Au atoms was significantly sluggish under low temperatures.[27] Metallic corrosion in electrochemical systems has also been widely investigated, in particular the selective dissolution (an etching process also called dealloying) of less-noble elements under applied anodic potentials.[28] Various electrochemical treatments like potential cycling method, constant-potential electrolysis method, differential normal pulse voltammetry, and linear voltammetry sweep,[29,31,3230] have been successfully utilized to fabricate porous Au by dealloying of Au-Zn or Au-Ag alloys. The final porous Au with controllable three dimension porosity could be able to achieve by tuning the starting alloy composition, dealloying temperature, and electrochemical parameters. Recently, some other electrochemical techniques like the anodization of pure Au in oxalate-containing solutions or direct Au deposition with hydrogen bubble as dynamic template have been constructed to engineering pure porous Au architectures,[33,34] which greatly facilitate the investigation of Au reactivity. The size and structure of the final porous foams can be modified significantly by applying different deposition conditions, such as

the electrolyte composition, deposition potential, and deposition time.[35]

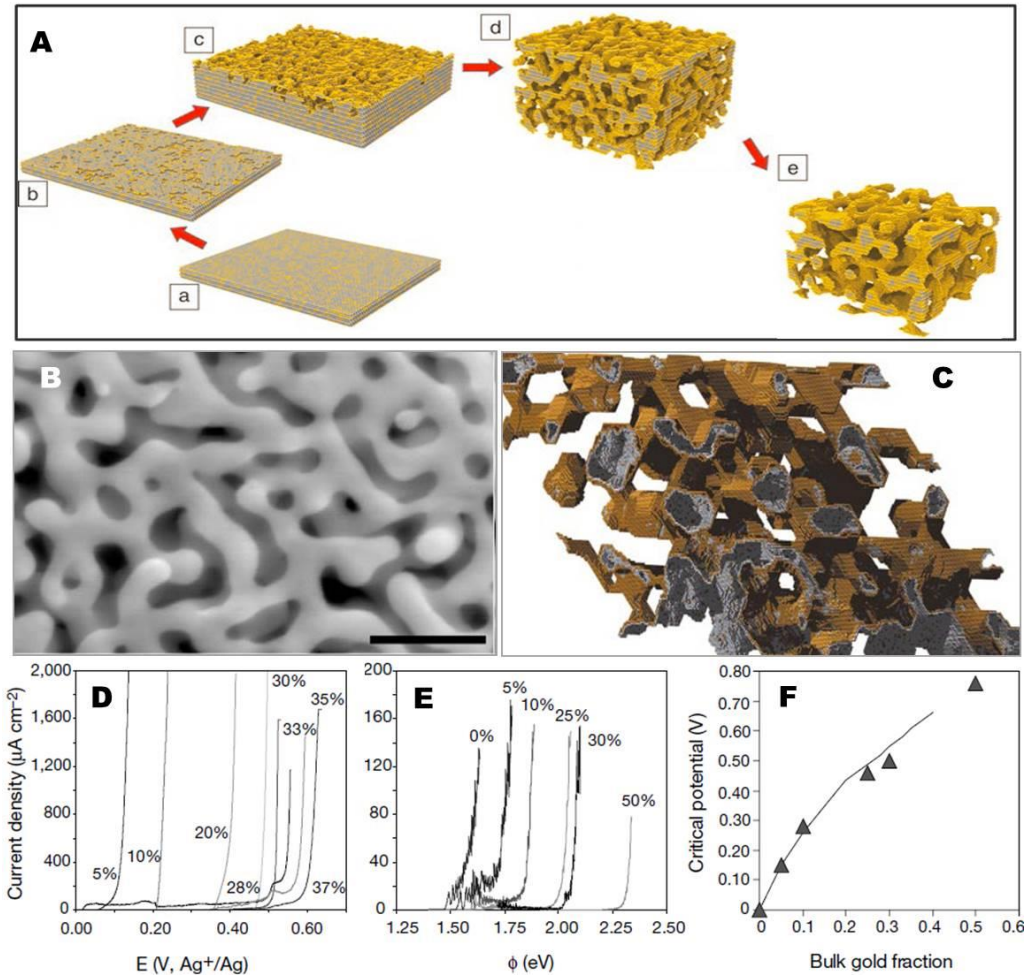

Figure 1.1. (A) Kinetic Monte Carlo simulations of atomic-scale dealloying processes during percolation dissolution. Reprinted with permission from reference 22.[22] Copyright 2018 Materials Research Society. (B) SEM of nanoporous Au made by percolation dealloying of $Au_{24}Ag_{76}$ alloy film. (C) Simulated porous Au structure with ligament widths of 2±5 nm. (D) Current-potential behavior for varying Ag-Au alloy compositions (at % Au) dealloyed in 0.1M $HClO_4$ + 0.1M Ag^+(reference electrode 0.1 M Ag^+/Ag). (E) Simulated current-potential behavior of Ag-Au alloys. (F) Comparison of experimental (line) and simulated (triangles) critical potentials; the zero of overpotential has been set equal to the onset of dissolution of pure silver both in simulation and in experiment. Reprinted with permission from reference 17.[17]Copyright 2001 Springer Nature.

1.2 Reactivity of Nanoporous Au Foam

A complete overview of a series of important oxidation and hydrogenation reactions on support-free nanoporous Au foam has been summarized by Wittstock et al.[9] A systematic

understanding of the catalytic properties of nanoporous Au is highly desirable, especially for the determination of active sites. In this review, we highlight two major factors that most studied including undercoordinated surface atoms and residual less-noble elements in dictating the intrinsic activity of nanoporous Au catalysts.

1.2.1 Undercoordinated Surface Atoms

The catalytic activity of unsupported nanoporous Au has been more extensively investigated since it was first reported by Zielasek et al. and shortly after by Ding et al.[36,37] They have demonstrated that nanoporous Au is highly active for CO oxidation even at lower temperatures without any activation pretreatment, and also displays outstanding durability that is in strikingly contrast to traditional oxide- supported Au nanocatalyst which requires preactivation by exposure to H_2 or O_2 at elevated temperatures.[38] Since then, rapid progress has been made in understanding the natural reactivity of nanoporous Au catalysts toward a variety of chemical or electrochemical reactions. It is has long been suggested that the reactivity of nanoporous Au originates from the high density of undercoordinated atoms present on the curved ligament surfaces.[11,39,40] On the basis of their degree of coordination and geometric characteristic, surface atoms of nanoporous Au can be sorted by three types including terrace atoms, step edge atoms, and kink sites, in the order of coordination decreasing (Figure 1.2A), and the latter two is in particular critical for catalysis due to their extremely high fraction of low-coordination.[11] While no direct evidences showing the presence of such step or kink sites on the curved nanoligament surface, SEM characterization clearly showed two-dimensionally curved surfaces that must contain a high concentration of step edge and kink site surface atoms. In addition, the fraction of low coordinations increases as the

ligament thickness decreases, which is similar with metallic Au nanocatalysts that become catalytically active as the surface atomic coordination number reduced.[41] Until very recent, direct verification of the presence of undercoordicated atoms has proven on basis of high resolution transmission electron microscopy. It has been clearly observed from high-angle annular dark-field scanning electron microscopy (HAADF-STEM) images that the locally curved surfaces of nanoporous Au are essentially enclosed by high densities of various types of undercoordinated Au atoms at steps and kinks (Figure 1.2B) which serve as the active sites providing higher binding energy sites for efficient CO adsorption on basis of experimental results as well as theoretical studies.[25] Furthermore, the activity deterioration of nanoporous Au film for electrocatalytic methanol oxidation in liquid phase caused by nanoligaments coarsening which seriously resulted in the vanishing of active undercoordinated atoms after long-time potential cycling indirectly confirmed the reactivity from the surface undercoordinations.[42] Consistent with this observation, some recent investigations have also demonstrated that the catalytic activity of nanoporous Au for CO oxidation in gas phase decreased with the nanoligament coarsening and loss of low-coordination sites associated with the surface atomic migration and segregation as a consequence of thermal treatment as the reaction prolonged, while the catalytic performance could be well maintained by introduction of a tiny amount of Pt (or Ag) on the nanoporus Au surface, surface defects, or surface coating that efficiently suppressed the surface atomic migrations or rearrangements, which provided strong evidences for the key role of undercoordinations in catalytic activity of nanoporous Au catalysts. [43,44]

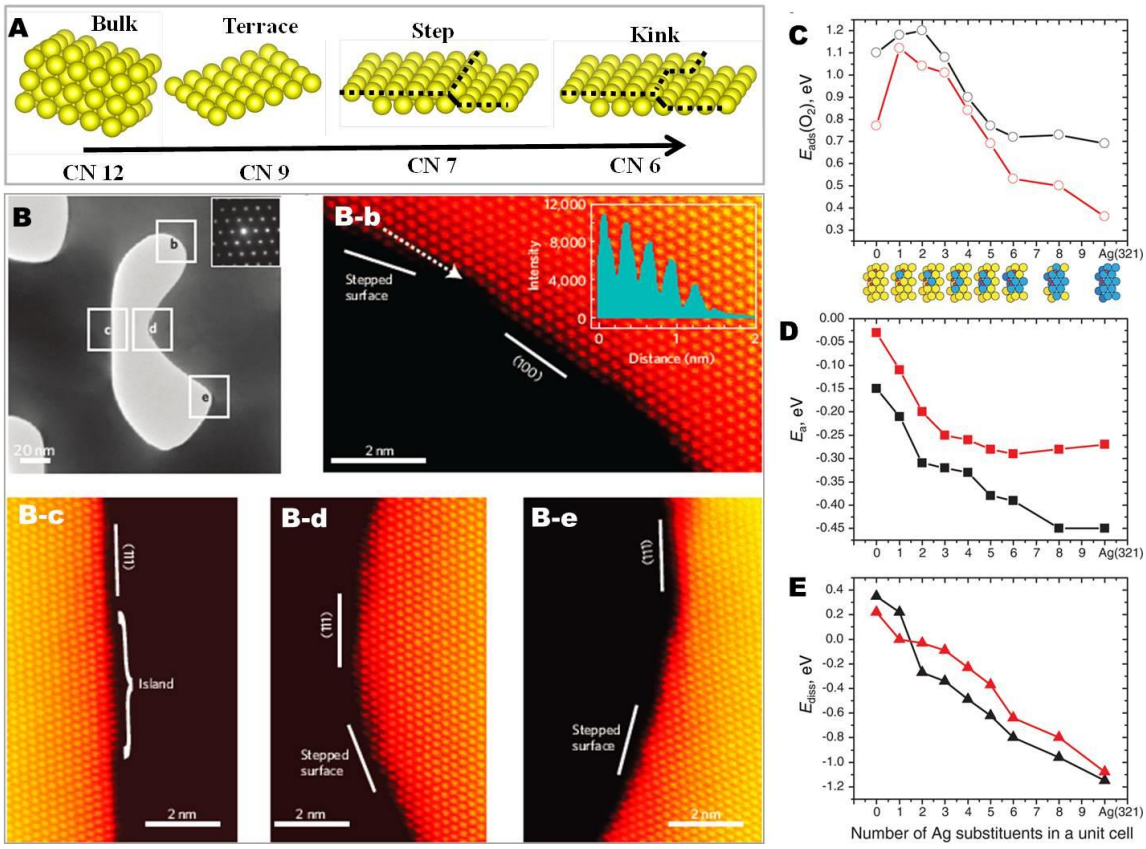

Figure 1.2. (A) Schemes illustrating of terrace, step edge, and kink site atoms with various undercoordinations generated during percolation dealloying. (B) HAADF-STEM images of four different sites from an individual Au nanoligament. Reprinted with permission from ref 25,[25] Copyright 2012 Springer Nature. (C) Adsorption energies of O_2, (D) the activation barrier for O_2 dissociation, and (E) the energy of dissociative adsorption (with respect to gas-phase O_2) as a function of the number of Ag substituents in the unit cell. Red and black lines indicate systems with and without co-adsorbed O, respectively. Transition state structures with co-adsorbed O are schematically depicted. Reprinted with permission from ref 45,[45] Copyright 2015 American Chemical Society.

However, it remains difficult to make a definitive conclusion that the presence of undercoordinated Au atoms is the exclusive reason for the remarkably active property of nanoporous Au catalysts. On the contrary, it is found that Au(211) surfaces of a typical step-terrace structure with high density of steps exhibit plain reactivity toward CO oxidation although showing strong CO chemisorption property which is an critical promotion factor for the reaction.[46] Besides, Friend et al. recently illustrated that even

extended Au (111) with oxygen atoms were seeded on the surface exhibited catalytic performance for selective oxidation of olefins, further indication the surface undercoordinated atoms were not the sole reason for active property of nanoporous-Au [47,4849]. Another study recently reported by Tao and co-workers shows that the nanoporous Au pretreated by ozone and then methanol which usually viewed as an efficient treatment for elimination of low coordination demonstrates highly active for selective oxidation of cyclohexene.[50] All these investigations suggest a more complex correlation of surface structure but not only surface atomic undercoordinations of nanoporous Au with its corresponding catalytic performance toward specific chemical reactions.

1.2.2 Residual Elements

As we mentioned in the section of nanoporous Au fabrication, it is well known that the less-noble elements could not be completely removed through percolation dealloying. It is later found that the contribution of residues such as Ag or Cu to the reactivity of nanoporous Au catalysis cannot be ignored. The earlier studies have demonstrated the critical role of Ag in boosting the catalytic activity of Au powders as well as Ag content-dependent activity of Au-Ag alloy toward CO oxidation because the Ag atoms probably provide specific sites for the dissociation of O_2 (oxygen activation) which is essential for oxide reactions.[51] While the content of the residual metal is low to 1 at %, it can enrich (segregate) at the surface and promote the molecular oxygen activation and thus improve the reactivity of nanoporous Au especially for oxidation reactions. This inference is well supported by the observation that the residual Ag provides more active sites for dissociative O_2 adsorption and greatly modifies the reactivity of the porous Au towards CO catalytic oxidation.[25] The promoting role of Ag is also confirmed by the recent study

showing an increase in the binding energy of molecular oxygen on Au surfaces by introducing Ag atoms in the surface region,[52] which is further verified by the theoretical analysis of the Au(321) model surface revealing the substituting surface Au atoms with Ag significantly reduce the O_2 dissociation barrier and can hence facilitate O_2 activation (Figure1.2C).[45] Besides, the residual Cu also has been reported to function as the similar role in enhancing the catalytic activity of porous Au membrane.[16]

More importantly, the selectivity as well as the overall durability of dealloyed nanoporous Au could also be dramatically improved by introduction of residual less-noble metals into Au matrix. The experiments conducted by Wittstock and co-workers showed methanol could be selectively oxidized into methyl formate and CO_2 on nanoporous Au samples with the same morphology but different amounts of residual Ag. A high Ag content (10 at %) facilitated the complete methanol combustion, while a low concentration (1 at %) promoted the partial oxidation product methyl formate.[14] In addition, Erlebacher and co-workers suggested small amounts of Pt added to the bulk of Ag-Au alloy membranes could accumulate around the surface atomic step edges to stabilize the undercoordinated atoms during percolation dealloying.[19] The reactivity of nanoporous Au modified by the residual Ag probably resulted from a local change of the d-band structure of Au due to the incorporation of residual metal into Au matrix or oxygen dissociation on Ag patches which then deliver the oxygen to the Au. The Ag distribution obviously has a profound influence on the catalytic mechanism,[36] whereas the present format of Ag on the nanoporous Au surface, pure Ag islands or intermixture with Au is difficult to accurately figure out, which might closely relate to the catalytic selectivity of nanoporous Au. For instance, Tao et al. recently presented nanoporous Au

with a Au-Ag alloy surface facilitated the formation of cyclohexene oxide during cyclohexene oxidation, while silver oxide surface could oxidize cyclohexene into cyclohexenyl hydroperoxide.[50] Similarly, Bäumer et al. also suggested that catalytic activity of nanoporous Au was likely dependent on the distribution and chemical state of surface Ag while undergoing different reaction mediums,[53] although their early study claimed there was no direct correlation between the catalytic activity and Ag amount at the nanoporous surface for CO oxidation at low temperature range.[36] Whereas it must emphasize that the pure np-Au made by electrochemical method that does not contain any residual Ag or other promoting elements like Cu demonstrated outstanding electro-oxidation activities,[54] indicating the synergistic effect but not the essential role of residues in reactivity of porous Au catalysis. The functions of residual less-noble metals in dealloyed nanoporous Au catalyst is a complex issue, various factors including the content, the distribution, and the chemical state, as well as the synergetic effects between each other, should be seriously taken into account to elucidate the effect of residual promotion elements.

1.2.3 Others

While it remains a controversial field about the intrinsic reactivity of nanoporous Au, it's worth to point out the origin of the catalytic activity and the active state surface of nanoporous Au catalysts also closely relate to the specific reactions and the surrounding reaction medium as well. For example, the nanoporous Au catalyst that is highly reactive for selective oxidative coupling of methanol showing no active for CO oxidation under standard operation conditions, although both reactions critically depend on O_2 activation.[47] In addition to the residual less noble metals, the Au-based nanoporous

materials containing un-leachable noble metals have also been of great interest due to their enhanced electrocatalytic performances and stability in electrochemical reactions compared with the monometallic nanoporous metals as a consequence of the alloy effect.[55] It is found that the catalytic activities of the nanoporous Au catalysts also showed strong dependence on the atomic ratio of Au and impure metal leftover such as Ag and Pd. For instance, Chen et al. demonstrated that the nanoporous PdAu catalyst with an optimal composition of $Au_{25}Pd_{75}$ possessed superior activity toward ethanol oxidation.[56] Generally, it is a case to case definition of the reactivity of nanoporous Au strongly dependent on the specific reaction, reaction environment, surface structures, et al.

1.3 Architectural Control of Porous Au Nanocatalyst

Very recently, Au catalysis has been further extended from dealloyed macroscopic membranes to particulate porous nanoarchitectures because dealloyed spongy nanoparticles exhibit a unique set of advantages in terms of catalytic performance, materials processing, reproducibility, and architectural tunability. First, a unique open system of a porous nanoparticle greatly promotes the accessibility for the catalytically active sites by the reactant molecules and a confined inside space allows easy diffusive fluxes of products, while both reactants and products must overcome long diffusion distances and convoluted paths to reach and escape from the actively reaction sites covered inside of a macroscopic nanoporous membrane. In that case, the product molecules might be concentrated within a shallow region near the outer surface of the nanoporous Au foam, leaving the majority of the material unused. Additionally, the natural structural heterogeneity due to significant difference in pore and ligament dimensions from the outer surface to the interior region of a bulk Au porous foam, gives

a rise to more complicated overall kinetics of the surface-catalyzed molecular transformations. These issues could be overcome by switching from bulk materials to nanoparticles which possess uniform ligament thickness and pore size as well as easily accessible 3D open surface structure. Second, colloidal nanoparticles can be made into an easily processable ink, which provides feasibility for direct assembly particles on a large variety of electrode substrates. Such convenient materials processing opens up great opportunities of colloidal porous nanoparticles for constructing high-performance but low-cost electrocatalysts in a wide range of applications such as electrolyzers and fuel cells. Lastly but most importantly, nanoparticulate alloy particles may undergo substantially more complex structural transformations in comparison to their macroscopic bulk counterparts exposure a planar surface to electrolyte during dealloying process. Therefore, architectural diversity and tunability of alloy nanoparticles offers a unique strategy to fine-tailor a series of geometric and compositional parameters and eventually fine-tune the catalytic properties of the dealloyed porous nanostructures at a level of precision and versatility that is unachievable on those dealloyed bulk materials. A diversity of porous nanoparticles with precisely controlled architectures such as a sponge-like particle with hierarchical nanoporosity[57,58] and a skeletal nanoframe covered by a noble metal skin[59,60] have been effectively achieved through percolation dealloying under appropriative conditions. The controllable introduction of porosity into metallic nanoparticles gives rise to promising properties and performances of the dealloyed porous nanoparticles. It has been shown that the dealloying-induced skeletal Pt_3Ni nanoframes with uniform hollow interior and well-defined open structures achieved a factor of 36 enhancement in mass activity in comparison to state-of-the-art Pt/C catalysts

toward oxygen oxidation reaction (ORR).[59] The spongy-like Pt nanoparticles by selective leaching Cu from $PtCu_3$ alloy nanoparticles exhibited drastically enhanced catalytic activity and durability for ORR as a consequence of the large electrochemical surface area and surface-to-volume ratio.[61] Nanoporous gold disks as surface-enhanced Raman scattering (SERS) substrate demonstrates a higher enhancement factor than that of nanoporous Au films.[62] In this section, we mainly highlight the current work on architectural control as well as structure-composition-property relationships underpinning the catalytic behaviors of the dealloyed porous Au nanoparticles as catalysts. The key thermodynamic, kinetic, and geometric factors dictating the structural evolution of multimetallic alloy nanoparticles during nanoporosity-evolving percolation dealloying have been discussed in details. The future challenges and outlooks on the structural control and catalytic optimization have also been touched.

1.3.1 Percolation Dealloyig

Similar but more complicated nanoporisity-evolving procedure relative to bulk alloy materials. It has been found the percolation dealloying of nanoscale alloy particles strongly depends on not only compositional stoichiometry, but also on particle size, crystalline structures, intraparticle compositional gradients of the starting alloy nanostructures, and dealloying condition as well. For example, Au-Ag nanoparticles with size larger than 10 nm evolved into nanospongies analogous to the behavior observed for the corresponding bulk alloy, while their sub-10 nm counterparts transformed into core-shell nanoparticles under identical dealloying conditions. Therefore, alloy nanoparticles beyond ~10 nm in size typically undergo dealloying-induced structural transformations analogous to those of their bulk counterparts with the same compositions. It is well

known that the nanoporosity evolution during percolation dealloying is synergistically dictated by two interplaying processes, pore expansion and ligament coarsening. For an alloy nanoparticle, the pore expansion is caused by the faster outward migration of less-noble metals than the inward migration of Au atoms in the alloy matrix, which is known as Kirkendall effect,[63] leading to increased overall particle size and pore volume during the nanoporisity evolving process. Ligament coarsening, on the other hand, results in thickening of the nanoligaments, decrease of overall particles size, and rearrangement of undercoordinated surface atoms into thermodynamically more stable close-packed configurations. One can speculate that a precise control over the nanoporosity evolution process and final architectural structures of dealloyed nanoparticles could be achieved by well balance of these two key factors. While independent kinetic control of these two processes remains a huge challenge because of their strong synergistic effect, the rates of ligament coarsening and pore expansion are both intimately tied to the leaching rate of less noble element, which can be rigorously maneuvered through choosing appropriate condition under which dealloying occurs. The redox potential and the concentration of the etchant as well as the dealloying temperature are all crucial factors determining the leaching rate of less noble metal. Our recent experimental observation shows the ligament thickness and pore volume as well as compositional stoichiometry could be systematically tuned through kinetically control of Cu leaching rate by exposure of Au-Cu binary alloy nanospheres to different etchants because the dealloying ends up with different thermodynamic equilibrium points determined by the natural standard redox potential of the etchant.[64] It has also demonstrated the partially dealloyed porous nanoparticle with different pore sizes, ligament thicknesses, and Au/Cu stoichiometries

could be kinetically trapped by separating the particles from the etchants.

Furthermore, incorporating a third element into a binary alloy nanoparticle provides another effective strategy to tune the final structures of the dealloyed nanoparticles during the nanoporosity-evolving dealloying process by modifying the atomic diffusion rate, which can be dated back to early 1990s. Addition of a small concentration of arsenic into Cu-Zn brasses effectively suppressed the dealloying due to the pinning of mobile Cu atomic step edges by surface-segregated arsenic.[65] Similarly, the recent relevant investigations have also found that tiny amount of Pt incorporation could segregate around the surface atomic step edges against ligament coarsening and significantly improved the stability of nanoporous Au membranes.[19,66] We also successfully generated the spongy Au nanoparticles with thinner nanoligaments and small pore sizes by percolation dealloying of Au-Ag-Cu ternary alloy nanoparticles.[67] Although it is hard to determine the exact location of the residual Ag atoms, as an outcome, it is clear to observe that the presence of Ag drastically accelerated the Cu leaching and led to much thinner nanoligaments with high surface-to-volume ratio of the final porous product in comparison with those of the dealloyed particles from Au-Cu binary alloy without Ag. Besides, a positive potential above the critical potential coupling with chemical etching might also could be applied to drive and modify the nanoporosity evolution.[37] All these discoveries lay a solid knowledge foundation to further develop detailed understanding of the intriguing structural transformations of multimetallic nanoparticles and enable us to fine-tune structures and compositions of the dealloyed spongy nanoparticles through rationally experimental design and finally pave a way to optimize their catalytic performances.

1.3.2 Galvanic Replacement Reactions

Galvanic replacement provides another robust but versatile approach to controllably transform a solid monometallic nanoparticle into a diverse set of architecturally more sophisticated multimetallic hollow nanostructures (Figures 1.3A and 1.3B).[68] Galvanic replacement occurring on metallic nanoparticles is essentially a unique nanoscale redox process that are unrealizable for bulk material systems, in which less noble metals get oxidized and dissolved accompanied by the reduction and deposition of noble metals on the sacrificial template surfaces. The resulting architectures are essentially determined by the intrinsic nature of sacrificial templates including redox potential, lattice mismatch between the replaced and deposited metals, atomic interdiffusion during the reaction, as well as the external effects companied with the reaction like chemical leaching, co-reduction, or surface passivation under the conditions that galvanic replacement occur. Over the past two decades, the model system intensively investigated has been single-crystalline Ag nanocubes, which evolve into a diverse set of multimetallic hollow nanostructures, such as nanobox, nanocage, or nanoframe upon straightforward galvanic replacement of Ag with Au, Pd, or Pt under deliberately controlled synthetic conditions (Figures 1.3C-1.3E).[69-73] While by employing sophisticated multimetallic hetero-nanostructures as the sacrificial templates, well-defined nanoparticles with more complicated interior and surface architectures, such as yolk-shell nanorattles,[74] multilayered nanomatryoshkas,[75] and ultrathin skeletal nanoframes [76] also become experimentally available.

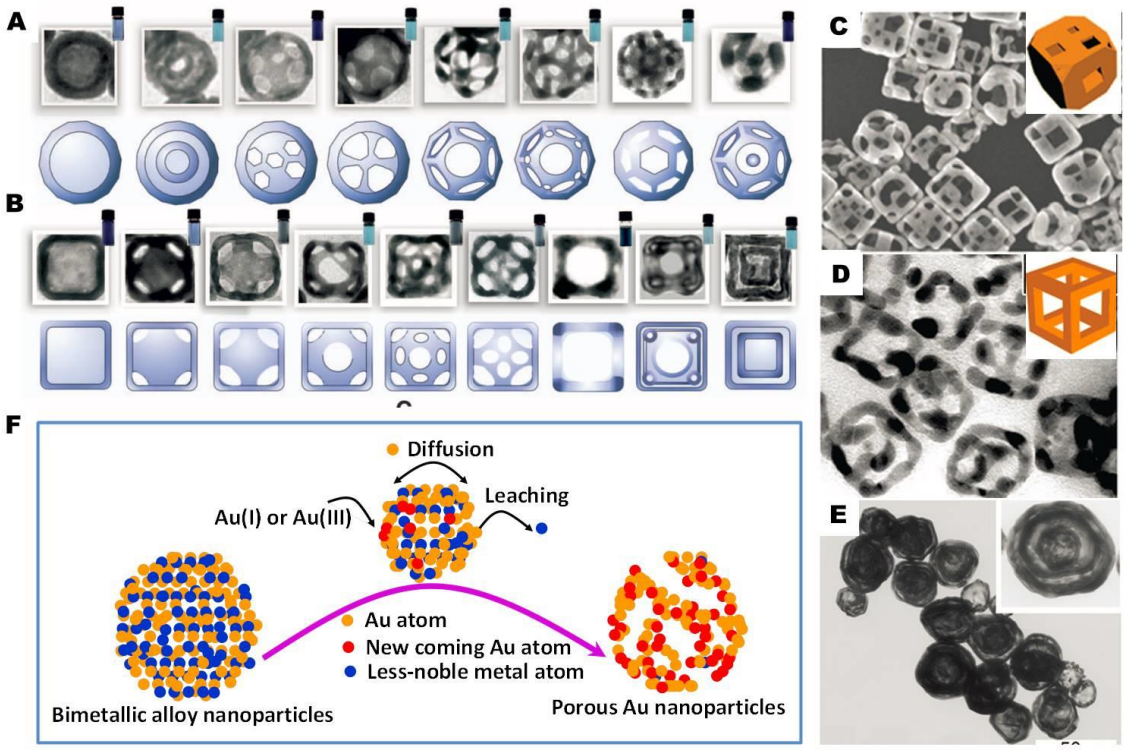

Figure 1.3. TEM images and the corresponding geometric morphology of various spherical (A) or cubic (B) hollow nanostructures obtained through galvanic-replacement reaction. Reprinted with permission from ref 68,[68] Copyright 2011 American Association for the Advancement of Science. (C) SEM image of Au nanocages obtained by galvanic replacement of pure Ag nanocubes by $HAuCl_4$. Reprinted with permission from ref 72,[72] Copyright 2004 American Chemical Society; (D) TEM image of Au nanoframes obtained by combining galvanic replacement and wet chemical etching. Reprinted with permission from ref 73,[73] Copyright 2007 American Chemical Society. (E) TEM image of multiple-walls of Au-Ag alloy nanoshells obtained by galvanic replacement of Au-Ag alloy core and Ag shell heteronanostructures. Reprinted with permission from ref 71,[71] Copyright 2004 American Chemical Society. (F) Schemes illustrating the formation of porous Au nanoparticles through the galvanic replacement of Au-containing bimetallic nanostructures.

Atomically intermixed bimetallic nanocrystals adopting either disordered alloy configurations or ordered intermetallic structures [77-79] may undergo galvanic replacement reaction-driven structural transformations that are substantially more sophisticated and versatile than those of monometallic nanocrystals or phase-segregated bimetallic heteronanostructures, when key structure-evolutionary pathways, less-noble metal dealloying, new noble-metal deposition, and Kirkendall diffusion are taken into

considerations, as illustrated in Figure 1.3F. More importantly, because of the strong oxidation capability of noble metal precursors such as $HAuCl_4$ and H_2PtCl_6 that commonly used to replace of less-noble metals, the nonoporousity evolutions of binary alloy with less-noble metal content below parting limit that are restricted by chemical/electrochemical percolation dealloying become achievable through galvanic replacement reaction. Thus it is expected to bring us more possibilities for constructing new porous architectures, for example, yolk-shell nanostructures, nanocages, or nanoshells, by using atomically well intermixed bimetallic nanoparticles as sacrificial templates during galvanic replacement reaction. Moreover, it is also demonstrated increasingly sophisticated interior and surface architectures, such as trimetallic hollow nanostructures and octahedral nanorattles have been controllably achieved by coupling galvanic replacement with kinetically controlled co-reduction, corrosion, or seed-mediated growth.[80,81] Therefore, it is also hypothesized that a modified galvanic replacement coupling with percolation dealloying or co-deposition could be able to achieve a new novel for precise control the surface composition and structure of the porous Au structures.

1.4 Catalytic Performance of Dealloyed Au Porous Nanoparticles

The precise control over architectural transformations of multimetallic nanoparticles through deliberately maneuvered dealloying induced by chemical etchants, applied anodic potentials or galvanic replacements, lays the foundation for us to quantitatively unravel the structure-composition-property correlations that underpin the catalytic behaviors of dealloyed porous nanocatalysts. In this section we mainly discuss current progress regarding the effects of several typical characteristics of dealloyed porous Au

nanocatalysts on their catalytic performances including catalytic activity and durability as well as selectivity toward various chemical or electrochemical reactions.

1.4.1 Optimization of Catalytic Activity

The representative factors that have usually been used to evaluate the catalytic activity of a catalyst are mass-specific activity and surface-specific activity. The specific surface area of a nanoparticle accessible for catalysis may drastically increase upon dealloying when a solid alloy nanoparticle is converted into a porous nanostructure with hollow interior and open surface structures. The enormous surface-to-mass and surface-to-volume ratios of the dealloyed spongy nanoparticles are highly advantageous for achieving superior mass-specific activities, which becomes especially crucial when precious noble metals, such as Au, Pt, and Pd, are used as the catalysts. The surface-specific activity of the nanoparticles, on the other hand, may also be greatly enhanced upon dealloying as a consequence of two intrinsically interconnected effects, geometric and electronic effects, both of which are intimately tied with the nature and density of the active sites on the nanoligament surfaces. It has been demonstrated that the primary surface active sites for electrocatalytic alcohol oxidation are the undercoordinated surface atoms located at the particle corners, edges, or the steps for noble metal nanoparticles, while the close-packed surface atoms on thermodynamically stable facets, such as [111] and [100] facets, are drastically less active.[42,82]

1.4.2 Enhancing the Catalytic Durability

The dealloyed macroscopic or nanoscale Au-rich porous materials comprising nanoligaments, despite their remarkable initial activities, inevitably undergo activity deterioration over time largely due to surface area/mass ratio decrease and loss of surface

active sites as a consequence of the thermodynamically driven ligament coarsening during the catalytic reactions. It has been evident that the residual less-noble elements can well preserve the nanoligament surface active sites during the catalytic reactions and remarkably improve the catalytic durability of the dealloyed Au porous foam,[25] although Erlebacher's nanoporosity-evolution model claims that less-noble residual elements remain alloyed with Au and homogeneously distributed in the ligaments.[17] The essential role of leachable residues introduced by co-leaching multiple less noble metal elements from multimetallic alloy nanoparticles or coupling galvanic replacement reactions in enhancing the catalytic durability of the dealloyed nanocatalysts arouses our great curiosities to investigate the effects of less-noble but nonleachable elements on catalytic behaviors of porous Au nanocatalysts. We assume the catalytic durability can be optimized by incorporation residual elements such as Ag or Pt into dealloyed porous Au nanoparticles because the surface atomic mobility of Pt is significantly lower than that of Au and Pt may locally accumulate around atomic step edges of Au to stabilize the undercoordinated Au surface atoms or form robust Au-Pt skin on the nanoligaments. Moreover, it is well known that porous Au nanoparticles demonstrated promising catalytic activity mainly in alkaline environment but Pt catalysts perform well in acidic condition,[20] thus we speculate it might be able to expand reactivity to acidic or neutral conditions for Au nanocatalysts by doping Pt as a consequence of the Au surface property modified by residual Pt. The catalytic activity as well as the durability may be optimized by tuning the abundance of residues.

1.4.3 Improving of Catalytic Selectivity

Equally important to the catalytic activity and durability is the selectivity of a

nanocatalyst toward particular reactions of interest, how to optimize the catalytic selectivity of Au nanocatalyst, nevertheless, remains a big challenge. Although this problem can be overcome by using (precious-metal catalysts) oxides-supported ultrasmall Au nanoparticles or Au nanoclusters for certain oxidation or hydrogenation reactions,[83-86] it is found that the selectivity strongly depends on the interaction between Au and the support and surface ligand modification. Wittstock and co-workers reported the dealloyed support-free microscopic Au foam showed selective gas-phase oxidative coupling of methanol but with residual Ag as a "helper" which played a crucial role in manipulating the selectivity by regulating the availability of reactive oxygen on the surface during the gas reaction.[14] Therefore, it has been long open questions and seems unexceptional to investigate the selectivity of dealloyed porous of Au nanocatalysts toward surface-catalyzed reactions due to their substantially more complicated surface structures. Inspired by the close correlation between catalytic performance and atomic-level surface structure over polyhedral Au nanocrystals enclosed by specific types of well-defined low-index and high-index facets with different surface atomic coordination numbers,[87-90] we thus hypothesize the catalytic selectivity of Au nanocatalyst is intimately tied to the surface atomic coordination numbers. In contrast to the achievement in fine-tuning of surface atomic-level structure through facet control, precise control over the local environment at an atomic level of dealloyed Au porous nanoparticles seems an extremely challenging task because highly curve nanoligaments obtained through percolation dealloying of atomic well-mixed random alloy nanoparticles are dominated by substantially more complicated surface comprising a mixture of various crystal facets. On basis of the our precious understanding of architectural control, the dealloying behaviors

of the nanoparticles might be modified by exposure nanoparticle of intraparticle compositional gradient or ordered intermetallics upon dealloying environments and generate dealloyed particles with obviously different local surface structures, which might provide us an intriguing system to make the catalytic selectivity of the dealloyed Au porous nanoparticles achievable. In addition, it also speculates selectivity to specific reactions possibly can be realized through incorporation of residues, in the presence of pure components or intermixed with Au on the Au nanoligament surfaces, which probably has a great impact on the geometric and electronic properties and thus catalytic property of porous Au nanoparticles.

1.5 Outline of the Dissertation

This dissertation is primarily focused a Synthesize-Measure-Correlate strategy, integrating research efforts on architectural control of nanoparticles, structure and property characterizations, and elucidation of detailed structure-composition-property relationships. I first focus on the fabrication and percolation dealloying of Au-Cu binary alloy nanoparticles as a model system and then expand the materials systems of interest to multimetallic nanoparticles systems that are structurally more sophisticated and compositionally more diverse. Two main aims are covered in the motivations behind this research: (a) to pinpoint the effects of key thermodynamic, kinetic, and geometric factors dictating the architectural evolution of multimetallic alloy nanoparticles during nanoporosity-evolving percolation dealloying; (b) to develop quantitative understanding of detailed structure-composition-property relationships underpinning the electrocatalytic behaviors of dealloyed spongy nanoparticles. In chapter 2, I demonstrate upon thermal annealing in a reducing atmosphere, Au@Cu_2O core-shell nanoparticles transform into

Au-Cu alloy nanoparticles with tunable compositional stoichiometries that are predetermined by the relative core and shell dimensions of their parental core-shell nanoparticle precursors. The Au-Cu alloy nanoparticles exhibit distinct dealloying behaviors that are dependent upon their Cu/Au stoichiometric ratios. For Au-Cu alloy nanoparticles with Cu atomic fractions above the parting limit, nanoporosity-evolving percolation dealloying occurs upon exposure of the alloy nanoparticles to appropriate chemical etchants, resulting in the formation of particulate spongy nanoframes with solid/void bicontinuous morphology composed of hierarchically interconnected nano-ligaments. The dealloyed nanoframes possess two unique structural features, large open surface areas accessible by the reactant molecules and high abundance of catalytically active undercoordinated atoms on the ligament surfaces, both of which are highly desirable for high-performance electrocatalysis. Using the room temperature electro-oxidation of methanol as a model reaction, we further demonstrate that through controlled percolation dealloying of Au-Cu alloy nanoparticles, both the electrochemically active surface areas and the specific activity of the dealloyed metallic nanoframes can be systematically tuned to achieve the optimal electrocatalytic activities. In chapter 3, I report that incorporation of Ag into Au-Cu binary alloy nanoparticles substantially enhances the Cu leaching kinetics while effectively suppressing ligament coarsening during nanoporosity-evolving percolation dealloying, enabling us to optimize both the specific surface areas and specific activities of the dealloyed Au nanosponge particles for electrocatalytic oxidation of alcohols. The residual Ag in the dealloyed nanosponge particles plays crucial roles in stabilizing the surface active sites and maintaining the specific surface areas during electrocatalytic reactions, thereby greatly

enhancing the durability of the electrocatalysts. The insights gained from this work shed light on the underlying roles of residual less-noble elements that are crucial to the rational optimization of electrocatalysis on noble metal nanostructures. In chapter 4, I find that colloidal Au@Cu_2O core-shell nanoparticles undergo stepwise structural transformations to sequentially evolve into Au@Cu core-shell nanoparticles, alloy nanoparticles with compositional gradient (Alloy-G), and homogeneous alloy nanoparticles (Alloy-H) upon thermal heating in polyol solution. By varying the reaction temperatures, we can maneuver the reactions kinetics to control the intraparticle compositional gradient. Upon percolation dealloying, the Alloy-G bimetallic nanoparticles gradually evolve into nanoparticles with solid Au cores surrounded by nanoporous shells, whereas Alloy-H nanoparticles transform into spongy nanoparticles that are nanoporous throughout the entire particles. The dealloyed nanoparticles possess different surface atomic undercoordinations, which result in their selectively catalytic behaviors toward an important electrocatalytic reaction. This provides a unique way of achieving catalytic selectivity optimization of Au nanocatalysts through deliberate control over the percolation dealloying of bimetallic nanoparticles with interior compositionally gradients. In chapter 5, using Au-Cu alloy and intermetallic nanoparticles as structurally and compositionally fine-tunable bimetallic sacrificial templates, I show that atomically intermixed bimetallic nanocrystals undergo galvanic replacement-driven structural transformations remarkably more complicated than those of their monometallic counterparts. I interpret the versatile structure-transforming behaviors of the bimetallic nanocrystals in the context of a unified mechanistic picture that rigorously interprets the interplay of three key structure-evolutionary pathways, dealloying, Kirkendall diffusion,

and Ostwald ripening. By deliberately tuning the compositional stoichiometry and atomic-level structural ordering of the Au-Cu bimetallic nanocrystals, I have been able to fine-maneuver the relative rates of dealloying and Kirkendall diffusion with respect to that of Ostwald ripening, through which an entire family of architecturally distinct complex nanostructures are created in a selective and controllable manner upon galvanic replacement reactions. The insights gained form my systematic comparative studies form a central knowledge framework that allows us to fully understand how multiple classic effects and processes interplay within the confinement by a nanoparticle to synergistically guide the structural transformations of complex nanostructures at both the atomic and the particulate levels. In chapter 6, I endeavor to further push the structural and compositional control of multimetallic hollow nanostructures to a new level of precision and sophistication by coupling the percolation dealloying with galvanic replacement using bimetallic nanoparticles as initial sacrificial templates. I show that spongy NPs with ultrathin nanoligaments comprising Au-Cu alloy cores and Au-Pt alloy shells could be controllably synthesized by galvanic replacement of $Au_{0.2}Cu_{0.8}$ alloy with H_2PtCl_6 in the presence of HCl. The thickness and the composition of the ligament could be precisely tailored by control over the Cu leaching rate determined by HCl concentration versus galvanic replacement rate. The unique ligaments feature greatly enhances the structural stability of the active sites on the ligament surfaces, allowing us to retain the superior catalytic activities over much longer periods toward alcohol oxidation reactions in both acidic and alkaline environments relative to the commercial Pt black. In chapter 7, through combination the GRRs with codeposition, I also demonstrate that architecture significantly different hollow nanoparticles including spongy-like

nanoparticles, Pt-decorated nanospongies, and nanoshells particles could be controllably fabricated by maneuvering the relative reaction rate between the galvanic replacement and the reduction reaction in different polyols that served as both reaction solvent and reducing agent under the same conditions. The catalytic performances of various Pt-based hollow nanostructures were evaluated by choosing electrochemical oxidation of formic acid and hydrogen evolution in acidic environments as model reactions. It is found that the spongy-like nanoparticles with ultrathin nanligaments comprising Au-Cu alloy cores and Au-Pt shells exhibit superior catalytic activities compared with commercial Pt/C catalyst. In chapter 8, I systematically investigate the epitaxial growth of both face-centered cubic (fcc) and hexagonal close-packed (hcp) Ni on fcc Au nanocrystal seeds in polyol solvents to shed light on the complex mechanisms underpinning the intriguing geometric evolution of lattice-mismatched bimetallic nanocrystals during seed-mediated heteroepitaxial overgrowth. My success in geometry-controlled syntheses of a series of Au-Ni bimetallic heteronanostructures, such as conformal core-shell nanoparticles, asymmetric heterodimers, and multibranched core-satellite nanocrystals, represents a significant step toward the extension of nanoscale interfacial heteroepitaxy from lattice-matched bimetallic systems to the ones exhibiting large lattice mismatches and even dissimilar crystalline structures. The insights gained from this work serve as a central design principle that guides the development of new synthetic approaches to architecturally sophisticated and compositionally diverse multimetallic heteronanostructures.

1.6 References

(1) Shastri, A. G.; Datye, A. K.; Schwank, J., *J Catal* **1984**, 87, 265.

(2) Masatake, H.; Tetsuhiko, K.; Hiroshi, S.; Nobumasa, Y., *Chem Lett* **1987**, 16, 405.

(3) Hvolbæk, B.; Janssens, T. V. W.; Clausen, B. S.; Falsig, H.; Christensen, C. H.; Nørskov, J. K., *Nano Today* **2007**, 2, 14.

(4) Valden, M.; Lai, X.; Goodman, D. W., *Science* **1998**, 281, 1647.

(5) Hughes, M. D.; Xu, Y.-J.; Jenkins, P.; McMorn, P.; Landon, P.; Enache, D. I.; Carley, A. F.; Attard, G. A.; Hutchings, G. J.; King, F.; Stitt, E. H.; Johnston, P.; Griffin, K.; Kiely, C. J., *Nature* **2005**, 437, 1132.

(6) Baker, T. A.; Liu, X.; Friend, C. M., *Phys Chem Chem Phys* **2011**, 13, 34.

(7) Takale, B. S.; Feng, X.; Lu, Y.; Bao, M.; Jin, T.; Minato, T.; Yamamoto, Y., *J Am Chem Soc* **2016**, 138, 10356.

(8) Janssens, T. V. W.; Clausen, B. S.; Hvolbæk, B.; Falsig, H.; Christensen, C. H.; Bligaard, T.; Nørskov, J. K., *Top Catal* **2007**, 44, 15.

(9) Wittstock, A.; Bäumer, M., *Accounts Chem Res* **2014**, 47, 731.

(10) Lemire, C.; Meyer, R.; Shaikhutdinov, S.; Freund, H.-J., *Angew Chem Int Ed* **2004**, 43, 118.

(11) Yim, W.-L.; Nowitzki, T.; Necke, M.; Schnars, H.; Nickut, P.; Biener, J.; Biener, M. M.; Zielasek, V.; Al-Shamery, K.; Klüner, T.; Bäumer, M., *J Phys Chem C* **2007**, 111, 445.

(12) Green, I. X.; Tang, W.; Neurock, M.; Yates, J. T., *Science* **2011**, 333, 736.

(13) Tappan, B. C.; Steiner, S. A.; Luther, E. P., *Angew Chem Int Ed* **2010**, 49, 4544.

(14) Wittstock, A.; Zielasek, V.; Biener, J.; Friend, C. M.; Bäumer, M., *Science* **2010**, 327, 319.

(15) Asao, N.; Ishikawa, Y.; Hatakeyama, N.; Menggenbateer; Yamamoto, Y.; Chen, M.;

Zhang, W.; Inoue, A., *Angew Chem Int Ed* **2010**, 49, 10093.

(16) Kameoka, S.; Tsai, A. P., *Catal Lett* **2008**, 121, 337.

(17) Erlebacher, J.; Aziz, M. J.; Karma, A.; Dimitrov, N.; Sieradzki, K., *Nature* **2001**, 410, 450.

(18) Yantong, X.; Xi, K.; Changchun, Y.; Shaofang, L.; Jie, Z.; Guofeng, C.; Drew, H.; Zhongwei, C.; Qing, L.; Gang, W., *Nanotechnology* **2014**, 25, 445602.

(19) Snyder, J.; Asanithi, P.; Dalton, A. B.; Erlebacher, J., *Adv Mater* **2008**, 20, 4883.

(20) Xu, C.; Wang, R.; Chen, M.; Zhang, Y.; Ding, Y., *Phys Chem Chem Phys* **2010**, 12, 239.

(21) Ding, Y.; Kim, Y. J.; Erlebacher, J., *Adv Mater* **2004**, 16, 1897.

(22) Weissmüller, J.; Sieradzki, K., *Mrs Bull* **2018**, 43, 14.

(23) Sieradzki, K.; Dimitrov, N.; Movrin, D.; McCall, C.; Vasiljevic, N.; Erlebacher, J., *J Electrochem Soc* **2002**, 149, B370.

(24) Wittstock, A.; Wichmann, A.; Bäumer, M., *ACS Catalysis* **2012**, 2, 2199.

(25) Fujita, T.; Guan, P.; McKenna, K.; Lang, X.; Hirata, A.; Zhang, L.; Tokunaga, T.; Arai, S.; Yamamoto, Y.; Tanaka, N.; Ishikawa, Y.; Asao, N.; Yamamoto, Y.; Erlebacher, J.; Chen, M., *Nat Mater* **2012**, 11, 775.

(26) Ding, Y.; Erlebacher, J., *J Am Chem Soc* **2003**, 125, 7772.

(27) Qian, L. H.; Chen, M. W., *Appl Phys Lett* **2007**, 91, 083105.

(28) Yu, J.; Ding, Y.; Xu, C.; Inoue, A.; Sakurai, T.; Chen, M., *Chem Mater* **2008**, 20, 4548.

(29) Jia, F.; Yu, C.; Ai, Z.; Zhang, L., *Chem Mater* **2007**, 19, 3648.

(30) Huang, J. F.; Sun, I. W., *Adv Funct Mater* **2005**, 15, 989.

(31) Chiu, H.-Y.; Liu, Y.-C.; Hsieh, Y.-T.; Sun, I. W., *ACS Omega* **2017**, 2, 4911.

(32) Dong, H.; Cao, X., *J Phys Chem C* **2009**, 113, 603.

(33) Nishio, K.; Masuda, H., *Angew Chem Int Ed* **2011**, 50, 1603.

(34) Fang, C.; Bandaru, N. M.; Ellis, A. V.; Voelcker, N. H., *J Mater Chem* **2012**, 22, 2952.

(35) Cherevko, S.; Chung, C.-H., *Electrochem Commun* **2011**, 13, 16.

(36) Zielasek, V.; Jürgens, B.; Schulz, C.; Biener, J.; Biener, M. M.; Hamza, A. V.; Bäumer, M., *Angew Chem Int Ed* **2006**, 45, 8241.

(37) Xu, C.; Su, J.; Xu, X.; Liu, P.; Zhao, H.; Tian, F.; Ding, Y., *J Am Chem Soc* **2007**, 129, 42.

(38) Comotti, M.; Della Pina, C.; Matarrese, R.; Rossi, M., *Angew Chem Int Ed* **2004**, 43, 5812.

(39) Janssens, T. V. W.; Carlsson, A.; Puig-Molina, A.; Clausen, B. S., *J Catal* **2006**, 240, 108.

(40) Zeis, R.; Lei, T.; Sieradzki, K.; Snyder, J.; Erlebacher, J., *J Catal* **2008**, 253, 132.

(41) Falsig, H.; Hvolbæk, B.; Kristensen, I. S.; Jiang, T.; Bligaard, T.; Christensen, C. H.; Nørskov, J. K., *Angew Chem Int Ed* **2008**, 47, 4835.

(42) Zhang, J.; Liu, P.; Ma, H.; Ding, Y., *J Phys Chem C* **2007**, 111, 10382.

(43) Fujita, T.; Tokunaga, T.; Zhang, L.; Li, D.; Chen, L.; Arai, S.; Yamamoto, Y.; Hirata, A.; Tanaka, N.; Ding, Y.; Chen, M., *Nano Lett* **2014**, 14, 1172.

(44) Bai, F.; Sun, Z.; Wu, H.; Haddad, R. E.; Coker, E. N.; Huang, J. Y.; Rodriguez, M. A.; Fan, H., *Nano Lett* **2011**, 11, 5196.

(45) Moskaleva, L. V.; Weiss, T.; Klüner, T.; Bäumer, M., *J Phys Chem C* **2015**, 119,

9215.

(46) Kim, J.; Samano, E.; Koel, B. E., *J Phys Chem B* **2006**, 110, 17512.

(47) Personick, M. L.; Zugic, B.; Biener, M. M.; Biener, J.; Madix, R. J.; Friend, C. M., *ACS Catalysis* **2015**, 5, 4237.

(48) Min, B. K.; Deng, X.; Pinnaduwage, D.; Schalek, R.; Friend, C. M., *Phys Rev B* **2005**, 72, 121410.

(49) Zielasek, V.; Xu, B.; Liu, X.; Bäumer, M.; Friend, C. M., *J Phys Chem C* **2009**, 113, 8924.

(50) Dou, J.; Tang, Y.; Nguyen, L.; Tong, X.; Thapa, P. S.; Tao, F. F., *Catal Lett* **2017**, 147, 442.

(51) Wang, A.-Q.; Liu, J.-H.; Lin, S. D.; Lin, T.-S.; Mou, C.-Y., *J Catal* **2005**, 233, 186.

(52) Stowers, K. J.; Madix, R. J.; Biener, M. M.; Biener, J.; Friend, C. M., *Catal Lett* **2015**, 145, 1217.

(53) Wittstock, A.; Neumann, B.; Schaefer, A.; Dumbuya, K.; Kübel, C.; Biener, M. M.; Zielasek, V.; Steinrück, H.-P.; Gottfried, J. M.; Biener, J.; Hamza, A.; Bäumer, M., *J Phys Chem C* **2009**, 113, 5593.

(54) Huang, W.; Wang, M.; Zheng, J.; Li, Z., *J Phys Chem C* **2009**, 113, 1800.

(55) Chen, Q.; Tanaka, S.; Fujita, T.; Chen, L.; Minato, T.; Ishikawa, Y.; Chen, M.; Asao, N.; Yamamoto, Y.; Jin, T., *Chem Commun* **2014**, 50, 3344.

(56) Chen, L. Y.; Chen, N.; Hou, Y.; Wang, Z. C.; Lv, S. H.; Fujita, T.; Jiang, J. H.; Hirata, A.; Chen, M. W., *ACS Catalysis* **2013**, 3, 1220.

(57) Gan, L.; Heggen, M.; O'Malley, R.; Theobald, B.; Strasser, P., *Nano Lett* **2013**, 13, 1131.

(58) Li, X.; Chen, Q.; McCue, I.; Snyder, J.; Crozier, P.; Erlebacher, J.; Sieradzki, K., *Nano Lett* **2014**, 14, 2569.

(59) Chen, C.; Kang, Y.; Huo, Z.; Zhu, Z.; Huang, W.; Xin, H. L.; Snyder, J. D.; Li, D.; Herron, J. A.; Mavrikakis, M.; Chi, M.; More, K. L.; Li, Y.; Markovic, N. M.; Somorjai, G. A.; Yang, P.; Stamenkovic, V. R., *Science* **2014**, 343, 1339.

(60) Ding, J.; Bu, L.; Guo, S.; Zhao, Z.; Zhu, E.; Huang, Y.; Huang, X., *Nano Lett* **2016**, 16, 2762.

(61) Wang, D.; Yu, Y.; Xin, H. L.; Hovden, R.; Ercius, P.; Mundy, J. A.; Chen, H.; Richard, J. H.; Muller, D. A.; DiSalvo, F. J.; Abruña, H. D., *Nano Lett* **2012**, 12, 5230.

(62) Qi, J.; Motwani, P.; Gheewala, M.; Brennan, C.; Wolfe, J. C.; Shih, W.-C., *Nanoscale* **2013**, 5, 4105.

(63) Yin, Y.; Rioux, R. M.; Erdonmez, C. K.; Hughes, S.; Somorjai, G. A.; Alivisatos, A. P., *Science* **2004**, 304, 711.

(64) Li, G. G.; Villarreal, E.; Zhang, Q.; Zheng, T.; Zhu, J.-J.; Wang, H., *ACS Applied Materials & Interfaces* **2016**, 8, 23920.

(65) Newman, R. C., *Corros Sci* **1992**, 33, 1653.

(66) Vega, A. A.; Newman, R. C., *J Electrochem Soc* **2014**, 161, C1.

(67) Li, G. G.; Lin, Y.; Wang, H., *Nano Lett* **2016**, 16, 7248.

(68) González, E.; Arbiol, J.; Puntes, V. F., *Science* **2011**, 334, 1377.

(69) Skrabalak, S. E.; Chen, J.; Sun, Y.; Lu, X.; Au, L.; Cobley, C. M.; Xia, Y., *Accounts Chem Res* **2008**, 41, 1587.

(70) Chen, J.; Wiley, B.; McLellan, J.; Xiong, Y.; Li, Z.-Y.; Xia, Y., *Nano Lett* **2005**, 5, 2058.

(71) Sun, Y.; Wiley, B.; Li, Z.-Y.; Xia, Y., *J Am Chem Soc* **2004**, 126, 9399.

(72) Sun, Y.; Xia, Y., *J Am Chem Soc* **2004**, 126, 3892.

(73) Lu, X.; Au, L.; McLellan, J.; Li, Z.-Y.; Marquez, M.; Xia, Y., *Nano Lett* **2007**, 7, 1764.

(74) Cho, E. C.; Camargo, P. H. C.; Xia, Y., *Adv Mater* **2010**, 22, 744.

(75) Hong, S.; Acapulco, J. A. I.; Jang, H. Y.; Park, S., *Chem Mater* **2014**, 26, 3618.

(76) Hong, X.; Wang, D.; Cai, S.; Rong, H.; Li, Y., *J Am Chem Soc* **2012**, 134, 18165.

(77) Yan, Y.; Du, J. S.; Gilroy, K. D.; Yang, D.; Xia, Y.; Zhang, H., *Adv Mater* **2017**, 29, 1605997.

(78) Ferrando, R.; Jellinek, J.; Johnston, R. L., *Chem Rev* **2008**, 108, 845.

(79) Weiner, R. G.; Smith, A. F.; Skrabalak, S. E., *Chem Commun* **2015**, 51, 8872.

(80) Liu, Y.; Hight Walker, A. R., *ACS Nano* **2011**, 5, 6843.

(81) Polavarapu, L.; Zanaga, D.; Altantzis, T.; Rodal-Cedeira, S.; Pastoriza-Santos, I.; Pérez-Juste, J.; Bals, S.; Liz-Marzán, L. M., *J Am Chem Soc* **2016**, 138, 11453.

(82) Tian, N.; Zhou, Z.-Y.; Sun, S.-G.; Ding, Y.; Wang, Z. L., *Science* **2007**, 316, 732.

(83) Choudhary, T. V.; Sivadinarayana, C.; Datye, A. K.; Kumar, D.; Goodman, D. W., *Catal Lett* **2003**, 86, 1.

(84) Gross, E.; Liu, J. H.-C.; Toste, F. D.; Somorjai, G. A., *Nature Chemistry* **2012**, 4, 947.

(85) Tan, Y.; Liu, X. Y.; Zhang, L.; Wang, A.; Li, L.; Pan, X.; Miao, S.; Haruta, M.; Wei, H.; Wang, H.; Wang, F.; Wang, X.; Zhang, T., *Angew Chem Int Ed* **2017**, 56, 2709.

(86) Mitsudome, T.; Kaneda, K., *Green Chem* **2013**, 15, 2636.

(87) Quan, Z.; Wang, Y.; Fang, J., *Accounts Chem Res* **2013**, 46, 191.

(88) Zhang, Q.; Wang, H., *ACS Catalysis* **2014**, 4, 4027.

(89) Zhang, Q.; Han, L.; Jing, H.; Blom, D. A.; Lin, Y.; Xin, H. L.; Wang, H., *ACS Nano* **2016**, 10, 2960.

(90) Chiu, C.-Y.; Chung, P.-J.; Lao, K.-U.; Liao, C.-W.; Huang, M. H., *J Phys Chem C* **2012**, 116, 23757.

CHAPTER 2

CONTROLLED DEALLOYING OF ALLOY NANOPARTICLES TOWARD OPTIMIZATION OF ELECTROCATALYSIS ON SPONGY METALLIC NANOFRAMES

2.1 Introduction

Multi-metallic nanoparticles (NPs), either heteronanostructures or homogeneous alloys, may undergo intriguing post-synthesis structural transformations upon intraparticle atomic migrations triggered by thermal,[1] electrical,[2] or chemical stimuli,[3] providing a unique way to deliberately fine-tailor the geometries and thereby fine-tune the optical, electronic, and catalytic properties of the NPs. The chemical or electrochemical dealloying of metallic alloy materials, which involves selective leaching of the less-noble components from the alloy matrices accompanied by structural remodeling of the more-noble components, represents an intriguing structural rearrangement that entangles multiple surface and bulk atomic dissolution and migration processes over the nanometer length-scale.[4] A prototypical system of particular interest has been the percolation dealloying of bulk membranes of Au-Ag bimetallic alloys, which results in the formation of a unique solid/void bicontinuous nanoporous structure consisting of a three-dimensional (3D) network of hierarchically interconnected Au-rich nano-ligaments.[4-6] In striking contrast to the bulk Au films that are catalytically inactive, the dealloyed nanoporous Au membranes exhibit exceptionally high catalytic activities commensurate with those of the oxide-supported sub-5 nm Au NPs that have long been used for heterogeneous catalysis.[6,7] The locally curved surfaces of the nano-ligaments are essentially enclosed by high densities of undercoordinated surface atoms, which serve as the active sites for catalyzing a series of interfacial chemical and electrochemical reactions.[7-9]

Alloy NPs may undergo dealloying-induced structural transformations that are substantially more complicated than those of their macroscopic bulk alloy counterparts

displaying a planar surface to the electrolyte. Upon dealloying, an alloy NP may evolve into a variety of distinct nanostructures, such as a core-shell heterostructure with a noble metal shell encasing an alloy core,[10-13] a sponge-like particle with hierarchical nanoporosity,[10-13] or a skeletal nanoframe (NF) covered by a noble metal skin,[14-16] depending on the size, crystalline structure, compositional stoichiometry, and compositional gradient of the starting alloy NPs as well as the conditions under which the dealloying occurs. While each one of these structural transformations gives rise to drastically enhanced catalytic activities,[10,13,14,17,18] the origin of the catalytic enhancements cannot be simply interpreted in the context of a single unified mechanism because multiple effects interplay and contribute synergistically to the overall catalytic activities. The specific surface area of a NP accessible for catalysis may drastically increase upon dealloying, especially when a solid alloy NP is converted into either a skeletal NF or a spongy nanoporous particle with hollow interior and open surface structures.[10,14,18] The specific catalytic activity of the NPs, on the other hand, may also be greatly enhanced upon dealloying as a consequence of two intrinsically interconnected effects, geometric and electronic effects, both of which are intimately tied with the density and nature of the active sites on the NP surfaces.[2,19-21] Unraveling the detailed structure-composition-activity correlations that underpin the intriguing catalytic behaviors of the dealloyed metallic NPs, however, has long been a challenging task due to the intrinsic structural and compositional complexity and diversity of the materials systems as well as lack of a versatile approach through which both the specific surface area and specific catalytic activity of a dealloyed NP can be precisely fine-tuned.

Here we endeavor to push the structural control of dealloyed metallic nanocatalysts to

an unprecedented level of precision and versatility with the goal of paving an avenue toward the rational optimization of electrocatalysis. Dealloyed spongy nanoframes (NFs) represent a particularly interesting geometry with unique structural characteristics highly desirable for electrocatalysis. The enormous surface-to-volume and surface-to-mass ratios of the spongy NFs are highly advantageous for achieving superior mass activities, which become especially crucial when precious noble metals, such as Au, Pt, and Pd, are used as the catalysts.[14,22-24] On the other hand, the locally curved surfaces of the nano-ligaments are rich of catalytically active sites occupied by coordinatively unsaturated surface atoms.[8,9] Using the methanol electro-oxidation as a model reaction, we demonstrate that both the catalytically active surface area and the density of active sites on the surfaces of spongy NFs can be deliberately tuned toward the optimization of electrocatalysis through controlled percolation dealloying of Au-Cu alloy NPs under mild conditions.

2.2 Experimental Section

Chemicals and Materials Polyvinylpyrrolidone (PVP, average MW 58,000), $Cu(NO_3)_2$, and $Fe(NO_3)_3$ were purchased from Alfa Aesar. Chloroauric acid ($HAuCl_4 \cdot 4H_2O$), HNO_3 (65%), $N_2H_4 \cdot 3H_2O$ solution (35 wt %), H_2SO_4 (98%), and Nafion perfluorinated resin solution (5 wt%) were purchased from Sigma-Aldrich. K_2CO_3 and 37% formaldehyde were purchased from J.T. Baker. Methanol, NaOH, KNO_3, and KOH were purchased from Fisher Scientific. Ammonium Hydroxide (28-30%) was purchased from British Drug Houses. All reagents were used as received without further purification. Ultrapure water (18.2MΩ resistivity, Milli-Q, Millipore) was used for all the experiments.

Synthesis of Au QSNPs and SRNPs. Au QSNPs (diameter of 104 $\pm$ 6.5 nm), which

were used as the core materials for Au@Cu_2O core-shell nanoparticle fabrication, were synthesized by reducing chloroauric acid with formaldehyde at room temperature.[25,26] Au SRNPs with overall particle diameters of 120 ± 7.2 nm were prepared following a protocol we recently published.[51, 27]

Synthesis of Au@Cu_2O Core-shell NPs. Au QSNPs (diameter of 104 ± 6.5 nm) were used as the core materials for the fabrication of Au@Cu_2O core-shell NPs following a previously published protocol.[26] Briefly, 9.6 mL of Au QSNPs was first introduced into 300 mL of 2 wt% PVP aqueous solution. Varying amount (0.3-3 mL) of 0.1 M $Cu(NO_3)_2$ solution, depending on the desired thickness of the resulting Cu_2O shells, was subsequently added. The reaction mixtures were transferred into an ice bath, and then 0.67 mL of 5 M NaOH and 0.3 mL of N_2H_4 $3H_2O$ solution were added under magnetic stir. The solutions were kept stirring for 10 min, and the NPs were subsequently separated from the reaction solution by centrifugation (2000 rpm, 10 min) and redispersion in ethanol. More details of the core-shell NP synthesis can be found in a paper previously published by our group.[26]

Synthesis of Au-Cu Alloy NPs. Au-Cu alloy NPs were prepared through thermal annealing of the Au@Cu_2O core-shell NPs at 450 ℃ in a flow of H_2 flow (50 sccm) under 100 Torr for 15 min in a tube furnace. The annealed samples were collected after cooling down to room temperature and were redispersed in 10 mL water. It was recently revealed by thermal gravimetric analysis that PVP in various nanocomposites underwent rapid thermal degradation at temperatures above ~420 ℃.[28-30] Therefore, thermal annealing at 450 ℃ enabled us not only to obtain fully alloyed NPs, but also to effectively remove the residual PVP possibly present on the NP surfaces (the synthesis of

Au@Cu_2O core-shell NPs involved the use of PVP).

Synthesis of Spongy NFs. Spongy NFs were fabricated through chemical dealloying upon the introduction of 1 mL of a chemical etchant, such as HNO_3, $Fe(NO_3)_3$ or NH_4OH, into 200 μL of colloidal Au-Cu alloy NPs at room temperature. After certain dealloying times, the dealloyed NFs were separated from the etchants through centrifugation and redispersion in water.

Electrochemical Measurements. All the electrochemical measurements were performed using a CHI 660E workstation (CH Instruments, Austin, Texas) at room temperature with a three-electrode system composed of a Pt wire as the auxiliary, a saturated calomel electrode (SCE) as the reference, and a glassy carbon electrode (GCE, 3 mm diameter) as the working electrode. Typically, the GCE was polished with 0.3 mm alumina slurry and followed by washing with water and ethanol before use. Dry powders of spongy NFs, Au-Cu alloy NPs, Au QSNPs, or Au SRNPs with certain total masses were first redispersed in H_2O to form colloidal suspensions (2.0 mg Au in 1.0 mL H_2O), and then 2 μL of the colloidal ink were drop-dried on each pretreated GCE at room temperature. Finally, 2 μL of Nafion solution (0.2 wt%) was drop-dried to hold the NPs on the electrode surfaces. The Au mass of the NPs loaded on each GCE was kept at 4.0 μg for comparison of the Mas and ECSAs of various samples. In a typical electrochemical test, CV scans were performed in a 0.5 M KOH solution with or without 1.0 M CH_3OH degassed with N_2 at a sweep rate of 10 mV s^{-1}. CV measurements for oxide stripping were conducted in N_2-saturated 0.5 M H_2SO_4 solution at various potential sweep rates in range of 5-500 mV s^{-1}. The polarization trace was normalized against the Au mass of the NPs loaded on each GCE.

Structural and Compositional Characterizations. The morphologies and structures of the NPs were characterized by TEM using a Hitachi H-8000 transmission electron microscope, which was operated at an accelerating voltage of 200 kV. All samples for TEM measurements were dispersed in ethanol and drop-dried on 400 mesh carbon-coated Cu grids. The structures and compositions of the nanoparticles were also characterized by SEM and EDS using a Zeiss Ultraplus thermal field emission scanning electron microscope. The samples for SEM and EDS measurements were dispersed in ethanol and drop-dried on silicon wafers. The atomic level structures of the nanoparticles were resolved by HAADF-STEM using a JEOL 2100F 200 kV FEG-STEM/TEM microscopy equipped with a CEOS CS corrector on the illumination system. The samples for HAADF-STEM/EDS measurements were dispersed in ethanol and drop-dried on Mo grids with ultrathin carbon support film. The optical extinction spectra of the NPs were measured on aqueous colloidal suspensions at room temperature using a Beckman coulter Du 640 spectrophotometer. PXRD patterns were record on Bruker axs D8 Discover (Cu Kα = 1.5406 Å). A Finnigan ELEMENT XR double focusing magnetic sector field inductively coupled plasma-mass spectrometer (SF-ICP-MS) was used for the analysis of Cu (65, MR), Au (197, MR) and internal standard Rh (103 MR). 0.2 mL min^{-1} Micromist U-series nebulizer (GE, Australia), quartz torch and injector (Thermo Fisher Scientific, USA) were used for sample introduction. Sample gas flow was at 1.08 mL min^{-1}. The forwarding power was 1250 W. The sample for ICP-MS measurements were prepared by adding 1 mL nitric acid and 3 mL of hydrochloric acid into Teflon digestion vessels containing the NP samples. The samples were digested using hot block at 180^{o}C for 4 h. The digestates were brought to 50 mL with water. A 3-point calibration curve was used

for Cu and Au. The calibration range was from 50 to 600 ppb. The R square values for the initial calibration curves were greater than 0.995. XPS measurements were carried out using a Krato AXIS Ultra DLD XPS system equipped with a monochromatic Al Kα source. The samples for XPS measurements were all freshly prepared and dried in vacuum before being loaded into the XPS chambers.

2.3 Results and Discussions

Our synthetic approach to the electrocatalytically active spongy NFs involves two key steps as schematically illustrated in Figure 2.1A. We started from Au@Cu_2O core-shell NPs, which underwent chemical reduction followed by intraparticle alloying[31] to evolve into Au-Cu alloy NPs upon thermal annealing in a reducing atmosphere, such as H_2. The Au-Cu alloy NPs further transformed into spongy NFs through percolation dealloying when exposed to a chemical etchant, such as nitric acid (HNO_3). We used a combination of scanning electron microscopy (SEM), transmission electron microscopy (TEM), energy-dispersive spectroscopy (EDS), and powder X-ray diffraction (PXRD) to systematically track the structural and compositional changes of the NPs during the nanoscale alloying and dealloying processes. The Au-Cu_2O hybrid NPs exhibited a well-defined core-shell heterostructure clearly resolvable by electron microscopies (Figure 2.1B) and EDS elemental analysis. After the core-shell NPs were thermally annealed in a flow of H_2 (50 sccm) under 100 Torr at 450 ℃ for 15 min, the contrast between the core and the shell in the SEM and TEM images completely disappeared (Figure 2.1C), indicating the formation of Au-Cu bimetallic alloy NPs.

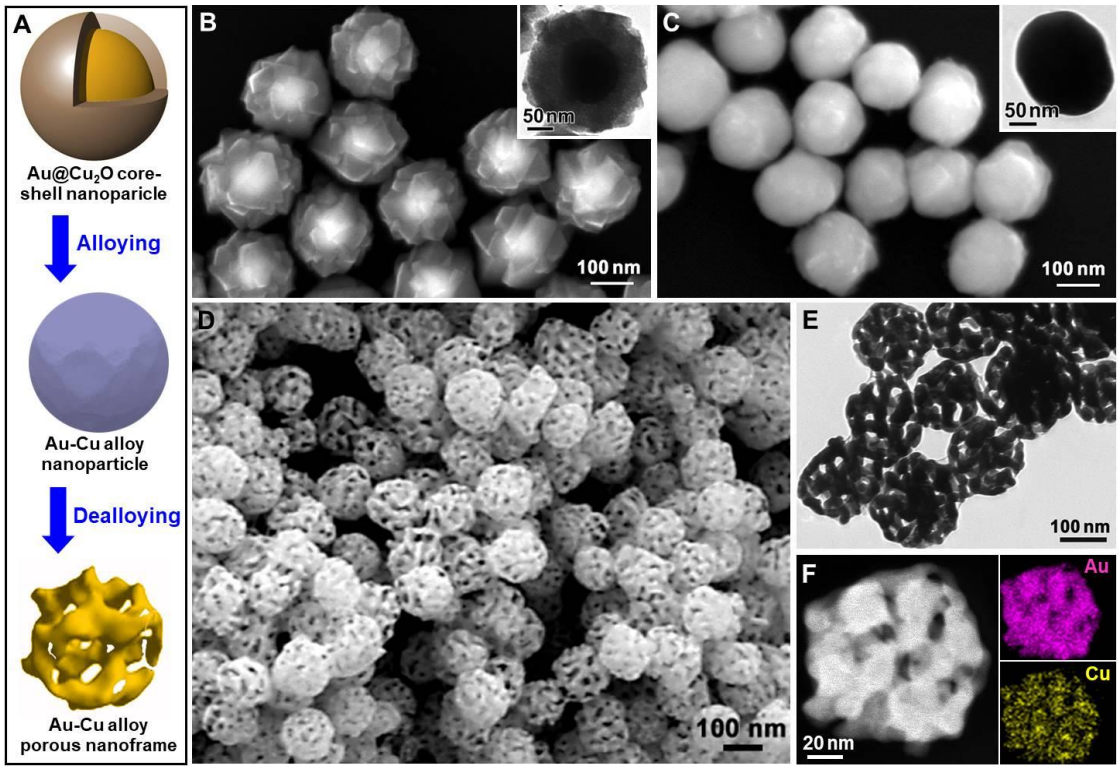

Figure 2.1. **Nanoparticle structural evolution during nanoscale alloying and dealloying.** (A) Schematic illustration of the transformation of $Au@Cu_2O$ core-shell NPs into Au-Cu alloy NPs upon alloying and the transformation of Au-Cu alloy NPs into spongy NFs upon dealloying. (B) SEM image of $Au@Cu_2O$ core-shell NPs (average core diameter of 104 nm and shell thickness of 51 nm). The inset shows a TEM image of an individual $Au@Cu_2O$ core-shell NP. (C) SEM image of $Au_{0.19}Cu_{0.81}$ alloy NPs. The inset shows a TEM image of an individual $Au_{0.19}Cu_{0.81}$ alloy NP. (D) SEM and (E) TEM images of spongy $Au_{0.72}Cu_{0.28}$ alloy NFs obtained through dealloying of the $Au_{0.19}Cu_{0.81}$ alloy NPs in 0.5 M HNO_3 for 3 h. (F) HAADF-STEM image (*left panel*) and EDS elemental distribution of Au (*upper right panel*) and Cu (*lower right panel*) of an individual $Au_{0.72}Cu_{0.28}$ alloy NF particle. The compositions of the alloy NPs and dealloyed NFs were quantified by EDS.

The EDS elemental mapping results further verified that the Au and Cu atoms were homogenously intermixed in the alloy NPs. During the percolation dealloying, the alloy NPs further evolved into compositionally Au-rich spongy NFs as Cu was selectively dissolved from the alloy matrix. Figures 2.1D, 2.1E, and 2.1F showed the SEM, TEM, and high-angle annular dark-field scanning electron microscopy (HAADF-STEM) images, respectively, of the spongy NFs obtained through dealloying of $Au_{0.19}Cu_{0.81}$ alloy NPs in 0.5 M HNO_3 for 3 hours at room temperature. Each particle exhibited a

bicontinuous nanoporous structure composed of nano-curved ligaments that were 5 nm to 25 nm thick with pore diameters in the range from 10 to 40 nm. While the Cu/Au atomic ratio significantly decreased after percolation dealloying, the ligaments of the dealloyed NFs were still composed of Au-Cu alloys rather than segregated monometallic domains (see STEM-EDS mapping results in Figure 2.1F).

The core and shell dimensions of the starting Au@Cu_2O core-shell NPs could be fine-controlled over a broad size range using a seed-mediated growth method we recently developed,[26] which allowed us to fine-tune the compositions of the alloy NPs. While the overall particle sizes shrank significantly upon alloying, both the quasi-spherical morphology and the Cu/Au stoichiometric ratios of the NPs were well-preserved. Therefore, the Cu/Au stoichiometric ratios of the alloy NPs were essentially determined by the relative core and shell dimensions of the Au@Cu_2O core-shell NP precursors and could be systematically tuned over a broad range approximately from 0.3 to 4. The as-fabricated Au-Cu alloy NPs were essentially composed of random alloys[21] rather than ordered Au-Cu intermetallics with specific Cu/Au stoichiometries, such as Au_3Cu, AuCu, or $AuCu_3$.[32,33] The lattice parameters of the face-centered cubic (fcc) Au-Cu alloy NPs were calculated using the Bragg's law

$$d_{hkl} = \frac{\lambda}{2\sin(\theta_{hkl})} \qquad (1),$$

where λ is the wavelength of the incident X-ray (λ = 1.5406 Å for Cu Kα), d_{hkl} is the lattice spacing of the crystalline plane with Miller index of {*khl*}, and θ_{hkl} is the angle of incidence on the {*khl*} plane. We calculated the Cu/Au stiochiometric ratios of various Au-Cu alloy NPs based on the position of the (111) diffraction peak, assuming that the

lattice parameters of a solid solution agree with a linear relationship between the two end points of alloying elements, an empirical rule known as the Vegard's law.[34] Although some bimetallic alloys may deviate significantly from the Vegard's law, Au-Cu binary random alloys only exhibit slight deviations from the Vegard's law.[35] The Cu/Au atomic ratios calculated from the PXRD results were in very good agreement with those quantified by inductively coupled plasma mass spectrometry (ICP-MS) and EDS. Colloidal Au@Cu_2O core-shell NPs exhibited strong dipolar plasmon resonances that progressively red-shifted from the visible into the near-infrared as the thickness of the Cu_2O shell increased[25,26,36]. The transformation of core-shell NPs into alloy NPs introduced drastic modifications to both the plasmon resonance frequencies and optical extinction spectral line-shapes of the NPs. As the Cu/Au stoichiometric ratio and the particle size increased, the plasmon resonance of the alloy NPs red-shifted, accompanied by significant peak broadening due to the plasmon damping caused by alloying of Au with Cu.[37-39] The key extinction spectral features observed experimentally were well reproduced by the Mie scattering theory calculations.

The Au-Cu alloy NPs exhibited interesting composition-dependent chemical dealloying behaviors. Upon exposure to 0.5 M HNO_3 at room temperature, Cu-rich alloy NPs with a Cu atomic percentage (at %) above ~ 70 % underwent nanoporosity-evolving percolation dealloying, during which the Cu/Au atomic ratios progressively deceased accompanied by ligament thickening and pore volume expansion until complete leaching of Cu within a few hours. In striking contrast, Au-rich alloy NPs (Cu at % < ~ 65 %) exhibited unnoticeable morphological and compositional changes over extended time periods up to even a few days under identical dealloying conditions. Such composition-

dependent dealloying behaviors of Au-Cu alloy NPs can be interpreted in the context of the parting limit and critical potential for the percolation dealloying.[11]

For a macroscopic $A_{1-p}B_p$ binary alloy (A and B represent the more-noble and the less-noble elements, respectively, and p is atomic fraction of B), percolation dealloying occurs only when the p is higher than a threshold value known as the parting limit. In Ag-Au alloys, this parting limit was measured to be ~55 at % Ag.[4] The corresponding electrochemical parameter signifying the onset of percolation dealloying is termed the critical potential, $\overline{E}_c$, which is related to the B/electrolyte interfacial free energy, $\gamma_{B/elec}$, the molar volume of A, Ω_A, and the equilibrium potential, $\overline{E}_{eq}$, above which the surface dealloying at the top-most atomic layer occurs. The relationship between $\overline{E}_c$ and $\overline{E}_{eq}$ is given by[40]

$$\overline{E}_c(p) = \overline{E}_{eq}(p) + \frac{4\gamma_{B/elec}\Omega_A}{nF\xi} \qquad (2),$$

where n is the number of electrons transferred upon oxidation of 1 atom of B, F is the Faraday constant, and ξ represents the local radius of the surface where a cylindrical pit is created at the initial stage of nanoporosity evolution. ξ is related to both p and the nearest-neighbor spacing, a, as shown by

$$\xi = \frac{1+p}{1-p} \times a \qquad (3).$$

For macroscopic bimetallic alloys, both the $\overline{E}_c$ and $\overline{E}_{eq}$ are functions of the alloy composition and the $\overline{E}_c$ values are more positive than $\overline{E}_{eq}$ when the solid-state mass transport is slower than the imposed rate of dealloying. At a potential above the $\overline{E}_c$, percolation dealloying results in the evolution of nanoporosity, while below $\overline{E}_c$ only

superficial dealloying can occur, forming a conformal surface atomic layer of the more-noble component which passivates the surface and thereby inhibits the nanoporosity formation.[41,42]

For a spherical $A_{1-p}B_p$ alloy NP of radius r, the critical potential becomes not only dependent on the composition but also on the size of the NP. Accordingly, the $E_c(p,r)$ of the alloy NP is given by[11]

$$E_c(p,r) = \overline{E}_c(p) - [\gamma_{Alloy}(\Omega_A) + f_{Alloy}(\overset{)}{\Omega}_A - <\Omega>)] \times (\frac{2}{nFr}) \quad (4),$$

where γ_{Alloy} is the alloy/electrolyte interfacial free energy, f_{Alloy} is the alloy/electrolyte interface stress, $\overset{)}{\Omega}_A$ is the partial molar volume of A in the alloy, and $\langle\Omega\rangle$ is the average molar volume of the alloy. When r is greater than ~5 nm, equations (2) and (4) provide virtually identical results because the maximum values of γ_{Alloy} and f_{Alloy} are ~ 2 and ~ 6 J m^{-2}, respectively.[43] Therefore, alloy NPs larger than ~ 10 nm typically undergo dealloying-induced structural transformations analogous to those of their bulk counterparts with the same compositions. It was shown that Au-Ag alloy NPs larger than 10 nm evolved into spongy nanoporous structures whereas their sub-10 nm counterparts transformed into core-shell NPs under identical dealloying conditions.[11] Since the particle sizes under the current investigations were far beyond 10 nm, the Au-Cu alloy NPs evolved into spongy NFs when the Cu content was higher than the parting limit, which was determined to be ~ 70 at % of Cu. Dealloying of the $Au_{0.31}Cu_{0.69}$ alloy NPs resulted in a mixture of solid alloy NPs and spongy NFs owing to the intrinsic particle-to-particle compositional variations within the sample.

The composition-dependent electrochemical dealloying behaviors of the Au-Cu alloy

NPs were further investigated by linear sweep voltammetry (LSV) measurements in 1.0 M KNO_3 electrolyte (pH = 7) at a sweep rate of 5.0 mV s^{-1} using a three-electrode system. During the positive potential sweep, the anodic current remained at a low level until reaching the E_c, at which point the anodic current started to increase rapidly due to percolation dealloying. The onset potential for Cu dissolution from the $Au_{0.19}Cu_{0.81}$ NPs was positively shifted in comparison to that of monometallic Cu NPs because the less-noble Cu was significantly stabilized when it was alloyed with the more-noble Au, a well-known characteristic of bulk binary alloy materials[4] that is yet still less explored in alloy NP systems.[44,45] For Au-Cu alloy NPs with Cu at % below the parting limit, however, only superficial dealloying could occur at the topmost atomic layer on the NP surfaces due to surface passivation by a Au-rich atomic layer or an oxide adlayer. As a consequence, the anodic peak currents decreased dramatically by more than 2 orders of magnitudes with the onset potential for dealloying shifted to significantly more positive values. Consistent with the structural evolutions upon chemical dealloying, the electrochemical percolation dealloying resulted in nanoporous spongy NFs as well, whereas the surface dealloying of the alloy NPs with Cu at % below the parting limit did not introduce any substantial morphological changes observable by TEM. The E_c was found to be dependent not only on the NP compositions but also on the pH of the electrolytes. In an acidic electrolyte, such as H_2SO_4, both the onset potential for percolation dealloying and the anodic peak potential negatively shifted with respect to those in the neutral electrolytes. However, the alloy NPs became much more resistive against percolation dealloying in an alkaline environment, e.g. KOH electrolyte, possibly due to the surface passivation by the oxide surface layers that formed at sufficiently high

potentials.

The nanoporosity evolution during percolation dealloying is essentially a multi-scale structural rearrangement governed by two intertwining and competing processes, ligament domain coarsening and framework expansion. The percolation dealloying was initiated upon the dissolution of a Cu atom at the alloy surface, leaving behind a terrace vacancy coordinated with undercoordinated Cu atoms that were more susceptible to further dissolution. As the entire terrace was stripped, the coordinatively unsaturated Au atoms left behind the dealloying frontiers underwent fast surface migration to agglomerate into Au-rich local islands. Therefore, the surface of the alloy upon initiation of dealloying was comprised of Au-rich domains that locally passivated the surface and patches of undealloyed material directly exposed to electrolyte.[4] As the percolation dealloying further proceeded, the interfacial dissolution of Cu atoms and coarsening of the Au-rich domains continued, gradually evolving into bicontinuous spongy structures. Meanwhile, the outward migration of Cu atoms was faster than the inward migration of Au atoms in the alloy matrix,[46] providing additional contribution to the expansion of the pores during the nanoporosity evolution. This effect, known as the Kirkendall effect, has been harnessed to fabricate hollow NPs with fine-tailored interior structures.[47-50] For an alloy NP, the ligaments domain coarsening resulted in the thickening of the ligaments and shrinkage of the overall particle size, whereas the framework expansion driven by the Kirkendall effect led to increased overall particle size and pore volumes. The relative rates of the ligament domain coarsening and framework expansion could be maneuvered by tuning the rates of Cu leaching during the percolation dealloying.

We systematically studied the kinetics and thermodynamics of the Cu leaching from

$Au_{0.19}Cu_{0.81}$ alloy NPs during percolation dealloying in the presence of three different chemical etchants, HNO_3, $Fe(NO_3)_3$, and ammonia, in aqueous environment under ambient conditions. Both HNO_3 and $Fe(NO_3)_3$ are oxidative etchants that directly oxidize metallic Cu and selectively dissolve the Cu from the alloy NPs, thereby giving rise to relatively fast Cu leaching upon percolation dealloying. The leaching of Cu from the alloy NPs exposed to ammonia, however, is essentially a consequence of oxidation of Cu by the oxygen dissolved in the aqueous solution followed by the formation of water-soluble $Cu(NH_3)_4^{2+}$ and $Cu(NH_3)_2^{+}$ complexes.[51] Therefore, the rate of Cu leaching upon dealloying in ammonia appeared much slower than those in HNO_3 and $Fe(NO_3)_3$. The Cu/Au atomic ratios progressively decreased as the percolation dealloying proceeded until reaching a thermodynamic equilibrium point. Because of their different standard redox potentials, HNO_3, $Fe(NO_3)_3$, and O_2/ammonia resulted in different equilibrium Cu/Au stoichiometries. While complete Cu leaching (less than 3 at % residual Cu) was achieved after dealloying within 1 h in 2.0 M HNO_3, $Fe(NO_3)_3$ and O_2/ammonia only resulted in partial leaching of Cu when reaching the thermodynamic equilibria. These partially dealloyed NFs obtained in $Fe(NO_3)_3$ or O_2/ammonia underwent further Cu leaching upon exposure to HNO_3.

The Cu leaching from the $Au_{0.19}Cu_{0.81}$ alloy NPs under the non-equilibrium conditions was observed to be a continuous process; however, once the particles were separated from the etchants through centrifugation followed by redispersion in water, further dealloying of the partially dealloyed NFs could be effectively inhibited, enabling us to kinetically trap spongy NFs with fine-controlled pore volumes, ligament thicknesses, and Cu/Au stoichiometries. As shown in Figure 2.2, the degree of Cu leaching and the

structural features of the dealloyed NFs could be systematically tuned by changing the etchants or the concentration of each etchant at fixed dealloying times. When fixing the dealloying time at 1 hour, increasing the HNO_3 concentration resulted in more Cu leaching, larger average pore sizes, thicker ligaments, and smaller overall sizes of the dealloyed NFs. In HNO_3, the leaching of Cu from the alloy NPs was faster than the atomic diffusion of Cu in the alloy matrix. Therefore, the nanoporosity evolution was dominated by the ligament domain coarsening rather than framework expansion, leading to significant thickening of the ligaments and shrinkage of the overall size of the dealloyed NFs as increasing amount of Cu was dissolved. A similar volume shrinkage of macroscopic Ag-Au alloy bulk materials by up to 30 vol % was previously observed during fast electrochemical dealloying as a consequence of the lattice defect formation and local plastic deformation both associated with ligament coarsening.[52] When the percolation dealloying occurred in ammonia, however, the overall particle sizes were observed to increase with the ammonia concentration when the dealloying time was fixed at 2 hours. In ammonia, as Cu leaching became slower than the atomic diffusion of Cu, the Kirkendall effects started to dominate the nanoporosity evolution, which resulted in the expansion of the particle frameworks. In $Fe(NO_3)_3$, the rates of Cu leaching and atomic diffusion of Cu were comparable, and thus the overall size of the dealloyed NFs remained almost unchanged regardless of the concentration of $Fe(NO_3)_3$ and the amount of Cu leached during the percolation dealloying.

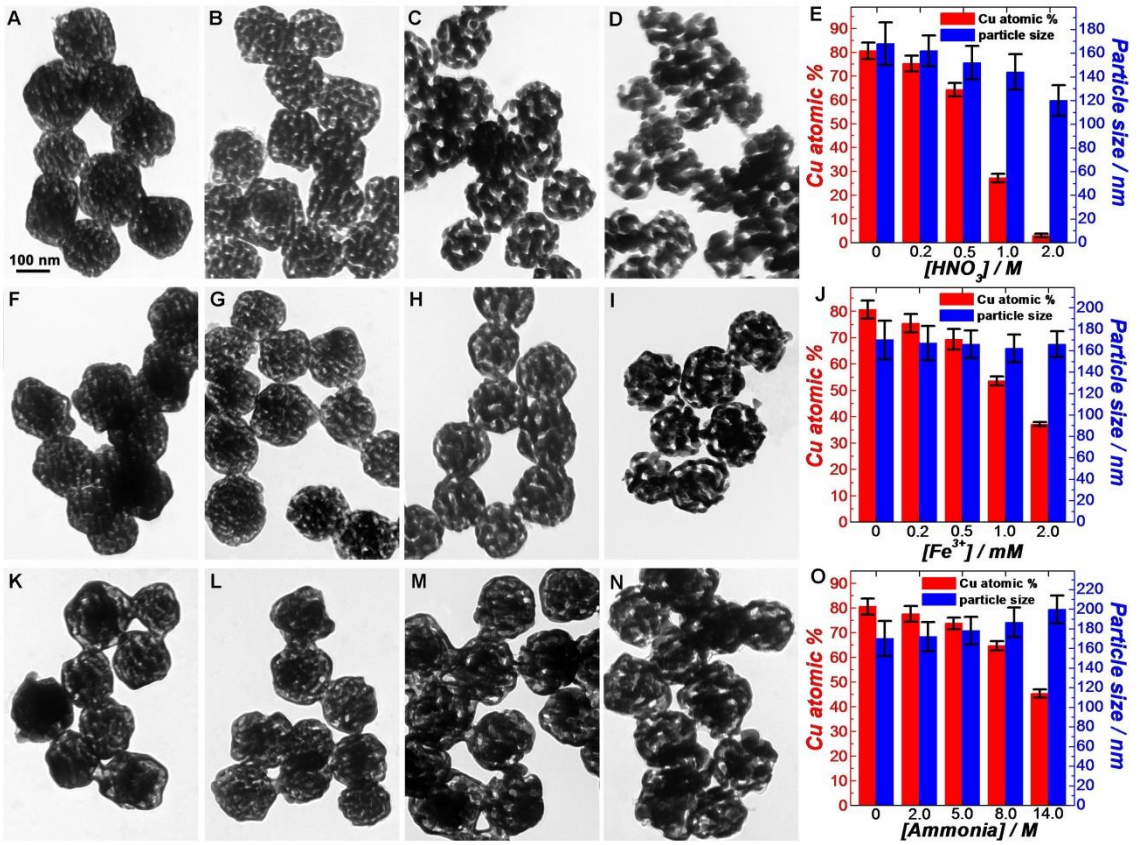

Figure 2.2. **Compositional and structural evolution of $Au_{0.19}Cu_{0.81}$ alloy NPs during percolation dealloying.** TEM images of spongy NFs obtained after exposure of $Au_{0.19}Cu_{0.81}$ alloy NPs to (A) 0.2 M, (B) 0.5 M, (C) 1.0 M, and (D) 2.0 M HNO_3 for 1 h. (E) Cu at % (quantified by EDS) and overall particle diameters of spongy NFs obtained after exposure of $Au_{0.19}Cu_{0.81}$ alloy NPs to various concentrations of HNO_3 for 1 h. TEM images of spongy NFs obtained after exposure of $Au_{0.19}Cu_{0.81}$ alloy NPs to (F) 0.2 M, (G) 0.5 M, (H) 1.0 M, and (I) 2.0 M $Fe(NO_3)_3$ for 2 h. (J) Cu at % and overall particle diameters of spongy NFs obtained after exposure of $Au_{0.19}Cu_{0.81}$ alloy NPs to various concentrations of $Fe(NO_3)_3$ for 2 h. TEM images of spongy NFs obtained after exposure of $Au_{0.19}Cu_{0.81}$ alloy NPs to (K) 2.0 M, (L) 5.0 M, (M) 8.0 M, and (N) 14.0 M NH_4OH for 2 h. (O) Cu at % and overall particle diameters of spongy NFs obtained after exposure of $Au_{0.19}Cu_{0.81}$ alloy NPs to various concentrations of ammonia for 2 h. All TEM images share the same scale-bar in panel A. The Cu atomic percentages were quantified by EDS and the error bars represent the standard deviation of 3 samples fabricated under exactly the same conditions. The average particle diameters and standard deviations were obtained from more than 100 particles in the TEM images of each sample.

We used high-resolution HAADF-STEM to characterize the atomic-level structures of the dealloyed NFs. As shown in Figure 2.3A, a representative particle in the dealloyed $Au_{0.97}Cu_{0.03}$ NF sample (obtained through dealloying of $Au_{0.19}Cu_{0.81}$ alloy NPs in 2.0 M HNO_3 for 1 h) exhibited a bicontinuous architecture consisting of hierarchically

interconnected nano-ligaments whose compositions were dominated by Au. Panels A-a and A-b show the high-resolution HAADF-STEM images of two regions in Panel A labeled as a and b, respectively, with the electron beam projected along the $[01\bar{1}]$ zone axis of the crystalline domains. The corresponding fast Fourier transform (FFT) patterns further confirmed the orientation of the crystalline domains in the ligaments. The lattice fringes corresponding to the face center cubic phase of Au were well resolved in the high-resolution HAADF-STEM images. No segregated monometallic Cu domains were observed either in the bulk or on the surfaces of the ligaments, suggesting that the residual Cu was randomly intermixed with Au. When the atomic fraction of the residual Cu was below 3 %, the Cu signals in EDS became indistinguishable from the noise, making it difficult to characterize the spatial distribution of Cu elements in the ligaments through EDS elemental mapping. However, the residual Cu was clearly resolvable by X-ray photoelectron spectroscopy (XPS), which is a sensitive surface analysis technique. While the binding energies of the Au 4f peaks slightly up-shifted by ~ 0.05 eV in comparison to those of the bulk Au, the Cu 2p XPS peaks exhibited more pronounced down-shifts by ~ 0.5 eV with respect to those of the bulk Cu due to the alloying of Cu with Au[53]. The surface Cu/Au atomic ratio was quantified to be ~ 0.02 by XPS, which was in agreement with the bulk Cu/Au atomic ratio obtained from EDS. The XPS and EDS results showed that the residual Cu in the fully dealloyed NFs was randomly intermixed with the Au matrix rather than being segregated on the ligament surfaces. The residual Cu was highly resistive against leaching. Further exposure of the $Au_{0.97}Cu_{0.03}$ NFs to 2.0 M HNO_3 for 12 hours did not result in any observable decrease in the surface Cu/Au atomic ratios according to the XPS results.

The surfaces of the ligaments were enclosed by a mixture of both high-index and low-index local facets (Figure 2.3A). The locally flat surface regions of a monocrystalline domain were typically enclosed by thermodynamically stable low-index facets, such as {111} facets, whereas in the locally curved regions, the surfaces were terminated with high-index facets with high densities of undercoordinated surface atoms at the atomic steps, kinks, and terrace edges. Coordinatively unsaturated surface atoms were also present at the boundaries between two twinned crystalline domains. The high abundance of undercoordinated surface atoms is a unique feature of NPs with highly curved surfaces, such as the catalytically active sub-5 Au NPs[54] and Au surface-roughened nanoparticles (SRNPs). We synthesized Au SRNPs with overall particle diameters of 120 $\pm$ 7.2 nm using a kinetically controlled, seed-mediated nanocrystal growth method previously developed by our group.[55] The Au SRNPs exhibited nanoscale surface roughness (Figure 2.3B) with high abundance of undercoordinated surface atoms at the locally curved surface sites (see more detailed structural characterizations in a previously published paper from our group[27]). The Au SRNPs exhibited much smaller specific surface areas than the dealloyed NF particles because of their solid interiors. In contrast to the Au SRNPs and dealloyed NFs, the surfaces of the multi-faceted Au QSNPs (diameter of 104 $\pm$ 6.5 nm) were essentially dominated by low-index facets bound with close-packed surface atoms (Figure 2.3C) with only a small fraction of undercoordinated surface atoms present at the particle corners, edges, crystalline boundaries, and surface defects.

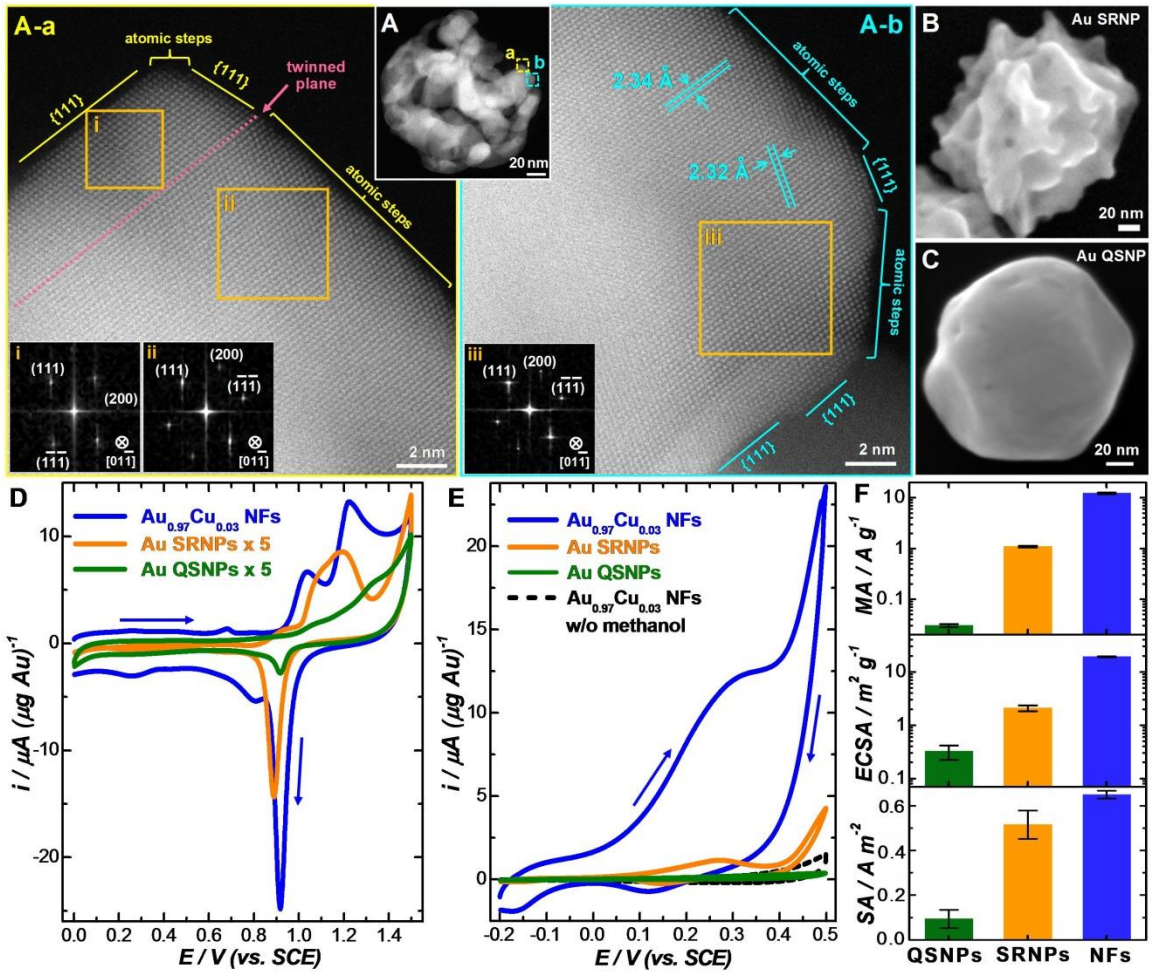

Figure 2.3. **Atomic-level surface structures and electrocatalytic activity of fully dealloyed spongy NFs.** (A) HAADF-STEM image of an individual $Au_{0.97}Cu_{0.03}$ NF particle. High-resolution HAADF-STEM images showing the atomic-level structures of regions a and b are shown in panel A-a and panel A-b, respectively. The insets in panels A-a and A-b are the FFT patterns of the regions labeled as i, ii, and iii, respectively. In the high-resolution HAADF-STEM images, the crystalline domains were projected along the $[01\bar{1}]$ zone axis. SEM images of (B) a Au SRNP with solid interior core and (C) a Au QSNP. (D) CV curves of $Au_{0.97}Cu_{0.03}$ NFs, Au SRNPs, and Au QSNPs in 0.5 M H_2SO_4 at a potential sweep rate of 5.0 mV s^{-1}. The electrochemical signals from SRNPs and QSNPs were multiplied by a factor of 5 for clearer comparison. (E) CV curves of $Au_{0.97}Cu_{0.03}$ NFs, Au SRNPs, and Au QSNPs in 1.0 M methanol and 0.5 M KOH at a potential sweep rate of 10 mV s^{-1}. CV curve of $Au_{0.97}Cu_{0.03}$ NFs in the absence of methanol is shown as the dash curve. (F) Mass activities (MAs), electrochemically active surface areas (ECSAs), and specific activities (SAs) of $Au_{0.97}Cu_{0.03}$ NFs, Au SRNPs, and Au QSNPs in 1.0 M methanol and 0.5 M KOH at a potential sweep rate of 10 mV s^{-1}.

We used cyclic voltammetry (CV) as an electrochemical tool to further characterize the atomic-level surface structures and specific surface areas of the dealloyed NFs, Au

SRNPs, and Au QSNPs. CV-based electrochemical oxide stripping is a method commonly used to study the surface structures of bulk Au[56,57] and more recently Au NPs[58-61] as well. Figure 2.3D showed the CV curves of various samples obtained in 0.5 M H_2SO_4 at a sweep rate of 5.0 mV s^{-1}. During the positive potential scans of the CV measurements, both the dealloyed $Au_{0.97}Cu_{0.03}$ NFs and Au SRNPs exhibited oxidation peaks in the range of 0.95-1.25 V *vs.* Saturated Calomel Electrode (SCE), whereas Au QSNPs exhibited an oxidation peak in higher potential range above 1.40 V (*vs.* SCE). The negative shift of oxidation peaks observed on the dealloyed NFs and SRNPs suggested that the surfaces of the NFs and SRNPs were easier to get oxidized to form an oxide surface layer due to the presence of highly abundant undercoordinated surface atoms while the close-packed surface atoms on Au QSNPs were more resistive against oxidation. During the negative potential scans, the sharp reduction peak centered around 0.9 V (*vs.* SCE) signified the electrochemical stripping of the surface oxide layers formed in the previous positive potential scan. Although the onset potentials of the surface atom oxidation were sensitively dependent on the surface atomic coordination numbers, the electrochemical stripping of the gold oxide surface layers occurred in essentially the same potential range from ~0.98 V to ~ 0.85 V (*vs.* SCE), which was in line with previous observations on Au bulk films[56,57] and NPs.[58-61] Assuming the specific charge associated with gold oxide stripping to be 450 μC cm^{-2},[62] the mass-specific electrochemically active surface area (ECSA) of the dealloyed NFs was estimated to be ~ 20 m^2 g^{-1}, approximately 1 order of magnitude higher than that of SRNPs and 2 orders of magnitude higher than that of the QSNPs, respectively, despite the fact that the dealloyed NFs, SRNPs, and QSNPs all had similar overall particle sizes.

We quantitatively compared the electrocatalytic activities of the dealloyed NFs, SRNPs, and QSNPs using the room-temperature electrocatalytic methanol oxidation reaction (MOR) in alkaline aqueous environment as a model reaction. As shown in Figure 2.3E, while the Au QSNPs exhibited poor electrocatalytic activity toward MOR, both the dealloyed $Au_{0.97}Cu_{0.03}$ NFs and Au SRNPs were much more active. The onset oxidation potential and peak potential for MOR were around 0.1 V (*vs.* SCE) and 0.3 V (*vs.* SCE), respectively. By normalizing the oxidation peak current against the mass of Au on each electrode, a mass activity (MA) of ~ 12 $\mu A\ \mu g^{-1}$ was obtained at 0.3 V on the dealloyed $Au_{0.97}Cu_{0.03}$ NFs at a sweep rate of 10.0 $mV\ s^{-1}$, which was about 1 order of magnitude higher than that of the SRNPs. For NPs of noble metals, such as Au, Pt, and Pd, the undercoordinated surface atoms have been identified to be the electrocatalytically active sites for MOR and other alcohol oxidation reactions.[2,63] Therefore, the superior electrocatalytic activity toward MOR observed on the dealloyed $Au_{0.97}Cu_{0.03}$ NFs originated from both their large specific ECSA and high density of surface active sites. By normalizing the MAs against ECSAs, the specific activities (SAs) of the NPs were obtained, which were directly related to the active site density on the NP surfaces. In Figure 3F, we compared the MAs, ECSAs, and SAs of the dealloyed $Au_{0.97}Cu_{0.03}$ NFs with those of the Au SRNPs and QSNPs. Interestingly, the Au SRNPs exhibited a SA only slightly lower than that of dealloyed NFs, indicating comparable densities of surface active sites, i.e. undercoordinated surface atoms, on the dealloyed NFs and Au SRNPs. However, the dealloyed NFs exhibited much higher MA than Au SRNPs because of their significantly larger ECSA. For a low-index faceting Au QSNP, the undercoordinated surface atoms are located at the particle corners and edges and thus only account for a

vanishingly small fraction of the surface atoms when the particle size becomes larger than 10 nm.[64] Therefore, the Au QSNPs exhibited diminished electrocatalytic activity for MOR due to their limited SA and ECSA.

The controlled percolation dealloying of Au-Cu alloy NPs allowed us to systematically tune both the ECSAs and the SAs of the dealloyed NFs to achieve the optimal MAs for MOR. In Figure 2.4A, we compared the MAs of 5 dealloyed NF samples with different degrees of Cu leaching. The NF samples labeled as NF-i, NF-ii, NF-iii, and NF-iv corresponded to the samples obtained through dealloying of $Au_{0.19}Cu_{0.81}$ alloy NPs in 0.2 M, 0.5 M, 1.0 M, and 2.0 M $Fe(NO_3)_3$ for 2 hours, respectively. The sample labeled as NF-v was obtained through dealloying of $Au_{0.19}Cu_{0.81}$ alloy NPs in 2.0 M HNO_3 for 1 hour. The HAADF-STEM images highlighting the key structural features of individual NF particles representing each sample were also shown as the insets of Figure 2.4A. From NF-i to NF-v, the Cu/Au stoichiometric ratios decreased (Figure 2.4B, top panel) while both the average ligament thicknesses and pore sizes increased. All the NF samples exhibited much higher MAs than the solid alloy NPs and NF-ii exhibited the highest MA among the NF samples. The MAs of the dealloyed NFs were primarily determined by both the NF surface areas and the active site densities on the ligament surfaces rather than the Cu/Au stoichiometric ratios. The dealloyed spongy NFs exhibited drastically higher activities than the solid Au-Cu alloy NPs with similar Cu/Au stoichiometric ratios.

We semi-quantitatively assessed the ECSAs of various NF samples based on the electrochemical oxide stripping results. For the Au-Cu alloy NFs, Cu leaching occurred during the electrochemical oxide stripping experiments at relatively slow potential sweep

rates (e.g. 5 mV s^{-1}), which prevented us from obtaining meaningful ECSA results. Therefore, to accurately measure the ECSAs of the Cu-containing alloy NFs, the CV measurements were carried out at much faster potential sweep rates to effective suppress the kinetically slow Cu leaching process. As demonstrated on $Au_{0.97}Cu_{0.03}$ NFs (no further Cu leaching during CV scans), the ECSA values measured at various potential sweep rates in the range from 5 mV s^{-1} to 500 mV s^{-1} were highly consistent, though the multi-peaked features in the potential range of 1.0-1.3 V (*vs.* SCE) signifying the electrochemical oxidation of the undercoordinated surface atoms became less well-resolved as the potential sweep rate increased. At sufficiently fast potential sweep rates (e.g. 500 mV s^{-1}), the Cu leaching from $Au_{0.30}Cu_{0.70}$ alloy NFs was effectively suppressed while the ECSA remained almost unchanged during multiple cycles of CV scans. In Figure 2.4B, we further compared the ECSAs and SAs of various NF samples and the solid alloy NPs. Upon the percolation dealloying, the ECSA first increased and then decreased as increasing amount of Cu was dissolved and NF-ii exhibited the largest ECSA among the NF samples. The SA of the dealloyed NFs, on the other hand, reached it maximum value upon initiation of nanoporosity formation and kept decreasing as the Cu leaching further proceeded during the nanoporosity evolution. At the initiate stage of percolation dealloying, the surface pitting upon Cu atomic dissolution created highly abundant undercoordinated surface atoms that contributed to the high SA of the NFs. As more Cu was dissolved from the alloy matrix, the ligament domain coarsening drove the migration of the undercoordinated surface atoms to form thermodynamically more stable local facets. As a consequence, the active sites became less abundant, resulting in decreased SA. Therefore, the optimization of the MAs on the spongy NFs requires

deliberate tuning of both the ECSA and SA of the NFs, which could be achieved through the controlled percolation dealloying of Au-Cu alloy NPs as demonstrated in this work.

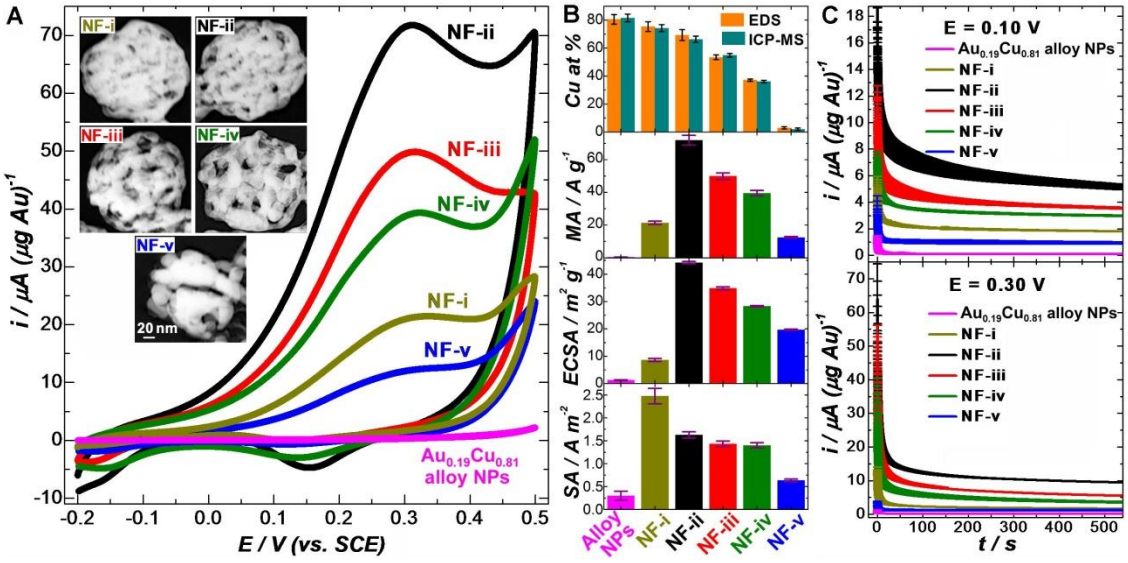

Figure 2.4. **Electrocatalytic performance of dealloyed NFs for MOR.** (A) CV curves of MOR on $Au_{0.19}Cu_{0.81}$ alloy NPs and various dealloyed NFs in 1.0 M methanol and 0.5 M KOH at a potential sweep rate of 10 mV s^{-1}. The NF samples labeled as NF-i, NF-ii, NF-iii, and NF-iv correspond to the samples obtained through dealloying of $Au_{0.19}Cu_{0.81}$ alloy NPs in 0.2 M, 0.5 M, 1.0 M, and 2.0 M $Fe(NO_3)_3$ for 2 h, respectively. The sample labeled as NF-v was obtained through dealloying of $Au_{0.19}Cu_{0.81}$ alloy NPs in 2.0 M HNO_3 for 1 h. HAADF-STEM images of one representative particle for each NF sample are also shown as the insets. All the HAADF-STEM images share the same scale bar. (B) Cu atomic percentages (quantified by EDS and ICP-MS), MAs, ECSAs, and SAs of Au-Cu alloy NPs and various dealloyed NFs. The error bars of particle compositions represent the standard deviations obtained from 3 samples. The error bars of the MAs and ECSAs represent the standard deviations obtained from 5 samples. (C) CA curves collected on $Au_{0.19}Cu_{0.81}$ alloy NPs and various dealloyed NFs for MOR at 0.1 V (*vs.* SCE) and 0.3 V (*vs.* SCE). All CA measurements were carried out in solutions containing 0.5 M KOH and 1.0 M methanol deoxygenated with N_2 and the error bars represent the standard deviations obtained from 3 samples.

Among the various dealloyed NF samples, NF-ii exhibited the highest MA and ECSA while NF-i exhibited the highest SA (Figure 2.4B). It was recently reported that nanoporous Au shells[59] and Au bowls[65] overgrown on sacrificial AgCl templates exhibited MAs approximately 1.4 and 2.3 times higher than that of the macroscopic dealloyed nanoporous Au foams,[9] respectively, for the electrocatalytic MOR in alkaline electrolytes. NF-ii was about 3 times better than the nanoporous Au bowls and 5 times

better than the nanoporous Au shells, respectively, in terms of the MAs normalized to Au mass. The ECSA of NF-ii was about 2.5 times higher than the largest ECSAs achievable on the nanoporous Au shells and bowls.[59,65] The SAs of the dealloyed spongy NFs, macroscopic nanoporous Au foams, and the nanoporous Au shells and bowls, however, were all comparable to each other possibly due to similar densities of the undercoordinated atoms on their highly curved surfaces.

To assess the electrocatalytic durability of the spongy NFs, chronoamperometry (CA) measurements were carried out at both the onset oxidation potential (0.1 V, *vs.* SCE) and the oxidation peak potential (0.3 V, *vs.* SCE). As shown in Figure 2.4C, the oxidation currents underwent a fast decay in the first few seconds followed by a much slower decay over minutes till reaching a steady-state plateau. The fast decay of the oxidation currents arose from the development of the electrochemical double-layer after a potential was applied on the samples till reaching the equilibrium after a few seconds. The slower current decay was found to be associated with the surface structural remodeling of the NFs during electrocatalytic reactions, which resulted in the activity deterioration to certain extent. Although the nanoporous morphology of the $Au_{0.30}Cu_{0.70}$ NFs (NF-ii) was well-preserved with limited amount of Cu further leached before the steady-state current was reached, thickening of the ligaments and expansion of pore sizes were clearly observed as a consequence of surface atomic migrations. Such surface structural remodeling during electrocatalytic reactions, which was previously also observed on dealloyed macroscopic Au membranes,[9] resulted in decrease of both the ECSAs and densities of active sites on the NF surfaces. The spongy NFs obtained through electrochemical dealloying exhibited significantly lower electrocatalytic activities than

their chemically dealloyed counterparts, further indicating that the undercoordinated surface atoms located at the catalytic active sites could migrate to form thermodynamically more stable but catalytically less active surface structures when a potential bias was applied to the NFs.

2.4 Conclusion

As demonstrated in this work, the percolation dealloying of Au-Cu alloy NPs is a multi-scale structural remodeling process involving nanoscale atomic dissolution and migration that lead to the formation of spongy NFs with unique structural characteristics highly desired for electrocatalysis. The solid-void bicontinuous NFs consisting of hierarchically interconnected nano-ligaments are found to be a unique structure generated from percolation dealloying of Au-Cu alloy NPs with Cu at % above the parting limit. The nanoporosity evolution during percolation dealloying is synergistically guided by two intertwining and competing structural rearrangement processes, ligament domain coarsening driven by thermodynamics and framework expansion driven by Kirkendall effects, both of which can be maneuvered by controlling the Cu leaching rates during the percolation dealloying. The controlled percolation dealloying of Au-Cu alloy NPs provides a unique way to systematically tune both the catalytically active surface areas and the surface densities of active sites of the dealloyed NFs such that the optimal electrocatalytic activity can be achieved. The undercoordinated surface atoms, which serve as the catalytically active sites, undergo nanoscale surface migrations over a time scale of minutes during electrocatalytic MOR till reaching the steady-state catalytic currents, resulting in structural remodeling of the NFs that causes partial deterioration of the catalytic activities. Development of new approaches to further stabilizing the surface

active sites on the dealloyed NFs through either incorporation of structure-stabilizing residual components or deliberate introduction of compositional gradients to the nano-ligaments is currently underway with the ultimate goal of retaining the superior mass-specific electrocatalytic activities of the spongy NFs over extended time periods for direct methanol fuel cell (DMFC) applications.

2.5 References

(1) Wang, D. L.; Xin, H. L. L.; Hovden, R.; Wang, H. S.; Yu, Y. C.; Muller, D. A.; DiSalvo, F. J.; Abruna, H. D., *Nat. Mater.* **2013**, 12, 81.

(2) Tian, N.; Zhou, Z. Y.; Sun, S. G.; Ding, Y.; Wang, Z. L., *Science* **2007**, 316, 732.

(3) Tao, F.; Grass, M. E.; Zhang, Y. W.; Butcher, D. R.; Renzas, J. R.; Liu, Z.; Chung, J. Y.; Mun, B. S.; Salmeron, M.; Somorjai, G. A., *Science* **2008**, 322, 932.

(4) Erlebacher, J.; Aziz, M. J.; Karma, A.; Dimitrov, N.; Sieradzki, K., *Nature* **2001**, 410, 450.

(5) Ding, Y.; Kim, Y. J.; Erlebacher, J., *Adv. Mater.* **2004**, 16, 1897.

(6) Wittstock, A.; Zielasek, V.; Biener, J.; Friend, C. M.; Bäumer, M., *Science* **2010**, 327, 319.

(7) Wittstock, A.; Baumer, M., *Accounts Chem. Res.* **2014**, 47, 731.

(8) Fujita, T.; Guan, P. F.; McKenna, K.; Lang, X. Y.; Hirata, A.; Zhang, L.; Tokunaga, T.; Arai, S.; Yamamoto, Y.; Tanaka, N.; Ishikawa, Y.; Asao, N.; Yamamoto, Y.; Erlebacher, J.; Chen, M. W., *Nat. Mater.* **2012**, 11, 775.

(9) Zhang, J. T.; Liu, P. P.; Ma, H. Y.; Ding, Y., *J. Phys. Chem. C* **2007**, 111, 10382.

(10) Gan, L.; Heggen, M.; O'Malley, R.; Theobald, B.; Strasser, P., *Nano Lett.* **2013**, 13, 1131.

(11) Li, X.; Chen, Q.; McCue, I.; Snyder, J.; Crozier, P.; Erlebacher, J.; Sieradzki, K., *Nano Lett* **2014**, 14, 2569.

(12) Oezaslan, M.; Heggen, M.; Strasser, P., *J. Am. Chem. Soc.* **2012**, 134, 514.

(13) Wang, D. L.; Yu, Y. C.; Xin, H. L. L.; Hovden, R.; Ercius, P.; Mundy, J. A.; Chen, H.; Richard, J. H.; Muller, D. A.; DiSalvo, F. J.; Abruna, H. D., *Nano Lett.* **2012**, 12, 5230.

(14) Chen, C.; Kang, Y. J.; Huo, Z. Y.; Zhu, Z. W.; Huang, W. Y.; Xin, H. L. L.; Snyder, J. D.; Li, D. G.; Herron, J. A.; Mavrikakis, M.; Chi, M. F.; More, K. L.; Li, Y. D.; Markovic, N. M.; Somorjai, G. A.; Yang, P. D.; Stamenkovic, V. R., *Science* **2014**, 343, 1339.

(15) Ding, J. B.; Bu, L. Z.; Guo, S. J.; Zhao, Z. P.; Zhu, E. B.; Huang, Y.; Huang, X. Q., *Nano Lett.* **2016**, 16, 2762.

(16) Ding, J. B.; Zhu, X.; Bu, L. Z.; Yao, J. L.; Guo, J.; Guo, S. J.; Huang, X. Q., *Chem. Commun.* **2015**, 51, 9722.

(17) Gan, L.; Heggen, M.; Rudi, S.; Strasser, P., *Nano Lett.* **2012**, 12, 5423.

(18) Snyder, J.; McCue, I.; Livi, K.; Erlebacher, J., *J. Am. Chem. Soc.* **2012**, 134, 8633.

(19) Bandarenka, A. S.; Koper, M. T. M., *J. Catal.* **2013**, 308, 11.

(20) Stamenkovic, V. R.; Fowler, B.; Mun, B. S.; Wang, G. F.; Ross, P. N.; Lucas, C. A.; Markovic, N. M., *Science* **2007**, 315, 493.

(21) Kim, D.; Resasco, J.; Yu, Y.; Asiri, A. M.; Yang, P. D., *Nat. Commun.* **2014**, 5, DOI: 10.1038/ncomms5948.

(22) Zhang, L.; Roling, L. T.; Wang, X.; Vara, M.; Chi, M. F.; Liu, J. Y.; Choi, S. I.; Park, J.; Herron, J. A.; Xie, Z. X.; Mavrikakis, M.; Xia, Y. N., *Science* **2015**, 349, 412.

(23) Huang, X. Q.; Zhao, Z. P.; Cao, L.; Chen, Y.; Zhu, E. B.; Lin, Z. Y.; Li, M. F.; Yan, A. M.; Zettl, A.; Wang, Y. M.; Duan, X. F.; Mueller, T.; Huang, Y., *Science* **2015**, 348, 1230.

(24) Mazumder, V.; Lee, Y.; Sun, S. H., *Adv. Funct. Mater.* **2010**, 20, 1224.

(25) Zhang, L.; Blom, D. A.; Wang, H., *Chem. Mat.* **2011**, 23, 4587.

(26) Zhang, L.; Jing, H.; Boisvert, G.; He, J. Z.; Wang, H., *ACS Nano* **2012**, 6, 3514.

(27) Zhang, Q. F.; Blom, D. A.; Wang, H., *Chem. Mat.* **2014**, 26, 5131.

(28) Amyab, S. P.; Saievar-Iranizad, E.; Bayat, A., *RSC Advances* **2016**, 6, 41937.

(29) Mali, S. S.; Kim, H.; Jang, W. Y.; Park, H. S.; Patil, P. S.; Hong, C. K., *Acs Sustainable Chemistry & Engineering* **2013**, 1, 1207.

(30) Jiang, C. L.; Nie, J.; Ma, G. P., *RSC Advances* **2016**, 6, 22996.

(31) Connell, J. G.; Al Balushi, Z. Y.; Sohn, K.; Huang, J. X.; Lauhon, L. J., *J. Phys. Chem. Lett.* **2010**, 1, 3360.

(32) Schaak, R. E.; Sra, A. K.; Leonard, B. M.; Cable, R. E.; Bauer, J. C.; Han, Y. F.; Means, J.; Teizer, W.; Vasquez, Y.; Funck, E. S., *J. Am. Chem. Soc.* **2005**, 127, 3506.

(33) Sra, A. K.; Ewers, T. D.; Schaak, R. E., *Chem. Mat.* **2005**, 17, 758.

(34) Vegard, L., *Zeitschrift für Physik* **1921**, 5, 17.

(35) Lubarda, V. A., *Mech Mater* **2003**, 35, 53.

(36) Liu, D. Y.; Ding, S. Y.; Lin, H. X.; Liu, B. J.; Ye, Z. Z.; Fan, F. R.; Ren, B.; Tian, Z. Q., *J. Phys. Chem. C* **2012**, 116, 4477.

(37) Henkel, A.; Jakab, A.; Brunklaus, G.; Sonnichsen, C., *J. Phys. Chem. C* **2009**, 113, 2200.

(38) Motl, N. E.; Ewusi-Annan, E.; Sines, I. T.; Jensen, L.; Schaak, R. E., *J. Phys. Chem.*

C **2010**, 114, 19263.

(39) Thota, S.; Chen, S. T.; Zhou, Y. D.; Zhang, Y.; Zou, S. L.; Zhao, J., *Nanoscale* **2015**, 7, 14652.

(40) Rugolo, J.; Erlebacher, J.; Sieradzki, K., *Nature Materials* **2006**, 5, 946.

(41) Wagner, K.; Brankovic, S. R.; Dimitrov, N.; Sieradzki, K., *J Electrochem Soc* **1997**, 144, 3545.

(42) Sieradzki, K.; Dimitrov, N.; Movrin, D.; McCall, C.; Vasiljevic, N.; Erlebacher, J., *J Electrochem Soc* **2002**, 149, B370.

(43) Cammarata, R. C., *Prog. Surf. Sci.* **1994**, 46, 1.

(44) Huang, J. F.; Zhu, Y. H.; Liu, C. X.; Zhao, Y. F.; Liu, Z. H.; Hedhili, M. N.; Fratalocchi, A.; Han, Y., *Small* **2015**, 11, 5214.

(45) Gao, C. B.; Hu, Y. X.; Wang, M. S.; Chi, M. F.; Yin, Y. D., *J. Am. Chem. Soc.* **2014**, 136, 7474.

(46) Liu, Y. L.; Walker, A. R. H., *ACS Nano* **2011**, 5, 6843.

(47) Yin, Y. D.; Rioux, R. M.; Erdonmez, C. K.; Hughes, S.; Somorjai, G. A.; Alivisatos, A. P., *Science* **2004**, 304, 711.

(48) Fan, H. J.; Gosele, U.; Zacharias, M., *Small* **2007**, 3, 1660.

(49) Gonzalez, E.; Arbiol, J.; Puntes, V. F., *Science* **2011**, 334, 1377.

(50) Sun, Y. G.; Xia, Y. N., *Science* **2002**, 298, 2176.

(51) Luo, Q.; Mackay, R. A.; Babu, S. V., *Chem. Mat.* **1997**, 9, 2101.

(52) Parida, S.; Kramer, D.; Volkert, C. A.; Rosner, H.; Erlebacher, J.; Weissmuller, J., *Phys. Rev. Lett.* **2006**, 97, 035504.

(53) Kim, M. J.; Na, H. J.; Lee, K. C.; Yoo, E. A.; Lee, M. Y., *J. Mater. Chem.* **2003**, 13,

1789.

(54) Haruta, M.; Date, M., *Appl. Catal. A-Gen.* **2001**, 222, 427.

(55) Zhang, Q. F.; Large, N.; Nordlander, P.; Wang, H., *J. Phys. Chem. Lett.* **2014**, 5, 370.

(56) Hamelin, A., *J. Electroanal. Chem.* **1996**, 407, 1.

(57) Hamelin, A.; Martins, A. M., *J. Electroanal. Chem.* **1996**, 407, 13.

(58) Zhang, J. A.; Langille, M. R.; Personick, M. L.; Zhang, K.; Li, S. Y.; Mirkin, C. A., *J. Am. Chem. Soc.* **2010**, 132, 14012.

(59) Pedireddy, S.; Lee, H. K.; Tjiu, W. W.; Phang, I. Y.; Tan, H. R.; Chua, S. Q.; Troadec, C.; Ling, X. Y., *Nat. Commun.* **2014**, 5, DOI: 10.1038/ncomms5947.

(60) Ma, Y. Y.; Kuang, Q.; Jiang, Z. Y.; Xie, Z. X.; Huang, R. B.; Zheng, L. S., *Angew. Chem.-Int. Edit.* **2008**, 47, 8901.

(61) Ming, T.; Feng, W.; Tang, Q.; Wang, F.; Sun, L. D.; Wang, J. F.; Yan, C. H., *J. Am. Chem. Soc.* **2009**, 131, 16350.

(62) Trasatti, S.; Petrii, O. A., *J. Electroanal. Chem.* **1992**, 327, 353.

(63) Lee, S. W.; Chen, S.; Suntivich, J.; Sasaki, K.; Adzic, R. R.; Shao-Horn, Y., *J. Phys. Chem. Lett.* **2010**, 1, 1316.

(64) Janssens, T. V. W.; Clausen, B. S.; Hvolbaek, B.; Falsig, H.; Christensen, C. H.; Bligaard, T.; Norskov, J. K., *Topics in Catalysis* **2007**, 44, 15.

(65) Pedireddy, S.; Lee, H. K.; Koh, C. S.; Tan, J. M.; Tjiu, W. W.; Ling, X. Y., *Small* **2016**, doi: 10.1002/smll.201601371.

CHAPTER 3

RESIDUAL AG ENHANCES BOTH ACTIVITY AND DURABILITY OF DEALLOYED AU NANOSPONGE PARTICLES TOWARD ELECTROCATALYTIC ALCOHOL OXIDATION

3.1 Introduction

Dealloying of alloys involves intriguing nanoscale structure-remodeling processes that profoundly influence the catalytic properties of the dealloyed materials.[1,2] This is best manifested by the percolation dealloying of Au-Ag alloy membranes, which results in nanoporous foams consisting of Au-rich nano-ligaments that are interconnected to form a unique 3D solid/void bicontinuous, sponge-like architecture.[2-5] Distinct from the catalytically inert bulk Au membranes, the dealloyed nanoporous Au foams exhibit superior catalytic activities commensurate with those of oxide-supported ultrasmall Au nanocatalysts (< ~2 nm) owing to the high abundance of catalytically active undercoordinated atoms on the highly curved ligament surfaces.[2-6] More recently, the percolation dealloying of binary alloys has been further extended from macroscopic membranes to particulate nanostructures, controllably introducing nanoporosity to free-standing or substrate-supported metallic nanoparticles (NPs).[7-14] Although compositionally dominated by the more-noble elements, the dealloyed nanoporous materials always contain residual less-noble elements that cannot be completely removed by dealloying.[2-14] Surprisingly, the residual less-noble elements may further enhance the catalytic activity of the dealloyed materials toward certain reactions. For example, residual Ag can promote the catalytic CO oxidation on dealloyed nanoporous Au foams possibly by enhancing the surface adsorption of O_2,[2,6] though the detailed mechanisms still remain ambiguous and open to further scrutiny. Despite their remarkable initial activities, the dealloyed nanoporous materials inevitably undergo activity deterioration over time during catalytic or electrocatalytic reactions due to reduced surface area/mass ratio and loss of surface active sites, both of which are caused by ligament

coarsening.[15,16] While it was recently observed by *in situ* environmental electron microscopy that residual Ag could locally stabilize the surface atomic steps (active sites) during catalytic CO oxidation,[4] how to rationally incorporate residual Ag into the Au nano-ligaments to optimize both the catalytic activity and durability of dealloyed materials still remains an open question.

Here we show that incorporating Ag into Au-Cu binary alloy NPs substantially accelerated Cu leaching while effectively suppressing ligament coarsening during nanoporosity-evolving percolation dealloying, providing a unique way to optimize both the surface area/mass ratios and specific activities of the dealloyed nanosponge (NS) particles for electrocatalytic alcohol oxidation. The residual Ag in the dealloyed NS particles greatly enhances the stability of the active sites on the ligament surfaces, allowing us to retain the superior catalytic activities over much longer periods than the NS particles without residual Ag.

3.2 Experimental Details

Materials Polyvinylpyrrolidone (PVP, average MW 58 000), $Cu(NO_3)_2$, and $AgNO_3$ (99.9995% metals basis) were purchased from Alfa Aesar. Chloroauric acid ($HAuCl_4\ 4H_2O$), HNO_3 (65%), $N_2H_4\ 3H_2O$ solution (35 wt %), H_2SO_4 (98%), and Nafion perfluorinated resion solution (5 wt%) were purchased from Sigma-Aldrich. K_2CO_3 and 37% formaldehyde were purchased from J.T. Baker. Methanol, ethanol, *iso*-propanol, ethylene glycol, NaOH and KOH were purchased from Fisher Scientific. All reagents were used as received without further purification. Ultrapure water (18.2MΩ resistivity, Milli-Q, Millipore) was used for all the experiments.

Synthesis of Au@Ag@Cu_2O Triple-Layer and Au@Cu_2O core-shell

Nanoparticles (NPs) Quasi-spherical Au NPs with diameters of 100 ± 5.5 nm were synthesized by reducing chloroauric acid with formaldehyde at room temperature.[17] In a typical synthesis, 50 mg of K_2CO_3 was dissolved in 200 mL of water, followed by addition of 3 mL of 25 mM $HAuCl_4$. The mixture solution was aged in the dark for 18 h before use. Then 1.34 mL of 37 % formaldehyde solution was added into the mixture under vigorous magnetic stir (300 rpm). After 30 min, the resulting Au NPs were centrifuged (2300 rcf), washed with water, and finally redispersed in 10 mL of water.

To synthesize Au@Ag core-shell NPs, 9.6 mL of Au colloidal solution was added into 300 mL of 1 wt % PVP aqueous solution. Then 500 μL of 0.1 M $AgNO_3$ and 2.0 mL of 0.5 M fresh-prepared ascorbic acid were added into the mixture under magnetic stir. The color of the solution changed from brick-red to beige in a few minutes, and the reaction mixture was kept stirring for 10 min. The resulting Au@Ag core-shell NPs were centrifuged (2200 rpm, 10 min), washed with 2 wt % PVP solution twice, and finally redispersed in 10 mL of water.

Au@Ag@Cu_2O triple-layer NPs were synthesized following a protocol we previously developed [18] with minor modifications. Typically, 9.6 mL of Au@Ag core-shell NPs were first introduced into 300 mL of 2 wt% PVP aqueous solution. Then 3.0 mL of 0.1 M $Cu(NO_3)_2$ solution was added. The reaction mixtures were transferred into an ice bath, and then 0.67 mL of 5 M NaOH and 0.3 mL of N_2H_4 $3H_2O$ solution were added under magnetic stir. The solution was kept stirring for 10 min, and the NPs were subsequently separated from the reaction solution by centrifugation (2000 rpm, 10 min) and redispersion in ethanol for storage.

Au@Cu_2O core-shell NPs were synthesized through seed-mediated growth of Cu_2O

naoshells on Au NP cores.[18] Briefly, 9.6 mL of Au NPs were introduced into 300 mL of 2 wt% PVP aqueous solution. Then 3.0 mL of 0.1 M $Cu(NO_3)_2$ solution was subsequently added. The reaction mixtures were transferred into an ice bath, and then 0.67 mL of 5 M NaOH and 0.3 mL of N_2H_4 $3H_2O$ solution were added under magnetic stir. After 10 min, and the NPs were separated from the reaction solution by centrifugation (2000 rpm, 10 min) and redispersion in ethanol for storage.

Synthesis of Au-Ag-Cu Trimetallic Alloy and Au-Cu Bimetallic Alloy NPs The colloidal Au@Ag@Cu_2O triple-layer NPs and Au@Cu_2O core-shell NPs were dried at room temperature to form dry powders. Au-Ag-Cu trimetallic and Au-Cu bimetallic alloy NPs were prepared by annealing the Au@Ag@Cu_2O triple-layer NPs and Au@Cu_2O core-shell NPs, respectively, at 450 ℃ in a hydrogen flow (50 sccm) under 100 Torr for 20 min in a tube furnace. After cooling down to room temperature, the samples were redispersed in 10 mL of water for storage.

Synthesis of Nanosponge (NS) Particles through Percolation Dealloying Spongy NS particles were fabricated through chemical dealloying upon exposure of the alloy NPs to 3 M HNO_3 at room temperature under ambient pressure. The dealloyed NS particles were separated from the reaction mixtures and finally redispersed in water. Specifically, the dealloyed NS particles denoted as NS-T were obtained through dealloying of $Au_{0.12}Ag_{0.15}Cu_{0.73}$ trimetallic alloy NPs in 3.0 M HNO_3 for 45 min. The dealloyed NS particles denoted as NS-B were obtained through dealloying of $Au_{0.17}Cu_{0.83}$ bimetallic alloy NPs in 3.0 M HNO_3 for 45 min.

Structural Characterization of NPs The morphologies and structures of the NPs were characterized by transmission electron microscopy (TEM) using a Hitachi H-8000

transmission electron microscope, which was operated at an accelerating voltage of 200 kV. All samples for TEM measurements were dispersed in ethanol and drop-dried on 400 mesh carbon-coated-Cu grids (Electron Microscopy Science Inc.). The structures and compositions of the nanoparticles were also characterized by Sweepning Electron Microscopy (SEM) and Energy Dispersive Spectroscopy (EDS) measurements using a Zeiss Ultraplus thermal field emission sweepning electron microscope. The samples for SEM and EDS measurements were dispersed in ethanol and drop-dried on silicon wafers. The sizes of the NPs were analyzed on the basis of SEM images using Nano Measurer analysis software (Department of Chemistry, Fudan University, China). The size distribution histograms were obtained from more than 100 NPs for each sample. X-ray Photoelectron Spectroscopy (XPS) measurements were carried out using a Krato AXIS Ultra DLD XPS system equipped with a monochromatic Al Kα source. The samples for XPS measurements were all freshly prepared and dried in vacuum before being loaded into the XPS chambers. Powder X-ray diffraction (PXRD) patterns were record on a SAXSLab Ganesha at the South Carolina SAXS Collaborative (Cu $K\alpha$ = 1.5406 Å).

Electrochemical Measurements All the electrochemical measurements were performed using a CHI 660E workstation (CH Instruments, Austin, TX) at room temperature with a three-electrode system composed of a Pt wire as the auxiliary, a saturated calomel electrode (SCE) as the reference, and a glassy carbon electrode (GCE, 3 mm diameter) as the working electrode. Typically, the GCE was polished with 0.3 mm alumina slurry and followed by washing with water and ethanol before use. Colloidal suspensions containing 4.0 μg dealloyed NS particles (NS-T or NS-B) were dropped and air-dried on the pretreated GCEs at room temperature, and then 2 μL of Nafion solution

(0.2 wt%) was dropped to hold the NPs. To evaluate the electrocatalytic activities of the dealloyed NS particles toward alcohol oxidation, cyclic voltammetry (CV) measurements were performed in a N_2-saturated 0.5 M KOH solution containing 1.0 M methanol, 1.0 M ethanol, 1.0 M *iso*-propanol, or 0.25 M ethylene glycol at a sweep rate of 10 mV s^{-1}. Electrochemical surface oxide stripping was investigated through CV measurements performed in N_2-saturated 0.5 M H_2SO_4 solution at a sweep rate of 5 mV s^{-1}. The polarization trace was normalized against the Au mass of the NS particles loaded on each electrode. The critical potentials for percolation dealloying of the alloy NPs were measured by linear sweep voltammetry (LSV) in 0.5 M H_2SO_4 electrolyte in the potential sweep range from 0 V (*vs.* SCE) to 1.0 V (*vs.* SCE) at a sweep rate of 5 mV s^{-1}. To assess the electrocatalytic durability of the dealloyed NS particles, chronoamperometry (CA) measurements were carried out at 0.2 V (*vs.* SCE) in 1.0 M methanol, 1.0 M ethanol, 1.0 M *iso*-propanol, or 0.25 M ethylene glycol in the presence of 0.5 M KOH electrolyte over 2h.

3.3 Results and Discussions

Our synthetic approach to the electrocatalytically active NS particles is schematically illustrated in Figure 3.1A. To synthesize Au NS particles with residual Ag, we started with Au@Ag@Cu_2O triple-layer NPs[18], which transformed into Au-Ag-Cu ternary alloy NPs when thermally annealed in a H_2 atmosphere at 450 ℃. The Au:Ag:Cu stoichiometric ratios of the alloy NPs were predetermined by the relative core and shell dimensions of their parental triple-layer NPs. Upon exposure to a chemical etchant, such as HNO_3, the alloy NPs further evolved into Au-rich NS particles as both Cu and Ag were selectively dissolved from the alloy matrix. Energy dispersive spectroscopy (EDS)

showed that the composition of fully dealloyed NS particles was dominated by Au with only trace amount of residual Ag and Cu present in the nano-ligaments. Powder X-ray diffraction (PXRD) results further verified the NP structural and compositional evolutions during the alloying and dealloying processes. For comparison, NS particles without residual Ag were fabricated following essentially the same procedure except that Au@Cu_2O core-shell NPs were used as the precursors[19] instead of Au@Ag@Cu_2O triple-layer NPs.

EDS results (Figure 3.1B) showed that more than 90 % of Cu was rapidly dissolved within 5 minutes upon exposure of $Au_{0.14}Ag_{0.14}Cu_{0.72}$ ternary alloy NPs to 3.0 M HNO_3, while the leaching of Ag proceeded more gradually at a slower rate until fully dealloyed NS particles (residual Cu and Ag both below 2 at. %) were obtained after 45 minutes. In contrast, Cu leaching from $Au_{0.16}Cu_{0.84}$ binary alloy NPs under identical dealloying conditions was drastically slower than that from the ternary alloy NPs (Figure 3.1C). Although their total atomic fractions of the leachable less-noble elements were similar, the ternary alloy NPs exhibited a significantly higher critical potential for percolation dealloying[10] than the binary alloy NPs, suggesting that the Ag-enhanced Cu leaching was essentially a kinetically-driven process rather than a thermodynamic effect.

Electron microscopy images (Figures 3.1D and 3.1E) showed that the fully dealloyed NS particles obtained after dealloying of $Au_{0.14}Ag_{0.14}Cu_{0.72}$ ternary alloy NPs in 3.0 M HNO_3 for 45 min (denoted as NS-T) were composed of significantly thinner ligaments with smaller average pore sizes in comparison to the fully dealloyed NS particles obtained from the $Au_{0.16}Cu_{0.84}$ binary alloy NPs (denoted as NS-B).

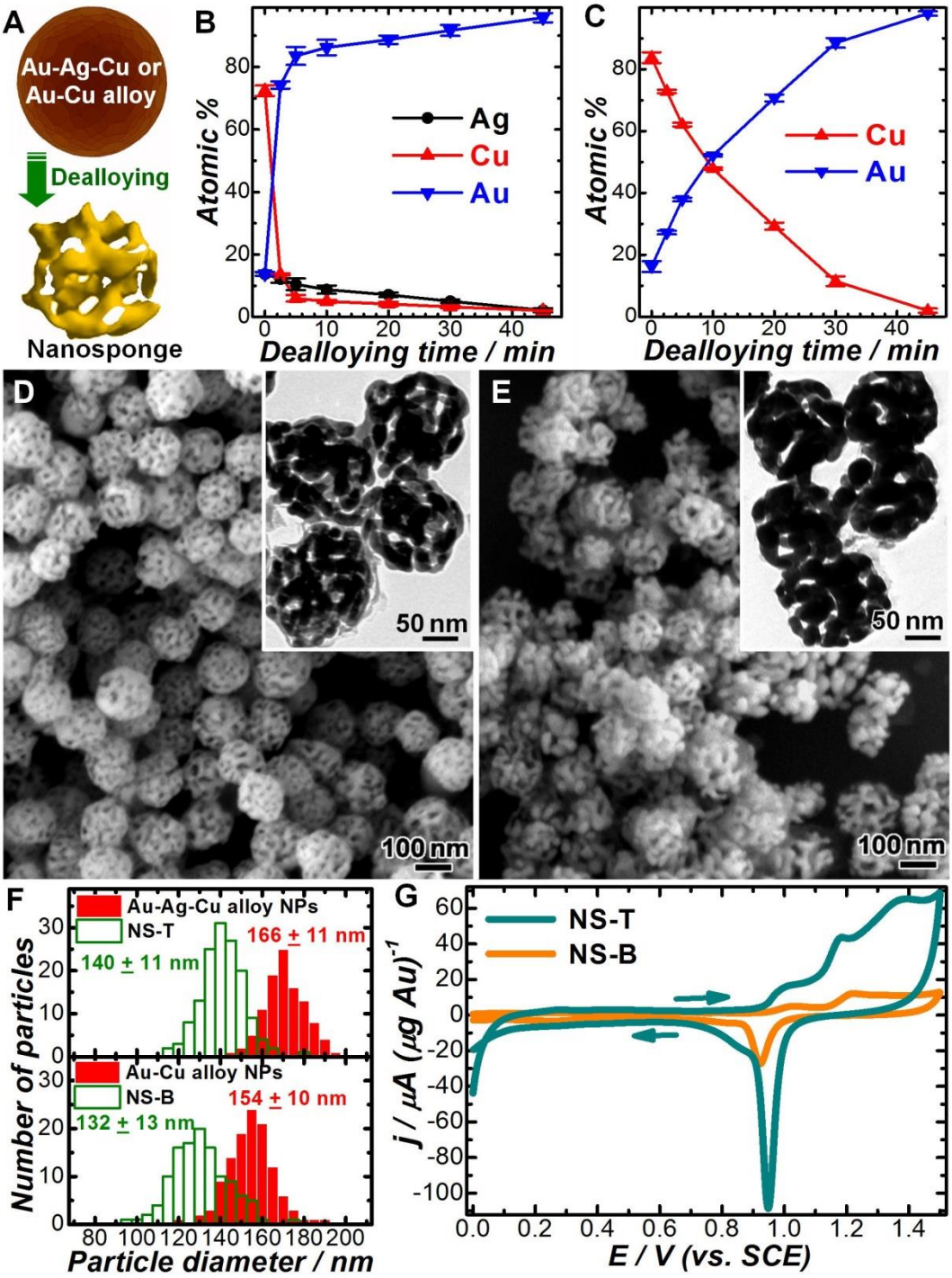

Figure 3.1. (A) Schematic illustration of structural transformation upon percolation dealloying. Compositional evolution during the percolation dealloying of (B) $Au_{0.14}Ag_{0.14}Cu_{0.72}$ alloy NPs and (C) $Au_{0.16}Cu_{0.84}$ alloy NPs in 3.0 M HNO_3. The error bars represent the standard deviations of 3 samples. SEM images and (*insets*) TEM images of (D) NS-T and (E) NS-B. (F) Size distributions of NS-T, NS-B, and alloy NPs. (G) CV curves of NS-T and NS-B in 0.5 M H_2SO_4 at a potential sweep rate of 5 mV s^{-1}. The currents were normalized against the Au mass loaded on each electrode.

Both the ternary and binary alloy NPs underwent similar volume shrinkages of ~ 40 % upon their transformations into fully dealloyed NS particles (Figure 3.1F).Although NS-T and NS-B possessed similar Au masses and pore volumes on a per-particle basis, NS-T exhibited a much larger surface area/mass ratio than NS-B owing to its thinner ligaments and smaller pore sizes. We used cyclic voltammetry (CV) as an electrochemical characterization tool to compare the specific surface areas and surface atomic structures of NS-T and NS-B (Figure 3.1G). Because the undercoordinated surface atoms are more susceptible to oxidation than their coordinatively saturated counterparts, the characteristic potentials for surface oxidation correlate well with the surface atomic coordination numbers (ACNs). During the anodic sweeps, both NS-T and NS-B exhibited oxidation peaks in the range of 0.90-1.25 V *vs.* saturated calomel electrode (SCE), signifying the oxidation of undercoordinated surface atoms with ACNs of 6 and 7,[19-22] while the oxidation of close-packed surface atoms with ACNs of 8 and 9 occurred above 1.3 V (*vs.* SCE).[19,21-23] During the cathodic sweep, a sharp reduction peak emerged around 0.94 V (*vs.* SCE), signifying the stripping of the surface oxide layer formed during the anodic sweep.[19-23] Assuming the specific charge associated with Au oxide stripping to be 450 μC cm^{-2},[24] the mass-specific electrochemically active surface area (ECSA) of NS-T was calculated to be ~ 80 $m^2 g^{-1}$, approximately 4 times higher than that of NS-B (~ 22 $m^2 g^{-1}$).

The nanoporosity evolution during percolation dealloying was synergistically maneuvered by two interplaying structural remodeling processes, leaching of the less noble elements and coarsening of the ligaments. According to the mechanism proposed by Erlebacher,[3] the percolation dealloying of a Au-Cu alloy NP was initiated upon the

dissolution of a Cu surface atom, leaving behind a terrace vacancy that was more susceptible to further Cu leaching. As the entire terrace was stripped, the coordinatively unsaturated Au atoms left behind the dealloying frontiers started to migrate to form agglomerated Au-rich local islands that were thermodynamically more stable. As the dealloying further proceeded, the interfacial dissolution of Cu atoms and coarsening of the Au-rich domains occurred concurrently, gradually evolving into bicontinuous spongy structures. While Cu leaching was the major driving force for the nanoporosity formation, the coarsening of the Au-rich domains led to thickening of the ligaments and decrease of surface area/mass ratios. Both the average pore sizes and ligament thicknesses gradually increased accompanied by decrease in overall particle sizes as the percolation dealloying of Au-Cu binary alloy NPs proceeded. In contrast, the Au-Ag-Cu ternary alloy NPs rapidly evolved into nanoporous particles within a few minutes upon initiation of dealloying due to Ag-enhanced Cu leaching, while both the pore sizes and ligament thickness were much better maintained as further leaching of both Ag and Cu proceeded. The structural evolution observed by TEM, together with the EDS results, provided compelling experimental evidence on the crucial roles of Ag in accelerating Cu leaching while suppressing ligament coarsening during the percolation dealloying of the ternary alloy NPs.

Erlebacher's working model for nanoporosity evolution also infers that the majority of residual less-noble elements should remain alloyed with Au and homogeneously distributed in the ligaments, though the less-noble residues may also locally segregate around the atomic steps and kinks on the topmost surface atomic layer.[3,4] Although it was difficult to precisely map the spatial distribution of residual Ag and Cu in NS-T using

EDS, both the residual Ag and Cu were clearly resolvable by X-ray photoelectron spectroscopy (XPS), a sensitive surface elemental analysis technique. While the binding energies of the Au 4f peaks remained essentially unchanged with respect to those of bulk Au, both the Cu 2p and Ag 3d peaks significantly down-shifted by 0.4 eV and 0.5 eV, respectively, with respect to those of bulk Cu and Ag, indicating that the residual Ag and Cu remained alloyed with Au[25]. The surface Ag/Au and Cu/Au atomic ratios quantified by XPS were similar to the bulk atomic ratios obtained from EDS, also suggesting that the residual Ag and Cu remained intermixed with Au rather than being segregated and accumulated on the ligament surfaces. Both the surface Ag/Au and Cu/Au atomic ratios of NS-T were found to be independent of the probe penetration depth of XPS, further confirming the intermix of residual Ag and Cu with Au. Without Ag, the residual Cu also remained alloyed with Au when Au-Cu binary alloy NPs were fully dealloyed.

While a glassy carbon electrode (GCE) itself was electrocatalytically inert, the dealloyed NS particles loaded on a GCE exhibited remarkable electrocatalytic activities toward a series of alcohol oxidation reactions at room temperature, including the methanol oxidation reaction (MOR), ethanol oxidation reaction (EOR), *iso*-propanol oxidation reaction (*i*-POR), and ethylene glycol oxidation reaction (EGOR). CV results clearly showed that NS-T were electrocatalytically more active than NS-B (Figures 3.2A-3.2D), exhibiting lower onset and peak oxidation potentials and higher peak currents during the anodic sweeps. A second oxidation peak emerged during the cathodic sweeps, signifying the oxidation of surface-adsorbed carbonaceous species not fully oxidized during the previous anodic sweeps.[26,27] We calculated the specific activities, which were intimately tied with the nature and density of surface active sites, by normalizing the

mass activities at the forward sweep peak potentials against the ECSAs. NS-T exhibited a larger ECSA, higher specific activities, and thereby significantly greater mass activities than NS-B (Figure 3.2E).

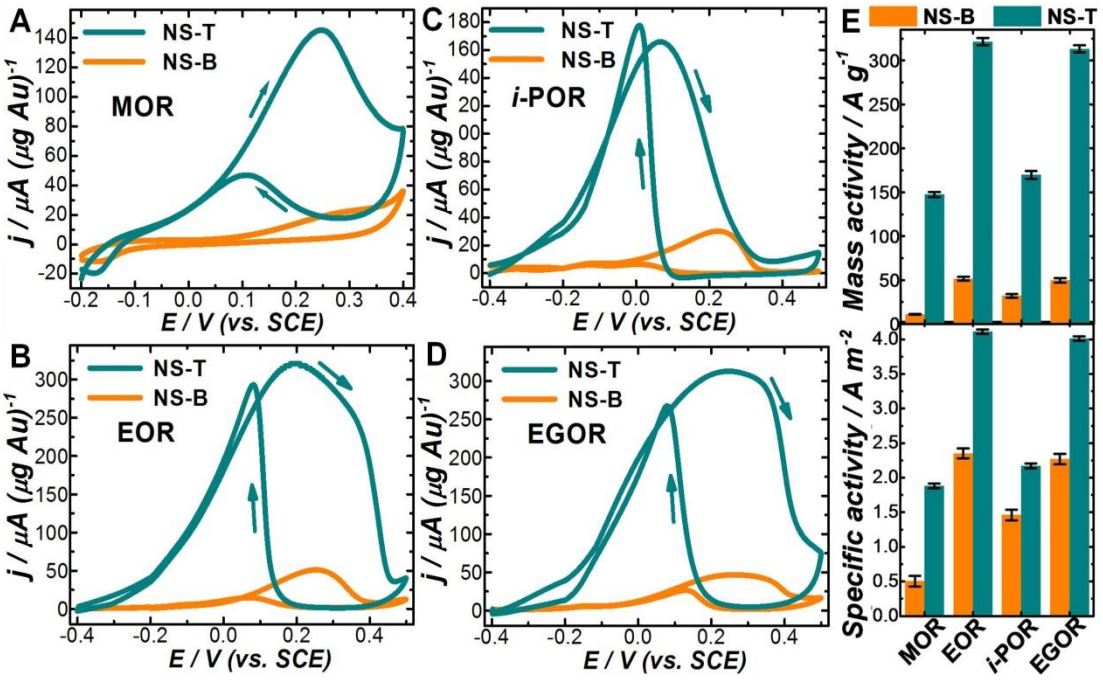

Figure 3.2. CV curves of NS-T and NS-B in 0.5 M KOH electrolyte solutions containing (A) 1 M methanol, (B) 1 M ethanol, (C) 1 M *iso*-propanol, and (D) 0.25 M ethylene glycol. The potential sweep rate was 5.0 mV s^{-1}. CV curves in panels A-C show the results of 1st sweep cycle on each sample and the CV curves in panel D show the results of 10th sweep cycle. (E) Mass activities and specific activities of NS-B and NS-T. The error bars represent the standard deviations of 5 samples.

The presence of Ag drastically changed the evolutions of ECSAs and specific activities during the percolation dealloying. The ECSA first increased upon nanoporosity formation and then decreased due to ligament coarsening as the percolation dealloying of $Au_{0.16}Cu_{0.84}$ binary alloy NPs proceeded. Meanwhile, the specific activity kept decreasing due to the surface restructuring driven by ligament coarsening. As a consequence, the maximal mass activity was achieved on the partially dealloyed NS particles. During the percolation dealloying of $Au_{0.14}Ag_{0.14}Cu_{0.72}$ ternary alloy NPs, however, the specific

activity continuously increased while the ECSA were well-maintained in range of 65-80 m^2 g^{-1}. The density of the active sites kept increasing as the co-leaching of Au and Cu proceeded and the active sites were well preserved by the residual Ag due to the suppression of ligament coarsening. Therefore, the fully dealloyed NS-T particles exhibited a higher mass activity than the partially dealloyed counterparts.

The residual Ag could stabilize the surface active sites during not only the nanoporosity-evolving percolation dealloying but also the electrocatalytic reactions. Chronoamperometry (CA) results showed that the catalytic activities of NS-T were significantly more robust than that of NS-B (Figures 3.3A-3.3D). Interestingly, for NS-T-catalyzed EGOR, the catalytic current even increased first before it started to decay till reaching the steady state current, whereas the current kept decreasing on NS-B. Multiple cycle CV results agreed with the CA results very well. The catalytic performances before and after CA measurements (0.2 V *vs.* SCE for 2 h) were further evaluated by CV The ratios of the final anodic peak currents after CA measurements, $j_{p,f}$, to the initial anodic peak current before CA measurements, $j_{p,i}$, were summarized in Figure 3.3E. While significant activity deterioration was observed on NS-B, the catalytic activities of NS-T were much better preserved during the reactions. The enhanced catalytic durability observed on NS-T essentially arose from the preservation of active sites and ECSA due to the presence of residual Ag. The partially dealloyed $Au_{0.86}Ag_{0.09}Cu_{0.05}$ NS particles with a higher fraction of residual Ag exhibited a similar catalytic durability but significantly lower mass activity toward MOR in comparison to the fully dealloyed NS-T, indicating that the residual Ag atoms stabilized the surface active sites rather than serving as the active sites themselves.

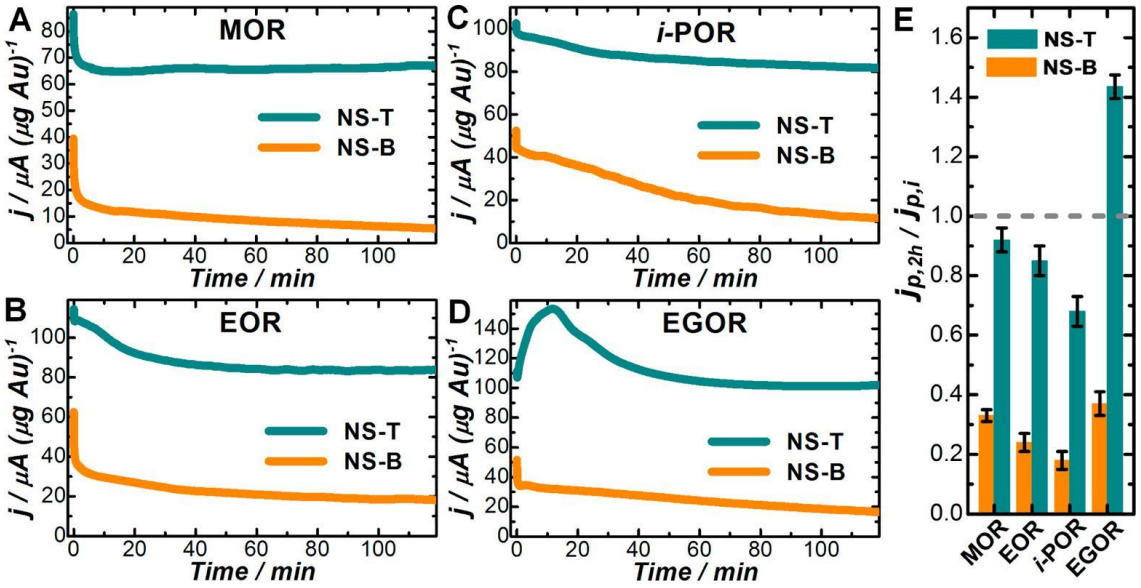

Figure 3.3. CA curves (at 0.20 V *vs.* SCE) of NS-T and NS-B in 0.5 M KOH electrolyte solutions containing (A) 1 M methanol, (B) 1 M ethanol, (C) 1 M *iso*-propanol, and (D) 0.25 M ethylene glycol. (E) $j_{p,f} / j_{p,i}$ for NS-B and NS-T. The error bars represent the standard deviations of 5 samples.

We further performed CV measurements at different potential sweep rates, v, for the alcohol oxidation reactions. The ratio of forward (anodic) sweep peak current to backward (cathodic) sweep peak current, j_f/j_b, which reflected the tolerance of the catalysts to the carbonaceous species accumulation, increased with v, suggesting that fast potential sweep favored oxidation of the surface adsorbed alcohols during the anodic sweeps. The highly curved surfaces of the nano-ligaments were enclosed by a mixture of surface atoms with various ACNs, thereby exhibiting highly heterogeneous catalytic activities from site to site. In addition, the molecular diffusion rates in the interior regions of the NS particles may be drastically different from those on the outer surfaces due to nanoconfined cage effects.[28] The anodic peak current was far from being proportional to either v or $v^{1/2}$, suggesting that the electrocatalytic reactions on the dealloyed NS particles may involve multiple site-specific electron transfer and molecular

diffusion rates and thereby are much more complicated than a simple diffusion- or surface-controlled process on a planar electrode surface.

3.4 Conclusion

The idea of incorporating a third non-leachable, noble element into the bulk of binary alloys to modify the dealloying behaviors of the alloys dates back to early 1990s.[29] Addition of a small concentration of arsenic into Cu-Zn brasses effectively suppressed the dealloying due to the pinning of mobile Cu atomic step edges by surface-segregated arsenic.[29] Similarly, small amounts of Pt added to the bulk of Ag-Au alloy membranes also accumulated around the surface atomic step edges to stabilize the undercoordinated atoms during percolation dealloying.[30] However, as a leachable less-noble element, Ag plays unique roles distinct from those of the non-leachable arsenic and Pt in the bulk alloys during the nanoporosity-evolving percolation dealloying. As demonstrated here, the co-leaching of Ag and Cu from Au-Ag-Cu ternary alloy NPs allows us to accelerate Cu leaching while suppressing ligament coarsening, resulting in dealloyed NS particles with substantially larger specific surface areas and higher surface active site densities than their Ag-less counterparts. The residual Ag in the fully dealloyed NS particles also stabilizes the active sites and the nanoporous architectures, thereby greatly enhancing the durability of electrocatalytic activities toward alcohol oxidation reactions. This work sheds light on the underlying roles of the less-noble residues that are crucial to the electrocatalytic competence of dealloyed metallic nanostructures, providing insightful knowledge that guides the rational optimization of electrocatalysis for fuel cell applications. In a broader context, the residual Ag exists not only in dealloyed Au nanoporous foams or NS particles, but also in a large variety of catalytically active Au

nanostructures, such as nanocages,[31] nanorods,[32] surface roughened NPs,[22] and high-index faceting nanopolyhedra,[21,33] due to the involvement of Ag in their shape-controlled syntheses. However, the underlying contributions of the residual Ag to the catalytic performances of these Au nanostructures still remain largely unexplored. The insights gained through this work provide important implications that germinate future work toward thorough understanding of the crucial roles of residual less-noble elements underpinning the intriguing catalytic behaviors of noble metal nanocatalysts.

3.5 References

(1) Chen, C.; Kang, Y. J.; Huo, Z. Y.; Zhu, Z. W.; Huang, W. Y.; Xin, H. L. L.; Snyder, J. D.; Li, D. G.; Herron, J. A.; Mavrikakis, M.; Chi, M. F.; More, K. L.; Li, Y. D.; Markovic, N. M.; Somorjai, G. A.; Yang, P. D.; Stamenkovic, V. R., *Science* **2014**, 343, 1339.

(2) Wittstock, A.; Zielasek, V.; Biener, J.; Friend, C. M.; Bäumer, M., *Science* **2010**, 327, 319.

(3) Erlebacher, J.; Aziz, M. J.; Karma, A.; Dimitrov, N.; Sieradzki, K., *Nature* **2001**, 410, 450.

(4) Fujita, T.; Guan, P. F.; McKenna, K.; Lang, X. Y.; Hirata, A.; Zhang, L.; Tokunaga, T.; Arai, S.; Yamamoto, Y.; Tanaka, N.; Ishikawa, Y.; Asao, N.; Yamamoto, Y.; Erlebacher, J.; Chen, M. W., *Nat. Mater.* **2012**, 11, 775.

(5) Wittstock, A.; Baumer, M., *Accounts Chem. Res.* **2014**, 47, 731.

(6) Moskaleva, L. V.; Rohe, S.; Wittstock, A.; Zielasek, V.; Kluner, T.; Neyman, K. M.; Baumer, M., *Phys. Chem. Chem. Phys.* **2011**, 13, 4529.

(7) Oezaslan, M.; Heggen, M.; Strasser, P., *J. Am. Chem. Soc.* **2012**, 134, 514.

(8) Snyder, J.; McCue, I.; Livi, K.; Erlebacher, J., *J. Am. Chem. Soc.* **2012**, 134, 8633.

(9) Wang, D. L.; Yu, Y. C.; Xin, H. L. L.; Hovden, R.; Ercius, P.; Mundy, J. A.; Chen, H.; Richard, J. H.; Muller, D. A.; DiSalvo, F. J.; Abruna, H. D., *Nano Lett.* **2012**, 12, 5230.

(10) Li, X.; Chen, Q.; McCue, I.; Snyder, J.; Crozier, P.; Erlebacher, J.; Sieradzki, K., *Nano Lett* **2014**, 14, 2569.

(11) Gan, L.; Heggen, M.; O'Malley, R.; Theobald, B.; Strasser, P., *Nano Lett.* **2013**, 13, 1131.

(12) Qi, J.; Motwani, P.; Gheewala, M.; Brennan, C.; Wolfe, J. C.; Shih, W. C., *Nanoscale* **2013**, 5, 4105.

(13) Vidal, C.; Wang, D.; Schaaf, P.; Hrelescu, C.; Klar, T. A., *ACS Photonics* **2015**, 2, 1436.

(14) Liu, K.; Bai, Y. C.; Zhang, L.; Yang, Z. B.; Zheng, H. Q.; Yin, Y. D.; Gao, C. B., *Nano Lett.* **2016**, 16, 3675.

(15) Zhang, J. T.; Liu, P. P.; Ma, H. Y.; Ding, Y., *J. Phys. Chem. C* **2007**, 111, 10382.

(16) Zhang, X. M.; Ding, Y., *Catal. Sci. Technol.* **2013**, 3, 2862.

(17) Zhang, L.; Blom, D. A.; Wang, H., *Chem. Mat.* **2011**, 23, 4587.

(18) Zhang, L.; Jing, H.; Boisvert, G.; He, J. Z.; Wang, H., *ACS Nano* **2012**, 6, 3514.

(19) Li, G. G.; Villarreal, E.; Zhang, Q. F.; Zheng, T. T.; Zhu, J. J.; H., W., *submitted.* **2016**.

(20) Hamelin, A.; Martins, A. M., *J. Electroanal. Chem.* **1996**, 407, 13.

(21) Zhang, J. A.; Langille, M. R.; Personick, M. L.; Zhang, K.; Li, S. Y.; Mirkin, C. A., *J. Am. Chem. Soc.* **2010**, 132, 14012.

(22) Pedireddy, S.; Lee, H. K.; Tjiu, W. W.; Phang, I. Y.; Tan, H. R.; Chua, S. Q.; Troadec, C.; Ling, X. Y., *Nat. Commun.* **2014**, 5, DOI: 10.1038/ncomms5947.

(23) Hamelin, A., *J. Electroanal. Chem.* **1996**, 407, 1.

(24) Trasatti, S.; Petrii, O. A., *J. Electroanal. Chem.* **1992**, 327, 353.

(25) Kim, M. J.; Na, H. J.; Lee, K. C.; Yoo, E. A.; Lee, M. Y., *J. Mater. Chem.* **2003**, 13, 1789.

(26) Sneed, B. T.; Young, A. P.; Jalalpoor, D.; Golden, M. C.; Mao, S. J.; Jiang, Y.; Wang, Y.; Tsung, C. K., *ACS Nano* **2014**, 8, 7239.

(27) Guo, S. J.; Zhang, S.; Sun, X. L.; Sun, S. H., *J. Am. Chem. Soc.* **2011**, 133, 15354.

(28) Mahmoud, M. A.; Narayanan, R.; El-Sayed, M. A., *Accounts Chem. Res.* **2013**, 46, 1795.

(29) Newman, R. C., *Corros Sci* **1992**, 33, 1653.

(30) Snyder, J.; Asanithi, P.; Dalton, A. B.; Erlebacher, J., *Adv. Mater.* **2008**, 20, 4883.

(31) Zeng, J.; Zhang, Q.; Chen, J. Y.; Xia, Y. N., *Nano Lett.* **2010**, 10, 30.

(32) Zhou, X. C.; Andoy, N. M.; Liu, G. K.; Choudhary, E.; Han, K. S.; Shen, H.; Chen, P., *Nat. Nanotechnol.* **2012**, 7, 237.

(33) Zhang, Q. F.; Wang, H., *ACS Catal.* **2014**, 4, 4027.

CHAPTER 4

SURFACE ATOMIC COORDINATION MATTERS: SELECTIVE ELECTROCATALYTIC ACTIVITY ON DEALLOYED NANOSPONGE PARTICLES

4.1 Introduction

Dealloying, which involves the selective dissolution of less-noble components from a metallic alloy matrix and concurrent structural rearrangements of the more-noble metals, provides a unique and versatile pathway to tailor the structures and compositions and thereby fine-tune the properties of the dealloyed materials.[1-5] The percolation dealloying of bulk Au/Ag or Au/Cu alloy membranes has been of particular interest, which results in the formation of nanoporous Au sponge composed of three-dimensional bicontinuous networks of interconnected Au-rich nanoligaments.[1,6] In striking contrast to their chemically inert bulk counterparts, the dealloyed nanoporous Au foam exhibits remarkably catalytic activities comparable to those of ultrasmall sub-5 nm Au nanoparticles (NPs) as a consequence of the high abundance of coordinatively unsaturated atoms located on the highly curved nanoligament surfaces, serving as catalytically active sites toward a variety of reactions.[1,2,4 7]

While dealloyed bulk systems exhibit promising performances, the percolation dealloying of alloys has been already pushed forward to particulate nanostructures, which enables controlled introduction of nanoporosity to metallic NPs with well-defined compositional (e.g., overall and surface/bulk ratios of metal A and B) and morphological (e.g., particle size and shape) configurations,[8-14] and eventually realizes the rational design of dealloyed NPs with unique physicochemical properties (highly efficient catalytic activities). Great success in systematically tuning the density of active sites on the ligament surfaces of Au-dominated dealloyed nanosponge particles (DNSPs) toward performance optimization has been achieved through kinetic control over percolation dealloying of alloy NPs and the active sites and structures could be well preserved by

incorporation of structure-stabilizing residual components into the dealloyed NPs.[15-17] Equally important to the catalytic activity and durability is the selectivity of Au nanocatalyst toward particular reaction of interest, which essentially depends on undercoordination environments on the local surface. How to optimize the electrocatalytic selectivity of Au nanocatalyst, nevertheless, remains a big challenge. While numerous studies have been focusing on the potential catalytic activity for partially redox reactions of supported ultrasmall Au NPs or Au clusters,[18-21] neither of which possesses the desired surface structures to study the catalytic selectivity of the Au nanocatalyst. In addition, strong synergistic effects among the interface to the supports, defect sites, and functional groups on the support as well as reaction conditions on the overall catalytic activity have limited the understanding of the underlying intrinsically catalytic selectivity of the Au nanocatalyst.[22-24] Much effort has been recently made to uncover the relationship between catalytic performance and atomic-level surface structure over support-free polyhedral Au NPs enclosed by specific types of well-defined low-index and high-index facets with different surface atomic coordination numbers,[25-29] but few attention has been paid on their surface-correlated catalytic selectivity. Building detailed correlation between the surface structure atomic coordination and the catalytic selectivity that underpins the Au DNSPs, seems unexceptional and has not been investigated so far. In contrast to the achievement in fine-tuning of surface atomic-level structure through facet control, the lack of precise control over the atomic coordination on Au DNSPs surface has been a huge barrier to quantitatively correlate the catalytic selectivity with the surface coordinations due to their substantially more complicated surface structures based on conventional percolation dealloying that typically started

from homogenous alloy NPs.

Here we endeavor to gain quantitative insights into the facet-selectivity relationship of Au NPs with well-defined facets using the room temperature electrocatalytic glucose oxidation as a model reaction,[30] and then further push the atomic-level surface structure control over Au DNSPs through percolation dealloying of Au-Cu bimetallic nanospheres with interior compositional gradients. Au-Cu bimetallic NPs could selectively transform into fully hollow nanostructures or partially porous structures with solid Au cores and interconnected ligament shells, which possess different coordination environments on the surface, making it possible to study the catalytic selectivity of Au DNSPs.

4.2 Experimental Details

Materials Polyvinylpyrrolidone (PVP, average MW 58 000), (1-Hexadecyl)trimethylammonium chloride (CTAC, 96%) chloroauric acid ($HAuCl_4 \cdot 4H_2O$), copper nitrate hydrate ($Cu(NO_3)_2 \cdot 3H_2O$), and tetraethylene glycol (TEG) were purchased from Alfa Aesar. Sodium borohydride ($NaBH_4$, 99%), L-ascorbic acid (AA, 99.5%), and hydrochloric acid (HCl, 37%), D-glucose, hydrazine solution ($N_2H_4 \cdot 3H_2O$ 35 wt %), nitric acid (HNO_3 65%), sulfuric acid (H_2SO_4 98%), and Nafion perfluorinated resion solution (5 wt%) were purchased from Sigma-Aldrich. Potassium carbonate (K_2CO_3) and formaldehyde (37 wt%) were purchased form J.T. Baker. Sodium hydroxide (NaOH), potassium nitrate (KNO_3), and potassium hydroxide (KOH) were purchased from Fisher Scientific. (1-Hexadecyl)trimethylammonium bromide (CTAB, > 98.0 %), D-gluconolactone, D-sucrose, and D-fructose were purchased from TCI America. D-glucaric acid potassium salt was purchased from MB Biomedicals, LLC. All reagents were used as received without further purification. Ultrapure Milli-Q water with a

resistivity of 18.2 MΩ (Millipore) was used for all the experiments.

Synthesis of Au Elongated Tetrahexahedral (ETHH) Nanoparticles Au ETHH nanoparticles were prepared following a reported seed-mediated protocol with minor modifications. Colloidal Au seeds were first prepared by the reducing $HAuCl_4$ with $NaBH_4$ in the presence of CTAB. In typical, 0.60 mL of ice-cold, freshly prepared $NaBH_4$ (10 mM) were quickly injected into a solution composed of CTAB (9.75 mL, 0.10 M) and $HAuCl_4$ (0.25 mL, 10 mM) under vigorous magnetic stirring (1000 rpm). The mixed solution was stirred for 1 min, left undisturbed for 2 h and then diluted by 50-fold with CTAB (0.10 M) to obtain the seed solution for the subsequent particles growth. The growth solution was prepared by adding $HAuCl_4$ (2.0 mL, 10 mM), $AgNO_3$ (0.40 mL, 10 mM), HCl (0.80 mL, 1.0 M), and AA (0.32 mL, 0.10M) into a CTAB (40.00 mL, 0.10 M) solution in succession. After gently mixing the growth solution for 30 s, the growth of Au ETHH nanoparticles was initiated by adding 0.1 mL of the Au seed solution. The reaction solution was gently mixed for 30 s immediately after the addition of Au seeds and then left undisturbed at 30 ^{o}C for overnight. The obtained Au ETHH nanoparticles were washed with water twice and finally redispersed in 5.0 mL of water.

Synthesis of Au Trisoctahedral (TOH) Nanoparticles Au TOH nanoparticles were prepared following a previous protocol based on seed-mediated growth. Colloidal Au seeds were prepared by the reducing $HAuCl_4$ with $NaBH_4$ in the presence of CTAC. In a typical procedure, 0.30 mL of ice-cold, freshly prepared $NaBH_4$ (10 mM) were quickly injected into a solution composed of CTAC (10.00 mL, 0.10 M) and $HAuCl_4$ (0.25 mL, 10 mM) under magnetic stir (1000 rpm). The mixed solution was stirred for 1 min, left undisturbed for 2 h and then diluted by 1000-fold with CTAC (0.10 M) to obtain the Au

seed solution for the subsequent particles growth. The growth solution was prepared by sequentially adding $HAuCl_4$ (0.50 mL, 10 mM) and AA (1.0 mL, 0.10 M) into a CTAC (10.00 mL, 0.10 M) solution. After gently mixing the growth solution for 30 s, the growth of Au TOH nanoparticles was initiated by adding 0.015 mL of the Au seed solution. The reaction solution was gently mixed for 30 s immediately after the addition of Au seeds and then left undisturbed at room temperature for 4 h. The obtained Au TOH nanoparticles were washed with water and finally redispersed in 5.0 mL of water.

Synthesis of Au@Cu_2O Core-shell Nanoparticles Quasi-spherical Au nanoparticles (QSNPs) were first synthesized by reducing $HAuCl_4$ with formaldehyde at room temperature. In a typical procedure, 50 mg of K_2CO_3 was dissolved in 200 mL of water, followed by addition of 3 mL of 25 mM $HAuCl_4$. The mixture solution was aged in the dark for 18 h before use. Then 1.34 mL of 37 % formaldehyde solution was added into the mixture under magnetic stir (300 rpm). After 30 min, the resulting Au QSNPs were centrifuged, washed with water, and redispersed in 10 mL of water.

Then 9.6 mL of Au QSNPs was introduced into 300 mL of 2 wt% PVP aqueous solution. 3.6 mL of 0.1 M $Cu(NO_3)_2$ was subsequently added. The reaction mixture was transferred into an ice bath, and then 0.67 mL of 5 M NaOH and 0.3 mL of N_2H_4 $3H_2O$ solution were added in successive under magnetic stir. The solutions were kept stirring for 15 min, and the obtained Au@Cu_2O core-shell nanoparticles were separated from the reaction solution by centrifugation (2000 rpm, 10 min) washed with ethanol and redispersed in 10 mL ethanol.

Synthesis of Au@Cu Core-shell and Au-Cu Alloy Nanoparticles Au@Cu core-shell and Au-Cu alloy nanoparticles were prepared through a polyol-assisted growth

method. Typically, 1.0 mL of Au@Cu_2O core-shell NPs was added into 20.0 mL TEG containing 0.1 g PVP. Au@Cu core-shell, Au-Cu alloy with compositional gradients (Alloy-G), and homogenous Au-Cu alloy (Alloy-H) nanoparticles were obtained by heating the mixture at 180 ^oC, 240 ^oC, and 300 ^oC for 30 min, respectively. The obtained nanoparticles were washed with ethanol five times, and finally redispersed in 1.0 mL of ethanol.

Synthesis of Dealloyed Au NPs and Au Nanosponges Dealloyed Au NPs, Au nanosponge particles with solid Au cores and nanoligament shells (DNSPs-G), and Au nanosponges with voids throughout the entire particles (DNSPs-H) were obtained through chemical etching upon exposure of 1.0 mL of the Au@Cu core-shell NPs, Alloy-G, and Alloy-H NPs to 3.0 mL of 3.0 M HNO_3 at room temperature for 45 min, respectively. The resulting dealloyed particles were washed by water three times and finally redispersed in 1 mL of water.

Structural Characterization of NPs The morphologies and structures of the NPs were characterized by transmission electron microscopy (TEM) using a Hitachi H-8000 transmission electron microscope, which was operated at an accelerating voltage of 200 kV. All samples for TEM measurements were dispersed in ethanol and drop-dried on 300 mesh Formvar/carbon-coated-Cu grids (Electron Microscopy Science Inc.). The structures and compositions of the NPs were also characterized by Scanning Electron Microscopy (SEM) and Energy Dispersive Spectroscopy (EDS) measurements using a Zeiss Ultraplus thermal field emission scanning electron microscope. The samples for SEM and EDS measurements were dispersed in ethanol and drop-dried on silicon wafers. The sizes of the NPs were analyzed on the basis of TEM images using Nano Measurer

analysis software (Department of Chemistry, Fudan University, China). The size distribution histograms were obtained from more than 100 NPs for each sample. XPS measurements were carried out using a Krato AXIS Ultra DLD XPS system equipped with a monochromatic Al Kα source. The samples for XPS measurements were all freshly prepared and dried in vacuum before being loaded into the XPS chambers. Powder X-ray diffraction (PXRD) patterns were record on a SAXSLab Ganesha at the South Carolina SAXS Collaborative (Cu $K\alpha$ = 1.5406 Å). Inductively coupled plasma-mass spectrometry (ICP-MS) measurements were performed using a Finnigan ELEMENT XR double focusing agnetic sector field inductively coupled plasma-mass spectrometer (SF-ICP-MS). 0.2 mL min^{-1} Micromist U-series nebulizer (GE, Australia), quartz torch and injector (Thermo Fisher Scientific, USA) were used for sample introduction. Sample gas flow was at 1.08 mL min^{-1}. The forwarding power was 1250 W. The sample for ICP-MS measurements were prepared by adding 1 mL of nitric acid and 3 mL of hydrochloric acid into Teflon digestion vessels containing the samples. The samples were digested using hot block at 180 ^{o}C for 4 h. The digestates were brought to 50 mL with water. A 3-point calibration curve was used for Cu and Au. The calibration range was from 50 to 600 ppb. The R^2 values for the initial calibration curves were greater than 0.995.

Electrochemical Measurements All the electrochemical measurements were performed using a CHI 660E workstation (CH Instruments, Austin, TX) at room temperature with a three-electrode system composed of a Pt wire as the auxiliary, a saturated calomel electrode (SCE) as the reference, and a glassy carbon electrode (GCE, 3 mm diameter) as the working electrode. Typically, the GCE was polished with 0.3 mm

alumina slurry and followed by washing with water and ethanol before use. Colloidal suspensions containing certain amount of Au TOH NPs, Au ETHH NPs, and Au NPs etched from Au@Cu core-shell NPs, DNSPs-G and DNSPs-H were dropped and air-dried on the pretreated GCEs at room temperature, and then 2 μL of Nafion solution (0.2 wt%) was dropped to hold the NPs. To evaluate the selectively electrocatalytic activities of Au NPs toward glucose oxidation, cyclic voltammetry (CV) measurements were performed in a N_2-saturated 0.5 M KOH solution containing 6.0 mM glucose, 6.0 mM gluconolactone, 6.0 mM glucaric acid, 6.0 mM sucrose, and 6.0 mM fructose at a potential sweep scan rate of 50 mV s^{-1}, respectively. Electrochemical surface oxide stripping was investigated through CV measurements performed in N_2-saturated 0.5 M H_2SO_4 solution at a scan rate of 5 mV s^{-1}. The polarization trace was normalized against the Au mass of the particles loaded on each electrode. The linear sweep voltammetry (LSV) of Au-Cu bimetallic NPs were measured in 1.0 M KNO_3 electrolyte in the potential scan range from 0 V to 0.8 V (*vs.* SCE) at a scan rate of 5 mV s^{-1}. To assess the electrocatalytic durability of Au TOH NPs, Au ETHH NPs, DNSPs-G and DNSPs-H, chronoamperometry (CA) measurements were carried out at 0.24 V or 0.40 V (*vs.* SCE) depending on their peak potentials for glucose oxidation in 6.0 mM glucose in the presence of 0.5 M KOH electrolyte for 2 h.

4.3 Results and Discussions

As illustrated in Figure 4.1A, glucose can be selectively oxidized to gluconolactone through a 2-electron process or glucaric acid through a 4-electron process.[31-34] In this work, Au trisoctahedral (TOH) and elongated tetrahexahedral (ETHH) NPs are firstly selected as representative model nanostructures due to their characteristic surface atomic

coordination numbers (SACNs). The detailed atomic-level surface structures of the Au TOH and THH NPs have been fully characterized by using a series of electron microscopy techniques as described in our previous publication,[27] the surfaces of Au TOH and Au ETHH NPs were dominated by [221] and [730] facets with a high fraction of surface undercoordination numbers of 7 and 6, respectively.

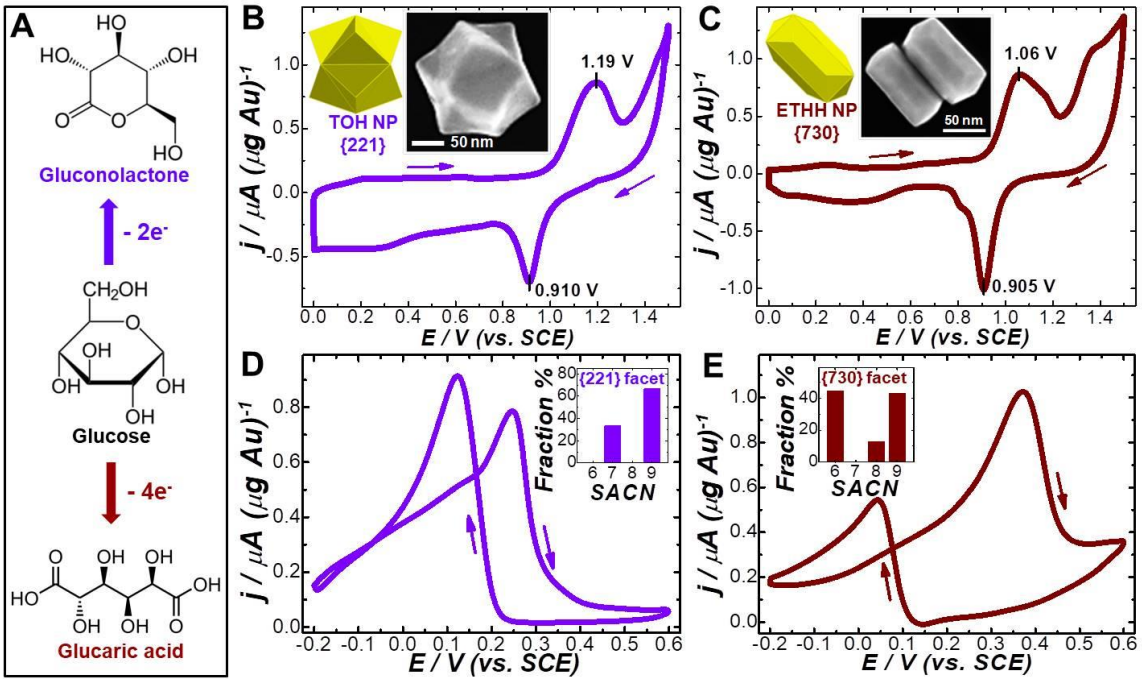

Figure 4.1. **Selective electrocatalytic oxidation of glucose on high-index faceting polyhedral NPs.** (A) Schematic illustration of selective oxidation of glucose to form gluconolactone and glucaric acid, respectively. CV curves of electrochemical surface oxide stripping of (B) Au TOH NPs and (C) Au ETHH NPs in 0.5 M H_2SO_4 at a potential sweep rate of 5 mV s^{-1}. The insets show the geometric models (left insets) and SEM images of the NPs (right insets). The surfaces of TOH and ETHH NPs are enclosed by high-index {221} and {730} facets, respectively. CV curves of (D) Au TOH NPs and (E) Au ETHH NPs in deoxygenated solutions containing 6.0 mM glucose and 0.5 M KOH electrolyte at a potential sweep rate of 50 mV s^{-1}. The insets of panels D and E show the distribution of the surface atomic coordination numbers (SACNs) for the {221} and {730} facets, respectively.

We further used cyclic voltammetry (CV) as an electrochemical tool to characterize the atomic-level surface structures and electrocatalytically active surface areas (ECSAs)

of the Au TOH and ETHH NPs because of well correlation between the SACNs and the characteristic potentials for surface oxidation.[35-38] As shown in Figures 4.1B and 4.1C, Au TOH and ETHH NPs exhibited oxidation peaks at ~1.19 V vs. saturated calomel electrode (SCE) and ~ 1.05 V vs. SCE during the anodic sweeps, signifying the oxidation of undercoordinated surface atoms with SACNs of 7 and 6,[35,37,38]respectively, whereas the oxidation of close-packed surface atoms with SACNs of 8 and 9 on the surfaces of Au quasi-spherical NPs (QSNPs) occurred above 1.3 V vs. SCE. During the cathodic sweeps, the reduction peak around 0.90 V (vs. SCE) signified the electrochemical stripping of the surface oxide layers formed in the previous anodic scans. Assuming the specific charge associated with Au oxide stripping to be 450 μC cm^{-2},[39] the mass-specific ECSAs of the Au TOH, ETHH NPs, and Au QSNPs were estimated to be ~ 0.56, 0.85 and 0.49 m^2 g^{-1}, respectively.

We systematically studied the electrocatalytic activities of the Au TOH, Au ETHH, and Au QSNPs NPs for glucose oxidation reaction (GOR). As shown in Figures 4.1 D and 4.1E, the Au TOH and ETHH display superior catalytic performances for glucose oxidation, while both naked glassy carbon electrode (GCE) and Au QSNPs (SACNs of 8 and 9) were electrochemically inert (Figure 4.2), suggesting the electrocatalytic activities essentially originate from the surface under-coordinated atoms. Whereas the Au TOH and ETHH display drastically distinct characteristics in the CV curves, the anodic peaks of Au TOH and ETHH NPs emerge at ~ 0.24 V (vs. SCE) and ~ 0.40 V (vs. SCE), respectively. Another oxidation peak during the cathodic sweeps resulted from the further oxidation of surface-adsorbed carbonaceous species not fully oxidized during the previous anodic sweep.[40,41] The result indicates that the electrocatalytic oxidation of

glucose on Au TOH and ETHH NPs probably proceeds along different pathways to selectively form alternate products, which was intimately tied to the distribution of undercoordinated surface atoms (the insets in Figures 4.1D and 4.1E).

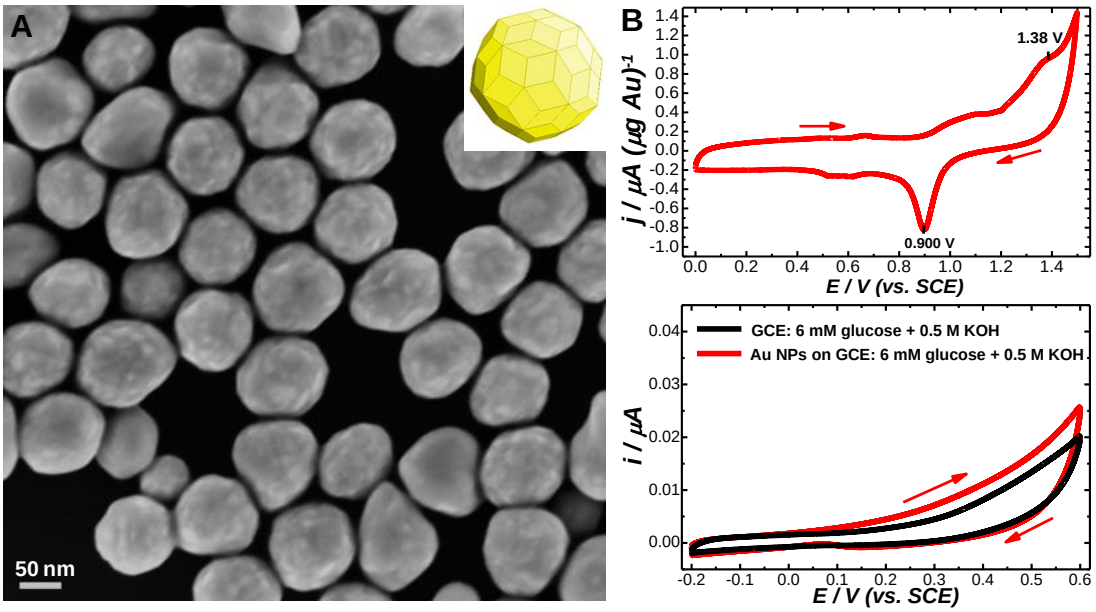

Figure 4.2. (A) SEM image of Au quasi-spherical nanoparticles (QSNPs) enclosed by low-index {111} and {100} facets. The inset shows the geometric model of an individual QSNP. (B) CV curve of electrochemical surface oxide stripping of Au QSNPs in 0.5 M H_2SO_4 at a potential sweep rate of 5 mV s^{-1}. (C) CV curves of a glassy carbon electrode (GCE) loaded with 4 μg of Au QSNPs and a GCE in a deoxygenated solution containing 6.0 mM glucose and 0.5 M KOH electrolyte at a potential sweep rate of 50 mV s^{-1}.

We further studied the electrocatalytic oxidation of gluconolactone and glucaric acid to clarify the oxidation products for GOR of the Au TOH and ETHH NPs (Figure 4.3). It is found that Au ETHH NPs can further catalyze the oxidation of gluconolactone at 0.40 V (vs. SCE), while Au TOH NPs demonstrate no activities for both gluconolactone and glucaric acid oxidations. The results indicated that the main product for GOR catalyzed by Au TOH NPs is gluconolactone, whereas complete oxidation of glucose into glucaric acid occurred on Au ETHH NPs. The observed facet-dependent catalytic selectivity correlated well with the characteristic distributions of undercoordinated surface atoms on

various facets. However, the catalytic activities of Au TOH and ETHH NPs are dramically restricted due to their limited ECSAs.

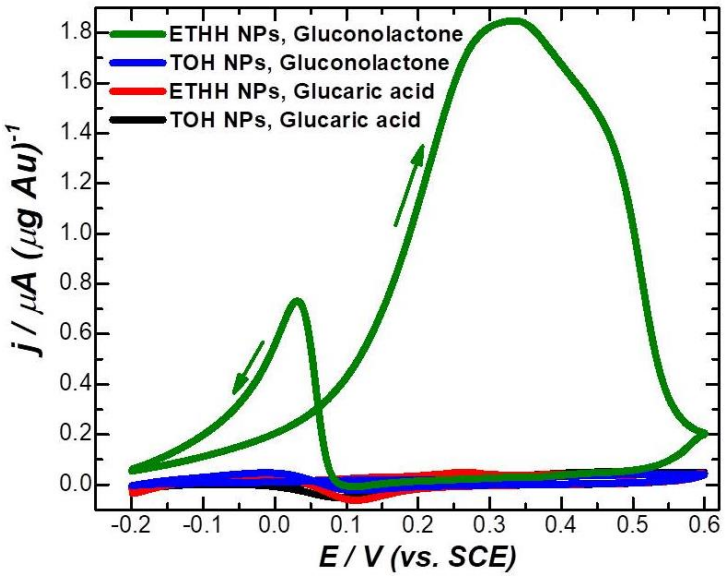

Figure 4.3. CV curves of Au TOH NPs and ETHH NPs in deoxygenated solutions of containing 6.0 mM gluconolactone or 6.0 mM glucaric acid in 0.5 M KOH electrolyte at a potential sweep rate of 50 mV s^{-1}.

Using percolation dealloying less-noble metals from alloys to form porous Au structures, the ECSAs can be greatly optimized compared with their solid counterparts.[17] Here we controllably fabricated spongy-like Au NPs with characteristic SACNs through percolation dealloying of Au-Cu bimetallic NPs with varying interior compositional gradients. The Au-Cu bimetallic NPs were first obtained by polyol-mediated reduction of the colloidal Au@Cu_2O core-shell NPs in tetraethylene glycol (TEG). The Cu/Au stoichiometric ratios of the alloy NPs are predetermined by the relative core and shell dimensions of the parental Au@Cu_2O core-shell NPs,[42] while the intraparticle compositional gradient of the bimetallic NPs could be fine tailored by the reaction temperature. We used scanning electron microcopy (SEM), energy-dispersive spectroscopy (EDS), transmission electron microscopy (TEM), powder X-ray diffraction

(PXRD), inductively coupled plasma mass spectrometry (ICP-MS), and X-ray photoelectron spectroscopy (XPS) to fully characterize the structures and compositions of the Au-Cu bimetallic NPs to illustrate the structural evolutions of Au@Cu_2O core-shell NPs upon thermal heating. As shown in Figure 4.4A, Au@Cu core-shell NPs with distinct core and shell heterostructures obtained by EDS elemental mapping were collected at 180 ^{0}C. When the reaction temperature increases to 240 ^{0}C, the Au and Cu atoms start to interdiffuse to form Au-Cu alloy NPs with compositional gradient (Au-rich alloy core and Cu-rich alloy shell), which are denoted as Alloy-G NPs (Figure 4.4B). Further increasing the temperature to 300 ^{0}C leads to the formation of Au-Cu alloy NPs with homogenous Au and Cu distributions (Figure 4.4C, denoted as Alloy-H NPs). TEM images also clearly demonstrate the contrast between the core and the shell gradually fade away and completely disappeared with the increase of reaction temperature, meanwhile the overall particle sizes significantly shrank. Figure 4.4D shows PXRD of the Au-Cu bimetallic NPs. Pure Au and Cu phases were determined for Au@Cu core-shell NPs, while a broad alloy feature accompanied with a tiny pure Au diffraction peak for Alloy-G NPs as a consequence of compositional gradients and well-defined alloy peaks of Alloy-H NPs were observed, respectively. We used linear sweep voltammetry (LSV) to study the electrochemical dealloying behaviors of Au-Cu bimetallic NPs (Figure 4.4E). Although their Au/Cu atomic ratios were the same, the onset potential for Cu oxidation from alloy NPs was positively shifted with respect to that of Au@Cu core-shell NPs because the Cu was stabilized by incorporating into Au matrix, and Alloy-H NPs exhibited a significantly higher critical potential to be oxidized.

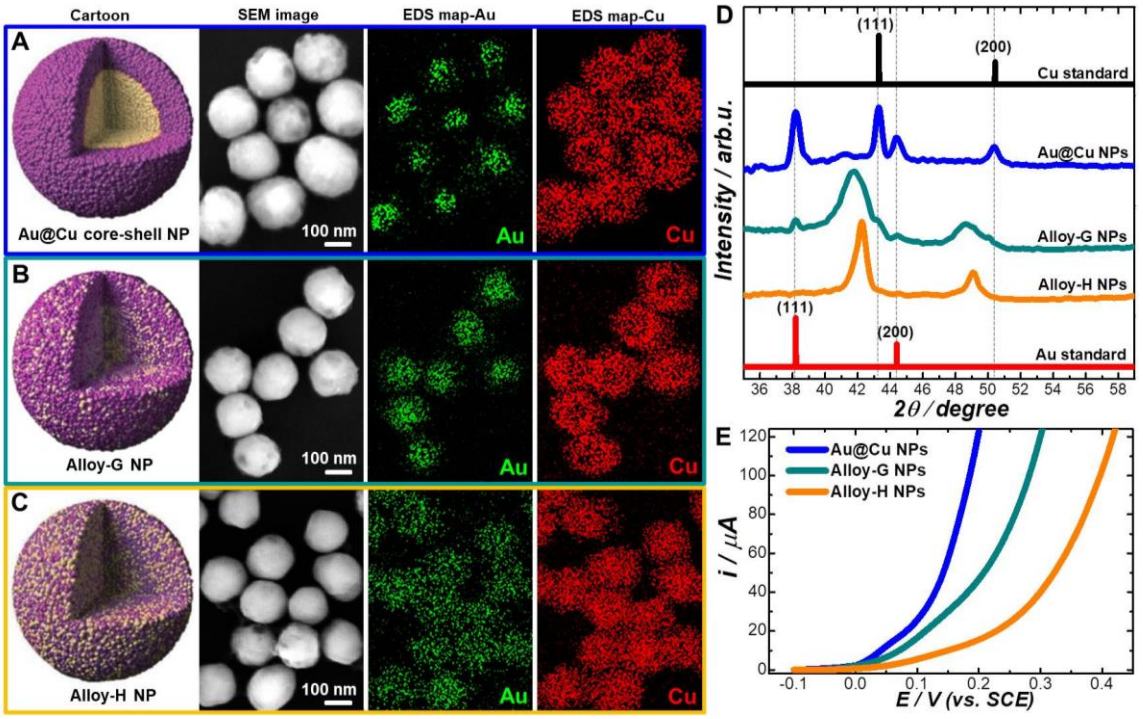

Figure 4.4. **Au-Cu bimetallic NPs with controlled intraparticle compositional gradient.** Cartoons, SEM images, and EDS elemental maps of (A) Au@Cu core-shell NPs, (B) Au-Cu alloy NPs with internal gradient (Alloy-G NPs), and (C) Au-Cu homogenous alloy NPs (Alloy-H NPs). (D) PXRD patterns of Au@Cu core-shell NPs, Alloy-G NPs, and Alloy-H NPs. The standard patterns for face center cubic (fcc) Au and Cu bulk materials are also shown for comparison. The PRXD patterns are offset for clarity. (E) Linear sweep voltammetry (LSV) curves of Au@Cu core-shell NPs, Alloy-G NPs, and Alloy-H NPs in 0.5 M KNO_3 solution at a potential sweep rate of 5.0 mV s^{-1}.

The results of element analysis based on EDS line scans further demonstrated the structural evolutions of the various Au-Cu bimetallic NPs (Figures 4.5A-4.5C). The Cu atomic ratios of the various bimetallic NPs measured from the EDS kept unchanged and were in good agreement with those quantified by ICP-MS (Figure 4.5D). XPS was used to characterize surface structures and compositions of the Au-Cu bimetallic NPs (Figure 4.6). For Au@Cu core-shell NPs, the binding energies of the Cu 2p peaks remained essentially unchanged with respect to those of bulk Cu, while Au 4f peaks up-shifted by ~ 0.45 eV with respect to those of bulk Au, accompanied by significant peak broadening caused by alloying of Au with Cu. With the interdiffusion of Au and Cu, a slight up shift

of ~ 0.2 eV of Au 4f peaks and almost no peak shift of Cu 2p peaks were observed on Alloy-G. While the Cu 2p XPS peaks of Alloy-H exhibited pronounced down-shift by ~0.6 eV with respect to those of the bulk Cu, no shift for Au 4f peaks was tested. The Cu atomic ratio quantified by XPS was much higher than that obtained from EDS for Au@Cu core-shell NPs due to fully covered pure Cu on the particle surface. The Cu atomic ratio of Alloy-G decreased but still higher than the bulk Cu atomic ratio, verifying their Cu-rich shell heterostructures. A similar Cu content for Alloy-H NPs quantified by XPS and EDS signified its homogenous structure.

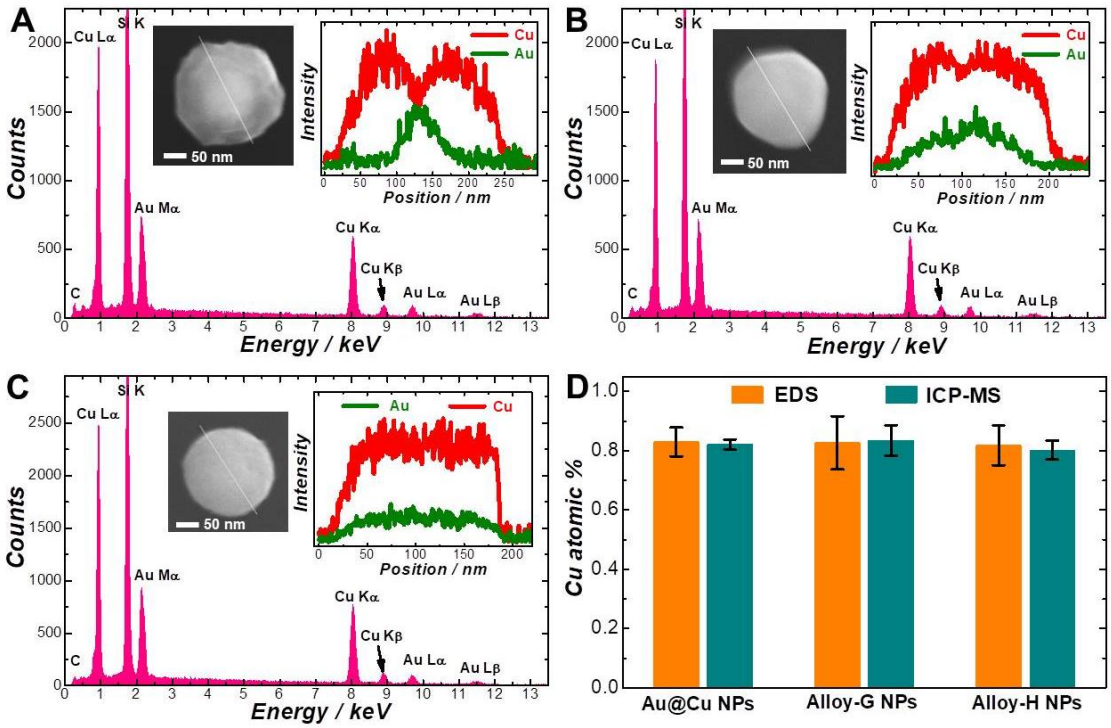

Figure 4.5. EDS of (A) Au@Cu core-shell NPs, (B) Alloy-G NPs, and (C) Alloy-H NPs. The insets show SEM images of individual NPs and the spatial elemental distributions of Au and Cu obtained from EDS line scan measurements. (D) Cu atomic percentages quantified by EDS and ICP-MS of Au@Cu core-shell NPs, Alloy-G NPs, and Alloy-H NPs.

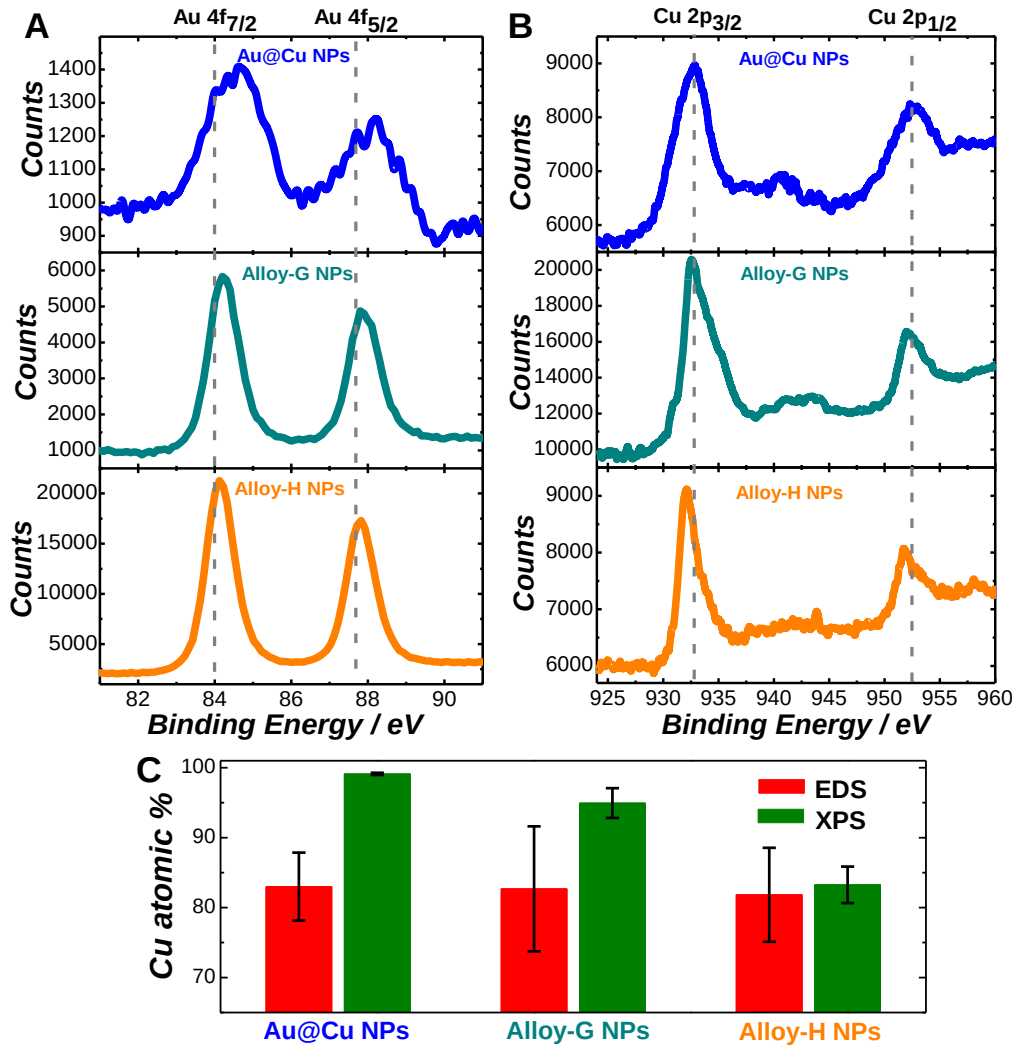

Figure 4.6. XPS of (A) Au 4f and (B) Cu2p regions of Au@Cu core-shell NPs, Alloy-G NPs, and Alloy-H NPs. The vertical dash lines indicate the peak positions of standard bulk Au and Cu. (C) The surface Cu atomic percentages quantified by XPS and the bulk Cu atomic percentages quantified by EDS of Au@Cu core-shell NPs, Alloy-G NPs, and Alloy-H NPs.

Upon exposure to chemical etchants, the Au-Cu bimetallic NPs exhibited structure-dependent compositional and structural evolutions. As shown in Figure 4.7A, the surface rough spherical Au NPs were obtained by treating Au@Cu core-shell NPs with 3.0 M HNO_3 for 45 min at room temperature. Alloy-G evolved into nanosponges (denoted as DNSPs-G in Figure 4.7B) with solid Au cores surrounded by nanoporous shells upon percolation dealloying, whereas Alloy-H transformed into well-defined nanosponges

with porosity throughout the entire particles (denoted as DNSPs-H in Figure 4.7C). PXRD, EDS, and ICP-MS all consistently showed that the dealloyed NPs was consisted of Au, and the overall particle size obviously shrank upon the percolation dealloying, while clearly resolvable down-shifted Cu 2p XPS peaks for both Au DNSPs indicated residual Cu remained alloyed with Au.[43]

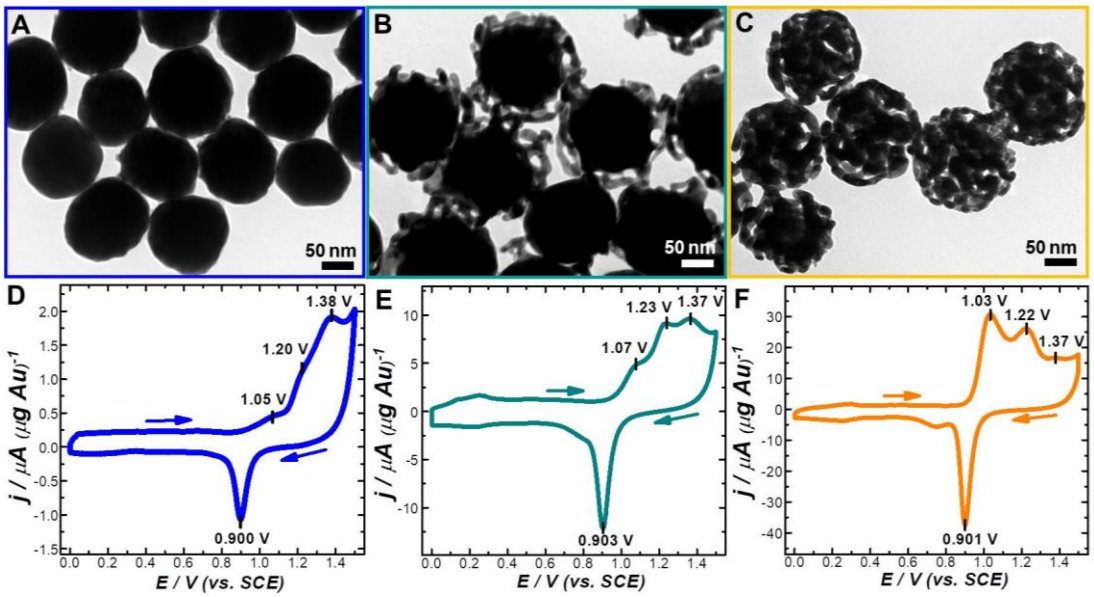

Figure 4.7. **Morphologies and surface structures of dealloyed nanosponge particles (DNSPs).** TEM images of (A) Au NPs obtained by etching the Au@Cu core-shell NPs in HNO_3, (B) DNSPs obtained through dealloying of Alloy-G NPs (DNSPs-G), and (C) DNSPs obtained through dealloying of Alloy-G NPs (DNSPs-H). CV curves of electrochemical surface oxide stripping of (D) Au NPs, (E) DNSPs-G, and (F) DNSPs-H in 0.5 M H_2SO_4 at a potential sweep rate of 5 mV s^{-1}.

We also used electrochemical oxide stripping to identify the surface atomic-level structure of the dealloyed Au NPs. As shown in Figure 4.7D, the oxidation of Au NPs etched from Au@Cu core-shell nanostructures occurred in a potential range above 1.3 V (vs. SCE). While DNSPs-G (Figure 4.7E) and DNSPs-H (Figure 4.7F) exhibited predominant oxidation peaks at ~ 1.23 V (vs. SCE) and ~ 1.03 V (vs. SCE) during the anodic scans, which were in very good agreement with the oxidation potentials occurred

on Au TOH and ETHH NPs with, respectively. The results signified that the surfaces of the DNSPs-G are dominated by undercoordinated surface atoms with a SACN of 7, while the surfaces of DNSPs-H are rich of surface atoms with an even lower SACN of 6, respectively. Based on cathodic stripping peaks, the mass-specific ECSAs of DNSPs-G and DNSPs-H were calculated to be approximately 10.9 and 30.1 m^2 g^{-1}, respectively, which is 20 and 50 times higher than that of the Au TOH and ETHH NPs with the same SACNs.

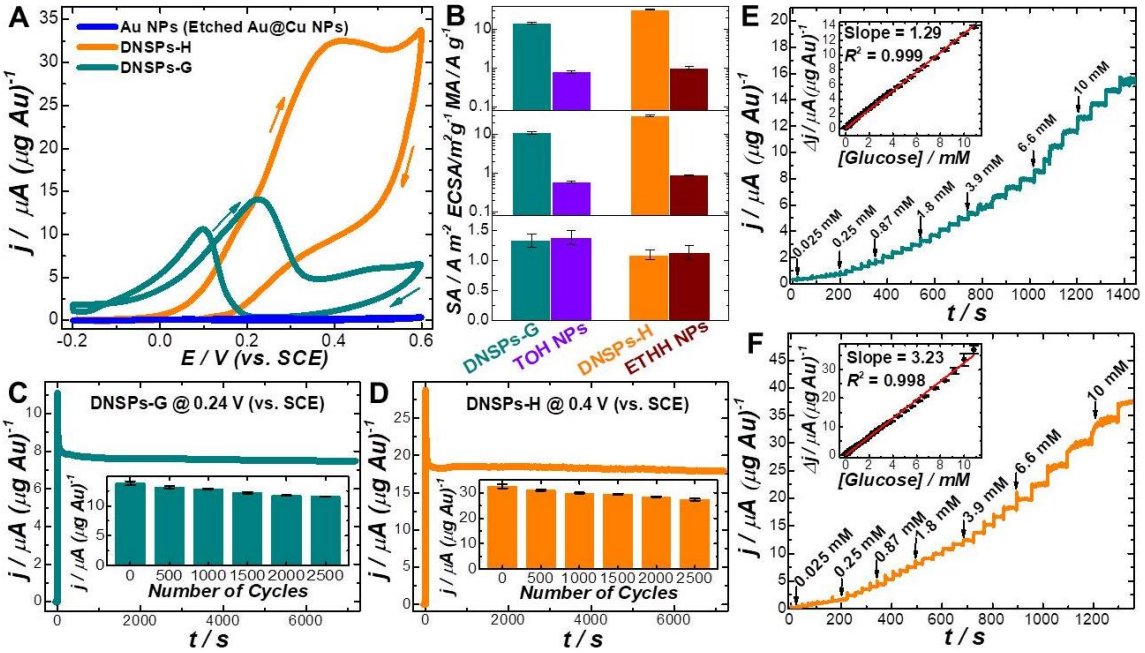

Figure 4.8. **Selective electrocatalytic oxidation of glucose on DNSPs.** (A) CV curves of Au NPs (etched Au@Cu core-shell NPs), DNSPs-G, and DNSPs-H in a deoxygenated solution containing 6.0 mM glucose and 0.5 M KOH electrolyte at a potential sweep rate of 50 mV s^{-1}. (B) Mass activity (MA), electrochemically active surface areas (ECSA), and specific activity (SA) of DNSPs-G, DNSPs-H, Au TOH NPs, and Au ETHH NPs. (C) CA curve of DNSPs-G at 0.24 V (*vs.* SCE). (D) CA curve of DNSPs-H at 0.40 V (*vs.* SCE). All CA measurements were carried out in solutions containing 6.0 mM glucose and 0.5 M KOH electrolyte. The insets of panel C and D show MAs of DNSPs-G and DNSPs-H after multiple CV cycles. (E) Amperometric response of DNSPs-G to successive additions of glucose at 0.24 V (*vs.* SCE). (F) Amperometric response of DNSPs-H to successive additions of glucose at 0.40 V (*vs.* SCE). The insets of panels E and F show the corresponding calibration curve for glucose detection.

To quantitatively unravel the correlation between the SACN and the electrocatalytic

selectivity, we investigated the electrocatalytic activities of the Au DNSPs and Au NPs for GOR. As shown in Figure 4.8A, in contrast to electrocatalytically inert of Au NPs, the Au DNSPs exhibited remarkable electrocatalytic activities. The oxidation peaks at ~ 0.24 V (vs. SCE) on DNSPs-G and ~ 0.40 V (vs. SCE) on DNSPs-H strongly indicated the oxidation product was glucnolactone and glucaric acid, respectively. This result strongly indicated electrocatalytic selectivity is sensitively dependent upon the surface atomic coordinations of the dealloyed Au NPs. By normalizing the oxidation peak current against the mass of Au on each electrode for GOR (Figure 4.8B), mass activities of ~ 14 μA μg^{-1} (at 0.24 V vs. SCE) and ~ 32 μA μg^{-1} (at 0.40 V vs. SCE) were obtained on the Au DNSPs-G and DNSPs-H NPs at a scan rate of 50.0 mV s^{-1}, which were about 20 and 30 orders of magnitude higher than those of the Au TOH (~ 0.73 μA μg^{-1} at 0.24 V vs. SCE) and ETHH NPs (~ 0.95 μA μg^{-1} at 0. 40 V vs. SCE), as a consequence of their significantly higher specific ECSA. The specific activates (SAs) of the Au DNSPs were calculated by normalizing the MAs against ECSAs, which were closely tied to the active site density on the NP surfaces. The Au DNSPs-G and DNSPs-H possessed similar SAs with those of Au TOH and ETHH NPs, respectively, which indicated the comparable densities of surface active sites on the surfaces of Au DNSPs-G and TOH NPs, as well as Au DNSPs-H and ETHH NPs. We used chronoamperometry (CA) measurements to assess the electrocatalytic durability of the DNSPs at their oxidation peak potentials. The catalytic activities of both Au DNSPs were significantly robust, as shown in Figures 4.8C and D. Multiple CV cycles showed slight decrease in oxidation currents (the insets of Figures 4.8C and 4.8D), which were consistent with the CA results. We further studied the Amperometric response of DNSPs for the successive injection of

glucose to 1 M KOH at their corresponding oxidation peaks and the typical *i*-t curves are displayed in Figures 4.8E and F. The corresponding current-concentration calibration plots clearly show that the linear relationship with R^2 of 0.999 and 0.998 for the DNSPs-G and DNSPs-H NPs, respectively. The sensitivity of the DNSPs-H determined by the slope of the linear fitting is 3.23 A g^{-1} mM^{-1}, which is obvious higher than that (1.29 A g^{-1} mM^{-1}) of the DNSPs-G NPs.

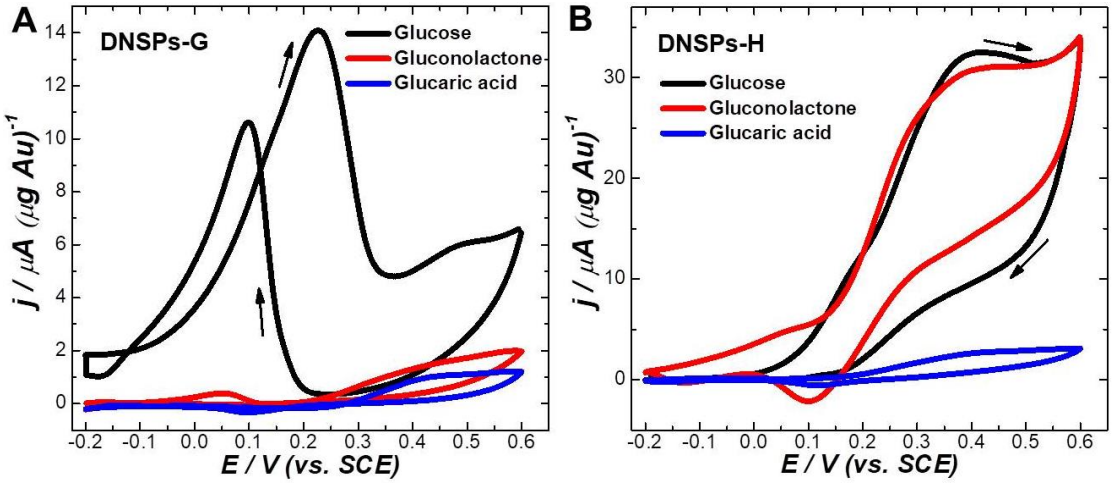

Figure 4.9. CV curves of (A) DNSPs-G and (B) DNSPs-H in deoxygenated solutions of 6.0 mM glucose, 6.0 mM gluconolactone, or 6.0 mM glucaric acid in 0.5 M KOH electrolyte at a potential sweep rate of 50 mV s^{-1}.

The SACN-dependent electrocatalytic selectivity of Au DNSPs was further verified by their electrocatalytic performances for gluconolactone and glucaric acid oxidation (Figure 4.9). The DNSPs-G exhibited dramatically diminished activity for gluconolactone oxidation whereas DNSPs-H efficiently catalyzed the further oxidation of gluconolactone into glucaric acid, and no activities were tested for glucaric acid oxidation on both Au DNSPs. Furthermore, we also investigated the electrocatalytic oxidation of fructose (a glucose isomer) and sucrose (a glucose fructose dimer) on the DNSPs to see whether the SACN-dependent electrocatalytic selectivity is a general

feature also for other small sugar molecules with similar structures to that of glucose. Similar selectivity observed in the reaction of fructose and sucrose oxidations further well verified the strong correlation between SACN and electrocatalytic selectivity (Figures 4.10A and 4.10B).

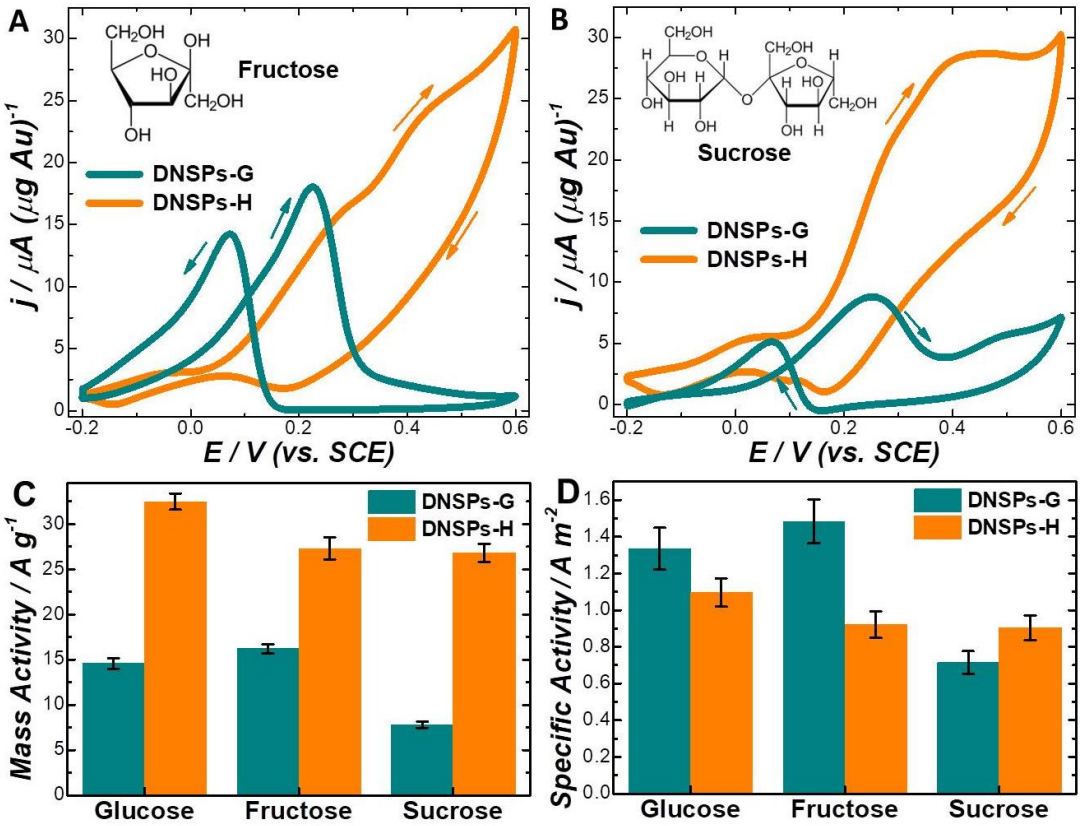

Figure 4.10. (A) CV curves of DNSPs-G and DNSPs-H in a deoxygenated solution of 6.0 mM fructose in 0.5 M KOH electrolyte at a potential sweep rate of 50 mV s^{-1}. (B) CV curves of DNSPs-G and DNSPs-H in a deoxygenated solution of 6.0 mM sucrose in 0.5 M KOH electrolyte at a potential sweep rate of 50 mV s^{-1}. (C) Mass activities and (D) specific activities of DNSPs-G and DNSPs-H for eletectrocatalytic oxidation of glucose, fructose, and sucrose.

The Mas and SAs of the Au DNSPs for fructose and sucrose oxidations were also estimated (Figures 4.10C and 4.10D). The remained catalytic performances after CA measurements were further evaluated by CV (Figure 4.11). The electrochemical surface oxide stripping after CA and multiple CV cycles measurements as well as TEM images after CA measurements suggested the porous structures and catalytically active sites of

the DNSPs were well-preserved during the GOR (Figure 4.12).

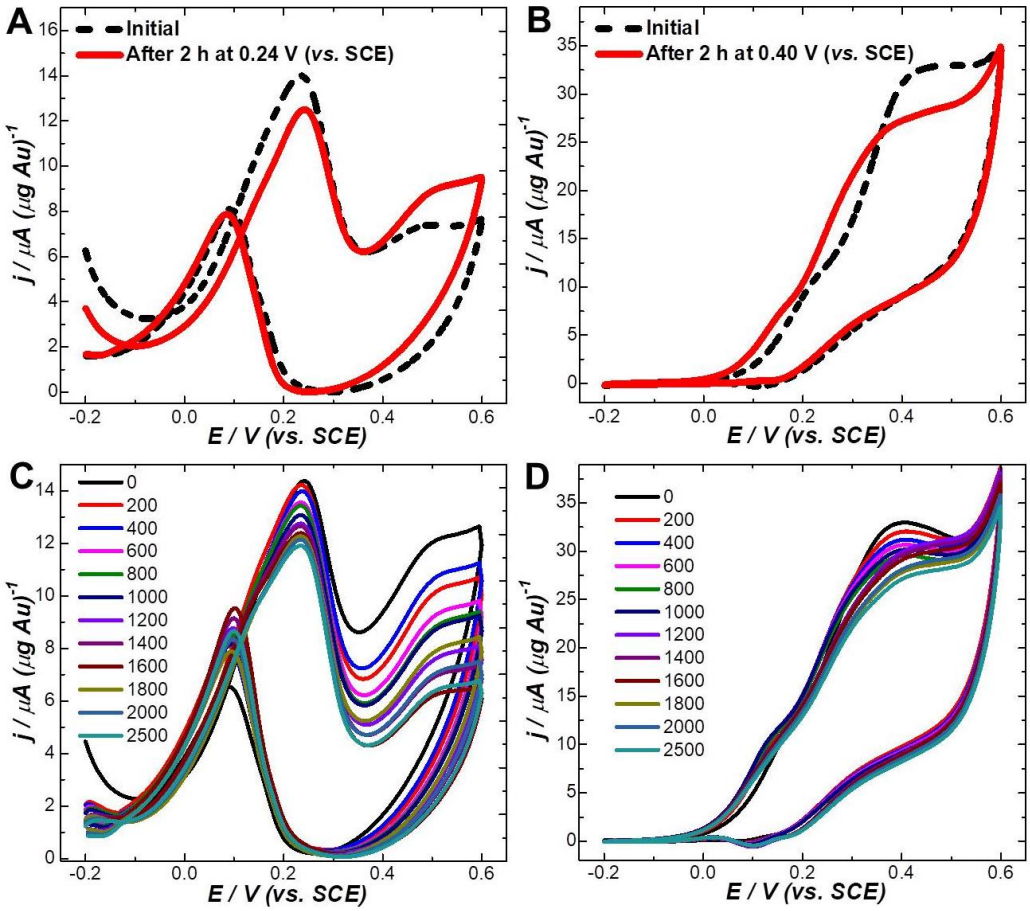

Figure 4.11. (A) CV curves of DNSPs-G before and after CA measurement (at 0.24 V *vs.* SCE for 2 h). (B) CV curves of DNSPs-H before and after CA measurement (at 0.4 V vs SCE for 2 h). Multiple cycle CV curves of (C) DNSPs-G and (D) DNSPs-H. The potential sweep cycle numbers are labeled in each panel. All the measurements were carried out in a deoxygenated solution containing 0.5 M KOH and 6.0 mM glucose at a potential sweep rate of 50 mV s^{-1}.

As a comparison, we also studied the electrocatlytic stabilities of the Au TOH and ETHH NPs (Figures 4.13 and 4.14). The catalytic activity of Au TOH NPs was more robust than that of Au ETHH NPs. The morphology and catalytic activity of the Au TOH NPs were well-preserved, whereas the corners and edges of Au ETHH NPs disappeared and catalytic current dramatically decreased accompany with negatively shifted oxidation peak after CA measurement. During multiple CV cycles, the catalytic current

gradually decreased and the peak potential negatively shifted until reaching to 0.24 V (vs. SCE) eventually, which arose from the loss of highly active surface undercoordinated atoms as a consequence of surface structural remodeling based on the oxidation stripping curves after CA.

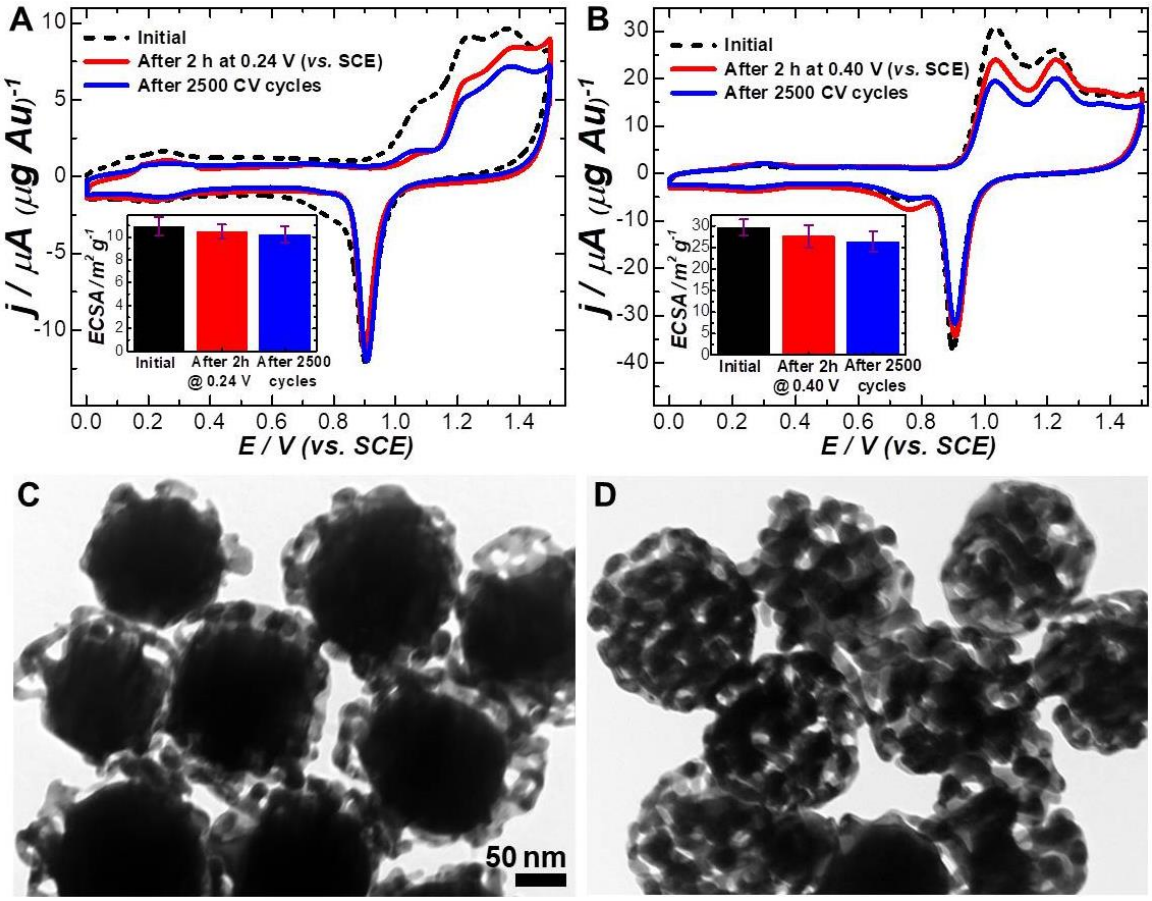

Figure 4.12. CV curves of electrochemical surface oxide stripping of (A) DSNPs-G and (B) DSNPs-H in 0.5 M H_2SO_4 at a potential sweep rate of 5.0 mV s^{-1} before and after CA measurement and after 2500 CV cycles. (C) TEM image of DSNPs-G after CA measurements (at 0.24 V *vs.* SCE for 2 h). (D) TEM image of DSNPs-H after CA measurements (at 0.4 V *vs.* SCE for 2 h).

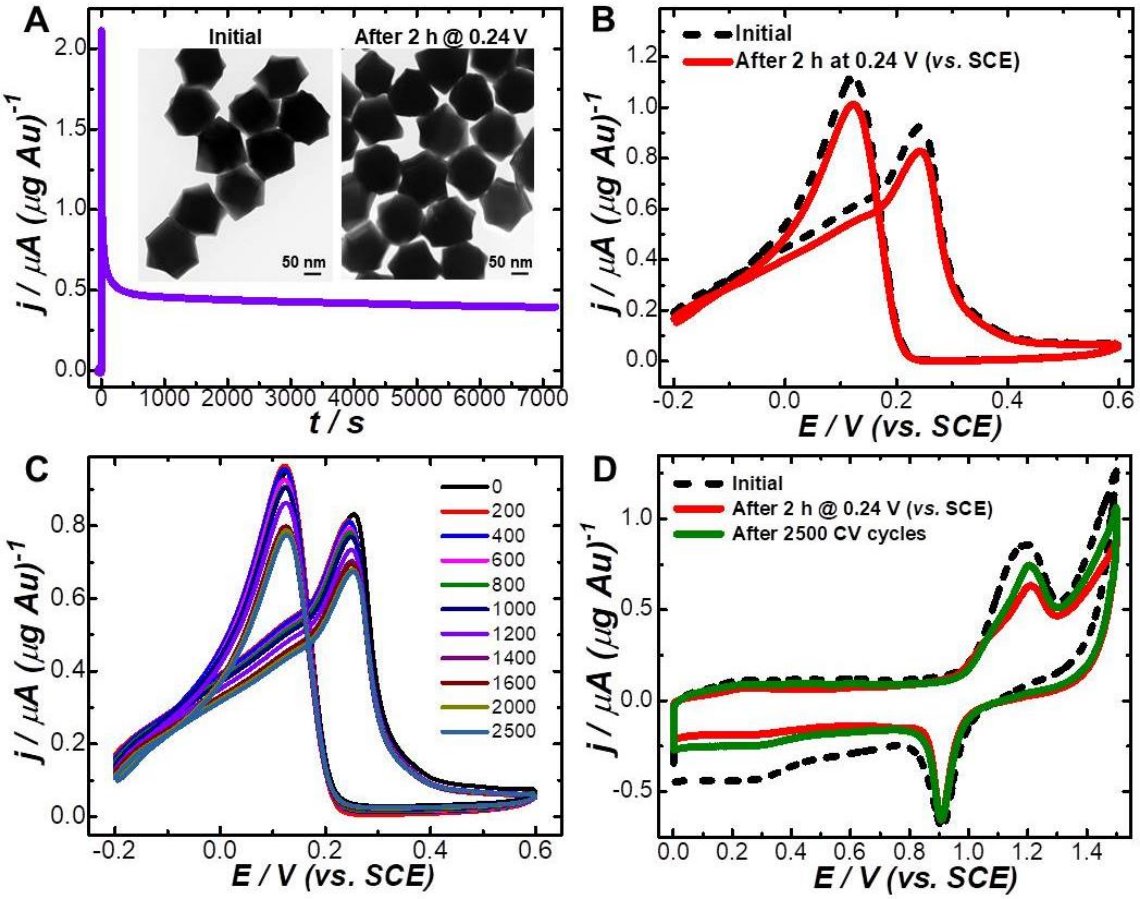

Figure 4.13. (A) CA curve of Au TOH NPs at 0.24 V (*vs.* SCE) in deoxygenated solution containing 0.5 M KOH and 6.0 mM glucose. The insets show the TEM images of the TOH NPs before and after CA measurements (at 0.24 V *vs.* SCE for 2 h). (B) CV curves of Au TOH NPs before and after CA measurements (at 0.24 V *vs.* SCE for 2 h) in a deoxygenated solution containing 0.5 M KOH and 6.0 mM glucose at a potential sweep rate of 50 mV s^{-1}. (C) Multiple-cycle CV curves of Au TOH NPs in deoxygenated solution containing 0.5 M KOH and 6.0 mM glucose at a potential sweep rate of 50 mV s^{-1}. (D) CV curves of electrochemical surface oxide stripping of Au TOH NPs, Au TOH NPs after CA measurements (at 0.24 V *vs.* SCE for 2 h), Au TOH NPs after 2500 CV cycles. The oxide stripping experiments were carried out in 0.5 M H_2SO_4 at a potential sweep rate of 5.0 mV s^{-1}.

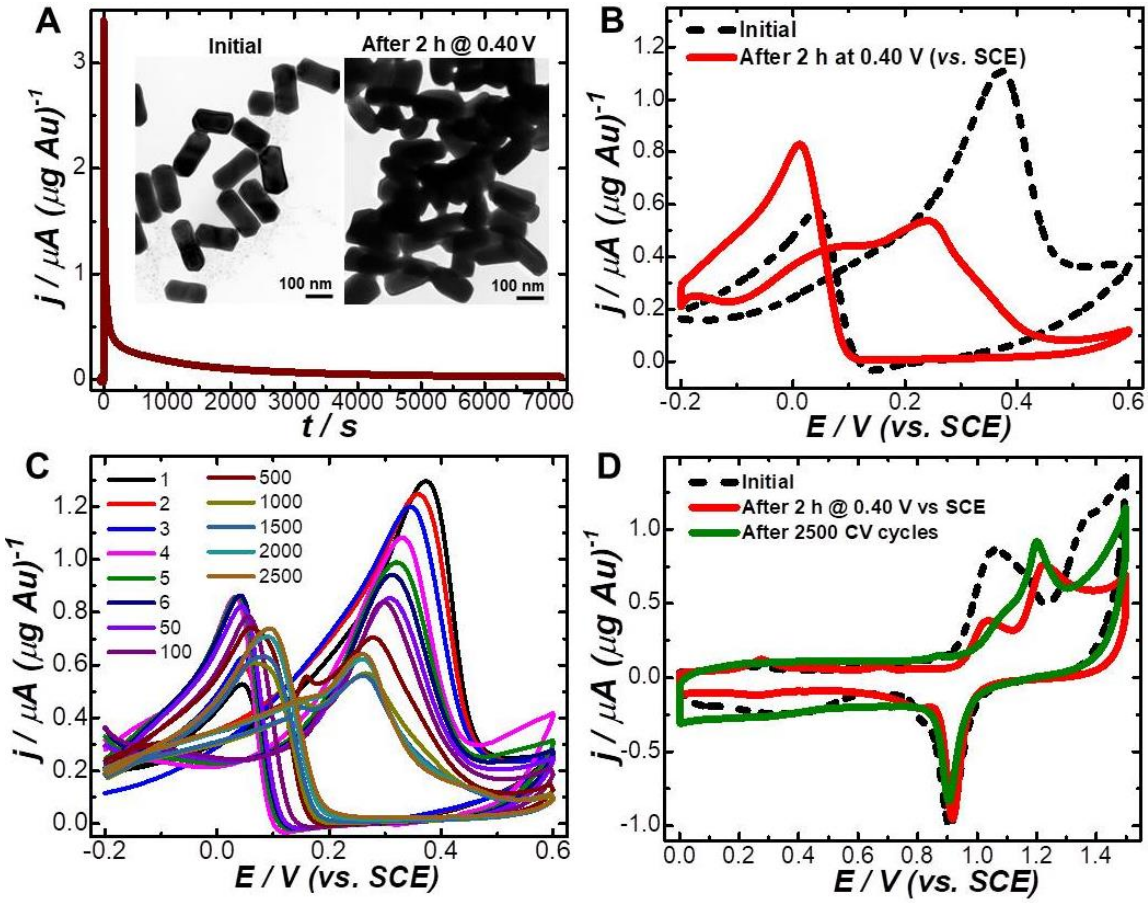

Figure 4.14. (A) CA curve of Au ETHH NPs at 0.40 V (*vs.* SCE) in deoxygenated solution containing 0.5 M KOH and 6.0 mM glucose. The insets show the TEM images of the ETHH NPs before and after CA measurements (at 0.40 V *vs.* SCE for 2 h). (B) CV curves of Au ETHH NPs before and after CA measurements (at 0.40 V *vs.* SCE for 2 h) in a deoxygenated solution containing 0.5 M KOH and 6.0 mM glucose at a potential sweep rate of 50 mV s^{-1}. (C) Multiple-cycle CV curves of Au ETHH NPs in deoxygenated solution containing 0.5 M KOH and 6.0 mM glucose at a potential sweep rate of 50 mV s^{-1}. (D) CV curves of electrochemical surface oxide stripping of Au ETHH NPs, Au ETHH NPs after CA measurements (at 0.40 V *vs.* SCE for 2 h), and Au ETHH NPs after 2500 CV cycles. The oxide stripping experiments were carried out in 0.5 M H_2SO_4 at a potential sweep rate of 5.0 mV s^{-1}.

4.4 Conclusion

We developed a versatile approach to precisely control the surface atomic coordination numbers (SACNs) of the dealloyed porous Au NPs by percolation dealloying of Au-Cu bimetallic NPs with interior compositional gradients or atomic well intermixed Au-Cu alloy. Using electrocatalytic oxidation of glucose and other small sugar molecules as

model reactions, we demonstrated that the catalytic selectivity of dealloyed porous Au NPs could be achieved based on the quantitative understanding of the relationship between the SACNs and the electrocatalytic activity. The insights gained from this work provide essential design principles for the optimization of noble metal nanostructures toward highly efficient and selective electrocatalytic oxidation of glucose and other small sugar molecules for the potential applications in biomass-based fuel cell and biomolecular sensing.

4.5 References

(1) Erlebacher, J.; Aziz, M. J.; Karma, A.; Dimitrov, N.; Sieradzki, K., *Nature* **2001**, 410, 450.

(2) Wittstock, A.; Zielasek, V.; Biener, J.; Friend, C. M.; Bäumer, M., *Science* **2010**, 327, 319.

(3) Chen, C.; Kang, Y.; Huo, Z.; Zhu, Z.; Huang, W.; Xin, H. L.; Snyder, J. D.; Li, D.; Herron, J. A.; Mavrikakis, M.; Chi, M.; More, K. L.; Li, Y.; Markovic, N. M.; Somorjai, G. A.; Yang, P.; Stamenkovic, V. R., *Science* **2014**, 343, 1339.

(4) Fujita, T.; Guan, P.; McKenna, K.; Lang, X.; Hirata, A.; Zhang, L.; Tokunaga, T.; Arai, S.; Yamamoto, Y.; Tanaka, N.; Ishikawa, Y.; Asao, N.; Yamamoto, Y.; Erlebacher, J.; Chen, M., *Nat Mater* **2012**, 11, 775.

(5) Niu, Z.; Becknell, N.; Yu, Y.; Kim, D.; Chen, C.; Kornienko, N.; Somorjai, G. A.; Yang, P., *Nat Mater* **2016**, 15, 1188.

(6) El Mel, A.-A.; Boukli-Hacene, F.; Molina-Luna, L.; Bouts, N.; Chauvin, A.; Thiry, D.; Gautron, E.; Gautier, N.; Tessier, P.-Y., *ACS Applied Materials & Interfaces* **2015**, 7, 2310.

(7) Wittstock, A.; Bäumer, M., *Accounts Chem Res* **2014**, 47, 731.

(8) Oezaslan, M.; Heggen, M.; Strasser, P., *J Am Chem Soc* **2012**, 134, 514.

(9) Snyder, J.; McCue, I.; Livi, K.; Erlebacher, J., *J Am Chem Soc* **2012**, 134, 8633.

(10) Wang, D.; Yu, Y.; Xin, H. L.; Hovden, R.; Ercius, P.; Mundy, J. A.; Chen, H.; Richard, J. H.; Muller, D. A.; DiSalvo, F. J.; Abruña, H. D., *Nano Lett* **2012**, 12, 5230.

(11) Li, X.; Chen, Q.; McCue, I.; Snyder, J.; Crozier, P.; Erlebacher, J.; Sieradzki, K., *Nano Lett* **2014**, 14, 2569.

(12) Gan, L.; Heggen, M.; O'Malley, R.; Theobald, B.; Strasser, P., *Nano Lett* **2013**, 13, 1131.

(13) Vidal, C.; Wang, D.; Schaaf, P.; Hrelescu, C.; Klar, T. A., *ACS Photonics* **2015**, 2, 1436.

(14) Lu, X.; Au, L.; McLellan, J.; Li, Z.-Y.; Marquez, M.; Xia, Y., *Nano Lett* **2007**, 7, 1764.

(15) Li, G. G.; Lin, Y.; Wang, H., *Nano Lett* **2016**, 16, 7248.

(16) Liu, K.; Bai, Y.; Zhang, L.; Yang, Z.; Fan, Q.; Zheng, H.; Yin, Y.; Gao, C., *Nano Lett* **2016**, 16, 3675.

(17) Li, G. G.; Villarreal, E.; Zhang, Q.; Zheng, T.; Zhu, J.-J.; Wang, H., *ACS Applied Materials & Interfaces* **2016**, 8, 23920.

(18) Tan, Y.; Liu, X. Y.; Zhang, L.; Wang, A.; Li, L.; Pan, X.; Miao, S.; Haruta, M.; Wei, H.; Wang, H.; Wang, F.; Wang, X.; Zhang, T., *Angew Chem Int Ed* **2017**, 56, 2709.

(19) Mitsudome, T.; Kaneda, K., *Green Chem* **2013**, 15, 2636.

(20) Gross, E.; LiuJack, H.-C.; Toste, F. D.; Somorjai, G. A., *Nat Chem* **2012**, 4, 947.

(21) Choudhary, T. V.; Sivadinarayana, C.; Datye, A. K.; Kumar, D.; Goodman, D. W.,

Catal Lett **2003**, 86, 1.

(22) Prati, L.; Villa, A.; Chan-Thaw, C. E.; Arrigo, R.; Wang, D.; Su, D. S., *Faraday Discuss* **2011**, 152, 353.

(23) Farnesi Camellone, M.; Zhao, J.; Jin, L.; Wang, Y.; Muhler, M.; Marx, D., *Angew Chem Int Ed* **2013**, 52, 5780.

(24) Liu, S.-S.; Sun, K.-Q.; Xu, B.-Q., *ACS Catalysis* **2014**, 4, 2226.

(25) Quan, Z.; Wang, Y.; Fang, J., *Accounts Chem Res* **2013**, 46, 191.

(26) Chiu, C.-Y.; Chung, P.-J.; Lao, K.-U.; Liao, C.-W.; Huang, M. H., *J Phys Chem C* **2012**, 116, 23757.

(27) Zhang, Q.; Wang, H., *ACS Catalysis* **2014**, 4, 4027.

(28) Zhang, Q.; Han, L.; Jing, H.; Blom, D. A.; Lin, Y.; Xin, H. L.; Wang, H., *ACS Nano* **2016**, 10, 2960.

(29) Zhou, X.; Andoy, N. M.; Liu, G.; Choudhary, E.; Han, K.-S.; Shen, H.; Chen, P., *Nat Nano* **2012**, 7, 237.

(30) Biella, S.; Prati, L.; Rossi, M., *J Catal* **2002**, 206, 242.

(31) Pasta, M.; La Mantia, F.; Cui, Y., *Electrochim Acta* **2010**, 55, 5561.

(32) Zhang, Y.; Xu, F.; Sun, Y.; Shi, Y.; Wen, Z.; Li, Z., *J Mater Chem* **2011**, 21, 16949.

(33) Rahman, M. M.; Saleh Ahammad, A. J.; Jin, J.-H.; Ahn, S. J.; Lee, J.-J., *Sensors (Basel, Switzerland)* **2010**, 10, 4855.

(34) Caras, S. D.; Petelenz, D.; Janata, J., *Anal Chem* **1985**, 57, 1920.

(35) Zhang, J.; Langille, M. R.; Personick, M. L.; Zhang, K.; Li, S.; Mirkin, C. A., *J Am Chem Soc* **2010**, 132, 14012.

(36) Ming, T.; Feng, W.; Tang, Q.; Wang, F.; Sun, L.; Wang, J.; Yan, C., *J Am Chem Soc*

2009, 131, 16350.

(37) Hamelin, A.; Martins, A. M., *J Electroanal Chem* **1996**, 407, 13.

(38) Hamelin, A., *J Electroanal Chem* **1996**, 407, 1.

(39) Trasatti, S.; Petrii, O. A., *J Electroanal Chem* **1992**, 327, 353.

(40) Sneed, B. T.; Young, A. P.; Jalalpoor, D.; Golden, M. C.; Mao, S.; Jiang, Y.; Wang, Y.; Tsung, C.-K., *ACS Nano* **2014**, 8, 7239.

(41) Guo, S.; Zhang, S.; Sun, X.; Sun, S., *J Am Chem Soc* **2011**, 133, 15354.

(42) Zhang, L.; Jing, H.; Boisvert, G.; He, J. Z.; Wang, H., *ACS Nano* **2012**, 6, 3514.

(43) Kim, M.-J.; Na, H.-J.; Lee, K. C.; Yoo, E. A.; Lee, M., *J Mater Chem* **2003**, 13, 1789.

CHAPTER 5

GALVANIC REPLACEMENT-DRIVEN TRANSFORMATIONS OF ATOMICALLY INTERMIXED BIMETALLIC NANOCRYSTALS: EFFECTS OF COMPOSITIONAL STOICHIOMETRY AND STRUCTURAL ORDERING

5.1 Introduction

Galvanic replacement reactions (GRRs), which involve the atomic exchange between metallic elements with different reduction potentials, represent an intriguing redox process that entangles matter exchange with structural remodeling of metallic materials over multiple length- and time-scales.[1-3] GRRs, when dictated by nanoparticulate templates, provide a simple but versatile pathway to controllably transform solid monometallic nanoparticles (NPs) into multimetallic hollow nanostructures that are typically unrealizable through other means,[2-11] tremendously enhancing our capabilities to fine-tune the optical, electronic, and surface properties of complex metallic nanostructures for widespread applications in sensing,[12-14] biomedicine,[15-17] and catalysis.[18-20] The remarkable level of architectural control exerted over metallic NPs through GRRs has been best manifested when using geometrically simple and synthetically tailorable Ag nanocrystals, such as nanospheres,[3,14] nanocubes,[2,4,21] nanoprisms,[22,23] and nanowires,[24] as the sacrificial templates for GRRs. A quintessential system intensively investigated over the past two decades has been single-crystalline Ag nanocubes, which evolve into a diverse set of multimetallic hollow nanostructures, selectively adopting nanobox, nanocage, or nanoframe geometries upon galvanic exchange of Ag with Au, Pd, or Pt under deliberately controlled synthetic conditions.[4,9,16,21,25,26] Multimetallic NPs exhibiting even more complicated interior and surface architectures, such as yolk-shell nanorattles,[24,27] multilayered nanomatryoshkas,[2,24,28,29] ultrathin skeletal nanoframes,[30,31] and popcorn-like nanostructures with multiple cavities,[32] become experimentally realizable when employing more sophisticated multimetallic heteronanostructures[29,33] or substrate-

supported NPs[34,35] as the sacrificial templates or by judiciously coupling GRRs with co-reduction,[13,36,37] corrosion,[30,31] Kirkendall diffusion,[2] seeded growth,[38] and regioselective surface passivation.[32,39,40] While rich information can be extracted empirically from previous observations, it has long been a challenging task to build a coherent mechanistic knowledge framework that unequivocally interprets how a series of key underlying thermodynamic, kinetic, and geometric factors rigorously modulate the interplay of multiple GRR-driven structure-rearranging processes and thereby profoundly influence the NP transformations.

Atomically intermixed bimetallic nanocrystals adopting either disordered alloy configurations or ordered intermetallic structures[41,42] may undergo GRR-driven structural transformations that are substantially more sophisticated and versatile than those of monometallic nanocrystals or phase-segregated bimetallic heteronanostructures. Here we demonstrate that the complex mechanisms dictating the GRR-driven transformations of alloy and intermetallic NPs can be fully elucidated within a central conceptual framework involving the interplay of three fundamentally intriguing structure-transforming pathways, namely dealloying, Kirkendall diffusion, and Ostwald ripening. Although both dealloying[43-46] and Kirkendall diffusion[47,48] have been intensively studied in bulk materials for decades, how they work synergistically within the confinement by a nanocrystal to guide the intricate nanoscale structural evolution upon initiation of GRRs still remains an open question. The nanocrystal transformations governed by dealloying and Kirkendall diffusion are further entangled with thermodynamically driven domain coarsening, a process known as Ostwald ripening.[49-51] How to kinetically manipulate the Ostwald ripening process with respect to dealloying and Kirkendall diffusion still

remains largely unexplored. Using Au-Cu alloy and intermetallic NPs as structurally and compositionally fine-tunable sacrificial templates for GRRs, we demonstrate that the compositional stoichiometry and structural ordering serve as two key factors that rigorously maneuver the relative rates of dealloying and Kirkendall atomic interdiffusion with respect to that of Ostwald ripening, enabling atomically intermixed Au-Cu bimetallic nanocrystals to selectively transform into an entire family of architecturally distinct complex nanostructures through straightforward GRRs under mild reaction conditions.

5.2 Experimental Details

Chemicals and Materials Polyvinylpyrrolidone (PVP, average MW 58000), chloroauric acid ($HAuCl_4 \cdot 4H_2O$), copper nitrate hydrate ($Cu(NO_3)_2 \cdot 3H_2O$), and tetraethylene glycol (TEG) were purchased from Alfa Aesar. Hydrazine solution ($N_2H_4 \cdot 3H_2O$, 35 wt %), nitric acid (HNO_3, 65 %), sulfuric acid (H_2SO_4, 98 %), Nafion perfluorinated resin solution (5 wt %), and bicinchoninic acid disodium salt hydrate (BCA, $C_{20}H_{10}N_2Na_2O_4 \cdot xH_2O$, ≥ 98.0 %) were purchased from Sigma-Aldrich. Potassium carbonate (K_2CO_3) and formaldehyde (37 wt %) were purchased form J.T. Baker. Ammonium hydroxide (28-30%) was purchased from British Drug Houses. Sodium hydroxide (NaOH) was purchased from Fisher Scientific. All reagents were used as received without further purification. Ultrapure Milli-Q water with a resistivity of 18.2 MΩ (Millipore) was used for all experiments.

Synthesis of Au@Cu_2O Core-shell Nanoparticles (NPs) Au quasi-spherical NPs with average diameter of 107 nm were synthesized by reducing $HAuCl_4$ with formaldehyde at room temperature.[52] Briefly, 50 mg of K_2CO_3 was dissolved in 200 mL

of water, followed by addition of 3 mL of 25 mM $HAuCl_4$. The mixture solution was aged in the dark for 18 h before use. Then 2.0 mL of 37 wt % formaldehyde solution was added into the mixture under vigorous magnetic stir (300 rpm). After 30 minutes, the Au NPs were centrifuged (2300 rcf), washed with water twice, and finally redispersed in 10 mL of water.

Au@Cu_2O core-shell nanoparticles were synthesized using our previously reported method with minor modifications.[53] 9.6 mL of the as-synthesized colloidal Au NPs was first introduced into 300 mL of 2 wt % PVP aqueous solution. 3.6, 1.2, or 0.4 mL of 0.1 M $Cu(NO_3)_2$ was subsequently added, depending on the targeted Au/Cu stoichiometric ratios of the resulting Au@Cu_2O core-shell NPs. The reaction mixture was placed in an ice bath, and then 0.67 mL of 5 M NaOH and 0.3 mL of $N_2H_4 \cdot 3H_2O$ solution were added under magnetic stir. The solutions were kept being stirred for 10 minutes. The resulting NPs were separated from the reaction mixtures by centrifugation and redispersed in 10 mL ethanol.

Monometallic Cu NPs were synthesized following a previously reported protocol.[54] Briefly, 0.2 mL of $N_2H_4 \cdot 3H_2O$ solution was added into 1 mL of 0.1 M $Cu(NO_3)_2$ solution under magnetic stir at room temperature. Cu NPs formed immediately as red precipitates and were centrifuged (1500 rpm, 5 min), washed with ethanol 3 times, and finally redispersed into 1 mL ethanol.

Synthesis of Au-Cu Alloy and Intermetallic NPs Au-Cu alloy and intermetallic NPs were synthesized using a polyol-assisted growth method. Typically, 1.0 mL of Au@Cu_2O core-shell NPs with Au/Cu of 1:3 were added into 20.0 mL tetraethylene glycol (TEG) containing 0.1 g PVP. $AuCu_3$ alloy (denoted as $AuCu_3$-A) and intermetallic NPs (denoted

as $AuCu_3$-I) were synthesized by keeping the reaction mixtures at 300 ^oC for 1 hour and 10 hours, respectively. AuCu alloy (denoted as AuCu-A) and intermetallic NPs (denoted as AuCu-I) were synthesized by keeping $Au@Cu_2O$ core-shell NPs with Au/Cu atomic ratio of 1:1 suspended in TEG at 300 ^oC for 30 minutes and 1 hour, respectively. Au_3Cu alloy (denoted as Au_3Cu-A) was synthesized by keeping $Au@Cu_2O$ core-shell NPs with Au/Cu atomic ratio of 3:1 suspended in TEG at 300 ^oC for 20 minutes. The as-synthesized alloy NPs were quickly cooled by incubating the samples in an ice bath, whereas the intermetallic NPs were cooled down to room temperature naturally under ambient air. The resulting NPs were washed with ethanol five times, and finally re-dispersed in 1.0 mL of water.

Galvanic Replacements of Au-Cu Alloy and Intermetallic NPs with $HAuCl_4$ In a typical galvanic replacement reaction (GRR), 100 μL of an aqueous suspension of Au-Cu alloy or intermetallic NPs were added into 1.0 mL deionized water in a small glass vial. Varying amount (10 ~ 150 μL) of 10 mM $HAuCl_4$ was subsequently added into the solution under magnetic stir at room temperature. The resulting NPs were separated by centrifugation, washed with ethanol, and finally redispersed in water.

Structural Characterizations of NPs The morphologies and structures of the NPs were characterized by transmission electron microscopy (TEM) using a Hitachi H-8000 transmission electron microscope, which was operated at an accelerating voltage of 200 kV. All samples for TEM measurements were dispersed in ethanol and drop-dried on 300 mesh Formvar/carbon-coated-Cu grids (Electron Microscopy Science Inc.). The structures and compositions of the NPs were also characterized by scanning electron microscopy (SEM) and energy dispersive spectroscopy (EDS) using a Zeiss Ultraplus

thermal field emission scanning electron microscope. The samples for SEM and EDS measurements were dispersed in ethanol and drop-dried on silicon wafers. The NP sizes were analyzed on the basis of SEM images using Nano Measurer analysis software (Department of Chemistry, Fudan University, China). The size distribution histograms were obtained from more than 100 NPs for each sample. Powder X-ray diffraction (PXRD) patterns were record on a SAXSLab Ganesha at the South Carolina SAXS Collaborative (Cu $K\alpha$ = 1.5406 Å). The optical extinction spectra were collected on colloidal NPs suspended in water at room temperature using a Beckman Coulter Du 640 spectrophotometer. Electrochemical measurements were performed using a CHI 660E workstation (CH Instruments, Austin, Texas) at room temperature with a three-electrode system composed of a Pt wire as the auxiliary, a saturated calomel electrode (SCE) as the reference, and a glassy carbon electrode (GCE, 3 mm diameter) loaded with NPs as the working electrode. The GCEs were polished with 0.3 μm alumina slurry, followed by washing with water and ethanol before use. 10 μL of colloidal suspensions containing 4 μg of alloy or intermetallic NPs were dropped and air-dried on the pretreated GCEs at room temperature, and then 2 μL of Nafion solution (0.2 wt %) was dropped to hold the NPs. The linear sweep voltammetry (LSV) of various NPs were measured at room temperature in 0.5 mM H_2SO_4 electrolyte in the potential scan range from 0 V to 0.7 V (*vs.* SCE) at a potential sweep rate of 50 mV s^{-1}.

Cluster Expansion Calculations The phase diagram of the Au-Cu binary system at 0 K was predicted using the Alloy Theoretic Automated Toolkit (ATAT) [55,56] software package. The ATAT code first invokes Density Functional Theory (DFT) code, in our case the Vienna Ab initio Simulation Package (VASP),[57] to determine the energy of

carefully selected ordered alloy structures. These DFT-computed energies were then used to determine the interaction parameters of the cluster expansion of an Ising-like Hamiltonian, from which the energies of other ordered and random alloys are determined according to the following equation:

$$E(\sigma) = J_0 + \sum_i J_i S_i(\sigma) + \sum_{j<i} J_{ij} S_i(\sigma) S_j(\sigma) + \sum_{k<j<i} J_{ijk} S_i(\sigma) S_j(\sigma) S_k(\sigma) + \cdots,$$

where, σ is a configuration of the alloy, S is the Ising spin variable which takes on values of either -1 or +1 depending on whether the site *i* was occupied by a Cu or Au atom, J's are the effective cluster interaction (ECI) energies. The results of these calculations were shown in Figure 5.1B. The energies of the monometallic Au and Cu shown here are those calculated from the cluster expansion. The deviation of these values from zero is thus a measure of the uncertainty in the results of the calculations (approximately 0.015 eV/atom).

5.3 Results and Discussions

Precise structural and compositional control over the Au-Cu bimetallic NPs was achieved through colloidal synthesis deliberately designed using the bulk phase diagram[58] as a guiding principle. As shown in Figure 5.1A, Au and Cu atoms are thermodynamically miscible over the entire stoichiometric range, forming face centered cubic (fcc) alloy structures spanning a broad temperature range up to the melting points of the alloys. Two atomically ordered intermetallic phases with specific Au/Cu stoichiometric ratios of 1:3 and 1:1 are thermodynamically favored at temperatures below ~ 400 ºC. Despite a decrease in entropy, the enthalpy-driven transitions of disordered alloys to intermetallic compounds become spontaneous at low temperatures because the formation of Au-Cu intermetallic bonds is energetically more favorable than that of Au-Au and Cu-Cu

bonds.[41] Cluster expansion calculations also predicted $AuCu_3$ and AuCu as two thermodynamically stable intermetallic phases for the Au-Cu binary system (Figure 5.1B), further confirming the prediction by the experimental phase diagram. The $AuCu_3$ intermetallic compound (denoted as $AuCu_3$-I; lattice parameter: a = 3.75 Å; space group: P 4/m – 3 2/m (221); Strukturbericht notation: $L1_2$) adopts the fcc structure (Figure 5.1C), while the atoms in the AuCu intermetallic compound (denoted as AuCu-I; lattice parameter: a = 3.96 Å, c = 3.67 Å; space group: P 4/m 2/m 2/m (123); Strukturbericht notation: $L1_0$) are organized into a face-centered tetragonal (fct) structure (Figure 5.1D). As schematically illustrated in Figure 5.1E, colloidal Au@Cu_2O core-shell NPs underwent a stepwise chemical reduction, intraparticle alloying, and structural ordering process to evolve into Au-Cu alloy and intermetallic NPs upon thermal treatment at 300 ºC in tetraethylene glycol (TEG), a liquid polyol serving as both the solvent and the reducing agent. The Au/Cu stoichiometric ratios of the alloy NPs were essentially predetermined by the relative core and shell dimensions of their parental Au@Cu_2O core-shell NPs, which could be fine-tuned over a broad range using a seed-mediated growth method we previously developed.[53] At Au/Cu stoichiometric ratios of 1:3 and 1:1, NPs of disordered alloys represented the metastable structures that were kinetically trapped immediately after the Au and Cu atoms were fully intermixed. The $AuCu_3$ and AuCu alloy NPs, denoted as $AuCu_3$-A and AuCu-A NPs respectively, further underwent a structural ordering process to form intermetallic NPs when maintained at 300 ºC in TEG over longer reaction times. The transformations of core-shell NPs into alloy and intermetallic NPs were visualized through transmission electron microscopy (TEM) imaging (Figures 5.1F and 5.1I) and further confirmed by correlated scanning electron

microcopy (SEM) imaging and energy-dispersive spectroscopy (EDS)-based elemental mapping (Figure 5.2).

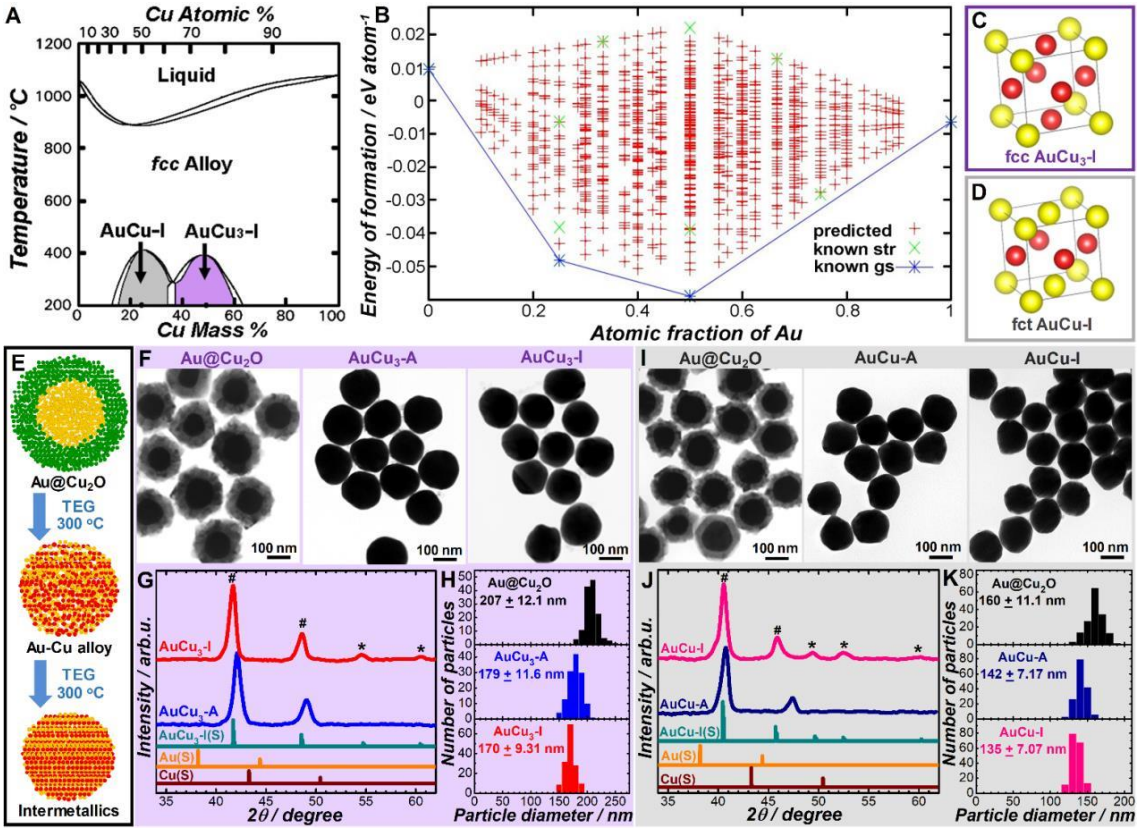

Figure 5.1. **Au-Cu alloy and intermetallic NPs.** (A) Experimental phase diagram of bulk Au-Cu bimetallic materials. (B) Formation energies of Au-Cu bimetallic structures with varying compositional stoichiometries calculated by cluster expansion calculations. The green ×s are the results of density functional theory (DFT) calculations. The red +s come from cluster analysis of the DFT results. The blue ×s identify the predicted thermodynamically stable structures. Unit cell structures of (C) fcc $AuCu_3$ intermetallic compound (denoted as $AuCu_3$-I) and (D) fct AuCu intermetallic compound (denoted as AuCu-I). The red and yellow spheres represent Cu and Au atoms, respectively. (E) Scheme illustrating the transformations of $Au@Cu_2O$ core-shell NPs into Au-Cu alloy and intermetallic NPs. (F) TEM images of $Au@Cu_2O$ core-shell NPs (average core diameter of 107 nm and shell thickness of 50 nm), $AuCu_3$ alloy nanoparticles (denoted as $AuCu_3$-A), and $AuCu_3$-I intermetallic NPs. (G) PXRD patterns of $AuCu_3$-A and $AuCu_3$-I NPs. The standard diffraction patterns for bulk Au (JCPDS no. 04-0784), Cu (JCPDS no. 04-0836), and $AuCu_3$-I (JCPDS no. 35-1537) are also included. The spectra are offset for clarity. (H) Size distributions of $Au@Cu_2O$ core-shell, $AuCu_3$-A, and $AuCu_3$-I NPs. (I) TEM images of $Au@Cu_2O$ core-shell NPs (average core diameter of 107 nm and shell thickness of 27 nm), AuCu alloy NPs (denoted as AuCu-A), and AuCu-I intermetallic NPs. (J) PXRD patterns of AuCu-A and AuCu-I NPs. The standard diffraction patterns for bulk Au, Cu, and AuCu-I (JCPDS no. 25-1220) are also shown. (K) Size distributions of $Au@Cu_2O$ core-shell, AuCu-A, and AuCu-I NPs.

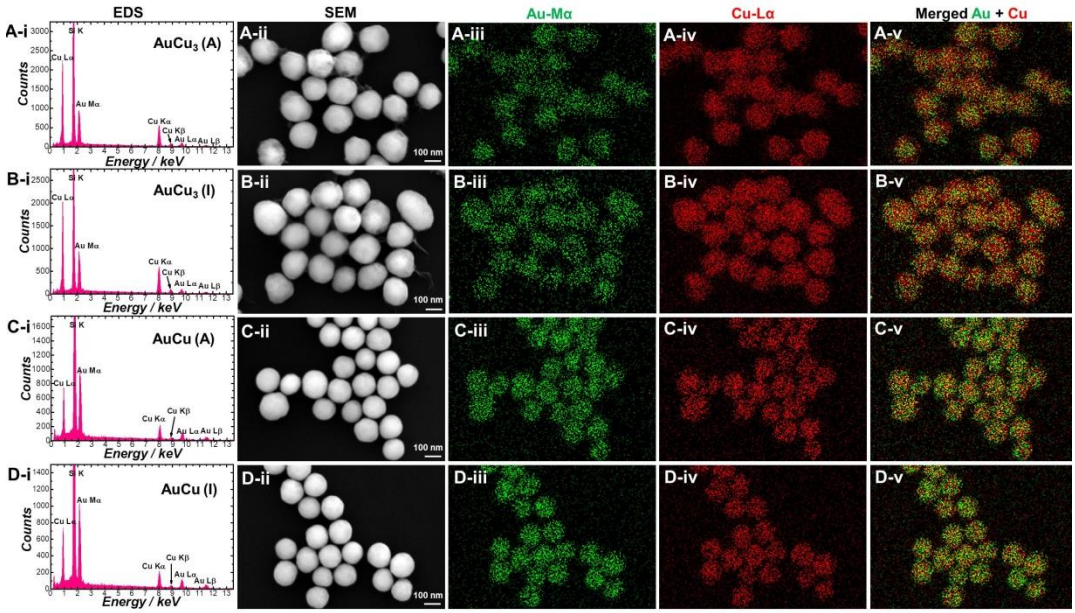

Figure 5.2. EDS elemental mapping results of (A) $AuCu_3$-A, (B) $AuCu_3$-I, (C) AuCu-A, and (D) AuCu-I NPs.

As revealed by powder X-ray diffraction (PXRD), the as-synthesized $AuCu_3$-A and AuCu-A NPs exhibited fcc homogenous alloy structures comprising fully intermixed Au and Cu atoms (Figures 5.1G and 5.1J), absent of any detectable phase-segregated monometallic Au or Cu domains or Cu_2O phases. Using the Bragg's law, we calculated the lattice parameters of the solid solutions based on the PXRD patterns, which allowed us to further calculate the Cu/Au stoichiometries of various alloy NP samples using the Vegard's law.[59] The Au/Cu atomic ratios calculated from the PXRD results agreed with those quantified by inductively coupled plasma mass spectrometry (ICP-MS) and EDS. Upon atomic ordering of the alloy NPs, the primary PXRD peaks (labeled with #) were shifted accompanied by the emergence of characteristic superlattice peaks (labeled with *), signifying the formation of $AuCu_3$ and AuCu intermetallic phases (Figures 5.1G and 5.1J). The $AuCu_3$-I and AuCu-I NPs exhibited PXRD features in excellent agreement with those of the standard patterns and previously reported intermetallic NP samples.[60-64]

While both the quasi-spherical NP morphology and Au/Cu stoichiometric ratios were well-preserved, the particle sizes decreased significantly upon transformations of Au@Cu_2O core-shell NPs into alloy NPs. Less significant but nonnegligible size shrinkage was also observed when the alloy NPs further evolved into intermetallic NPs (Figures 5.1H and 5.1K).

The structurally and compositionally tunable Au-Cu bimetallic NPs provided a unique materials system for us to pinpoint the effects of compositional stoichiometry and atomic-level structural ordering on GRR-driven NP transformations. We conducted the GRRs at room temperature in an aqueous environment using colloidal Au-Cu alloy or intermetallic NPs as the sacrificial templates and $HAuCl_4$ as the Au precursor in the absence of any additional surface capping ligands. Under our GRR conditions, Cu was oxidized into Cu(II) rather than Cu(I) ionic species while $HAuCl_4$ was reduced to form metallic Au, exhibiting a net reaction outcome of every three Cu atoms substituted by two Au atoms.

The galvanic exchange between Cu and Au involved selective etching of Cu from the Au-Cu alloy or intermetallic matrices, a process known as dealloying. Bimetallic alloys exhibit interesting composition-dependent dealloying behaviors. For example, a macroscopic Au-Ag alloy membrane may selectively evolve into a three-dimensional solid/void bicontinuous foamy structure consisting of Au-rich nanoligaments through percolation dealloying or form a surface-passivating atomic layer of Au at the membrane/electrolyte interfaces through surface dealloying, depending on the atomic fraction of Ag and detailed dealloying conditions.[46,65] The electrochemical parameter signifying the onset potential of percolation dealloying is termed as critical potential, E_c.[66] The E_c of a spherical binary alloy NP with a radius of r and a compositional formula

of $A_{1-p}B_p$(A and B represent the nonleachable noble and the leachable less-noble elements, respectively, and p is atomic fraction of B) is a function of both p and r, as expressed as follows:[66]

$$E_c(p,r) = \overline{E}_c(p) - [\gamma_{Alloy}(\Omega_A) + f_{Alloy}(\Omega_A' - <\Omega>)] \times (\frac{2}{nFr}) \quad (1),$$

where γ_{Alloy} and f_{Alloy} are the free energy and the stress at the alloy/electrolyte interface, respectively. Ω_A' is the partial molar volume of A in the alloy. ⟨Ω⟩ represents the average molar volume of the alloy. n is the number of electrons every B atom loses upon oxidation. F is the Faraday constant. $\overline{E}_c$ is the critical potential of the bulk alloy, which is a function of p and related to the molar volume of A, Ω_A, the interfacial free energy of B exposed to the electrolyte, $\gamma_{B/elec}$, the local radius of the surface where a cylindrical pit is created upon dealloying, ξ, and the equilibrium potential, $\overline{E}_{eq}$, above which the surface dealloying at the top-most atomic layer occurs, as shown by the following equation [67]

$$\overline{E}_c(p) = \overline{E}_{eq}(p) + \frac{4\gamma_{B/elec}\Omega_A}{nF\xi} \quad (2).$$

Because the maximum possible values of γ_{Alloy} and f_{Alloy} are ~ 2 and ~ 6 J m^{-2}, respectively,[68] E_c becomes virtually equivalent to $\overline{E}_c$ when an alloy NP becomes larger than 10 nm (r>5 nm). To eliminate additional complications associated with the NP size effects, here we focused on Au-Cu bimetallic NPs significantly larger than 10 nm, which exhibited composition-dependent dealloying behaviors analogous to those of their bulk counterparts. When exposed to certain electrochemical or chemical oxidizing environments, almost all binary alloys have been observed to display a characteristic threshold p value known as the parting limit, above which percolation dealloying occurs. The parting limits of Au-Ag and Au-Cu alloys were measured to be ~55 atomic % of

Ag[69] and ~ 70 atomic % of Cu,[54,70] respectively, in acidic electrolytes at room temperature. The origin of the characteristic parting limits of alloys can be fully interpreted in the context of the composition-dependent E_c as discussed above.

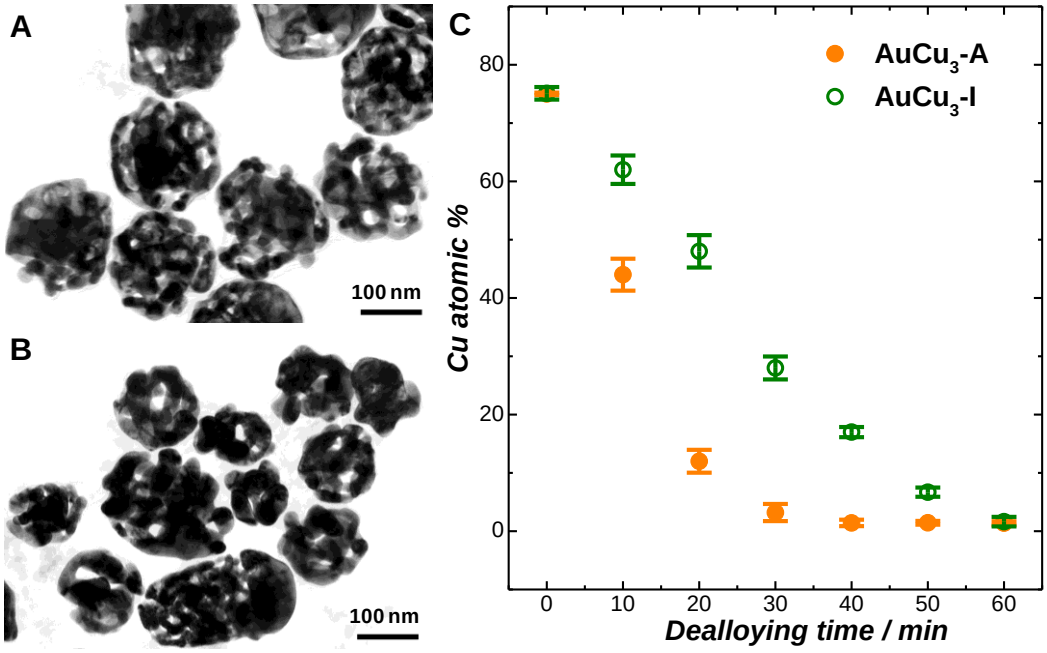

Figure 5.3. TEM images of fully dealloyed NPs obtained after exposing (A) $AuCu_3$-A and (B) $AuCu_3$-I NPs to 1 M HNO_3 at room temperature for 1 hour. (C) Temporal evolution of Cu atomic % of the NPs upon exposure of $AuCu_3$-A and $AuCu_3$-I NPs to 1 M HNO_3 at room temperature. The Cu atomic % was quantified by EDS and the error bars represent the standard deviation of three samples.

We systematically investigated the GRR-driven transformations of Au-Cu alloy and intermetallic NPs in two strikingly distinct compositional regimes divided by the parting limit for percolation dealloying (~ 70 atomic % of Cu). $AuCu_3$-A and $AuCu_3$-I NPs, both of which possessed Cu content above the parting limit, underwent nanoporosity-evolving percolation dealloying when exposed to 1 M nitric acid at room temperature, resulting in the formation of bicontinuous, sponge-like NPs composed of Au-rich nanoligaments (Figure 5.3). When $AuCu_3$-A and $AuCu_3$-I NPs underwent galvanic exchange with $HAuCl_4$, their structural transformations became remarkably more complicated than those

induced by dealloying alone. The deposition of Au at the NP-electrolyte interfaces not only modified the local surface structures of the evolving nanoligaments, but also profoundly influenced the energetics and dynamics associated with the surface atomic migrations. More importantly, the deposition of Au on the surfaces of an alloy NP created interfacial compositional gradient, which triggered the interdiffusion of Au and Cu atoms across the interface between the alloy and monometallic Au. The nonequivalent diffusion rates of Cu and Au atoms caused the alloy/Au interface to migrate toward one direction while forming cavities at the materials boundaries, a classic effect of atomic interdiffusion known as the Kirkendall effect.[47,71] The velocity at which the boundary interface travels can be described by the Darken's equation[72]

$$v = (D_A - D_B)\frac{dN_A}{dx} \quad (3),$$

where D_A and D_B are the diffusion coefficients of component A and B, respectively. dN_A/dx represents the compositional gradient of A across the boundary. Previously observed GRR-induced hollowing of metallic NPs can all be interpreted in the context of the Kirkendall effect.[2,3,6,11,14,32,36,38]

To ensure complete galvanic exchange between Cu and Au, we exposed the $AuCu_3$-A and $AuCu_3$-I NPs to excessive $HAuCl_4$ for 48 h. We tracked the temporal evolution of the NP structures and compositions during the GRRs using PXRD (Figures 5.4A and 5.4B), EDS (Figure 5.4C), optical extinction spectroscopy (Figure 5.4D), SEM (Panels a in Figures 5.4E-5.4H), and TEM (Panels b in Figures 5.4E-5.4H).

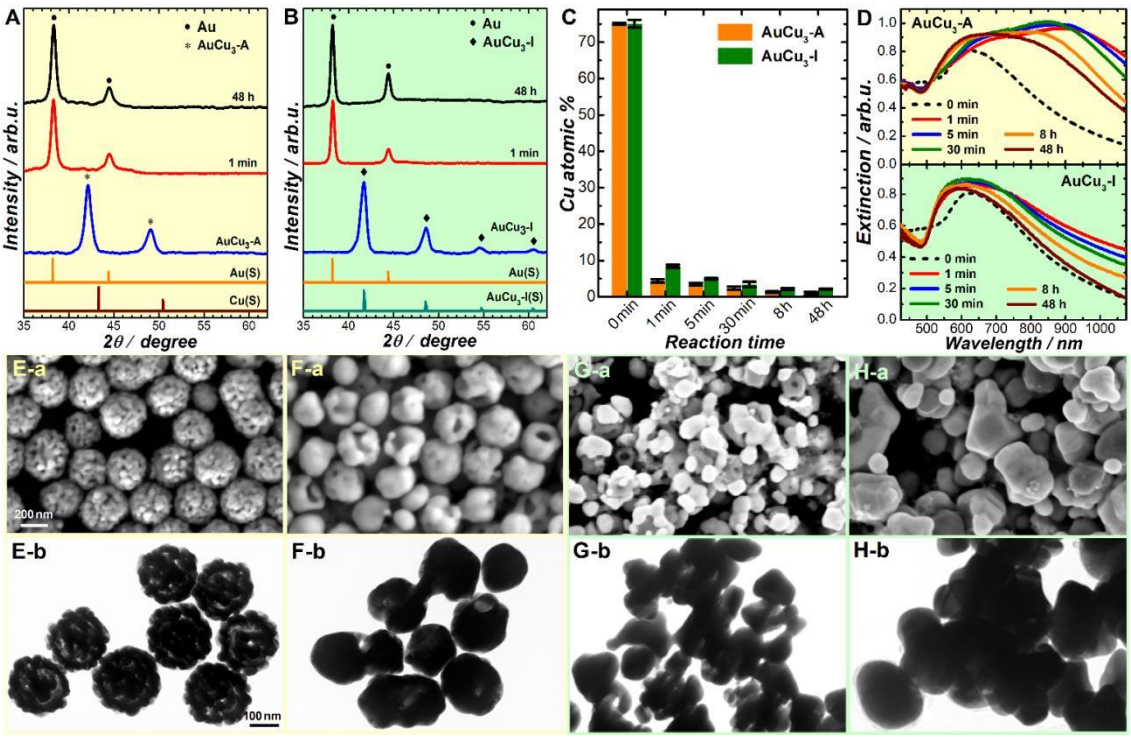

Figure 5.4. **Structural and compositional evolutions of $AuCu_3$-A and $AuCu_3$-I NPs upon exposure to $HAuCl_4$.** PXRD patterns of NPs obtained after mixing 1 mL colloidal (A) $AuCu_3$-A and (B) $AuCu_3$-I NPs with 150 μL of 10 mM $HAuCl_4$ at room temperature for 1 and 30 minutes. The standard diffraction patterns for bulk Au, Cu, and $AuCu_3$-I are also included. Temporal evolutions of (C) Cu atomic % and (D) optical extinction spectra of the NPs after mixing $AuCu_3$-A and $AuCu_3$-I NPs with 150 μL of 10 mM $HAuCl_4$. SEM (X-a, X = E, F, G, H) and TEM (X-b) images of NPs obtained after exposing $AuCu_3$-A or $AuCu_3$-I NPs to $HAuCl_4$ for various reaction times: (E) $AuCu_3$-A, 1 min; (F) $AuCu_3$-A, 48 h; (G) $AuCu_3$-I, 1 min; (H) $AuCu_3$-I, 48 h. All the SEM images share the same scale bar in Panel E-a, and all the TEM images share the same scale in Panel E-b.

While the $AuCu_3$-A NPs evolved into similar bicontinuous spongy morphologies (Figure 5.4E), the GRRs were observed to be drastically faster than the percolation dealloying essentially due to GRR-triggered interdiffusion of Au and Cu atoms in the alloy NPs. More than 90 % of the Cu in the $AuCu_3$-A NPs was rapidly replaced by Au within 1 minute upon initiation of GRRs (Figures 5.4A-5.4C), whereas the leaching of Cu during the percolation dealloying occurred over much long time periods. In addition, the Kirkendall atomic interdiffusion further boosted the cavity formation and volume

expansion of the NPs.[71] Although the percolation dealloying caused significantly shrinkage of the overall particle sizes, the spongy NPs formed through GRRs of $AuCu_3$-A NPs exhibited ~ 90 % increase in the total particle volume in comparison to their parental alloy NPs (Figure 5.4E). In contrast to the disordered alloys, atomically ordered intermetallic structures exhibit higher energy barriers for the atomic interdiffusion.[73,74] The $AuCu_3$-I NPs evolved into fragmented, irregularly-shaped ligaments during GRRs instead of forming bicontinuous spongy structures (Figure 5.4G) as a consequence of suppressed Kirkendall interduffsion of Au and Cu atoms. The selective leaching of Cu from $AuCu_3$-I NPs was also observed to be significantly slower than that from $AuCu_3$-A NPs during percolation dealloying, resulting in the formation of thicker ligaments and smaller overall particle sizes in comparison to the fully dealloyed $AuCu_3$-A NPs.

Although the majority of Cu atoms in the $AuCu_3$-A and $AuCu_3$-I NPs were galvanically replaced by Au atoms within 1 minute, the NPs continued to undergo domain coarsening processes and evolved into thermodynamically more stable structures driven by Ostwald ripening, a phenomenon first observed by Wilhelm Ostwald back in 1896.[49] During a typical Ostwald ripening process, smaller nanocrystals are dissolved and re-deposited onto larger nanocrystals, resulting in the growth of larger NPs at the expense of smaller NPs.[75,76] For a solid nanocrystal suspended in a liquid, the chemical potential of atoms at the solid/liquid interface increases with decreasing particle size, and the solute concentration at equilibrium for a small particle is therefore much higher than for a large particle. Such differences in the local equilibrium concentrations, due to variations in particle sizes and surface curvatures, set up concentration gradients that drive the Ostwald ripening. The growth rate of the larger NPs is related to the interfacial energy, σ,

the molar volume, V_m, the solubility, C_∞, and the diffusion coefficient, D, of the particle material, as shown in the following equation [75]

$$\frac{dr}{dt} = \frac{2\sigma V_m^2 C_\infty}{RT(1/D + 1/k_d r)} \times \frac{(1/r_b - 1/r)}{r} \quad (4),$$

where r is the radius of the NP, t is time, R is the ideal gas constant, and T is the absolute temperature. k_d is the rate constant of surface deposition reaction obeying simple first-order kinetics. r_b is defined as the critical radius, which separates the smaller particles ($r < r_b$) shrinking in size from the larger growing particles ($r > r_b$). For a given material/solvent system, the values of σ, V_m, D, k_d, and r_b are all essentially fixed. However, the kinetics of particle coarsening can be further maneuvered through modulation of C_∞ by coupling Ostwald ripening with deliberately designed redox reactions.[76] In this case, we found that the Ostwald ripening of the NPs after completion of GRRs was essentially triggered by the excessive $HAuCl_4$ in the solution, which significantly increased the solubility, C_∞, of Au through a reversible disproportionation reaction as shown below[77]

$$2Au + AuCl_4^- \rightleftharpoons 3Au^+ + 4Cl^- \quad (5).$$

During Ostwald ripening, the bicontinuous spongy NPs underwent a ligament coarsening processes and eventually transformed into nanocups as the ligaments coalesced into a continuous shell, leaving one side of the shell open (Figure 5.4F).

The fragmented Au ligaments formed upon GRR of $AuCu_3$-I NPs also underwent domain coarsening to form larger particles with faceted surfaces (Figure 5.4H). Interestingly, when the bicontinuous spongy NPs were separated from the reaction mixtures through centrifugation and redispersion in water immediately after the GRRs went to completion, the Ostwald ripening became kinetically sluggish because of limited

solubility of Au in pure water and thus, the bicontinuous spongy morphology was well-preserved even after 48 hours (Figure 5.5).

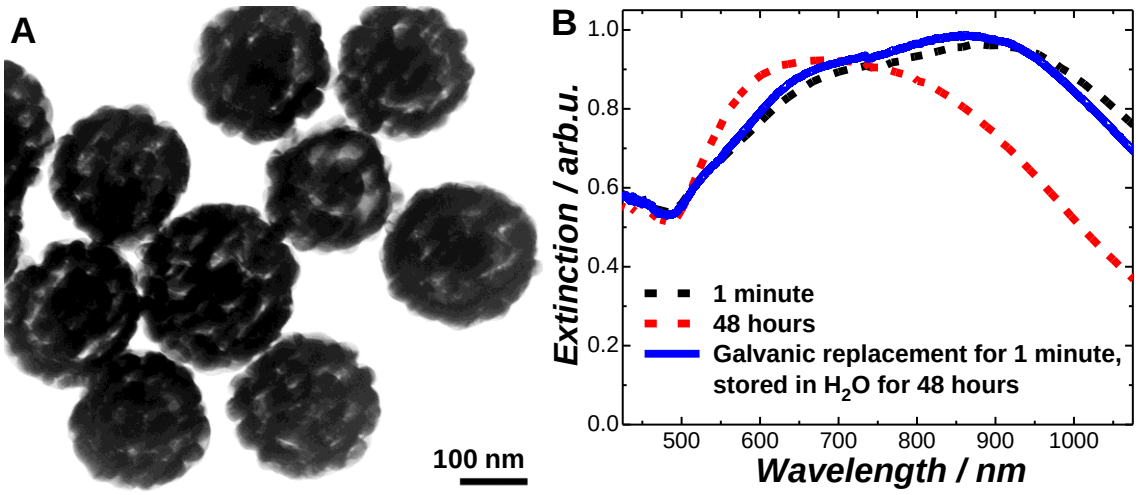

Figure 5.5. (A) TEM image of spongy NPs obtained after galvanic replacement reaction for 1 minute and stored in H_2O for 48 hours. 1 mL of colloidal $AuCu_3$-A NPs was first mixed with 150 μL of 10 mM $HAuCl_4$ for 1 minute. Then the resulting NPs were centrifuged, redispersed in H_2O, and stored in in H_2O for 48 hours. (B) Optical extinction spectrum of NPs obtained after galvanic replacement for 1 minute and stored in H_2O for 48 hours (solid blue curve). The extinction spectra of NPs obtained after exposure of $AuCu_3$-A NPs to 150 μL of 10 mM $HAuCl_4$ for 1 minute (black dash curve) and 48 hours (red dash curve) were also shown for comparison.

The structural evolution during Ostwald ripening could also be tracked based on the temporal evolution of optical extinction spectral features (Figure 5.4D). The spongy NPs exhibited a characteristic broad plasmon resonance band spanning much of the visible and near infrared spectral regions,[78] which progressively blue shifted as the ligaments underwent the coarsening process. The Ostwald ripening of the fragmented ligaments also led to blue-shift of the plasmon resonance bands, though the spectral shift was much less significant in comparison to that of the bicontinuous spongy NPs.

While the kinetics of Ostwald ripening-driven structural evolution could be clearly resolved, it remained challenging to directly track the detailed structural evolution of

$AuCu_3$-A and $AuCu_3$-I NPs during the kinetically much faster GRRs. Alternatively, we titrated the $AuCu_3$-A and $AuCu_3$-I NPs with insufficient amounts of $HAuCl_4$ to trap the intermediate structures at various stages of GRRs. We set the reaction time at 30 minutes, which was sufficiently long for the establishment of the equilibria upon adequate consumption of $HAuCl_4$ available for the GRRs. The GRRs of $AuCu_3$-A NPs with $HAuCl_4$ was initiated upon the dissolution of Cu and deposition of Au nanocrystallites at the alloy/liquid interfaces, which subsequently induced Kirkendall interdiffusion of Au and Cu atoms in the alloy matrices, forming cavities at the alloy/Au interfaces. The growth of the Au nanocrystallites and the expansion of the cavities led to the formation of a yolk-shell structure composed of a Au-Cu alloy core encapsulated by a polycrystalline Au shell (Figure 5.6A). As the GRRs further proceeded, the cavities continued to expand accompanied by Au domain coarsening (Figure 5.6B) until the Au domains merged into bicontinuous nanoligaments when a sufficient amount of $HAuCl_4$ was available for galvanic exchange with Cu (Figure 5.6C). The formation of cavities inside the NPs upon Kirkendall diffusion gave rise to significantly increased overall particle sizes.

The structural evolution of $AuCu_3$-I NPs during GRRs, nevertheless, appeared drastically different from that of $AuCu_3$-A NPs because the ordering of the atomic configurations effectively suppressed the Kirkendall diffusion process. As a consequence, monometallic Au was deposited on the outer surfaces of the intermetallic NPs without forming cavities during the GRRs (Figure 5.6D-5.6F). As an increasing amount of Cu was exchanged with Au, the surface-deposited Au domains increased in size and the intermetallic cores were progressively consumed, eventually evolving into fragmented Au ligaments with irregular shapes. When titrating the NPs with insufficient amounts of

$HAuCl_4$, the Ostwald ripening process became extremely slow because of depletion of $HAuCl_4$ in the solution upon completion of GRRs, allowing us to well-preserve the as-formed intermediate nanostructures over extended time periods even without separating the NPs from the reaction mixtures.

We also used PXRD to study the evolution of the crystalline structures of NPs during GRRs. A striking difference between the $AuCu_3$-A and $AuCu_3$-I NPs was that the atomic fractions of Cu in the alloy domains of the NPs progressively decreased (Figure 5.6G), whereas the Au/Cu atomic ratios and the ordered atomic configurations of the intermetallic domains were both well-preserved (Figure 5.6H) as the galvanic exchange between Cu and Au proceeded, further verifying that the formation of atomically ordered intermetallic structures effectively suppressed the Kirkendall diffusion, restricting the atomic exchange and migration exclusively at the evolving NP/liquid interfaces. We further used the linear-sweep-voltammetry (LSV) to measure the onset potentials for Cu dissolution from the $AuCu_3$-A and $AuCu_3$-I NPs (Figure 5.6I). The alloying of Cu with Au at the Au/Cu ratio of 1:3 positively shifted the onset potential by about 0.1 V, and the atomic ordering of the alloy NPs further positively shifted the onset potential by about 0.2 V, further proving that the Cu atoms in the $AuCu_3$-I NPs were significantly less mobile and thus more resistive against migration and leaching than those in the $AuCu_3$-A NPs. Although $AuCu_3$-A and $AuCu_3$-I NPs underwent distinct structure-transforming processes during GRRs, they exhibited similar fractions of Cu exchanged with Au when titrated with the same amount of $HAuCl_4$ (Figure 5.6J), suggesting that the ordering of the atomic configurations of the NPs slowed down the atomic interdiffusion process without significantly shifting the equilibria of the GRRs.

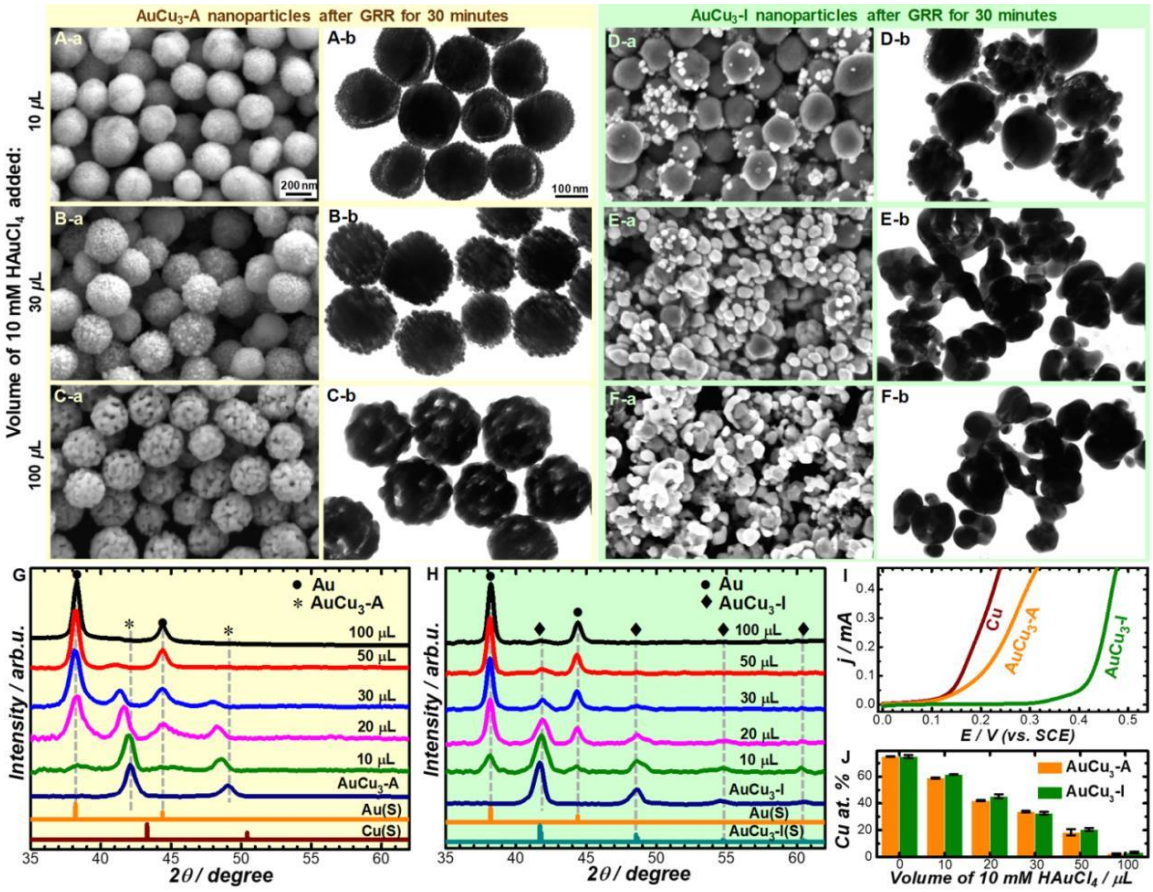

Figure 5.6. **GRR-induced structural transformations of $AuCu_3$ alloy and intermetallic NPs.** (X-a, X = A, B, C) SEM and (X-b) TEM images of NPs obtained by titrating 1 mL colloidal $AuCu_3$-A NPs with (A) 10 μL, (B) 30 μL and (C) 100 μL of 10 mM $HAuCl_4$. (Y-a, X = D, E, F) SEM and (Y-b) TEM images of NPs obtained by titrating 1 mL colloidal $AuCu_3$-I NPs with (D) 10 μL, (E) 30 μL, and (F) 100 μL. All the SEM images share the same scale bar in Panel A-a, and all the TEM images share the same scale in Panel A-b. The reaction time was 30 minutes. PXRD patterns of NPs obtained by titrating (G) $AuCu_3$-A NPs and (H) $AuCu_3$-I NPs with various volumes of 10 mM $HAuCl_4$. The standard diffraction patterns for bulk Au, Cu, and $AuCu_3$-I are also included. The spectra were offset for clarity. (I) LSV curves of Cu, $AuCu_3$-A, and $AuCu_3$-I NPs supported on glassy carbon electrodes in 0.5 M H_2SO_4 electrolyte in the potential sweep range from 0 V to 0.7 V (*vs.* SCE) at a sweep rate of 50 mV s^{-1}. (J) Cu atomic % of NPs obtained by titrating 1 mL colloidal $AuCu_3$-A and $AuCu_3$-I NPs with various volumes of 10 mM $HAuCl_4$.

In the case of Cu-rich $AuCu_3$-A and $AuCu_3$-I NPs, the GRRs and Ostwald ripening were kinetically distinguishable because they took place over two drastically different time scales. According to the Darken's equation, decreasing the Cu/Au stoichiometric ratio of the NPs should decelerate the GRRs with respect to Ostwald ripening. It has been

recently shown that the kinetics of GRRs occurring on colloidal Cu-Au bimetallic nanorods are sensitively dependent upon the local Cu/Au atomic ratios and an asymmetric hollowing process was observed due to the intrinsic compositional gradient in the nanorods.[79,80] For AuCu-A and AuCu-I NPs, both GRRs and Ostwald ripening were observed to occur concurrently over the same time scale. Because their Cu atomic fractions were below the parting limit for percolation dealloying, both AuCu-A and AuCu-I NPs underwent a surface dealloying process upon exposure to 1 M HNO_3, forming a surface passivating Au atomic layer that inhibited further leaching of Cu from the NPs. Interestingly, when exposing the AuCu-A NPs to excessive $HAuCl_4$, the GRR-induced Kirkendall diffusion effectively triggered the migration of Cu atoms from the NP interior to the NP/liquid interfaces, allowing the dealloying to proceed continuously until all Cu were galvanically replaced by Au. Upon initiation of GRRs, the AuCu-A NPs first underwent a hollowing and volume expansion process to transform into a yolk-shell structure (Figure 5.7A) due to the dealloying and Kirkendall effects. The rate of Kirkendall atomic diffusion in the AuCu-A NPs should be slower than that in $AuCu_3$-A NPs because of the smaller compositional gradient across the alloy/Au interfaces. Therefore, GRRs of AuCu-A NPs with $HAuCl_4$ resulted in cavity volumes significantly smaller than those in the bicontinuous spongy NPs derived from $AuCu_3$-A NPs. In addition, the GRR-induced structural transformations of AuCu-A NPs was entangled with the Ostwald ripening-driven domain coarsening, resulting in the formation of continuous Au-rich shells instead of the bicontinuous nanoligaments. As the GRRs further proceeded, the alloy domains became fully dealloyed while the Au-rich shells became significantly thicker, resulting in the formation of nanocups, each of which was

composed of a cavity enclosed by an Au-rich shell with an opening on one side (Figure 5.7B). The nanocups further evolved into thermodynamically more stable solid quasi-spherical NPs essentially driven by Ostwald ripening (Figure 5.7C). Ostwald ripening-driven surface remodeling of the quasi-spherical NPs eventually led to the formation of thermodynamically more favored {111} and {100} crystallographic facets when the NPs were aged in the reaction mixtures for a few days (Figure 5.8). In striking contrast to the AuCu-A NPs, AuCu-I NPs evolved into heterostructured quasi-spherical core-shell NPs, each of which was composed of a AuCu intermetallic core surrounded by a monometallic Au shell (Figure 5.7D). The absence of observable hollowing process during the GRRs of AuCu-I NPs with $HAuCl_4$ suggested that the Kirkendall atomic interdiffusion was suppressed due to the formation of the intermetallic phases. As the reaction time further increased, the surfaces of the quasi-spherical core-shell NPs became increasingly faceted due to Ostwald ripening (Figures 5.7E and 5.7F). Such Ostwald ripening-driven faceting of NPs became unobservable when the AuCu-A and AuCu-I NPs were exposed to insufficient amounts of $HAuCl_4$ for GRRs because of the elimination of Ostwald ripening upon depletion of $HAuCl_4$ (Figure 5.9). The spatial distributions of Au and Cu atoms in the yolk-shell and core-shell NPs were mapped by correlated SEM/EDS. The structural and compositional evolutions of the AuCu-A and AuCu-I NPs were further tracked using *ex situ* PXRD (Figures 5.7G and 5.7H) and EDS elemental analysis (Figure 5.7I), both of which clearly showed that the leaching of Cu from AuCu-I NPs was significantly slower than that from AuCu-A NPs, further verifying that structural ordering slowed down the rate of Au and Cu atomic interdiffusion.

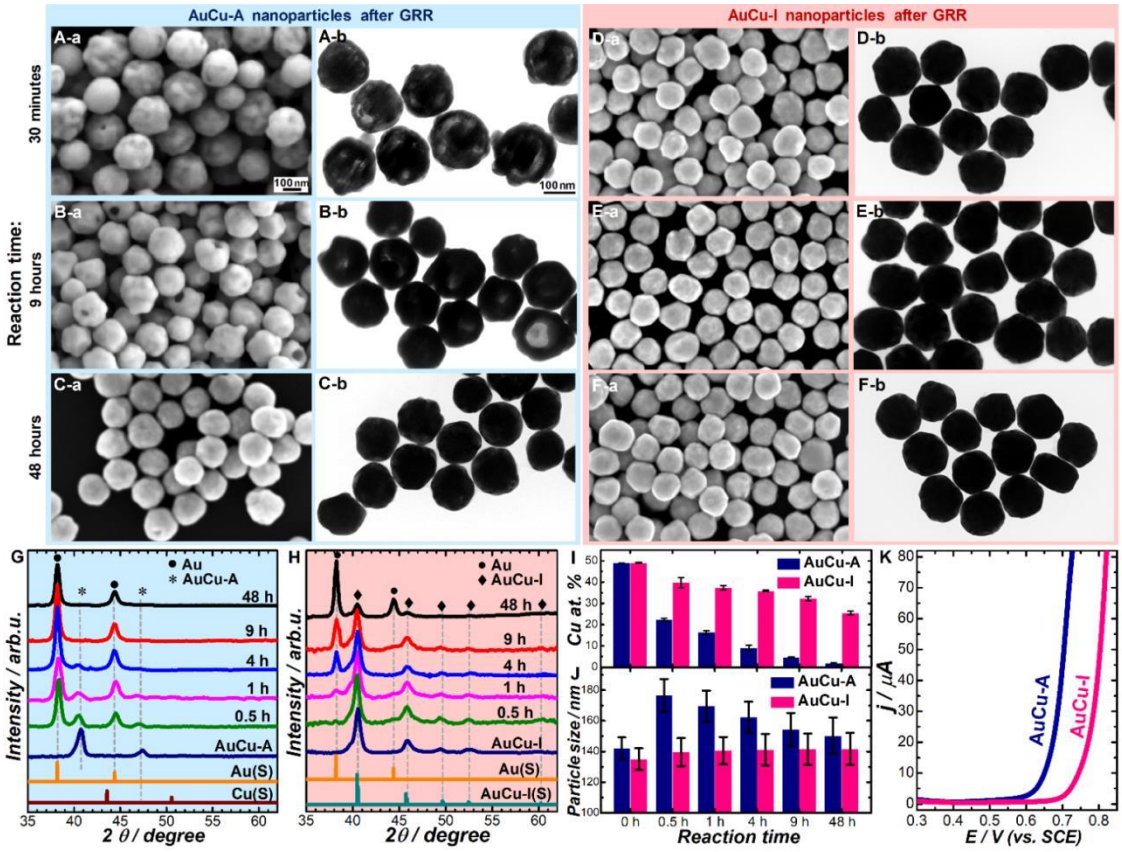

Figure 5.7. **Structural and compositional evolutions of AuCu alloy and intermetallic NPs during GRRs.** (X-a, X = A, B, C) SEM and (X-b) TEM images of NPs obtained after mixing 1 mL colloidal AuCu-A NPs with 150 μL of 10 mM $HAuCl_4$ for (A) 30 minutes, (B) 9 hours, and (C) 48 hours. (Y- a, X = D, E, F) SEM and (Y-b) TEM images of NPs obtained by mixing 1 mL colloidal AuCu-I NPs with 150 μL of 10 mM $HAuCl_4$ for (D) 30 minutes, (E) 9 hours, and (F) 48 hours. All the SEM images share the same scale bar in Panel A-a, and all the TEM images share the same scale in Panel A-b. PXRD patterns of NPs obtained after mixing (G) AuCu-A and (H) AuCu-I NPs with $HAuCl_4$ for various reaction times. The standard diffraction patterns for bulk Au, Cu, and AuCu-I are also included. Temporal evolutions of (I) Cu atomic % and (J) particle size of the NPs after mixing AuCu-A and AuCu-I NPs with 150 μL of 10 mM $HAuCl_4$. (K) LSV curves of AuCu-A and AuCu-I NPs in 0.5 M H_2SO_4 electrolyte at a sweep rate of 50 mV s^{-1}.

The sizes of the AuCu-A NPs first increased at the early stage of GRRs due to the Kirkendall effects and then progressively decreased as the Ostwald ripening started to dominate the structure-transforming process, whereas the particle sizes remained almost unchanged throughout the entire process when AuCu-I NPs were exposed to $HAuCl_4$ for GRRs (Figure 5.7J). At the Au/Cu atomic ratio of 1:1, the transition of alloy NPs into

intermetallic NPs raised the energy barriers for Cu-Au atomic interdiffusion and thereby positively shifted the onset potential for Cu dissolution (Figure 5.7K), which was in line with the trend observed in the $AuCu_3$-A and $AuCu_3$-I NPs.

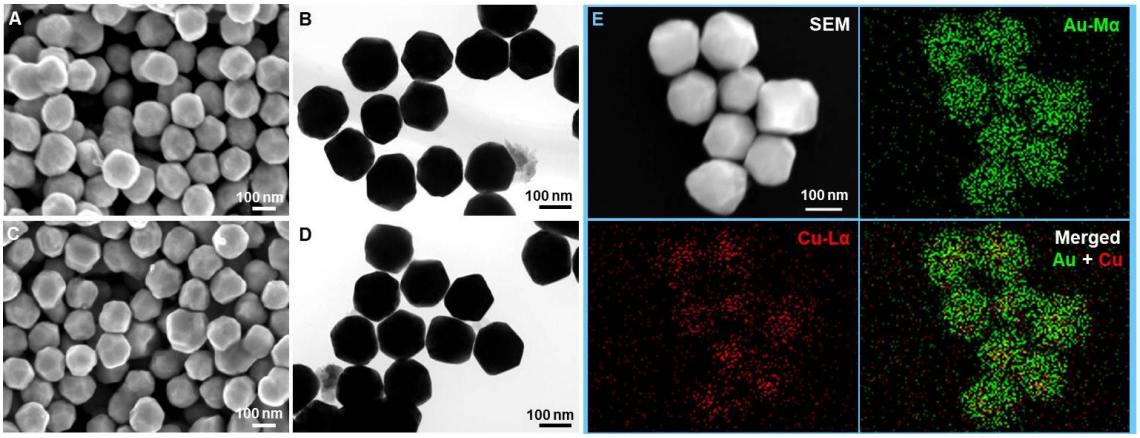

Figure 5.8. (A) SEM and (B) TEM images of NPs obtained after mixing 1 mL colloidal AuCu-A NPs with 150 μL of 10 mM $HAuCl_4$ for 120 hours. (C) SEM image, (D) TEM image, and (E) EDS elemental distribution maps of NPs obtained after mixing 1 mL colloidal AuCu-I NPs with 150 μL of 10 mM $HAuCl_4$ for 120 hours.

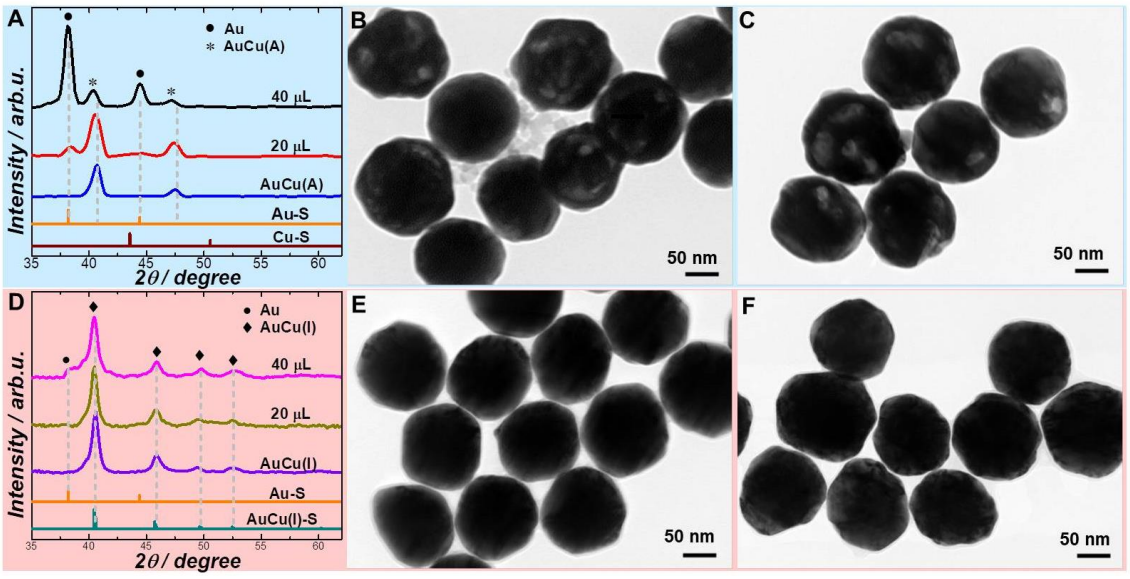

Figure 5.9. (A) PXRD patterns of NPs obtained by mixing 1 mL colloidal AuCu-A NPs with various volumes of 10 mM $HAuCl_4$ for 30 minutes. TEM images of NPs obtained after mixing 1 mL colloidal AuCu-A NPs with (B) 20 μL and (C) 40 μL of 10 mM $HAuCl_4$ for 30 minutes. (D) PXRD patterns of NPs obtained by mixing 1 mL colloidal AuCu-I NPs with various volumes of 10 mM $HAuCl_4$ for 30 minutes. TEM images of NPs obtained after mixing 1 mL colloidal AuCu-I NPs with (B) 20 μL and (C) 40 μL of 10 mM $HAuCl_4$ for 30 minutes.

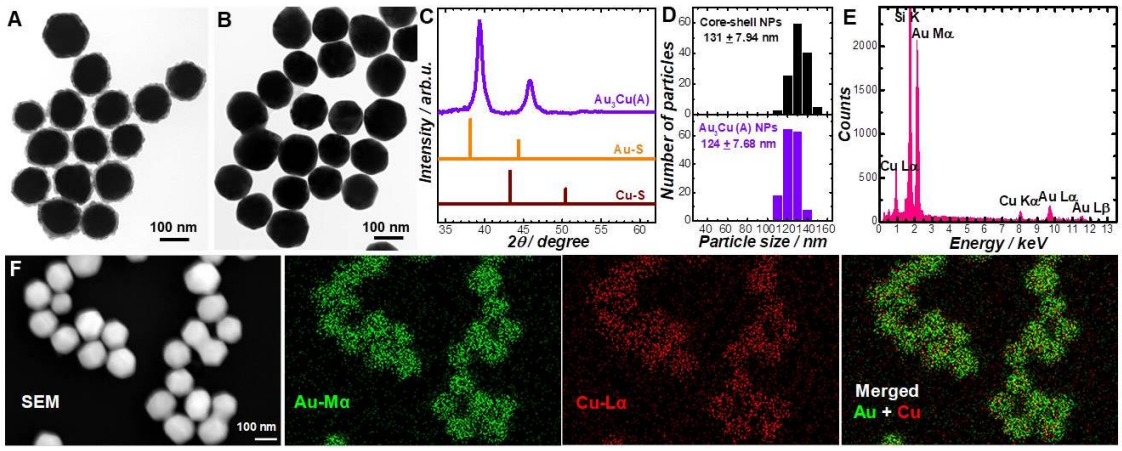

Figure 5.10. TEM images of (A) Au@Cu_2O core-shell NPs (average core diameter of 107 nm and shell thickness of 10 nm), and (B) Au_3Cu alloy NPs (denoted as Au_3Cu-A NPs). (C) PXRD pattern of Au_3Cu-A NPs. The standard diffraction patterns for bulk Au and Cu were also included. (D) Particle size distributions of Au@Cu_2O core-shell NPs and Au_3Cu-A NPs. (E) EDS spectrum and (F) EDS elemental distribution maps of Au_3Cu-A NPs.

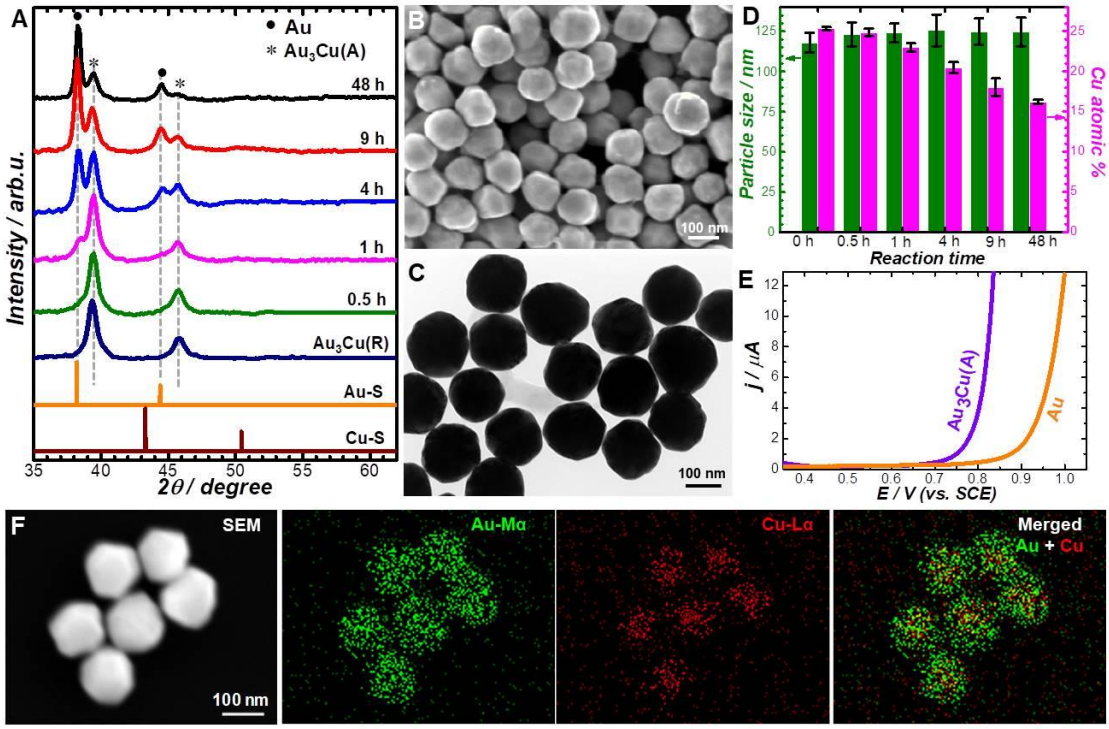

Figure 5.11. (A) PXRD patterns of NPs obtained after mixing Au_3Cu-A NPs with 150 μL of 10 mM $HAuCl_4$ for various reaction times. (B) SEM and (C) TEM images of NPs obtained after mixing Au_3Cu-A NPs 150 μL of 10 mM $HAuCl_4$ for 9 hours. (D) Temporal evolutions of Cu atomic % and particle size during GRRs. (E) LSV curves of Au and Au_3Cu-A NPs in 0.5 M H_2SO_4 electrolyte at a sweep rate of 50 mV s^{-1}.

We further investigated the GRR-driven structural transformations of Au-rich alloy NPs with a Au/Cu atomic ratio of 3:1 (Figure 5.10). For the Au_3Cu alloy NPs, both Cu leaching and Kirkendall diffusion became kinetically much slower than that in the AuCu-A NPs. Therefore, the Au_3Cu alloy NPs transformed into alloy core-Au shell NPs through a GRR-driven structural evolution process similar to that of the AuCu-I NPs. Neither cavity formation nor particle size expansion was observed on the Au_3Cu alloy NPs throughout the entire GRR process (Figure 5.11).

5.4 Conclusion

This work exemplifies how classic effects and paradigms, when applied to nanoparticulate materials systems, can be revisited from a different perspective and interlinked within a coherent conceptual network to generate new insights into the complex mechanisms underpinning the intriguing atomic exchange, matter relocation, and structural remodeling processes both at the atomic and nanoparticulate levels. Using the atomically intermixed Au-Cu bimetallic NPs as a model materials system, we have demonstrated that the versatile structural evolutions of multimetallic NPs driven by GRRs are synergistically dictated by three intertwining structure-transforming processes, dealloying, Kierkendall diffusion, and Ostwald ripening. Through systematic comparative studies, we have identified the compositional stoichiometries and the atomic-level structural ordering of the bimetallic NPs as two key factors that kinetically maneuver the dealloying and Kirkendall diffusion processes during GRRs, while the rate of the Ostwald ripening-driven domain coarsening can be further modulated by coupling the GRRs with reversible disproportionation reactions. Because dealloying, Kirkendall diffusion, and Ostwald ripening are all broadly involved in the growth, deformation, and

restructuring of a large library of multimetallic NPs, the insights gained from this work may serve as a bridge transcending our current knowledge gaps and blind zones toward thorough understanding of nanoscale structural transformations when revisiting the ample examples already existing in the literature. This work also provides generic design principles guiding the rational development of new synthetic approaches to multimetallic nanostructures with further enhanced architectural complexity, compositional diversity, and property tunability.

5.5 References

(1) Sun, Y. G.; Xia, Y. N., *J. Am. Chem. Soc.* **2004**, 126, 3892.

(2) Gonzalez, E.; Arbiol, J.; Puntes, V. F., *Science* **2011**, 334, 1377.

(3) Moreau, L. M.; Schurman, C. A.; Kewalramani, S.; Shahjamali, M. M.; Mirkin, C. A.; Bedzyk, M. J., *J. Am. Chem. Soc.* **2017**, 139, 12291.

(4) Sun, Y. G.; Xia, Y. N., *Science* **2002**, 298, 2176.

(5) Jones, M. R.; Osberg, K. D.; Macfarlane, R. J.; Langille, M. R.; Mirkin, C. A., *Chem. Rev.* **2011**, 111, 3736.

(6) Xia, X. H.; Wang, Y.; Ruditskiy, A.; Xia, Y. N., *Adv. Mater.* **2013**, 25, 6313.

(7) Wang, X. J.; Feng, J.; Bai, Y. C.; Zhang, Q.; Yin, Y. D., *Chem. Rev.* **2016**, 116, 10983.

(8) Cobley, C. M.; Xia, Y. N., *Mater. Sci. Eng. R-Rep.* **2010**, 70, 44.

(9) Skrabalak, S. E.; Chen, J. Y.; Sun, Y. G.; Lu, X. M.; Au, L.; Cobley, C. M.; Xia, Y. N., *Accounts Chem. Res.* **2008**, 41, 1587.

(10) Goris, B.; Polavarapu, L.; Bals, S.; Van Tendeloo, G.; Liz-Marzan, L. M., *Nano Lett.* **2014**, 14, 3220.

(11) Zhang, Q.; Wang, W. S.; Goebl, J.; Yin, Y. D., *Nano Today* **2009**, 4, 494.

(12) Mahmoud, M. A.; El-Sayed, M. A., *J. Am. Chem. Soc.* **2010**, 132, 12704.

(13) Yang, Y.; Zhang, Q.; Fu, Z. W.; Qin, D., *ACS Appl. Mater. Interfaces* **2014**, 6, 3750.

(14) Sun, Y. G.; Xia, Y. N., *Anal. Chem.* **2002**, 74, 5297.

(15) Hu, M.; Chen, J. Y.; Li, Z. Y.; Au, L.; Hartland, G. V.; Li, X. D.; Marquez, M.; Xia, Y. N., *Chem. Soc. Rev.* **2006**, 35, 1084.

(16) Chen, J.; Saeki, F.; Wiley, B. J.; Cang, H.; Cobb, M. J.; Li, Z. Y.; Au, L.; Zhang, H.; Kimmey, M. B.; Li, X. D.; Xia, Y. N., *Nano Lett.* **2005**, 5, 473.

(17) Xia, Y. N.; Li, W. Y.; Cobley, C. M.; Chen, J. Y.; Xia, X. H.; Zhang, Q.; Yang, M. X.; Cho, E. C.; Brown, P. K., *Accounts Chem. Res.* **2011**, 44, 914.

(18) Zeng, J.; Zhang, Q.; Chen, J. Y.; Xia, Y. N., *Nano Lett.* **2010**, 10, 30.

(19) Mahmoud, M. A.; Saira, F.; El-Sayed, M. A., *Nano Lett* **2010**, 10, 3764.

(20) Mahmoud, M. A.; Narayanan, R.; El-Sayed, M. A., *Accounts Chem. Res.* **2013**, 46, 1795.

(21) Chen, J. Y.; Wiley, B.; McLellan, J.; Xiong, Y. J.; Li, Z. Y.; Xia, Y. N., *Nano Lett.* **2005**, 5, 2058.

(22) Aherne, D.; Gara, M.; Kelly, J. M.; Gun'ko, Y. K., *Adv. Funct. Mater.* **2010**, 20, 1329.

(23) Sun, Y. G.; Xia, Y. N., *Adv. Mater.* **2003**, 15, 695.

(24) Sun, Y. G.; Wiley, B.; Li, Z. Y.; Xia, Y. N., *J. Am. Chem. Soc.* **2004**, 126, 9399.

(25) Skrabalak, S. E.; Au, L.; Li, X. D.; Xia, Y. N., *Nat. Protoc.* **2007**, 2, 2182.

(26) Zheng, T.; Zhang, Q.; Feng, S.; Zhu, J.-J.; Wang, Q.; Wang, H., *J. Am. Chem. Soc.* **2014**, 136, 2288.

(27) Cho, E. C.; Camargo, P. H. C.; Xia, Y. N., *Adv. Mater.* **2010**, 22, 744.

(28) Zhang, W. Q.; Rahmani, M.; Niu, W. X.; Ravaine, S.; Hong, M. H.; Lu, X. M., *Sci Rep* **2015**, 5, 8382.

(29) Hong, S.; Acapulco, J. A. I.; Jang, H. Y.; Park, S., *Chem. Mater.* **2014**, 26, 3618.

(30) Hong, X.; Wang, D. S.; Cai, S. F.; Rong, H. P.; Li, Y. D., *J. Am. Chem. Soc.* **2012**, 134, 18165.

(31) McEachran, M.; Keogh, D.; Pietrobon, B.; Cathcart, N.; Gourevich, I.; Coombs, N.; Kitaev, V., *J. Am. Chem. Soc.* **2011**, 133, 8066.

(32) Zhang, W. Q.; Yang, J. Z.; Lu, X. M., *ACS Nano* **2012**, 6, 7397.

(33) Xiong, W.; Sikdar, D.; Walsh, M.; Si, K. J.; Tang, Y.; Chen, Y.; Mazid, R.; Weyland, M.; Rukhlenko, I. D.; Etheridge, J.; Premaratne, M.; Li, X. Y.; Cheng, W. L., *Chem. Commun.* **2013**, 49, 9630.

(34) Neretina, S.; Hughes, R. A.; Gilroy, K. D.; Hajfathalian, M., *Accounts Chem. Res.* **2016**, 49, 2243.

(35) Hajfathalian, M.; Gilroy, K. D.; Golze, S. D.; Yaghoubzade, A.; Menumerov, E.; Hughes, R. A.; Neretina, S., *ACS Nano* **2016**, 10, 6354.

(36) Jing, H.; Wang, H., *Chem. Mat.* **2015**, 27, 2172.

(37) Weiner, R. G.; Smith, A. F.; Skrabalak, S. E., *Chem. Commun.* **2015**, 51, 8872.

(38) Polavarapu, L.; Zanaga, D.; Altantzis, T.; Rodal-Cedeira, S.; Pastoriza-Santos, I.; Perez-Juste, J.; Bals, S.; Liz-Marzan, L. M., *J. Am. Chem. Soc.* **2016**, 138, 11453.

(39) Liu, Y. L.; Walker, A. R. H., *ACS Nano* **2011**, 5, 6843.

(40) Sun, X. J.; Kim, J.; Gilroy, K. D.; Liu, J. Y.; Konig, T. A. F.; Qin, D., *ACS Nano* **2016**, 10, 8019.

(41) Yan, Y. C.; Du, J. S. S.; Gilroy, K. D.; Yang, D. R.; Xia, Y. N.; Zhang, H., *Adv.*

Mater. **2017**, 29.

(42) Ferrando, R.; Jellinek, J.; Johnston, R. L., *Chem. Rev.* **2008**, 108, 845.

(43) Newman, R. C.; Sieradzki, K., *Science* **1994**, 263, 1708.

(44) Williams, D. E.; Newman, R. C.; Song, Q.; Kelly, R. G., *Nature* **1991**, 350, 216.

(45) Forty, A. J., *Nature* **1979**, 282, 597.

(46) Erlebacher, J.; Aziz, M. J.; Karma, A.; Dimitrov, N.; Sieradzki, K., *Nature* **2001**, 410, 450.

(47) Smigelskas, A. D.; Kirkendall, E. O., *Trans. Am. Inst. Min. Metall. Eng.* **1947**, 171, 130.

(48) Nakajima, H., *JOM-J. Miner. Met. Mater. Soc.* **1997**, 49, 15.

(49) Ostwald, W. *Lehrbuch der Allgemeinen Chemie, vol. 2, part 1*, Leipzig, Germany, 1896.

(50) Ostwald, W., *Zeitschrift für physikalische Chemie.* **1897**, 222, 289.

(51) In *Compendium of Chemical Terminology, 2nd ed. (the "Gold Book")* IUPAC: 1997.

(52) Zhang, L.; Blom, D. A.; Wang, H., *Chem. Mater.* **2011**, 23, 4587.

(53) Zhang, L.; Jing, H.; Boisvert, G.; He, J. Z.; Wang, H., *ACS Nano* **2012**, 6, 3514.

(54) Li, G. G.; Villarreal, E.; Zhang, Q. F.; Zheng, T. T.; Zhu, J. J.; Wang, H., *ACS Appl. Mater. Interfaces* **2016**, 8, 23920.

(55) Zhang, Q.; Han, L.; Jing, H.; Blom, D. A.; Lin, Y.; Xin, H. L.; Wang, H., *ACS Nano* **2016**, 10, 2960.

(56) van de Walle, A.; Ceder, G., *J. Phase Equilib.* **2002**, 23, 348.

(57) Kresse, G.; Furthmuller, J., *Phys. Rev. B* **1996**, 54, 11169.

(58) Xu, C.; Wang, R.; Chen, M.; Zhang, Y.; Ding, Y., *Phys Chem Chem Phys* **2010**, 12,

239.

(59) Vegard, L., *Zeitschrift für Physik* **1921**, 5, 17.

(60) Sra, A. K.; Ewers, T. D.; Schaak, R. E., *Chem. Mat.* **2005**, 17, 758.

(61) Wang, G. W.; Xiao, L.; Huang, B.; Ren, Z. D.; Tang, X.; Zhuang, L.; Lu, J. T., *J. Mater. Chem.* **2012**, 22, 15769.

(62) Sra, A. K.; Schaak, R. E., *J. Am. Chem. Soc.* **2004**, 126, 6667.

(63) Chen, W.; Yu, R.; Li, L. L.; Wang, A. N.; Peng, Q.; Li, Y. D., *Angew. Chem. Int. Ed.* **2010**, 49, 2917.

(64) Zhan, W. C.; Wang, J. L.; Wang, H. F.; Zhang, J. S.; Liu, X. F.; Zhang, P. F.; Chi, M. F.; Guo, Y. L.; Guo, Y.; Lu, G. Z.; Sun, S. H.; Dai, S.; Zhu, H. Y., *J. Am. Chem. Soc.* **2017**, 139, 8846.

(65) Wittstock, A.; Zielasek, V.; Biener, J.; Friend, C. M.; Bäumer, M., *Science* **2010**, 327, 319.

(66) Li, X. Q.; Chen, Q.; McCue, I.; Snyder, J.; Crozier, P.; Erlebacher, J.; Sieradzki, K., *Nano Lett.* **2014**, 14, 2569.

(67) Rugolo, J.; Erlebacher, J.; Sieradzki, K., *Nat. Mater.* **2006**, 5, 946.

(68) Cammarata, R. C., *Prog. Surf. Sci.* **1994**, 46, 1.

(69) Artymowicz, D. M.; Erlebacher, J.; Newman, R. C., *Philos. Mag.* **2009**, 89, 1663.

(70) Xia, J. X.; Ambrozik, S.; Crane, C. C.; Chen, J. Y.; Dimitrov, N., *J. Phys. Chem. C* **2016**, 120, 2299.

(71) Yin, Y. D.; Rioux, R. M.; Erdonmez, C. K.; Hughes, S.; Somorjai, G. A.; Alivisatos, A. P., *Science* **2004**, 304, 711.

(72) Darken, L. S., *Trans. Am. Inst. Min. Metall. Eng.* **1948**, 175, 184.

(73) Mehrer, H., *Mater. Trans. JIM* **1996**, 37, 1259.

(74) Butrymowicz, D. B.; Manning, J. R.; Read, M. E., *J. Phys. Chem. Ref. Data* **1974**, 3, 527.

(75) Viswanatha, R.; Sarma, D. D. In *Nanomaterials Chemistry*; Rao, C. N. R., Muller, A., Cheetham, A. K., Eds.; WILEY-VCH Verlag GmbH & Co. KGaA, Weinheim: 2007.

(76) Zhang, Z. R.; Wang, Z. N.; He, S. N.; Wang, C. Q.; Jin, M. S.; Yin, Y. D., *Chem. Sci.* **2015**, 6, 5197.

(77) Gammons, C. H.; Yu, Y. M.; WiliamsJones, A. E., *Geochim. Cosmochim. Acta* **1997**, 61, 1971.

(78) Zheng, T.; Li, G. G.; Zhou, F.; Wu, R.; Zhu, J.-J.; Wang, H., *Adv. Mater.* **2016**, 28, 8218.

(79) Thota, S.; Chen, S. T.; Zhao, J., *Chem. Commun.* **2016**, 52, 5593.

(80) Liu, K.; Bai, Y. C.; Zhang, L.; Yang, Z. B.; Fan, Q. K.; Zheng, H. Q.; Yin, Y. D.; Gao, C. B., *Nano Lett.* **2016**, 16, 3675.

CHAPTER 6

ELECTROCATALYTICALLY ACTIVE TRIMETALLIC SPONGY NANOPARTICLES WITH ULTRATHIN LIGAMENTS

6.1 Introduction

Galvanic replacement provides a versatile pathway to controllably transform a solid monometallic nanoparticle (NP) into a diverse set of architecturally more sophisticated multimetallic hollow nanostructures.[1-4] Galvanic replacement occurring on metallic nanoparticles (NPs) is essentially a unique nanoscale redox process that are unrealizable for bulk material systems, in which less noble metals get oxidized and dissolved accompanied by the reduction and deposition of noble metals on the sacrificial template surfaces. The resulting architectures are essentially determined by the intrinsic nature of sacrificial templates including redox potential, lattice mismatch between the replaced and deposited metals, atomic interdiffusion during the reaction, as well as the external effects companied with the reaction like chemical leaching, co-reduction, or surface passivation under the conditions that galvanic replacement occur. Over the past two decades, great success in synthesis of a diverse set of multimetallic hollow nanostructures, such as nanobox, nanocage, or nanoframe has been achieved using single-crystalline Ag nanocubes as sacrificial templates.[5,6] While by employing sophisticated multimetallic heteronanostructures as the sacrificial templates, well-defined nanoparticles with more complicated interior and surface architectures, such as yolk-shell nanorattles,[7,8] multilayered nanomatryoshkas,[8-10] and ultrathin skeletal nanoframes [11,12] could also be able to achieve.

Atomically intermixed bimetallic nanocrystals adopting either disordered alloy configurations or ordered intermetallic structures [13-15] may undergo galvanic replacement reaction-driven structural transformations that are substantially more sophisticated and versatile than those of monometallic nanocrystals or phase-segregated bimetallic

heteronanostructures, when key structure-evolutionary pathways, less-noble metal dealloying, new noble-metal deposition, and Kirkendall diffusion are taken into considerations. Here we endeavor to further push the structural and compositional control of multimetallic hollow nanostructures to a new level of precision and sophistication by coupling the percolation dealloying with galvanic replacement by using bimetallic NPs as initial sacrificial templates. We show that spongy NPs with ultrathin nanoligaments comprising Au-Cu alloy cores and Au-Pt alloy shells could be controllably synthesized by galvanic replacement of $Au_{0.2}Cu_{0.8}$ alloy with H_2PtCl_6. The thickness and the composition of the ligament could be precisely tailored by control over the leaching rate of Cu versus galvanic replacement rate. The unique ligaments feature greatly enhances the structural stability of the active sites on the ligament surfaces, allowing us to retain the superior catalytic activities over much longer periods toward alcohol oxidation in both acidic and alkaline environments relative to the commercial Pt black.

6.2 Experimental Section

Materials Polyvinylpyrrolidone (PVP, average MW 58 000), chloroauric acid ($HAuCl_4$ $4H_2O$), copper nitrate hydrate ($Cu(NO_3)_2$ $3H_2O$), and tetraethylene glycol (TEG) were purchased from Alfa Aesar. Hydrazine solution (N_2H_4 $3H_2O$ 35 wt %), nitric acid (HCl 37%), sulfuric acid (H_2SO_4 98%), chloroplatinic acid hexahydrate (H_2PtCl_6 $6H_2O$), and Nafion perfluorinated resion solution (5 wt%) were purchased from Sigma-Aldrich. Potassium carbonate (K_2CO_3) and formaldehyde (37 wt%) were purchased form J.T. Baker. Sodium hydroxide (NaOH) and potassium hydroxide (KOH) was purchased from Fisher Scientific. All reagents were used as received without further purification. Ultrapure Milli-Q water with a resistivity of 18.2 MΩ (Millipore) was used for all the

experiments.

Synthesis of Au-Cu Alloy NPs Quasi-spherical Au nanoparticles (QSNPs) were first synthesized by reducing $HAuCl_4$ with formaldehyde at room temperature. In a typical procedure, 50 mg of K_2CO_3 was dissolved in 200 mL of water, followed by addition of 3 mL of 25 mM $HAuCl_4$. The mixture solution was aged in the dark for 18 h before use. Then 1.34 mL of 37 % formaldehyde solution was added into the mixture under magnetic stir (300 rpm). After 30 min, the resulting Au QSNPs were centrifuged, washed with water, and redispersed in 10 mL of water.

Then 1.0 mL of Au QSNPs was introduced into 100 mL of 2 wt% PVP aqueous solution. 0.4 mL of 0.1 M $Cu(NO_3)_2$ was subsequently added. The reaction mixture was transferred into an ice bath, and then 0.22 mL of 5 M NaOH and 0.11 mL of N_2H_4 $3H_2O$ solution were added in successive under magnetic stir. The solutions were kept stirring for 15 min, and the obtained $Au@Cu_2O$ core-shell nanoparticles were separated from the reaction solution by centrifugation (2000 rpm, 10 min) washed with ethanol and redispersed in 1.0 mL ethanol.

Au-Cu alloy nanoparticles were prepared through a polyol-assisted growth method. Typically, 1.0 mL of $Au@Cu_2O$ core-shell NPs was added into 15 mL TEG containing 0.1 g PVP. Au-Cu alloy nanoparticles were obtained by heating the mixture at 300 ^oC for 30 min. The obtained nanoparticles were washed with ethanol five times, and finally redispersed in 2.0 mL of water.

Galvanic Replacement of Au-Cu Alloy NPs with H_2PtCl_6 In a typical galvanic replacement reaction, 100 μL of an aqueous suspension of Au-Cu alloy NPs were added into 1.0 mL of 2 wt % PVP aqueous solution in a small glass vial. Then 100 μL of 10

mM H_2PtCl_6 and 100 μL of HCl with varying concentrations (0.01 M, 0.02 M, 0.05 M, 0.1 M, or 0.2 M) were subsequently added into the solution. The mixture was kept at 60 ^oC under magnetic stirring for 30 min. The resulting NPs were separated by centrifugation and washed with water three times and dispersed into 20 μL water for further characterization and electrochemical measurement.

Structural Characterizations of NPs The morphologies and structures of the NPs were characterized by transmission electron microscopy (TEM) using a Hitachi H-8000 transmission electron microscope, which was operated at an accelerating voltage of 200 kV. All samples for TEM measurements were dispersed in ethanol and drop-dried on 200 mesh carbon-coated-Ni grids (Electron Microscopy Science Inc.). High-angle annular dark-field scanning electron microscopy (HAADF-STEM) imaging of spongy NPs drop-dried on Ni grids with ultrathin carbon support film were carried out using a JEOL 2100F 200 kV FEGSTEM/TEM microscope equipped with a CEOS CS corrector on the illumination system. The structures and compositions of the NPs were also characterized by Scanning Electron Microscopy (SEM) and Energy Dispersive Spectroscopy (EDS) measurements using a Zeiss Ultraplus thermal field emission scanning electron microscope. The samples for SEM and EDS measurements were dispersed in ethanol and drop-dried on silicon wafers. The size distribution histograms were obtained from more than 100 NPs for each sample. Powder X-ray diffraction (PXRD) patterns were record on a SAXSLab Ganesha at the South Carolina SAXS Collaborative (Cu $K\alpha$ = 1.5406 Å). XPS measurements were carried out using a Krato AXIS Ultra DLD XPS system equipped with a monochromatic Al Kα source. The samples for XPS measurements were all freshly prepared and dried in vacuum before being loaded into the XPS chambers. A

Finnigan ELEMENT XR double focusing magnetic sector field inductively coupled plasma-mass spectrometer (SF-ICP-MS) was used for the analysis of Cu (65, MR), Au (197, MR), and internal standard Rh (103 MR). A 0.2 mL min^{-1} Micromist U-series nebulizer (GE, Australia), quartz torch, and injector (Thermo Fisher Scientific, USA) were used for sample introduction. Sample gas flow was at 1.08 mL min^{-1}. The forwarding power was 1250 W. The samples for ICP-MS measurements were prepared by adding 1 mL of nitric acid and 3 mL of hydrochloric acid into Teflon digestion vessels containing the NP samples. The samples were digested using hot block at 180 ℃ for 4 h. The digestates were brought to 50 mL with water. A 3-point calibration curve was used for Cu, Au and Pt. The calibration range was from 50 to 600 ppb. The R^2 values for the initial calibration curves were greater than 0.995.

Electrochemical Measurements All the electrochemical measurements were performed using a CHI 660E workstation (CH Instruments, Austin, Texas) at room temperature with a three-electrode system composed of a Pt wire as the auxiliary, a saturated calomel electrode (SCE) as the reference, and a glassy carbon electrode (GCE, 3 mm diameter) as the working electrode. Typically, the GCE was polished with 0.3 mm alumina slurry and followed by washing with water and ethanol before use. Colloidal suspensions containing 5.0 μL Au-Cu-Pt trimetallic spongy colloidal NPs were dropped and air-dried on the pretreated GCEs at room temperature, and then 2 μL of Nafion solution (0.2 wt%) was dropped to hold the NPs. The electrochemically active surface area (ECSAs) were determined by integrating the hydrogen desorption charge on the CV at room temperature in N_2-saturated 0.5 M H2SO4 solution at a potential sweep rate of 50 mV s^{-1}. The polarization trace was normalized against the Pt mass of the spongy NPs

loaded on each electrode. To evaluate the electrocatalytic activities of the Au-Cu-Pt trimetallic spongy NPs toward alcohol oxidation, cyclic voltammetry (CV) measurements were performed in a N_2-saturated 0.5 M H_2SO_4 or 0.5 M KOH electrolytes containing 1.0 M methanol, 1.0 M ethanol, or 1.0 M *iso*-propanol at a potential sweep rate of 50 mV s^{-1}. To assess the electrocatalytic durability of the Au-Cu-Pt trimetallic spongy NPs, multiple CV cycles were carried out in 1.0 M methanol, 1.0 M ethanol, or 1.0 M isopropanol in the presence of 0.5 M H_2SO_4 or 1 M KOH electrolytes.

6.3 Results and Discussions

The model materials system we start with is the Au-Cu alloy nanoparticles obtained by thermal heating of Au@Cu_2O core-shell nanoparticles in tetraethylene glycol (TEG). The Au/Cu stoichiometric ratios of the alloy NPs were predetermined by the relative core and shell dimensions of their parental core-shell NPs. As shown in Figures 6.1A and 6.1B, uniform solid spherical-like Au-Cu alloy nanoparticles with Au/Cu atomic ratio of ~1/4 has been fabricated. We used high-angle annular dark-field scanning electron microscopy (HAADF-STEM) to characterize the structures of the alloy nanoparticle. Panels 6.1 C-a and C-b show the high-resolution HAADF-STEM images of two regions in a single Au-Cu alloy nanoparticle, with the electron beam projected along the [110] zone axis of the crystalline domains. The corresponding fast Fourier transform (FFT) patterns further confirmed the orientation of the crystalline domains. The lattice fringes corresponding to the face center cubic phase of Au-Cu alloy were well resolved (Figure 6.1C).

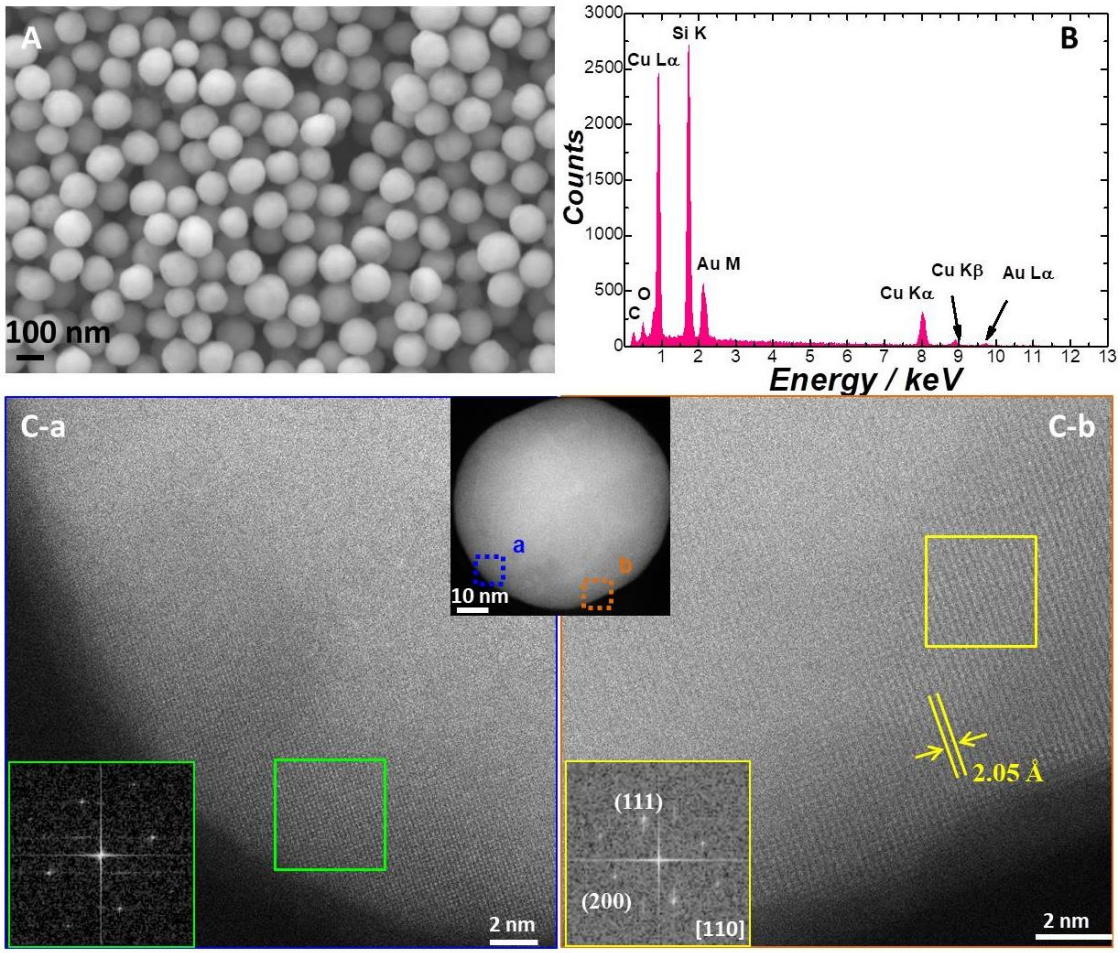

Figure 6.1. (A) SEM image, (B) EDS spectrum, and (C) HAADF-STEM images of $Au_{0.21}Cu_{0.79}$ alloy nanoparticles.

Upon expose to an H_2PtCl_6 aqueous solution containing HCl under air atmosphere, the $Au_{0.2}Cu_{0.8}$ alloy nanoparticles simultaneously undergoes nanoporosity-evolving process induced by galvanic replacement with H_2PtCl_6 and oxidative etching by the O_2 dissolved in water with the aid of Cl^- in an acidic environment, as illustrated in Figure 6.2A.[16-20] In this case, galvanic replacement and percolation dealloying can be considered as two completing processes that play intertwining roles in guiding the nanoparticle structural evolution. We used high-resolution HAADF-STEM, high resolution STEM-energy-dispersive spectroscopy (EDS) measurements, powder X-ray diffraction (PXRD), EDS,

inductively coupled plasma mass spectrometry (ICP-MS), and X-ray photoelectron spectroscopy (XPS) to characterize the structure and morphology of the nanospongy particles. After exposing $Au_{0.21}Cu_{0.79}$ alloy nanoparticles to an aqueous solution containing 2.8 mM HCl and 2.8 mM H_2PtCl_6 at 60 ^{0}C for 1 hour, the HAADF-STEM images clearly show that the alloy nanoparticles transform into spongy nanoparticles with voids throughout the entire particle comprising ultrathin ligaments with average thickness of only ~ 3 nm (denoted as NS-i, Figures 6.2B-6.2D). High resolution STEM-EDS measurements reveal that each ligament is composed of a Au-Cu alloy core about 1.6 nm thick encapsulated by a sub-nm thick Au-Pt alloy skin (Figures 6.2E-6.2G). The Au-Pt alloy skin working as passivation layers prevents the further Cu leaching from the Au-Cu alloy matrix. This unexpected approach for formation of Au-Pt alloy skin paved a way to further optimize the property of porous Au nanoparticles since bulk Au and Pt are thermodynamic totally immiscible over a wide composition range, and the fabrication of Au-Pt alloy nanostructure has been thought to be a huge challenge simple "bottom-up" methods.[21,22] Figures 6.2E and 6.2F show the high-resolution HAADF-STEM images of two regions of one single spongy particle, with the electron beam projected along the [011] zone axis of the crystalline domains. The corresponding fast Fourier transform (FFT) patterns further confirmed the orientation of the crystalline domains in the ligaments. The lattice fringes corresponding to the face center cubic phase of Au-Pt and Au-Cu alloy were well resolved in the high-resolution HAADF-STEM images. The inset of Figure 6.2F showed the EDS line scan profile as well as the EDS (Figure 6.2G) obtained from a single untrathin ligament, which provides further evidence of core-shell cable structure of the ligaments.

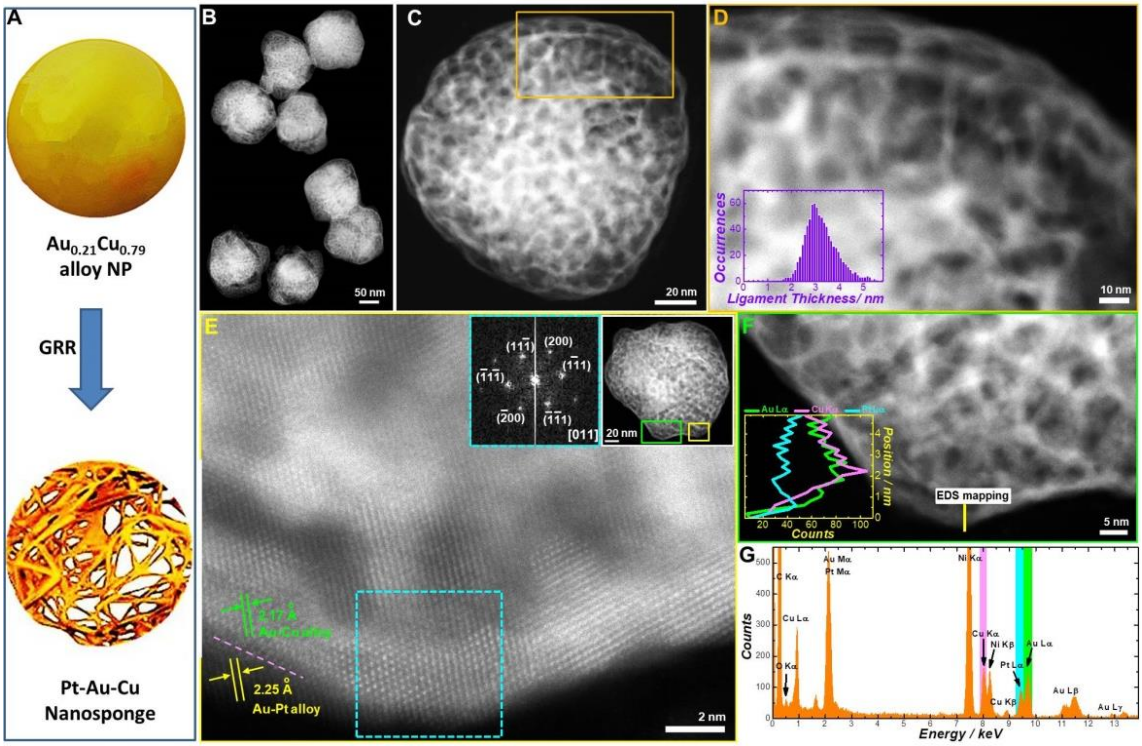

Figure 6.2. **Atomic-level surface structures of Au-Cu-Pt trimetallic spongy NPs**. (A) Illustration of the transformation of $Au_{0.21}Cu_{0.79}$ into spongy NP with ultrathin ligaments. (B) HAADF-STEM image of Au-Cu-Pt trimetallic spongy NPs. (C) HAADF-STEM image of an individual Au-Cu-Pt trimetallic spongy NP. (D) High-resolution HAADF-STEM image of the selected region shown in C. The inset shows the ligament thickness distribution of Au-Cu-Pt trimetallic spongy NP. (E) High-resolution HAADF-STEM image showing the atomic-level structures of the selected region from the individual NP in the inset. The inset show the FFT pattern and HAADF-STEM image of the corresponding individual Au-Cu-Pt trimetallic spongy NP. In the high-resolution HAADF-STEM images, the crystalline domains were projected along the [011] zone axis. (F) High-resolution HAADF-STEM image of the selected region from the individual particle shown in E. The inset shows EDS line scan elemental analysis of a single ultrathin ligament. (G) EDS spectrum of the single ultrathin ligament.

The diffraction peaks corresponding to the fcc $Au_{0.2}Cu_{0.8}$ alloy split into two sets of fcc diffraction peaks, which could be assigned to the fcc Au-Cu and Au-Pt alloy structures (Figure 6.3A). PXRD results further confirms the Au-Cu cores and Au-Pt alloy shells of ligaments and the small feature sizes of the ligaments are manifested by the significant broadening of the diffraction peaks.

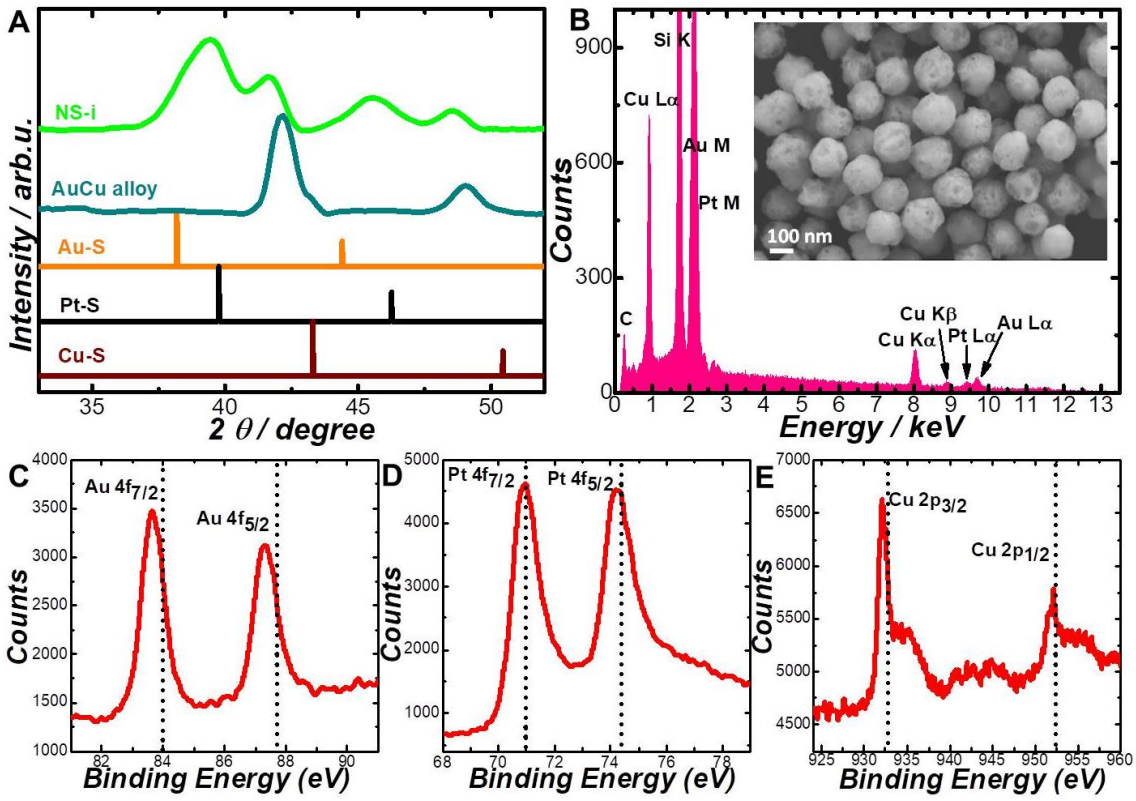

Figure 6.3. (A) XRD pattern of Au-Cu-Pt trimetallic spongy NPs (NS-i) synthesized through galvanic replacement of $Au_{0.21}Cu_{0.79}$ alloy NPs with H_2PtCl_6 aqueous solution containing 2.8 mM HCl concentrations. The standard XRD patterns of bulk Au, Cu, and Pt are also included. (B) EDS spectrum of NS-i. The inset shows the SEM image of NS-i. XPS of (C) Au 4f, (D) Pt 4f, and (E) Cu2p regions of NS-i. The vertical dash lines indicate the peak positions of standard bulk Au, Pt, and Cu.

The stoichiometric quantification of $Pt_{0.24}Au_{0.38}Cu_{0.38}$ trimetallic spongy nanoparticles determined by EDS is consistent well with the result measured by ICP-MS (Figure 6.3B). While the Pt-to-Au atomic ratio quantified by XPS ($Pt_{0.58}Au_{0.31}Cu_{0.11}$) were higher than the bulk atomic ratio obtained from EDS, further suggesting that the formation of Au-Pt layers on the ligament surfaces. The binding energies of the Pt 4f peaks slightly down shift with respect to those of bulk Pt, whereas both the Cu 2p and Au 4f peaks slightly down-shifted with respect to those of bulk Cu and Au, indicating that the Au alloyed with Pt (Figures 6.3C-6.3E).[23] The existence of Au-Pt overlayers probably make a significant

contribution to the stabilization of the porous structure. It has been recently observed that a small amount of Pt atoms on nanoporous Au surface could greatly stabilize the nanostructure during electrocatalytic reactions.[24] It has also been reported that residual Pt could effectively stabilize the large surface active area of nanoporous Au during dealloying,[25] which was correlated to a much slower surface diffusion rate of Pt as compared with Au.[26]

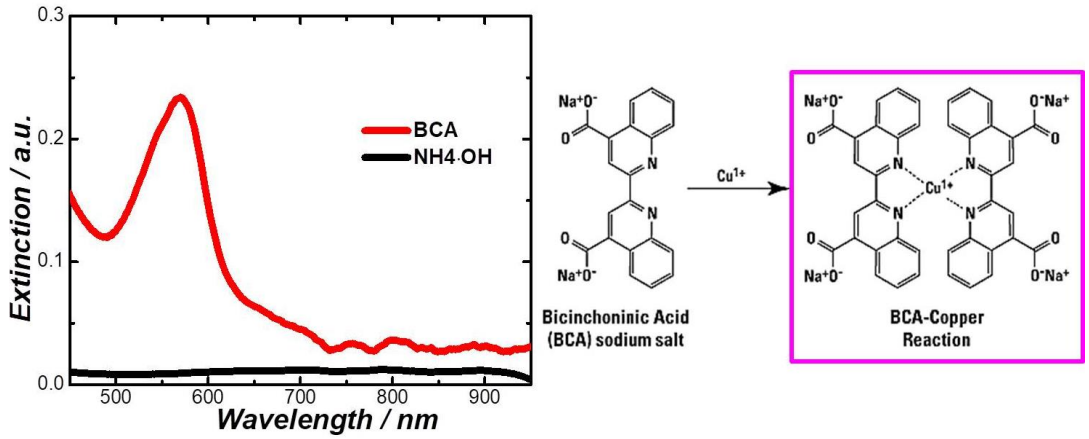

Figure 6.4. UV-visible-near infrared spectra of the supernatant after GRRs between $Au_{0.21}Cu_{0.79}$ alloy NPs and 200 μL of 10 mM H_2PtCl_6. The NPs were separated from the supernatant through centrifugation. To distinguish Cu(I) and Cu(II) ionic species in the supernatant, 200 μL of 100 mM BCA (a Cu(I)-targeting ligand) or 200 μL of 1 M NH_4OH (a Cu(II)-targeting ligand) were added into 1 mL of the supernatant. Upon addition of BCA into the supernatant, the solution color turned pink and an absorption peak at 560 nm emerged, which was the characteristic peak of Cu (I)-BCA complexes. This indicated that the metallic Cu in the alloy NPs was oxidized into Cu(I) after the GRRs, which was further verified by the directly mixing 1.2 mL of 1 mM $Cu(NO_3)_2$ with 200 μL of 1 M ammonia. The characteristic absorption peak (centered at 650 nm) of Cu(II)-ammonia complex was not observed upon addition of NH_4OH, indicating the absence of Cu(II) ionic species in the supernatant.

Under the current experimental conditions, Cu was oxidized into Cu(I) rather than Cu(II) ionic species while Pt(IV) was reduced to metallic Pt through galvanic replacement, exhibiting a net reaction outcome of every four Cu atoms substituted by one Pt atom. Meanwhile, the percolation dealloying in HCl also resulted in formation of Cu(I) ions, which form a complex with bicinchoninic acid (BCA) with a characteristic

absorption band around 550 nm[27] and no Cu(II) ions at detectable concentration levels have been identified by titration excessive ammonia into the supernatant after reactions (Figure 6.4).

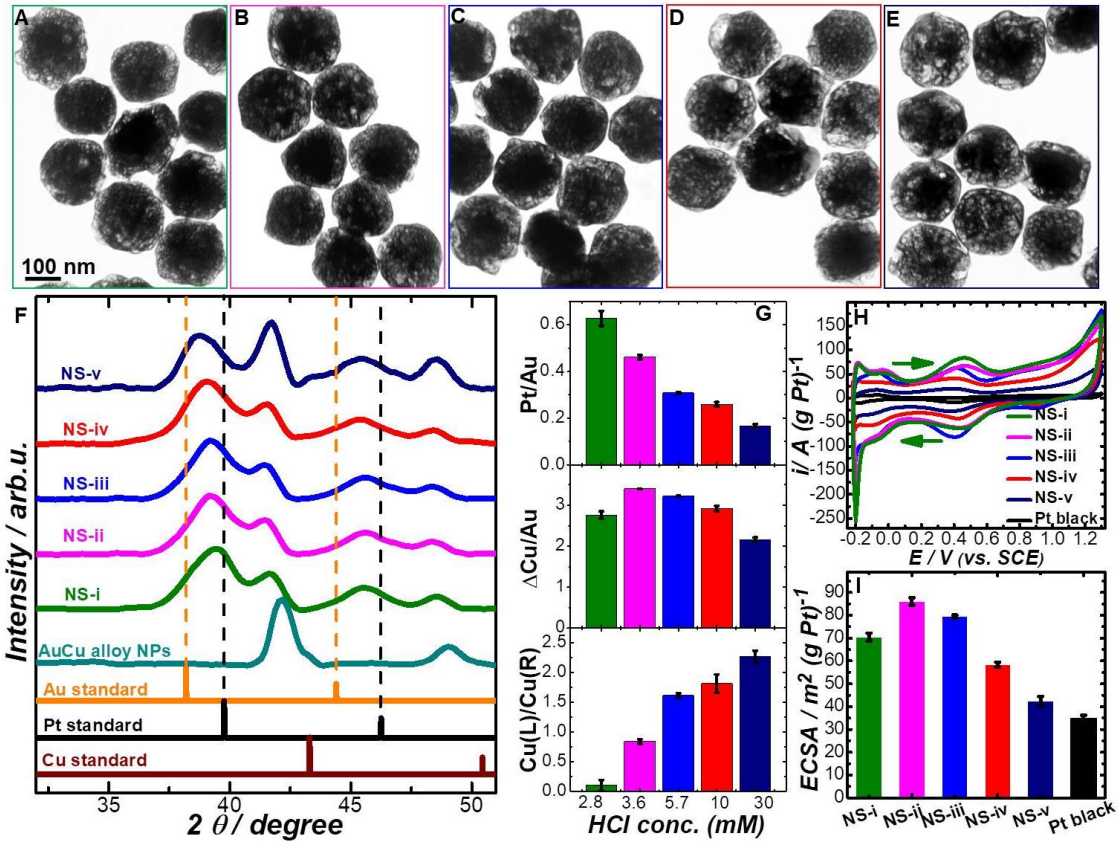

Figure 6.5. **Structure and composition of Au-Cu-Pt trimetallic spongy NPs.** TEM images of Au-Cu-Pt trimetallic spongy NPs synthesized through galvanic replacement of Au-Cu alloy NPs with H_2PtCl_6 aqueous solution containing various concentrations of HCl. (A) 2.8 mM, (B) 3.6 mM, (C) 5.7 mM, (D), 10 mM, (E) 30 mM. (F) XRD patterns of Au-Cu-Pt trimetallic spongy NPs synthesized through galvanic replacement of Au-Cu alloy NPs with H_2PtCl_6 aqueous solution containing various HCl concentrations. The standard XRD patterns of bulk Au, Cu, and Pt are also included. (G) Atomic ratio evolutions of Pt and Cu during the GRR with the increase of HCl concentration. (H) CV curves of various spongy NPs in 0.5 M H_2SO_4 at a potential sweep rate of 50 mV s^{-1}. The currents were normalized against the Pt mass loaded on each electrode. (I) ECSA of various spongy NPs estimated based on the hydrogen desorption peak area.

We can systematically tailor the atomic ratios of the dealloyed nanospongies without obvious morphological changes by control over the percolation dealloying and galvanic replacement kinetics through changing the molar ratio between HCl and H_2PtCl_6 during

the porosity-evolving process. We use TEM and PXRD to monitor the structural and compositional evolutions of the Au-Cu alloy structures with the increasing of the HCl concentration during the reaction. While no obvious morphological changes were observed from the TEM images (Figures 6.5A-6.5E), it is clear to see a striking difference in PXRD patterns (Figure 6.5F). The diffraction peaks of Au-Pt phase gradually shift to pure Au, indicating a progressively decreased Pt fraction of nanospongy particles with HCl concentration increase, whereas Au-Cu alloy phase remains almost unchanged as a consequence of the formation of passivated Au-Pt layer which prevented the further Cu leaching. The atomic fractions of Au, Pt, and Cu for various nanospongies from NS-i to NS-v quantified by EDS and ICP-MS keep a good consistence (Table 1). The ratio between leached Cu induced by HCl (denoted as L_{cu}) and replaced Cu by H_2PtCl_6 (denoted as R_{Cu}) reflects relative rate of percolation dealloying with respect to that of galvanic replacement. The Pt/Au atomic ratio kept decreasing with the HCl concentration increase, while the total loss Cu content increased first and then decreased. Based on the quantification results, we are able to calculate the ratios of Cu atoms leached (L_{cu}) with respect to those galvanically replaced by Pt (R_{Cu}) using the Au quantity as internal reference. As shown in Figure 6.5G, the L_{Cu}/R_{Cu} gradually increases with the increase of HCl amount during the reaction because a higher HCl concentration accelerates the Cu leaching while the galvanic replacement reaction keeps unchanged. We also used cyclic voltammetry (CV) as an electrochemical characterization tool to compare the specific surface areas and surface atomic structures of various nanospongies (Figure 6.5H). The peaks appearing in the range from -0.23 to 0.15 V are attributed to hydrogen underpotential formation/stripping (HUPD) and are used to estimate the

electrochemically active surface area (ECSA) of the NSs by assuming the charge density passed during the hydrogen adsorption was 210 μC/cm^2 for a flat Pt surface.[28] The peaks at 0.3-0.6 V originate from oxidation and reduction of surface Pt atoms. The ECSA first increased and then decreased as an increasing amount of HCl concentration and NS-ii exhibited the largest ECSA among the NS samples. The ECSA of NSs was calculated to be 70.5, 86.1, 79.4, 58.4, 42.4 m^2/g for NS-i, NS-ii, NS-iii, NS-iv, and NS-iv respectively, all of which are higher than that of commercial Pt black which is estimated to 35.1 m^2/g (Figure 6.5I).

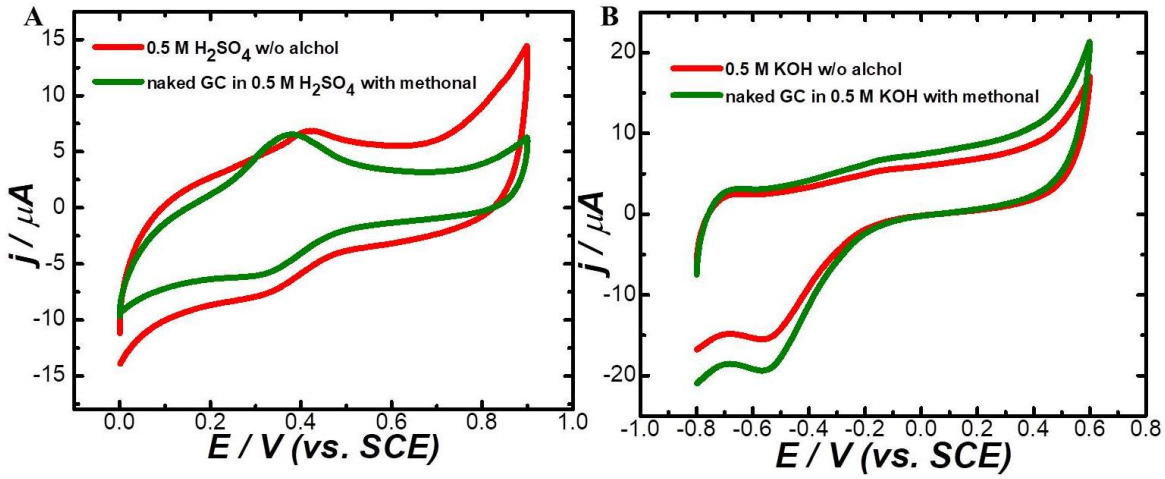

Figure 6.6. CV curves obtained on a GCE loaded with NS-i in deoxygenated solution containing (A) 0.5 M H_2SO_4 and (B) 1.0 M KOH without methanol, a naked GCE in deoxygenated 0.5 M H_2SO_4 and 1.0 M KOH and 1 M methanol. The potential sweep rate was 50.0 mV s^{-1}.

We used room-temperature electro-oxidation of alcohols in both acidic and alkaline environments as model reactions to assess the electrocatalytic performances of the obtained NS particles. The glassy carbon electrode (GCE) itself was electrocatalytically inert neither in H_2SO_4 or KOH electrolytes (Figures 6.6A and 6.6B), while spongy nanoparticles exhibited remarkable electrocatalytic activities toward the methanol oxidation reaction (MOR), ethanol oxidation reaction (EOR), and isopropanol oxidation

reaction (i-POR).

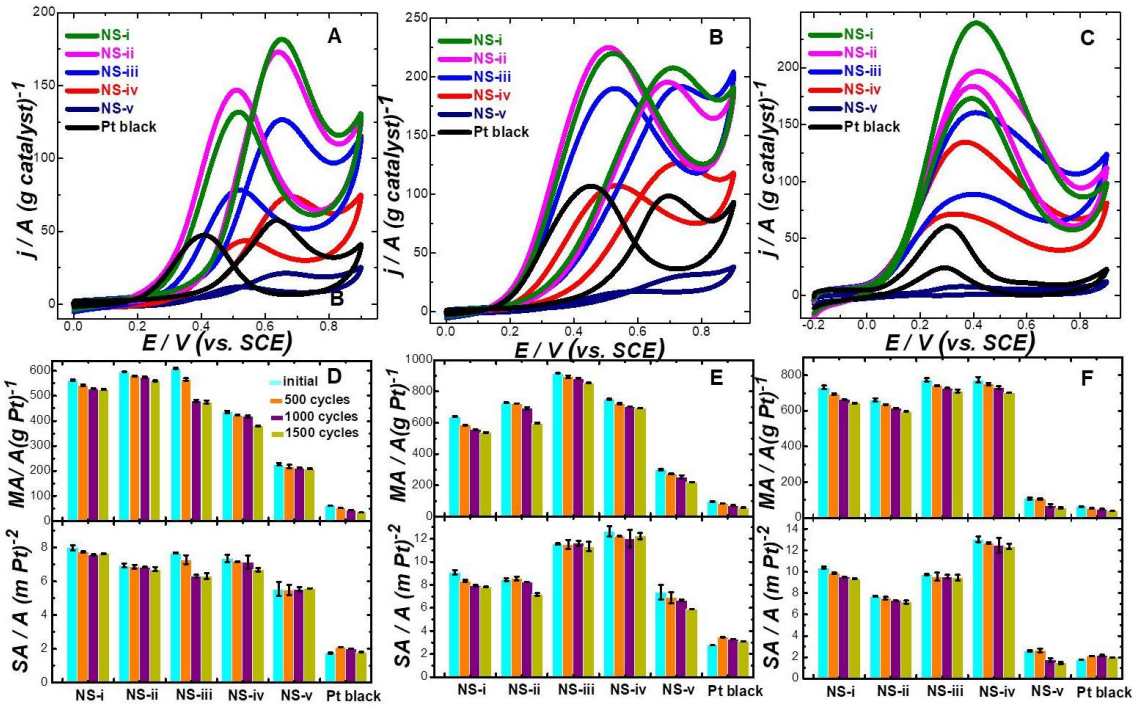

Figure 6.7. CV curves of various spongy NPs and commercial Pt black in N_2-saturated 0.5 M H_2SO_4 electrolyte solutions containing (A) 1 M methanol, (B) 1 M ethanol, and (C) 1 M isopropanol. The potential sweep rate was 50.0 mV s^{-1}. Mass activities and specific activities of various spongy NPs and commercial Pt black for the 1st sweep cycle and after multiple sweep cycles in in N_2-saturated 0.5 M H_2SO_4 electrolyte solutions containing (D) 1 M methanol, (E) 1 M ethanol, and (F) 1 M isopropanol.

CV results clearly show that almost all the NSs with different compositions are electrocatalytically more active than commercial Pt black in N_2-saturated 0.5 M H_2SO_4 electrolyte solutions containing 1 M methanol, 1 M ethanol, and 1 M isopropanol (Figures 6.7A-6.7C), exhibiting lower onset and peak oxidation potentials and higher peak currents during the anodic sweeps. A second oxidation peak emerged during the cathodic sweeps resulted from the further oxidation of surface-adsorbed carbonaceous species not fully oxidized during the previous anodic sweeps.[29,30] By normalizing the oxidation peak current against the mass of Pt on each electrode, mass activities (MAs) of various NSs were calculated, which were obvious higher than that of the commercial Pt

black. The superior electrocatalytic activity toward alcohol oxidation reactions observed on the porous NSs originated from both their large specific ECSA and high density of surface active sites. By normalizing the MAs against ECSAs, the specific activities (SAs) of the NPs were obtained, which were directly related to the active site density on the NP surfaces. As shown in Figures 6.7D-6.7F, all NSs exhibited larger SAs with respective of commercial Pt black. More importantly, the NSs were significantly robust, and both MA and SA were well preserved after thousands of CV cycles.

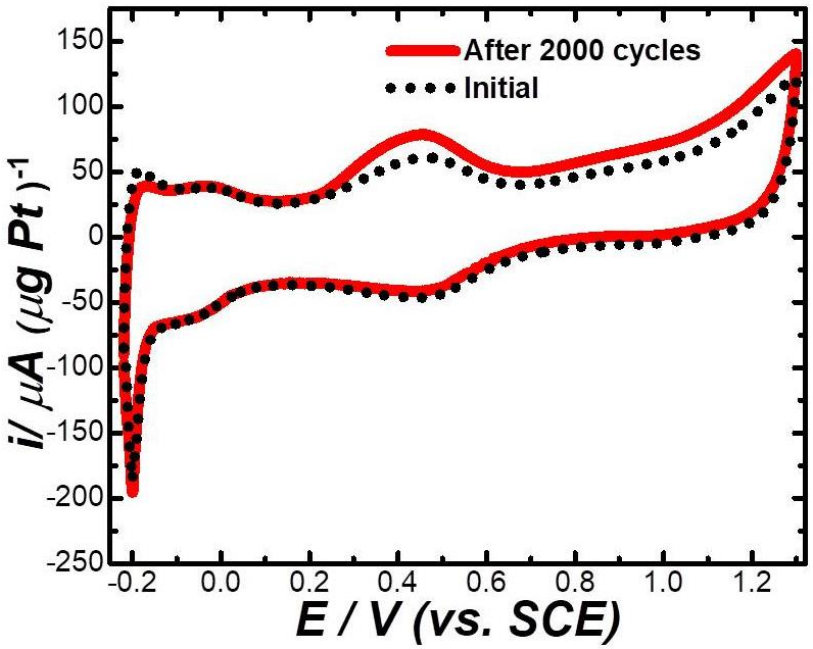

Figure 6.8. CV curves for electrochemical oxide stripping measurements of NS-i before and after CA measurements (at 0.6 V *vs.* SCE for 2 hours, 1 M methanol, 0.5 M H_2SO_4 electrolyte).

In addition, the CV measurement after multiple cycles further confirmed the well-preserved active sites and ECSA during the reactions due to the presence of Au-Pt skin on the ligament surfaces (Figure 6.8). We also evaluated the catalytic performances of NSs in alkaline environment.

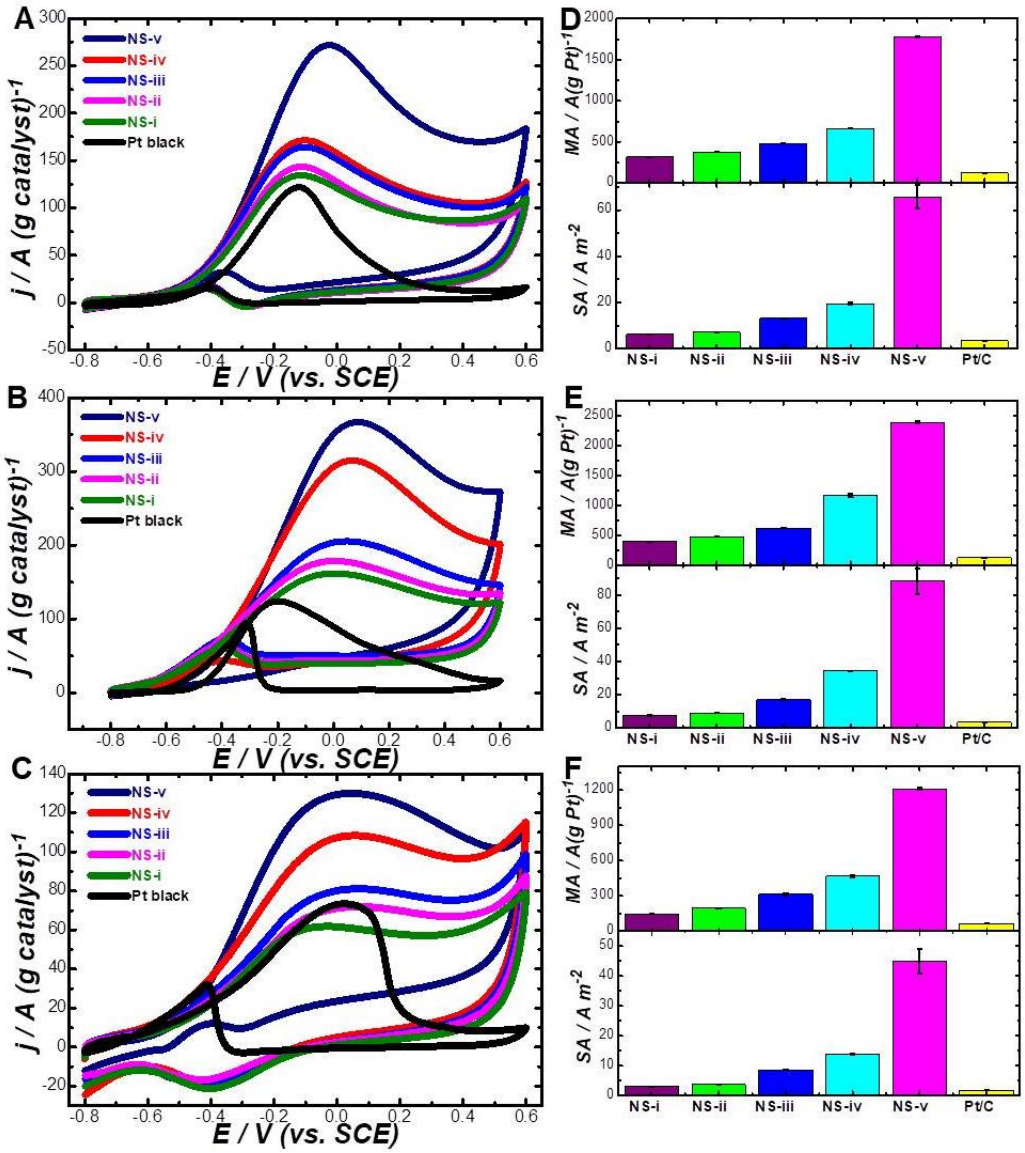

Figure 6.9. CV curves of various spongy NPs and commercial Pt black in N_2-saturated 1 M KOH electrolyte solutions containing (A) 1 M methanol, (B) 1 M ethanol, and (C) 1 M isopropanol. The potential sweep rate was 50.0 mV s^{-1}. Mass activities and specific activities of various spongy NPs and commercial Pt black for the 1st sweep cycle and after multiple sweep cycles in in N_2-saturated 1 M KOH electrolyte solutions containing (D) 1 M methanol, (E) 1 M ethanol, and (F) 1 M isopropanol.

Figure 6.9 shows CV measurements of NSs toward various electrocalytic oxidation alcohols in alkaline environment and the corresponding MAs normalized to Pt mass and SAs. The NS nanoparticles exhibit larger MAs and SAs relative to commercial Pt black.

6.4 Conclusion

This work opens up a new opportunity for precise control over the architectures of dealloyed porous nanostructures with ultrathin ligaments composed of Au-Cu alloy cores and Au-Pt alloy shells by using bimetallic alloy as sacrificial templates though coupling galvanic replacement reaction with percolation dealloying. The fine structures of the ligaments including thickness and composition could be precisely controlled by tuning the rate of Cu leaching relative with that of galvanic replacement. It is demonstrated the Au-Pt shells could inhibit the further Cu leaching and stabilize the structures of spongy nanoparticles meanwhile during the reaction, which allow us to well maintain the superior catalytic activities over much longer periods or multiple cycles toward alcohol oxidation reactions in both acidic and alkaline environments relative to the commercial Pt black.

6.5 References

(1) Gonz áez, E.; Arbiol, J.; Puntes, V. F., *Science* **2011**, 334, 1377.

(2) Sun, Y.; Xia, Y., *Science* **2002**, 298, 2176.

(3) Cobley, C. M.; Xia, Y., *Materials science & engineering. R, Reports : a review journal* **2010**, 70, 44.

(4) Xia, X.; Wang, Y.; Ruditskiy, A.; Xia, Y., *Adv Mater* **2013**, 25, 6313.

(5) Skrabalak, S. E.; Chen, J.; Sun, Y.; Lu, X.; Au, L.; Cobley, C. M.; Xia, Y., *Accounts Chem Res* **2008**, 41, 1587.

(6) Chen, J.; Wiley, B.; McLellan, J.; Xiong, Y.; Li, Z.-Y.; Xia, Y., *Nano Lett* **2005**, 5, 2058.

(7) Cho, E. C.; Camargo, P. H. C.; Xia, Y., *Adv Mater* **2010**, 22, 744.

(8) Sun, Y.; Wiley, B.; Li, Z.-Y.; Xia, Y., *J Am Chem Soc* **2004**, 126, 9399.

(9) Hong, S.; Acapulco, J. A. I.; Jang, H. Y.; Park, S., *Chem Mater* **2014**, 26, 3618.

(10) Jing, H.; Wang, H., *Chem Mater* **2015**, 27, 2172.

(11) Hong, X.; Wang, D.; Cai, S.; Rong, H.; Li, Y., *J Am Chem Soc* **2012**, 134, 18165.

(12) McEachran, M.; Keogh, D.; Pietrobon, B.; Cathcart, N.; Gourevich, I.; Coombs, N.; Kitaev, V., *J Am Chem Soc* **2011**, 133, 8066.

(13) Yan, Y.; Du, J. S.; Gilroy, K. D.; Yang, D.; Xia, Y.; Zhang, H., *Adv Mater* **2017**, 29, 1605997.

(14) Ferrando, R.; Jellinek, J.; Johnston, R. L., *Chem Rev* **2008**, 108, 845.

(15) Weiner, R. G.; Smith, A. F.; Skrabalak, S. E., *Chem Commun* **2015**, 51, 8872.

(16) Ruditskiy, A.; Vara, M.; Huang, H.; Xia, Y., *Chem Mater* **2017**, 29, 5394.

(17) Zheng, Y.; Zeng, J.; Ruditskiy, A.; Liu, M.; Xia, Y., *Chem Mater* **2014**, 26, 22.

(18) Wen, T.; Zhang, H.; Tang, X.; Chu, W.; Liu, W.; Ji, Y.; Hu, Z.; Hou, S.; Hu, X.; Wu, X., *J Phys Chem C* **2013**, 117, 25769.

(19) Zhang, H.; Xia, X.; Li, W.; Zeng, J.; Dai, Y.; Yang, D.; Xia, Y., *Angew Chem Int Ed* **2010**, 49, 5296.

(20) Tsung, C.-K.; Kou, X.; Shi, Q.; Zhang, J.; Yeung, M. H.; Wang, J.; Stucky, G. D., *J Am Chem Soc* **2006**, 128, 5352.

(21) Luo, J.; Maye, M. M.; Petkov, V.; Kariuki, N. N.; Wang, L.; Njoki, P.; Mott, D.; Lin, Y.; Zhong, C.-J., *Chem Mater* **2005**, 17, 3086.

(22) Zhou, S.; Jackson, G. S.; Eichhorn, B., *Adv Funct Mater* **2007**, 17, 3099.

(23) Kim, M.-J.; Na, H.-J.; Lee, K. C.; Yoo, E. A.; Lee, M., *J Mater Chem* **2003**, 13, 1789.

(24) Zhang, J.; Liu, P.; Ma, H.; Ding, Y., *J Phys Chem C* **2007**, 111, 10382.

(25) Snyder, J.; Asanithi, P.; Dalton, A. B.; Erlebacher, J., *Adv Mater* **2008**, 20, 4883.

(26) Seebauer, E. G.; Allen, C. E., *Prog Surf Sci* **1995**, 49, 265.

(27) Brenner, A. J.; Harris, E. D., *Anal Biochem* **1995**, 226, 80.

(28) Lee, E. P.; Peng, Z.; Cate, D. M.; Yang, H.; Campbell, C. T.; Xia, Y., *J Am Chem Soc* **2007**, 129, 10634.

(29) Sneed, B. T.; Young, A. P.; Jalalpoor, D.; Golden, M. C.; Mao, S.; Jiang, Y.; Wang, Y.; Tsung, C.-K., *ACS Nano* **2014**, 8, 7239.

(30) Guo, S.; Zhang, S.; Sun, X.; Sun, S., *J Am Chem Soc* **2011**, 133, 15354.

CHAPTER 7

STRUCTURAL EVOLUTION OF AU-CU BIMETALLIC NANOPARTICLES THROUGH COUPLING GALVANIC REPLACEMENT WITH CODEPOSITION

7.1 Introduction

Nanoscale galvanic replacement provides a synthetically powerful approach for transformation of solid monometallic nanoparticles into more complex multimetallic nanostructures with hollow interiors.[1,2] Over the past decade, remarkable progress has been made for fabrication of a series of sophisticate multimetallic hollow nanostructures through galvanic replacement reactions, and Ag-based bimetallic or trimetallic hollow nanoparticles with tunable structures and properties in particular have attracted intensive interesting by using Ag nanoparticles as sacrificial templates under appropriate conditions.[3-6] It has shown that the starting templates have profound impacts on the architectures, compositions, and crystallinity of the resulting hollow nanoparticles.[7,8] It has been recently found that a variety of nanostructures with increasingly sophisticated interior and surface architectures could be achieved by a modified galvanic replacement combination with sequentially deposited templates,[9-11] the Kirkendall effects,[2] or combined co-reduction and corrosion,[12,13] which provide new opportunities for us to further fine-tune the architectures and compositions of the resultant hollow products and eventually optimize their chemical/physical properties. In the past few years, various fantastic Ag-based hollow nanostructures including Ag-Au, Ag-Pd, and Ag-Pt, could be controllably fabricated through galvanic replacements.[5,14-17] Pt-containing alloy nanoparticles with hollow interiors and open surface structures, are of particular interest for high-performance nanocatalysis due to the anticipated enhancements toward the catalytic activity as a consequence their of high surface-to-volume ratio, and fine tailored structures with excellent surface accessibility and high densities of catalytically active sites.[18-21] However, direct galvanic replacement offers rather poor control over the

geometries of Pt-based bimetallic hollow nanostructures because of the poor miscibility of Pt with other precious system like Ag-Pt, or Au-Pt binary systems, the Pt-based hollow nanostructures obtained through galvanic replacement typically exhibit poor morphology with bumpy and polycrystalline heterostructured walls.[18,22] It is thus highly desirable to explore appropriate method by alternating template materials and/or modifications to the existing approaches to target the synthesis of hollow Pt nanostructures with fine-tuned architectures and compositions. Here we show that coupling codeposition with the galvanic replacement between Au-Cu bimetallic nanoparticles and H_2PtCl_6 in polyol allows us to fine tailor the geometries of the Au-Cu-Pt trimetallic hollow nanostructures with increased architectural complexity and thus greatly enhances our capabilities to optimize the catalytic performance of Pt-based hollow nanostructures.

7.2 Experimental Section

Materials Polyvinylpyrrolidone (PVP, average MW 58 000), chloroauric acid ($HAuCl_4 \cdot 4H_2O$), copper nitrate hydrate ($Cu(NO_3)_2 \cdot 3H_2O$), ethylene glycol (EG), diethylene glycol (DEG), and tetraethylene glycol (TEG) were purchased from Alfa Aesar. Hydrazine solution ($N_2H_4 \cdot 3H_2O$ 35 wt %), sulfuric acid (H_2SO_4 98%), chloroplatinic acid hexahydrate ($H_2PtCl_6 \cdot 6H_2O$), trizma base (TB), and Nafion perfluorinated resion solution (5 wt%) were purchased from Sigma-Aldrich. Trisodium citrate dehydrate ($Na_3C_6H_5O_7 \cdot 2H_2O$), sodium hydroxide (NaOH), and potassium hydroxide (KOH) was purchased from Fisher Scientific. All reagents were used as received without further purification. Ultrapure Milli-Q water with a resistivity of 18.2 MΩ (Millipore) was used for all the experiments.

Synthesis of Au-Cu Alloy NPs Quasi-spherical Au NPs with an average diameter of

48.2 nm were synthesized using a previously reported seed-mediated growth method. Colloidal Au seeds with an average size of 17 nm were first synthesized by reducing chloroauric acid with citrate. Briefly, 0.5 mL of 25 mM $HAuCl_4$ aqueous solution were added into 48 mL of boiling water under magnetic stir, followed by further reflux for 10 minutes. Subsequently, 1.5 mL of 1 wt % trisodium citrate aqueous solution was rapidly injected into the refluxing reactant solution. The reaction solution was further refluxed for 30 minutes under magnetic stir, and then cooled to room temperature for further use. To synthesize ~ 48 nm quasi-spherical Au NPs, 8 mL of 0.1 M TB aqueous solution were added into 185 mL of boiling water. After being gently stirred for 10 minutes, 4 mL of the as-synthesized colloidal Au seeds and 3 mL of 25 mM $HAuCl_4$ solution were successively added to the TB solution, followed by further reflux for 30 minutes under magnetic stir. The total volume of the final reaction solution was 200 mL. The Au quasi-spherical NPs were subsequently separated from the reaction solution by centrifugation (3500 rpm, 10 min) and redispersion in 4 mL water for further use.

Then 1.0 mL of Au QSNPs was introduced into 240 mL of 2 wt% PVP aqueous solution. 0.73 mL of 0.1 M $Cu(NO_3)_2$ was subsequently added. The reaction mixture was transferred into an ice bath, and then 0.58 mL of 5 M NaOH and 0.26 mL of N_2H_4 $3H_2O$ solution were added in successive under magnetic stir. The solutions were kept stirring for 15 min, and the obtained $Au@Cu_2O$ core-shell nanoparticles were separated from the reaction solution by centrifugation (3000 rpm, 10 min) washed with ethanol and redispersed in 3.0 mL ethanol.

Au-Cu alloy nanoparticles were prepared through a polyol-assisted growth method. Typically, 1.0 mL of $Au@Cu_2O$ core-shell NPs was added into 10.0 mL TEG containing

0.1 g PVP. Au-Cu alloy nanoparticles were obtained by heating the mixture at 300 ^{o}C for 10 min. The obtained nanoparticles were washed with ethanol five times, and finally redispersed in 2.0 mL of ethanol.

Galvanic Replacement of Au-Cu Alloy NPs with H_2PtCl_6 in Polyol In a typical galvanic replacement reaction, 500 L of Au-Cu alloy colloidal NPs were added into 8.3 mL polyol (EG, DEG, or TEG) in a small glass vial. Then 1.66 mL of 5 mM H_2PtCl_6 polyol solution was subsequently added. The mixture was kept in an oil bath at 130 ^{0}C under magnetic stirring for 30 min. The resulting NPs were separated by centrifugation and washed with ethanol five times and dispersed into 125 μL water for further characterizations and electrochemical measurements.

Structural Characterizations of NPs The morphologies and structures of the NPs were characterized by transmission electron microscopy (TEM) using a Hitachi H-8000 transmission electron microscope, which was operated at an accelerating voltage of 200 kV. All samples for TEM measurements were dispersed in ethanol and drop-dried on 200 mesh carbon-coated-Ni grids (Electron Microscopy Science Inc.). The structures and compositions of the NPs were also characterized Energy Dispersive Spectroscopy (EDS) measurements using a Zeiss Ultraplus thermal field emission scanning electron microscope. The samples for SEM and EDS measurements were dispersed in ethanol and drop-dried on silicon wafers. The size distribution histograms were obtained from more than 100 NPs for each sample. Powder X-ray diffraction (PXRD) patterns were record on a SAXSLab Ganesha at the South Carolina SAXS Collaborative (Cu $K\alpha$ = 1.5406 Å). XPS measurements were carried out using a Krato AXIS Ultra DLD XPS system equipped with a monochromatic Al Kα source. The samples for XPS measurements were

all freshly prepared and dried in vacuum before being loaded into the XPS chambers.

Electrochemical Measurements All the electrochemical measurements were performed using a CHI 660E workstation (CH Instruments, Austin, Texas) at room temperature with a three-electrode system composed of a Pt wire as the auxiliary, a saturated calomel electrode (SCE) as the reference, and a glassy carbon electrode (GCE, 3 mm diameter) as the working electrode. Typically, the GCE was polished with 0.3 mm alumina slurry and followed by washing with water and ethanol before use. 4.0 μL of the synthesized Au-Cu-Pt colloidal NPs was dropped and air-dried on the pretreated GCEs at room temperature, and then 2 μL of Nafion solution (0.2 wt%) was dropped to hold the NPs. The electrochemically active surface area (ECSAs) were determined by integrating the hydrogen desorption charge on the CV at room temperature in N_2-saturated 0.5 M H2SO4 solution at a potential sweep rate of 50 mV s^{-1}. The polarization trace was normalized against the Pt mass of the porous NPs loaded on each electrode. To evaluate the electrocatalytic activities of the Au-Cu-Pt trimetallic porous NPs toward formic acid oxidation, cyclic voltammetry (CV) measurements were performed in a N_2-saturated 0.5 M H_2SO_4 electrolyte containing 1.0 M formic acid at a potential sweep rate of 50 mV s^{-1}. To assess the electrocatalytic durability of the Au-Cu-Pt trimetallic porous NPs, multiple CV cycles were carried out in 1.0 M formic acid in the presence of 0.5 M H_2SO_4 electrolyte. The linear sweep voltammetry (LSV) of the Au-Cu-Pt trimetallic porous NPs toward hydrogen evolution was carried out in 0.5 M H_2SO_4 (pH 0.3) which was bubbled with N_2 gas for 20 min before use and continuously bubbled during the tests at a scan rate of 50 mV/s.

7.3 Results and Discussions

Operation of galvanic replacement in a reducing atmosphere allows us to manipulate the dealloying and coreduction processes, which have a profound impact on the structural evolution of the sacrificial nanoparticles. In this work, we demonstrate the use of polyol as a solvent as well as a reducing agent during the galvanic replacement of $AuCu_3$ alloy with H_2PtCl_6 to fine-tailor structural and compositional evolutions of Au-Cu binary nanoparticles by manipulating the direct Pt deposition rate versus galvanic replacement rate. In a typical synthesis, the $AuCu_3$ alloy transformed into hollow nanostructures through galvanic replacement by addition of H_2PtCl_6 solution in polyol and a drastically different architectural transformation process was observed on the final Au-Cu-Pt trimetallic product in different solvents. We used transmission electron microscopy (TEM), energy-dispersive spectroscopy (EDS), powder X-ray diffraction (PXRD), inductively coupled plasma mass spectrometry (ICP-MS), and X-ray photoelectron spectroscopy (XPS) to characterize the structure, composition, and morphology of the final products. As shown in Figure 7.1A, spongy-like nanoparticles with ultrathin ligament (denoted as S1) were obtained when we carried out the galvanic replacement reaction in EG at 130 ℃ for 30 min. While when DEG was used as solvent, $AuCu_3$ alloy nanoparticles transformed into nanospongies with small Pt dots attaching on the ligament surface (Figure 7.1B) due to a synergistic effect between galvanic replacement reaction and Pt deposition as a consequence of a mild reducing capability of DEG under the identical reaction conditions (denoted as S2). Interestingly, when the reaction solvent was switched to TEG, which was found to significantly promote both the hollowing and deposition processes during the reaction, the hollow nanoshell structures with clear size

expansion were formed (denoted as S3) and the TEM image clearly shows that the nanoshells were essentially composed of small grainy Pt nanocrystals and were thus highly porous in nature (Figure 7.1C). The drastic differences in structural transformation in various polyol solvent probably result from the different reducing abilities that have great effect on the Pt deposition rate under the same reaction temperature. Lower deposition rates accompanied with GRR led to spongy structures with uniform and smooth nanoligament in EG, while the faster rates resulted in more grainy and rougher nanoshells, probably as a result of increased direct Pt deposition relative to galvanic replacement and corresponding corrosion of the template in TEG. PXRD patterns displayed in Figure 7.1D further verify the structures of hollow nanoparticles. At the same time, the compositions of the hollow nanoparticles qualitatively detected by EDX demonstrated the highest Pt content in nanoshells (S3) while the lowest amount in spongy nanoparticles formed in EG (S1), which provide further evidence to support the significantly accelerated Pt deposition rate by TEG. PXRD results further confirms the spongy nanoparticles composed of nanoligaments which possess a cable structure with Au-Cu cores and Au-Pt alloy shells, the significant broadening the diffraction peaks indicate their thin ligaments as well as small pore sizes (Figure 7.1D). While for the hollow particles S2 and S3 obtained in DEG and TEG, besides Au-Cu alloy features, strong and broadening diffractions were detected, which could be contributed by Au-Pt alloy phase and pure Pt as well (Figure 7.1D).

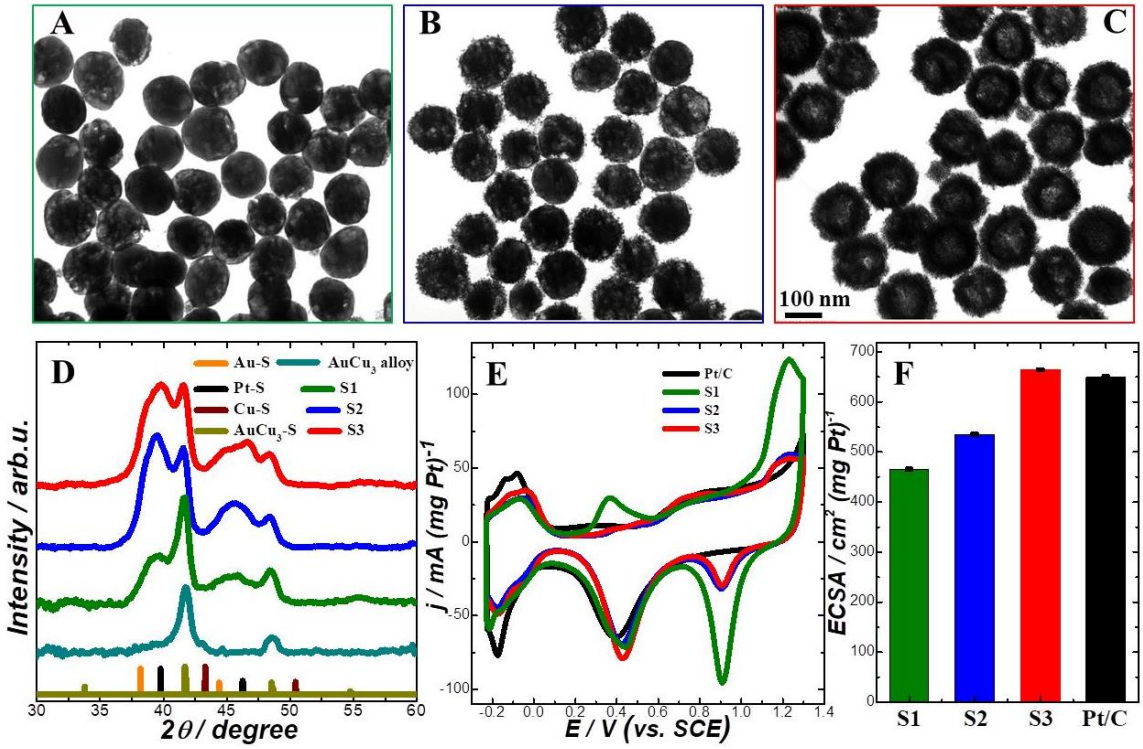

Figure 7.1. **Structure and composition of Au-Cu-Pt trimetallic hollow NPs.** TEM images of Au-Cu-Pt trimetallic spongy NPs synthesized through galvanic replacement of Au-Cu alloy NPs with H_2PtCl_6 in various polyol solutions at 130 ^{0}C. (A) EG, S1; (B) DEG, S2; (C) TEG, S3. (D) XRD patterns of Au-Cu-Pt trimetallic spongy NPs synthesized through galvanic replacement of Au-Cu alloy NPs with H_2PtCl_6 in polyol solutions. The standard XRD patterns of bulk Au, Cu, Pt, and $AuCu_3$ alloy are also included. (E) CV curves of various spongy NPs in 0.5 M H_2SO_4 at a potential sweep rate of 50 mV s^{-1}. The currents were normalized against the Pt mass loaded on each electrode. (F) ECSA of various spongy NPs estimated based on the hydrogen desorption peak area.

We also used cyclic voltammetry (CV) as an electrochemical characterization tool to analyze surface atomic structures of various hollow nanoparticle and estimate the specific active surface areas (Figure 7.1E). The peaks at 0.3-0.6 V (*vs.* SCE) and 0.8-1.3 V (*vs.* SCE) originate from oxidation of surface Pt and Au atoms and the corresponding reductions of the oxide layers formed during anodic scan, respectively, indicating the exposure of Pt and Au on the surfaces. The peaks appearing in the range from -0.23 to 0.15 V (*vs.* SCE) are attributed to hydrogen underpotential formation-stripping and we chose the hydrogen desorption peaks to estimate the electrochemically active surface area

(ECSA) of the various hollow nanoparticles by assuming the charge density passed during the hydrogen adsorption was 210 μC/cm^2 for a flat Pt surface.[23] The hollow nanoparticles show comparable ECSAs with commercial Pt/C, which are calculated to be 465.3, 535.0, 664.9, and 649.7 cm^2/mg for S1, S2, S3, and Pt/C, respectively (Figure 7.1F).

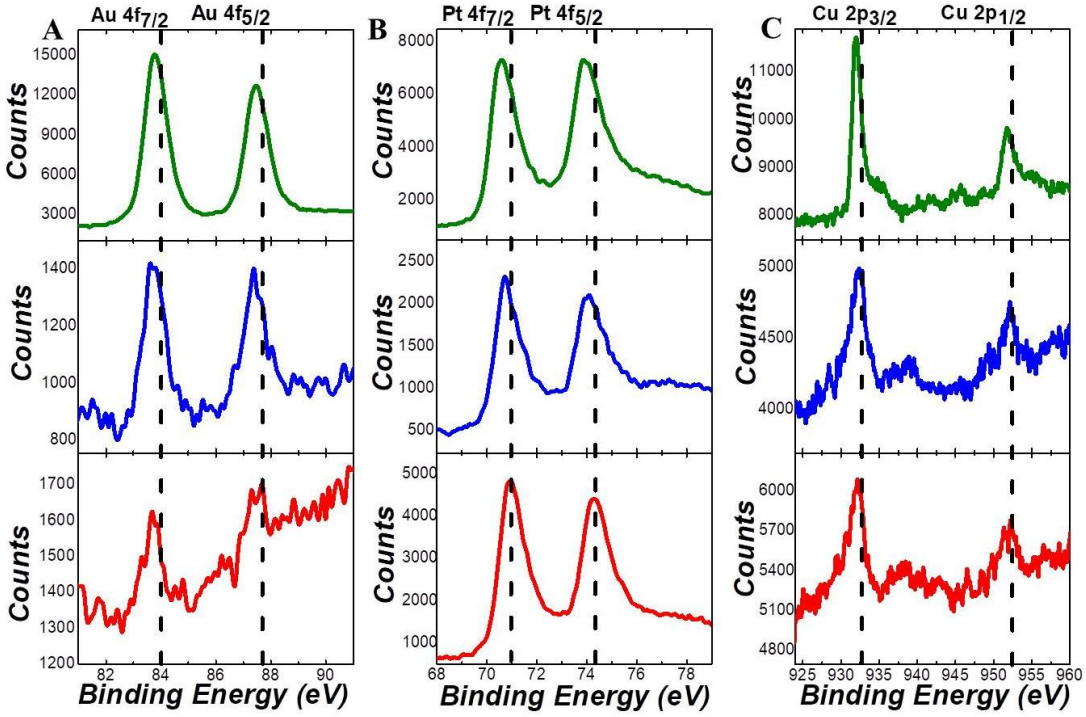

Figure 7.2. XPS of (A) Au 4f, (B) Pt 4f, and (C) Cu2p regions of S1 (green curves), S2 (blue curves), and S3 (red curves). The vertical dash lines indicate the peak positions of standard bulk Au, Pt, and Cu.

We also employed XPS to characterize the surface structures and near surface compositions of various hollow nanoparticles (Figure 7.2). The of Pt 4f, Au 4f and Cu 2p regions gradually shifted to lower binding energies for the spongy nanoparticles obtained in EG, as compared with the corresponding pure bulk metals, which probably resulted from the formation of the Au-Pt alloy [24] that modified the charge transfer between Au and Pt,[25,26] while slightly downshifted Pt 4f of Pt decorated spongy nanoparticles S2 and

hollow nanoshells S3 could be ascribed to the formation of pure metallic Pt on the particle surface and the binding energies shift was mainly caused by lattice strain existing on the Pt nanoislands. At the same time, the near surface compositions quantified by XPS are dramatically different with the bulk compositions detected by EDS. The higher surface Pt/Au ratios calculated by XPS of various hollow nanoparticles further verified their Pt-rich surfaces. The existence of Au-Pt or Pt overlayers apparently contributed to the stabilization of the hollow structure due to a much slower surface diffusion rate of Pt relative with Au.[27]

We quantitatively compared the electrocatalytic activities of the spongy nanoparticles, Pt-decorated nanospongies, and hollow nanoshells using the room temperature electrocatalytic formic acid oxidation reaction (FOR) in an acidic aqueous environment as a model reaction. As shown in Figure 7.3A, the naked glassy carbon electrode (GCE) exhibited catalytically inert toward FOR, while the obtained hollow nanostructures showed superior electrocatalytic activities and even more active relative with the commercial Pt/C catalysts. A second oxidation peak emerged during the cathodic sweeps originate from the further oxidation of surface-adsorbed carbonaceous species that were not completely oxidized during the previous anodic scans. The spongy nanoparticles with Au-Pt alloy skin in particular demonstrated the higher mass activity and specific activity than Pt-decorated nanospongies and nanoshells (Figure 7.3B). To assess the electrocatalytic stability of the obtained hollow nanoparticles, chronoamperometry (CA) measurements were carried out at the oxidation peak potential (0.6 V, vs SCE). As shown in Figure 7.3C, the oxidation currents underwent a fast decay in the first few seconds followed by a much slower decay over minutes until reaching a steady-state plateau. The

fast decay was ascribed to the development of the electrochemical double-layer after a potential bias was applied on the samples until reaching the equilibrium after a few seconds. The slower current decay was probably due to the accumulation of incomplete oxidation products on the particle surfaces which greatly impacted the accessible reactants during the reactions.

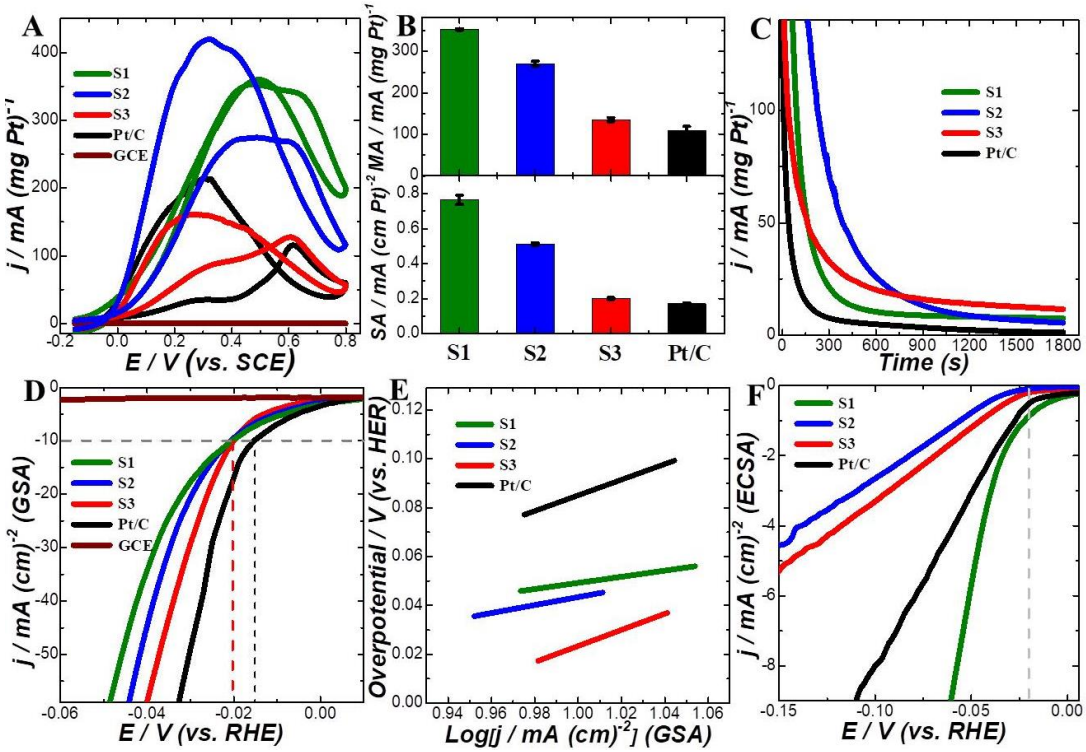

Figure 7.3. **Electrocatalytic performance of trimetallic hollow NPs.** (A) CV curves of formic acid oxidation on naked glassy carbon electrode (GCE), commercial Pt/C, and various porous NPs in 1.0 M formic acid and 0.5 M H_2SO_4 at a potential sweep rate of 50 mV s^{-1}. The samples labeled as S1, S2, and S3 correspond to the samples obtained through galvanic replacement of $AuCu_3$ alloy NPs by H_2PtCl_6 in EG, DEG, and TEG at 130 ^{0}C for 30 min, respectively. (B) MAs and SAs of Pt/C and various porous NPs. (C) CA curves collected on Pt/C and various porous NPs for formic acid oxidation reaction at 0.6 V (vs SCE). All CA measurements were carried out in solutions containing in 1.0 M formic acid and 0.5 M H_2SO_4 deoxygenated with N_2. (D) Polarization curves of Pt/C and various porous NPs toward hydrogen evolution reaction (HER) with current densities normalized to GSA, and (E) the corresponding Tafel plots. (F) Polarization curves of Pt/C and various porous NPs with current densities normalized to ECSA.

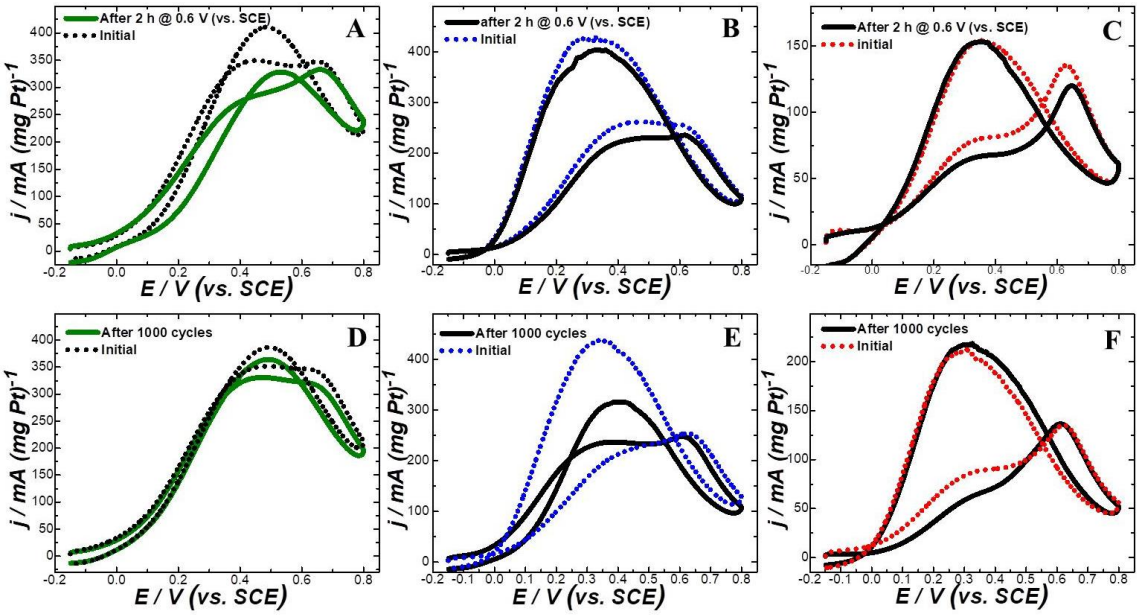

Figure 7.4. CV curves of formic acid oxidation on various porous NPs in 1.0 M formic acid and 0.5 M H_2SO_4 at a potential sweep rate of 50 mV s^{-1} after CA measurements and multiple cycles (S1, A and D; S2, B and E; S3, C and F).

We also investigate the hydrogen evolution reaction (HER) performance of various hollow nanoparticles with a three-electrode setup in 0.5 M H_2SO_4. Figure 7.3D and 7.3E shows HER polarization curves normalized against geometric surface area of the glassy carbon electrode (GSA) and corresponding Tafel slopes of the as-prepared samples and the commercial Pt/C catalysts as well. The hollow nanoparticles demonstrate comparable overpotentials (~20 mV versus RHE) to generate a current density of 10 mA/cm^2 with that of commercial Pt/C catalyst (15 mV versus RHE). The corresponding Tafel slopes are 126, 320, 330, and 163 mV/dec for samples S1, S2, S3, and Pt/C catalyst respectively. The lowest Tafel slope of spongy nanoparticles S1 indicated its best HER performance compared with other samples and commercial Pt/C catalyst. Figure 7.3F shows the polarization curves of different samples with current densities normalized to ECSA. The HER current density of spongy nanoparticles at an overpotential of 19 mV is 0.99 mA

cm^{-2}, which is higher than that of Pt/C commercial catalyst (0.49 mA cm^{-2}).

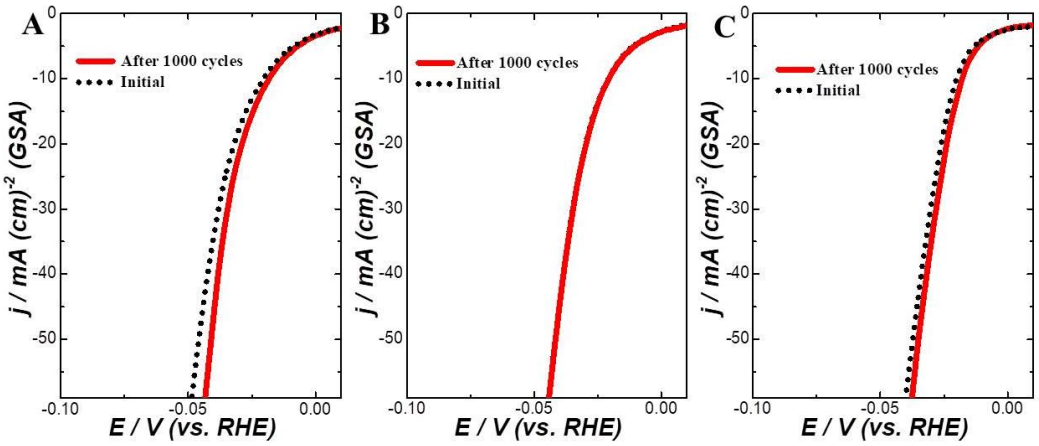

Figure 7.5. Polarization curves of (A) spongy NPs, (B) Pt-decorated nanospongies, and (C) nanoshells toward HER with current densities normalized to GSA before and after multiple CV cycles.

The catalytic performances of the various samples for oxidation of formic acid were also evaluated after CA measurements and multiple cycles in acidic electrolyte, as shown in Figure 7.4. No obvious activity degenerations were detected, indicating the robust properties of various hollow structures during reactions. Moreover, we also investigated their catalytic activities for HER after multiple cycles. All the prepared hollow structure nanoparticles exhibit no obvious loss of activity after 1000 CV sweeps between 50 mV to -200 mV vs RHE at a scan rate of 100 mV s^{-1}. Interestingly, the overpotential of various hollow nanostructures even slightly decreased to generate a current density of 10 mA cm^{-2} after 1000 cycles relative with the corresponding initial overpotentials, suggesting their high stability under acidic conditions (Figure 7.5). In addition, the morphology and structure of the prepared hollow nanoparticles are well-retained after cycling for 1000 cycles.

7.4 Conclusion

In this work, we demonstrate that architecture significantly hollow nanoparticles including spongy-like nanoparticles, Pt-decorated nanospongies, and nanoshells particles could be controllably fabricated by maneuvering the relative reaction rate between the galvanic replacement and the reduction reaction in different polyols that served as both reaction solvent and reducing agent under the same conditions. The catalytic performances of various Pt-based hollow nanostructures were evaluated by choosing electrochemical oxidation of formic acid and hydrogen evolution in acidic environments as model reactions. It is found that the spongy-like nanoparticles with ultrathin nanligaments comprising Au-Cu alloy cores and Au-Pt shells exhibit superior catalytic activities compared with commercial Pt/C catalyst.

7.5 References

(1) Sun, Y.; Xia, Y., *Science* **2002**, 298, 2176.

(2) Gonz áez, E.; Arbiol, J.; Puntes, V. F., *Science* **2011**, 334, 1377.

(3) Skrabalak, S. E.; Chen, J.; Sun, Y.; Lu, X.; Au, L.; Cobley, C. M.; Xia, Y., *Accounts Chem Res* **2008**, 41, 1587.

(4) Skrabalak, S. E.; Au, L.; Li, X.; Xia, Y., *Nature Protocols* **2007**, 2, 2182.

(5) Xia, Y.; Li, W.; Cobley, C. M.; Chen, J.; Xia, X.; Zhang, Q.; Yang, M.; Cho, E. C.; Brown, P. K., *Accounts Chem Res* **2011**, 44, 914.

(6) Chen, J.; McLellan, J. M.; Siekkinen, A.; Xiong, Y.; Li, Z.-Y.; Xia, Y., *J Am Chem Soc* **2006**, 128, 14776.

(7) Sun, Y.; Wiley, B.; Li, Z.-Y.; Xia, Y., *J Am Chem Soc* **2004**, 126, 9399.

(8) Sun, Y.; Xia, Y., *J Am Chem Soc* **2004**, 126, 3892.

(9) Khalavka, Y.; Becker, J.; Sönnichsen, C., *J Am Chem Soc* **2009**, 131, 1871.

(10) Cho, E. C.; Camargo, P. H. C.; Xia, Y., *Adv Mater* **2010**, 22, 744.

(11) Yang, Y.; Zhang, Q.; Fu, Z.-W.; Qin, D., *ACS Applied Materials & Interfaces* **2014**, 6, 3750.

(12) McEachran, M.; Keogh, D.; Pietrobon, B.; Cathcart, N.; Gourevich, I.; Coombs, N.; Kitaev, V., *J Am Chem Soc* **2011**, 133, 8066.

(13) Hong, X.; Wang, D.; Cai, S.; Rong, H.; Li, Y., *J Am Chem Soc* **2012**, 134, 18165.

(14) Chen, J.; Wiley, B.; Li, Z. Y.; Campbell, D.; Saeki, F.; Cang, H.; Au, L.; Lee, J.; Li, X.; Xia, Y., *Adv Mater* **2005**, 17, 2255.

(15) Yavuz, M. S.; Cheng, Y.; Chen, J.; Cobley, C. M.; Zhang, Q.; Rycenga, M.; Xie, J.; Kim, C.; Schwartz, A. G.; Wang, L. V.; Xia, Y., *Nature materials* **2009**, 8, 935.

(16) Chen, J.; Wiley, B.; McLellan, J.; Xiong, Y.; Li, Z.-Y.; Xia, Y., *Nano Lett* **2005**, 5, 2058.

(17) Mahmoud, M. A.; El-Sayed, M. A., *Langmuir* **2012**, 28, 4051.

(18) Zhang, W.; Yang, J.; Lu, X., *ACS Nano* **2012**, 6, 7397.

(19) Chen, C.; Kang, Y.; Huo, Z.; Zhu, Z.; Huang, W.; Xin, H. L.; Snyder, J. D.; Li, D.; Herron, J. A.; Mavrikakis, M.; Chi, M.; More, K. L.; Li, Y.; Markovic, N. M.; Somorjai, G. A.; Yang, P.; Stamenkovic, V. R., *Science* **2014**, 343, 1339.

(20) Mahmoud, M. A.; Saira, F.; El-Sayed, M. A., *Nano Lett* **2010**, 10, 3764.

(21) Zhang, H.; Jin, M.; Liu, H.; Wang, J.; Kim, M. J.; Yang, D.; Xie, Z.; Liu, J.; Xia, Y., *ACS Nano* **2011**, 5, 8212.

(22) Gilroy, K. D.; Farzinpour, P.; Sundar, A.; Hughes, R. A.; Neretina, S., *Chem Mater* **2014**, 26, 3340.

(23) Lee, E. P.; Peng, Z.; Cate, D. M.; Yang, H.; Campbell, C. T.; Xia, Y., *J Am Chem Soc* **2007**, 129, 10634.

(24) Kim, M.-J.; Na, H.-J.; Lee, K. C.; Yoo, E. A.; Lee, M., *J Mater Chem* **2003**, 13, 1789.

(25) Ge, X.; Yan, X.; Wang, R.; Tian, F.; Ding, Y., *J Phys Chem C* **2009**, 113, 7379.

(26) Xu, C.; Wang, R.; Chen, M.; Zhang, Y.; Ding, Y., *Phys Chem Chem Phys* **2010**, 12, 239.

(27) Seebauer, E. G.; Allen, C. E., *Prog Surf Sci* **1995**, 49, 265.

CHAPTER 8

OVERCOMING THE INTERFACIAL LATTICE MISMATCH: GEOMETRY CONTROL OF GOLD-NICKEL BIMETALLIC HETERONANOSTRUCTURES

8.1 Introduction

Heteroepitaxial overgrowth of a secondary metal on a morphology-controlled metallic nanocrystal seed provides a unique pathway to fine-tailor the geometries and thereby fine-tune the properties of bimetallic heteronanostructures.[1-6] The degree of lattice mismatch between the two constituent metals has been identified as a key factor dictating the structural evolution of a large library of geometrically distinct bimetallic heteronanostructures during seed-mediated heteroepitaxial overgrowth.[7-21] For metals possessing similar crystalline structures, interfacial heteroepitaxial growth requires moderate lattice mismatch typically within 5%,[1,7,8,22] whereas for metal pairs with larger lattice mismatches or dissimilar crystalline structures, discrete islands or polycrystalline dendritic shells normally form on the seed surfaces due to lack of epitaxial relationships between the two constituent metals.[8,22-27] Although such lattice mismatch limitation sets up a stringent criterion for interfacial heteroepitaxy, recent advances in seed-mediated colloidal syntheses have further expanded the heteroepitaxial growth to bimetallic nanocrystal systems with lattice mismatches beyond 5%, such as Au-Rh (7.0%),[14] Pd-Cu (7.1%),[28] Au-Cu (11.4%),[29] and Au-Ni (13.6%).[30-32] Au-Ni bimetallic nanocrystals constitute a particularly interesting model system for investigating nanoscale heteroepitaxy in lattice-mismatched systems. While colloidal Au-Ni bimetallic nanoparticles have been synthesized through seed-mediated nonepitaxial growth[33-35] or one-pot coreduction reactions,[36-38] expitaxial growth of Ni seeded by single-crystalline polyhedral Au nanocrystals enclosed by well-defined crystallographic facets enables structural control of bimetallic nanocrystals at a remarkably higher level of precision and versatility.[30,31]

However, it still remains challenging to epitaxially grow conformal Ni shells with fine-controlled thicknesses on multitwinned (quasi-) spherical Au cores whose surfaces are highly curved and enclosed by a myriad of different facets. In addition to the naturally adopted face-centered cubic (fcc) structures, metallic Ni may also crystallize into the hexagonal close-packed (hcp) phase under some specific conditions.[39-41] Previously reported Au@Ni core-shell nanoparticles synthesized by seed-mediated expitaxial growth, nevertheless, are exclusively composed of fcc Au cores and fcc Ni shells.[30-32] It has been recently reported that some thermodynamically unexpected metastable polymorphic crystalline phases may form *via* seed-mediated heteroepitaxial growth at specifically tailored interfaces.[42-45] For example, Ru, which typically exists in hcp phase, adopts an unconventional fcc structure when expitaxially deposited on fcc Pd nanocrystal seeds.[44,45] Whether hcp Ni can be epitaxially deposited onto a fcc Au seed to form conformal core-shell nanostructures retaining certain types of structural correlations between the core and the shell is still a fundamentally intriguing open question. A (quasi-) spherical nanocrystal with a conformal but lattice-mismatched core-shell geometry constitutes a metastable heterostructure. How to break the symmetry of a core-shell nanoparticle to form thermodynamically more stable heteronanostructures, such as asymmetric heterodimers, remains largely unexplored.

Here we demonstrate that both fcc and hcp Ni can be epitaxially grown on multitwinned quasi-spherical Au nanocrystals to form conformal core-shell nanocrystals that faithfully inherit the key crystalline characteristics of their parental seeds. In addition, we have synthesized geometrically asymmetric Au@hcp Ni heteronanostructures with tunable Ni domain sizes under thermodynamically more favored nanocrystal growth

conditions, without forming alloy structures at the Au-Ni interfaces. Furthermore, we show that the Ni domains in the heteronanostructures exhibit markedly enhanced stability against etching compared to the monometallic Ni nanocrystals, primarily due to the synergy between the Ni and Au domains.

8.2 Experimental Section

Chemicals and Materials Chloroauric acid ($HAuCl_4 \cdot 4H_2O$), polyvinylpyrrolidone (PVP, average MW 58 000), ethylene glycol (EG), and tetraethylene glycol (TEG) were purchased from Alfa Aesar. Nickel nitrate hexahydrate ($Ni(NO_3)_2 \cdot 6H_2O$), nickel chloride ($NiCl_2$), trizma base (TB), sulfuric acid (H_2SO_4, 98%), and nafion perfluorinated resin solution (5 wt%) were purchased from Sigma-Aldrich. Sodium hydroxide (NaOH) and trisodium citrate dihydrate ($Na_3C_6H_5O_7 \cdot 2H_2O$) were purchased from Fisher Scientific. Ethanol was purchased from Decon Labs Inc. All reagents were used as received without further purification. Ultrapure water (18.2 MΩ resistivity, Milli-Q, Millipore) was used for all the experiments.

Synthesis of Au Nanoparticles (NPs) Quasi-spherical Au NPs with an average diameter of 48.2 nm were synthesized using a previously reported seed-mediated growth method.[46] Colloidal Au seeds with an average size of 17 nm were first synthesized by reducing chloroauric acid with citrate. Briefly, 0.5 mL of 25 mM $HAuCl_4$ aqueous solution were added into 48 mL of boiling water under magnetic stir, followed by further reflux for 10 minutes. Subsequently, 1.5 mL of 1 wt % trisodium citrate aqueous solution was rapidly injected into the refluxing reactant solution. The reaction solution was further refluxed for 30 minutes under magnetic stir, and then cooled to room temperature for further use.

To synthesize ~ 48 nm quasi-spherical Au NPs, 8 mL of 0.1 M TB aqueous solution were added into 185 mL of boiling water. After being gently stirred for 10 minutes, 4 mL of the as-synthesized colloidal Au seeds and 3 mL of 25 mM $HAuCl_4$ solution were successively added to the TB solution, followed by further reflux for 30 minutes under magnetic stir. The total volume of the final reaction solution was 200 mL. The Au quasi-spherical NPs were subsequently separated from the reaction solution by centrifugation (3500 rpm, 10 min) and redispersion in 5 mL water for further use.

Synthesis of Au@Ni Bimetallic Heteronanostructures Au@Ni bimetallic heteronanostructures were synthesized through seed-mediated growth of face-centered cubic (fcc) or hexagonal close-packed (hcp) Ni on Au quasi-spherical NPs in polyol solvents. To synthesize the Au@fcc Ni core-shell nanoparticles (CSNPs), 150 μL of colloidal Au NPs (average diameter of 48.2 nm) were added into 20 mL EG containing 0.05 g PVP, 0.2 mM $Ni(NO_3)_2$, and 14 mM NaOH. The reaction mixtures were kept at 180 ^oC for 1 hour, and then cooled to room temperature. The resulting particles were washed with ethanol 5 times through centrifugation-redispersion cycles and finally redispersed in ethanol for further characterizations. By varying the concentration of $Ni(NO_3)_2$ while keeping the molar ratio of $Ni(NO_3)_2$:NaOH fixed at 1:70, the thickness of the fcc Ni shell on Au NP cores could be tuned.

Au@hcp Ni CSNPs were synthesized at 300 ^oC in TEG. Briefly, 150 μL of the quasi-spherical Au NPs were added into in 20 mL TEG containing 0.05 g PVP and 0.2 mM $Ni(NO_3)_2$. The reaction mixtures were kept at 300 ^oC for 1 hour, and then cooled to room temperature. The resulting particles were washed with ethanol 5 times through centrifugation-redispersion cycles and finally redispersed in ethanol for further

characterizations. By varying the concentration of $Ni(NO_3)_2$ while keeping the other synthetic parameters unchanged, the thickness of the hcp Ni shell on Au NP cores could be tuned.

Au@hcp Ni heterodimer nanoparticles (HDNPs) were synthesized by heating 20 mL TEG containing 150 μL of the quasi-spherical Au NPs, 0.05 g PVP, and 0.2 mM $NiCl_2$ at 300 ^oC for 1 hour. The obtained particles were washed with ethanol 5 times through centrifugation-redispersion cycles, and finally redispersed in ethanol for further characterizations. By varying the concentration of $NiCl_2$ while keeping the other synthetic parameters unchanged, the sizes of the Ni domains in the resulting HDNPs could be tuned.

Au@hcp Ni multi-branched nanoparticles (MBNPs) were synthesized by heating 20 mL TEG containing 0.05 g PVP, 0.2 mM $NiCl_2$, and 1.4 mM NaOH under 300 ^oC for 1 hour. The obtained particles were washed with ethanol 5 times through centrifugation-redispersion cycles, and finally redispersed in ethanol for further characterizations.

Synthesis of Monometallic fcc and hcp Ni NPs Monometallic Ni NPs were synthesized by reducing $Ni(NO_3)_2$ in polyols following the procedures described above without Au seeds. Briefly, fcc Ni NPs were synthesized by heating 20 mL EG containing 0.05 g PVP, 0.5 mM $Ni(NO_3)_2$, and 35 mM NaOH at 180 ^oC for 1 hour. hcp Ni NPs were synthesized by heating 20 mL TEG containing 0.05 g PVP and 0.5 mM $Ni(NO_3)_2$ at 300 ^oC for 1 hour. The resulting particles were washed with ethanol 5 times through centrifugation-redispersion cycles, and finally redispersed in ethanol for further characterizations.

Etching of Au@Ni Bimetallic Heteronanostructures and Monometallic Ni NPs

The chemical etching of the Au@Ni bimetallic heteronanostructures and monometallic Ni NPs was carried out by exposing the NPs to 1.0 mM H_2SO_4 at room temperature under ambient pressure for certain time periods. The resulting particles were separated from the etchant by centrifugation and finally redispersed in ethanol.

Structural Characterizations The morphologies and structures of the NPs were characterized by transmission electron microscopy (TEM) using a Hitachi H-8000 transmission electron microscope operated at an accelerating voltage of 200 kV. All samples for TEM measurements were dispersed in ethanol and drop-dried on 300 mesh Formvar/carbon-coated-Cu grids (Electron Microscopy Science Inc.). Scanning electron microscopy (SEM) imaging and energy dispersive spectroscopy (EDS) measurements were performed on NPs supported on silicon wafers using a Zeiss Ultraplus thermal field emission scanning electron microscope. The NP sizes were analyzed on the basis of TEM images using Nano Measurer analysis software (Department of Chemistry, Fudan University, China). High-angle annular dark-field scanning transmission electron microscopy (HAADF-STEM) imaging of Au@Ni heteronanostructures was carried out using a JEOL 2100F 200 kV FEGSTEM/TEM microscope equipped with a CEOS CS corrector on the illumination system. The samples for HAADF-STEM measurements were dispersed in ethanol and drop-dried on 400 mesh Cu grids with ultrathin carbon support film (Electron Microscopy Science Inc.). Powder X-ray diffraction (PXRD) patterns were record on a SAXSLab Ganesha at the South Carolina SAXS Collaborative (Cu $K\alpha$ = 1.5406 Å). The optical extinction spectra were collected on colloidal NPs suspended in water at room temperature using a Beckman Coulter Du 640 spectrophotometer.

Electrochemical Measurements Electrochemical measurements were performed using a CHI 660E workstation (CH Instruments, Austin, Texas) at room temperature with a three-electrode system composed of a Pt wire as the auxiliary, a saturated calomel electrode (SCE) as the reference, and a glassy carbon electrode (GCE, 3 mm diameter) as the working electrode. Typically, the GCE was polished with 0.3 μm alumina slurry, followed by washing with water and ethanol before use. Colloidal suspensions containing 4 μg of fcc Ni NPs, hcp Ni NPs, Au@fcc Ni CSNPs, Au@hcp Ni CSNPs, Au@hcp Ni HDNPs, or Au@hcp Ni MBNPs were dropped and air-dried on the pretreated GCEs at room temperature, and then 2 μL of Nafion solution (0.2 wt %) was dropped to hold the NPs. The linear sweep voltammetry (LSV) of various NPs were measured in 1 mM H_2SO_4 electrolyte in the potential scan range from -0.4 V to 0.6 V (*vs.* SCE) at a sweep rate of 50 mV s^{-1}.

Cluster Expansion Calculations The Alloy Theoretic Automated Toolkit (ATAT) [2,3] software package was used to predict the zero-temperature phase diagram of the Ni-Au system. The ATAT code first invokes Density Functional Theory (DFT) code, in our case the Vienna Ab initio Simulation Package (VASP),[4] to determine the energy of carefully selected ordered alloy structures. These DFT-computed energies are then used to determine the interaction parameters of the cluster expansion of an Ising-like Hamiltonian, from which the energies of other ordered and random alloys are determined according to the following equation:

$$E(\sigma) = J_0 + \sum_i J_i S_i(\sigma) + \sum_{j<i} J_{ij} S_i(\sigma) S_j(\sigma) + \sum_{k<j<i} J_{ijk} S_i(\sigma) S_j(\sigma) S_k(\sigma) + \cdots,$$

where, σ is a configuration of the alloy, S is the Ising spin variable which takes on values of -1 or +1 depending on the site I occupied by an Ni or Au atom, J's are the effective

cluster interaction (ECI) energies. The cluster expansion approach predicts Au and Ni to be immiscible, which is consistent with the experimental phase diagram. The energies of the pure materials, Ni and Au shown here are those calculated from the cluster expansion; the deviation of these values from zero is thus a measure of the uncertainty in the results of the calculations (approximately 0.015 eV/atom).

8.3 Results and Discussions

The geometry-controlled syntheses of Au-Ni bimetallic heteronanostructures were accomplished through kinetically maneuvered, Au nanocrystal-seeded reduction of Ni precursors in polyols, which played a unique dual role as both the solvent and the reducing agent[47]. We followed a previously reported protocol[46] to synthesize the multitwinned Au nanocrystal seeds, which exhibited a highly uniform quasi-spherical morphology enclosed by highly curved surfaces with an average size of 48.2 $\pm$ 2.8 nm. The reaction temperature, the polyol solvent, the Ni precursor, and the surface capping agent, which was polyvinylpyrrolidone (PVP) in this case, were all found to be crucial synthetic parameters determining the geometries of the resulting Au-Ni heteronanostructures as well as the crystalline phases of the Ni domains.

As illustrated in Figure 8.1A, with $Ni(NO_3)_2$ serving as the Ni precursor, conformal Au@Ni core-shell nanoparticles (CSNPs) with fcc and hcp Ni shells can be selectively synthesized in NaOH-containing ethylene glycol (EG) at 180 ^{o}C and in tetraethylene glycol (TEG) at 300 ^{o}C, respectively. The powder X-ray diffraction (PXRD) patterns displayed in Figure 8.1B clearly showed that the as-synthesized Au-Ni bimetallic nanocrystals were composed of phase segregated fcc Au and fcc or hcp Ni without any detectable Au-Ni alloy phases, in line with the phase diagram of bulk Au-Ni and the

prediction by cluster expansion calculations.

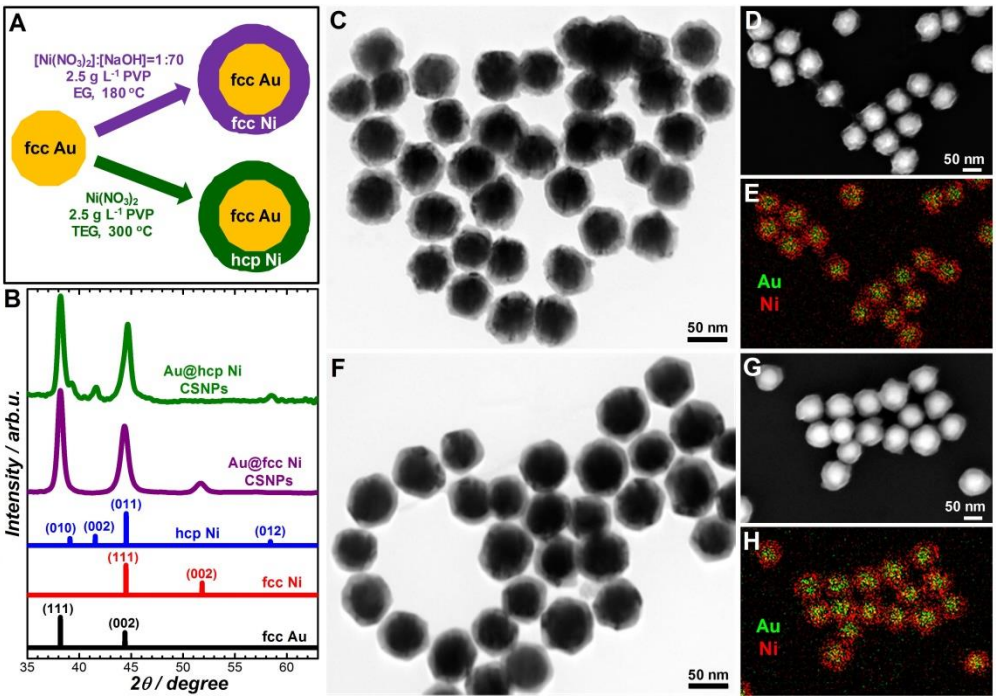

Figure 8.1. **Au@fcc Ni and Au@hcp Ni CSNPs.** (A) Schematic illustration of syntheses of Au@fcc Ni and Au@hcp Ni CSNPs in polyols. Au@fcc Ni CSNPs were synthesized in EG containing 0.2 mM $Ni(NO_3)_2$ and 2.5 g L^{-1} PVP and 14 mM NaOH at 180 ^oC for 1 h. Au@hcp Ni CSNPs were synthesized in TEG containing 0.2 mM $Ni(NO_3)_2$ and 2.5 g L^{-1} PVP at 300 ^oC for 1 h. (B) PXRD patterns of Au@fcc Ni CSNPs and Au@hcp Ni CSNPs. The standard diffraction patterns for fcc Au (JCPDS no. 04-0784), fcc Ni (JCPDS no. 04-0850), and hcp Ni (JCPDS no. 45-1027) are also shown for comparision. The PXRD patterns are offset for clarity. (C) TEM image, (D) SEM image, and (E) EDS elemental map of Au@fcc Ni CSNPs. (F) TEM image, (G) SEM image, and (H) EDS elemental map of Au@hcp Ni CSNPs.

The conformal core-shell heterostructures were well-resolved based on the clear contrast between the core and the shell of each nanoparticle in the transmission electron microscopy (TEM) images (Figures 8.1C and 8.1F). The bimetallic nanocrystals were further characterized by energy dispersive spectroscopy (EDS), which allowed us to quantify the Au/Ni compositional stoichiometries based on the Au Mα and Ni Lα lines. Supporting Correlated scanning electron microscopy (SEM) imaging and EDS elemental mapping further confirmed the Au core-Ni shell heterostructure in each nanoparticle

(Figures 8.1D, 8.1E, 8.1G, and 8.1H).

By varying the amount of $Ni(NO_3)_2$ precursor under otherwise identical reaction conditions, the thicknesses of both the fcc and hcp Ni shells could be fine-tuned in the range from ~ 3 nm up to ~ 16 nm while well-preserving the quasi-spherical conformal core-shell geometry. A series of Au@fcc Ni and Au@hcp Ni CSNPs with the same average core size but different average shell thicknesses were fully characterized by PXRD, TEM, and EDS. The Ni atomic percentages of the CSNPs quantified by EDS showed very good agreement with those calculated based on the average core and shell dimensions obtained from TEM. Synthesis of conformal core-shell nanoparticles with Ni shells thicker than ~ 16 nm, however, still remained challenging because further increasing the amount of $Ni(NO_3)_2$ precursor led to the growth of nanoscale surface protrusions, resulting in the formation of surface roughened Au@fcc Ni CSNPs and spiky multibranched Au@hcp Ni CSNPs, respectively. As schematically illustrated, the growth of Ni shells seeded by the quasi-sperhical Au nanocrystals can be best decribed as a nanoscale analog of the epitaxial thin film growth on a single crystal surface following the Stranski–Krastanov model, a hybrid layer-plus-island growth mechanism involving the transition from the layer-by-layer growth mode (Frank–van der Merwe growth) to island-based growth mode (Volmer–Weber growth) at a critical shell thickness.[48] The onset thickness for such growth mode transition varies significantly among different materials systems, depending on the materials compositions, the crystalline structures, the curvature of the interfaces, and the conditions under which the epitaxial growth occurs. For the Au@Ni CSNPs synthesized under the current conditions, the transition from the layer-by-layer to the island-based growth mode was observed at a critical Ni shell

thickness around 16 nm.

The crystalline phase of the Ni shells grown on the Au cores was essentially controlled by the reaction temperature. The formation of Au@fcc Ni CSNPs involved the seed-mediated reduction of $Ni(NO_3)_2$ by EG at 180 ^oC, a temperature close to the boiling point of EG (197^oC), at a NaOH/$Ni(NO_3)_2$ molar ratio of 70:1. The presence of NaOH provided an alkaline environment that kinetically boosted the the reduction of $Ni(NO_3)_2$ by EG, in line with previous observations reported by Tsuji and coworkers.[30] Without NaOH, the reduction of $Ni(NO_3)_2$ by EG at 180 ^oC was kinetically sluggish with no observable Ni shell growth even after 12 hours. The formation of hcp Ni shells required a further elevated reaction temperature above ~ 270 ^oC. Therefore, TEG, a polyol with a boiling point around 314 ^oC, was used instead of EG for the synthesis of Au@hcp Ni CSNPs. At 300 ^oC, the reduction of $Ni(NO_3)_2$ by TEG became kinetically much faster than at lower temperatures, resulting in rapid growth of hcp Ni shells on the Au cores even in the absence of NaOH. Adding NaOH into the reactant mixtures did not introduce any observable structural modifications to the resulting Au@hcp CSNPs. The Ni shells in the Au@fcc Ni CSNPs underwent a complete fcc-to-hcp phase transition upon thermal heating in TEG at 300 ^oC for 2 hours while the quasi-spherical conformal core-shell geometry was well-preserved with no observable interfacial alloying between Au and Ni. We also found that the polyol solvents exhibited sufficient reducing capabilities only when the reaction temperatures were close to their boiling points (within ~25 ^oC below the boiling points). When switching the solvent from EG to TEG, no Ni deposition was observed after keeping the reaction mixture containing $Ni(NO_3)_2$, PVP, and NaOH at 180 ^oC for 8 hours.

We used high-angle annular dark-field scanning transmission electron microscopy (HAADF-STEM) as a high-resolution imaging tool to resolve the the atomic-level structures at the Au-Ni interfaces of the CSNPs. Figure 8.2A shows the detailed structural information of an individual Au@fcc Ni CSNP with well-resolved lattice fringes of both Au (111) and Ni (111). Moiré patterns with parallel fringes were clearly observed at the regions where the Au core and Ni shell overlapped (Figure 8.2A-i), strongly indicating an epitaxial relationship between the fcc Au core and fcc Ni shell with lattice-mismatched (111) planes. The spacing of the Moiré fringes, *D*, was measured to be 1.52 nm, which was consistent with the *D* value of 1.49 nm calculated using the following equation

$$D = \frac{d_{Au(111)} \times d_{Ni(111)}}{|d_{Au(111)} - d_{Ni(111)}|},$$

where $d_{Au(111)}$ and $d_{Ni(111)}$ were the lattice spacings of Au (111) and Ni (111), respectively ($d_{Au(111)}$ = 0.2355 nm; $d_{Ni(111)}$ = 0.2034 nm). The fast Fourier transform (FFT) patterns further confirmed the epitaxial relationship between the core and the shell with crystalline orientations aligned along the same zone axis. Figure 8.2B shows the HAADF-STEM images and FFT patterns of several regions of a Au@hcp Ni CSNP. Interestingly, the (001) plane of fcc Au core was observed to be aligned with the (011) plane of hcp Ni most likely due to the small mismatch between the lattice spacings of Ni (011) and Au (002) ($d_{Au(002)}$ = 0.20390 nm; $d_{Ni(011)}$ = 0.20334 nm). Such unconventional orientational arrangement of hcp Ni shell with respect to the fcc Au core reveals that even for core and shell materials with different crystalline phases, it is still possible to establish a rigorous structural correlation between the core and the shell through interfacial heteroepitaxial growth by appropriately stacking crystalline planes with different Miller indices.

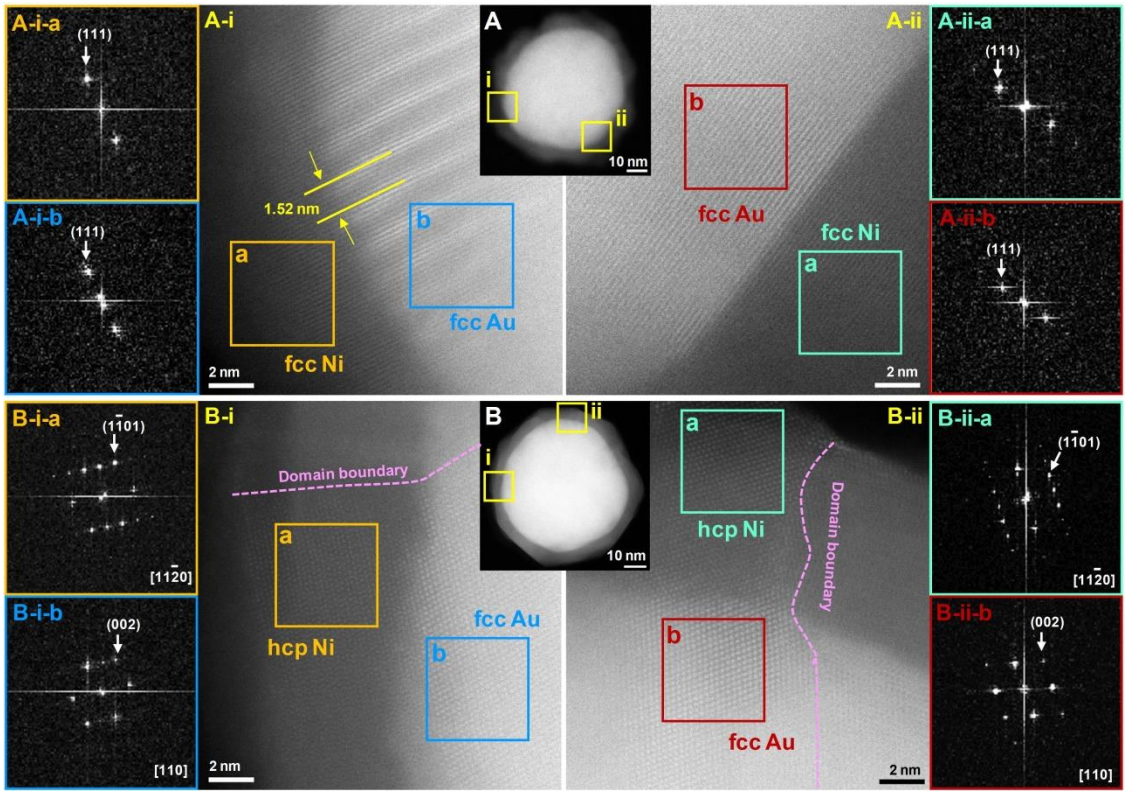

Figure 8.2. **Atomic-level structures of Au@fcc Ni and Au@hcp Ni CSNPs.** (A) HAADF-STEM image of an individual Au@fcc Ni CSNP. (A-x, x = i, ii) High-resolution HAADF-STEM images showing the atomic-level structures of regions i and ii in panel A. (A-x-a and A-x-b) FFT patterns of the regions labeled as a and b in panels A-x. (B) HAADF-STEM image of an individual Au@hcp Ni CSNP. (B-x, x = i, ii) High-resolution HAADF-STEM images showing the atomic-level structures of regions i and ii in panel B. (B-x-a and B-x-b) FFT patterns of the regions labeled as a and b in panels B-x.

Besides the reaction temperature and the addition of NaOH, the kinetics of the seed-mediated growth of Ni on Au could be further maneuvered by changing the Ni precursors. The reduction of Ni by polyol became significantly slower when switching the Ni precursor from $Ni(NO_3)_2$ to $NiCl_2$,[49] allowing the nanocrystals to evolve into thermodynamically more stable bimetallic nanostructures, such as asymmetric heterodimer nanoparticles (HDNPs). When using $NiCl_2$ as the Ni precursor and EG as the solvent, no Ni reduction was observed after refluxing the reaction mixture in the presence of NaOH at the boiling point of EG even for 8 hours. In TEG, Ni reduction became

kinetically observable only when the reaction temperature was higher than ~ 250 ^{o}C.

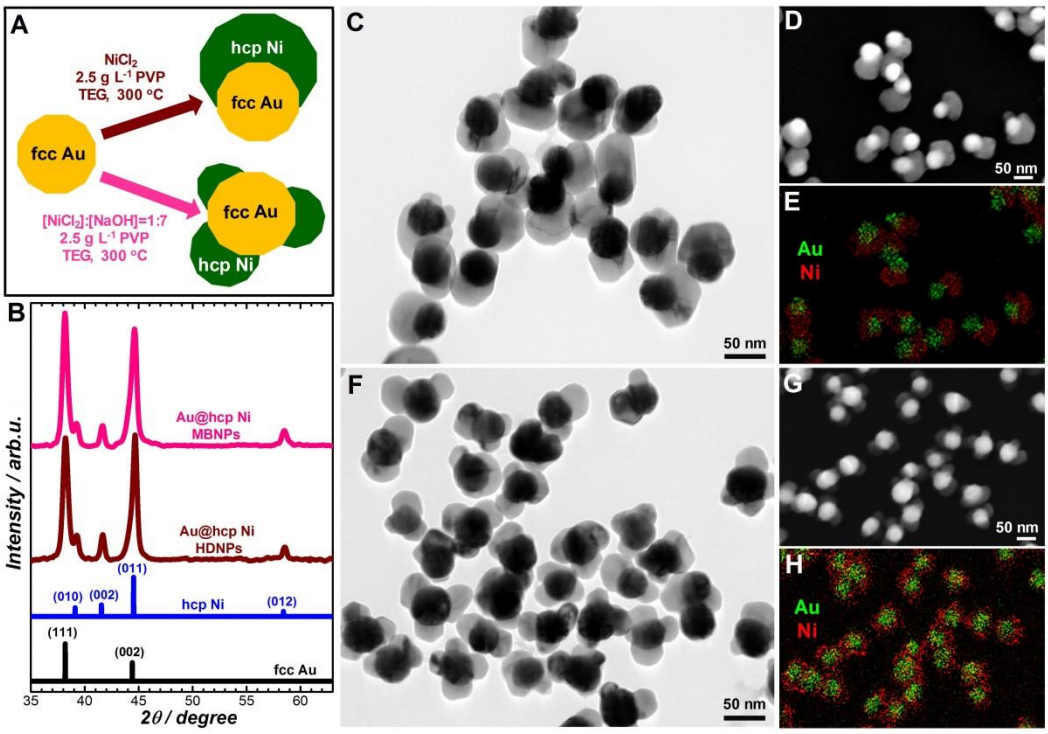

Figure 8.3. **Au@hcp Ni HDNPs and MBNPs.** (A) Schematic illustration of syntheses of Au@hcp Ni HDNPs and Au@hcp Ni MBNPs. Au@hcp Ni HDNPs and Au@hcp Ni MBNPs were synthesized in TEG containing 0.2 mM $NiCl_2$ and 2.5 g L^{-1} PVP without and with 1.4 mM NaOH, respectively, at 300 ^{o}C for 1 h. (B) PXRD patterns of Au@hcp Ni HDNPs and Au@hcp Ni MBNPs. The standard diffraction patterns for fcc Au and hcp Ni are also included. The PXRD patterns are offset for clarity. (C) TEM image, (D) SEM image, and (E) EDS elemental map of Au@hcp Ni HDNPs. (F) TEM image, (G) SEM image, and (H) EDS elemental map of Au@hcp Ni MBNPs.

As schematically illustrated in Figure 8.3A, using $NiCl_2$ as Ni precursor and TEG as the solvent at a reaction temperature of 300 ^{o}C, the seed-mediated growth resulted in the formation of Au@Ni HDNPs in the absence of NaOH, whereas Au@Ni multibranched nanoparticles (MBNPs) with multiple Ni domains attached to each Au core were obtained in the presence of appropriate amount of NaOH (NaOH/$NiCl_2$ molar ratio of 7:1). PXRD results showed that the Ni domains in both the HDNPs and MBNPs were composed of hcp Ni (Figure 8.3B). The bimetallic compositions were verified by EDS and the spatial

arrangements of the Au and Ni domains were thoroughly characterized by TEM, SEM, and EDS elemental mapping (Figures 8.3C-8.3H). By varying the amount of $NiCl_2$ while keeping the other synthetic conditions the same, we were able to tune the hcp Ni domain sizes of the HDNPs. For MBNPs, as increasing amount of Ni was deposited on the Au core, the Ni domains started to merge into a continuous, flower-like shell structure.

While fast nanocrystal growth allowed us to kinetically trap the conformal CSNPs, the asymmetric HDNPs represented a thermodynamically more stable structure formed under slow nanocrystal growth conditions. In this context, the MBNPs appeared to be a unique "metastable" geometry resulting from the intermediate nanocrystal growth kinetics that fell between the thermodynamically controlled and kinetically favored regimes. Increasing the $NaOH/NiCl_2$ molar ratio from 7:1 to 70:1 futher accelerated the Ni growth, resulting in Au@hcp Ni CSNPs with a conformal core-shell geometry essentially identical to the ones synthesized using $Ni(NO_3)_2$ as the Ni precursor. The nanocrystal growth kinetics could also be maneuvered through controlled surface passivation of the nanocrystals with PVP. While Au@hcp Ni HDNPs were synthesized in the presence of 2.5 g mL^{-1} PVP, increasing the PVP concentration to 25.0 g mL^{-1} effectively slowed down the nanocrystal growth as a consequence of surface passivation, allowing us to obtain Au@hcp Ni MBNPs with nearly 100 % yield.

We further investigated the stability of various Au@Ni bimetallic heterostructures against chemical and electrochemical etching. Starting with various Au@Ni bimetallic heteronanostructures with similar Ni atomic percentages, we systematically tracked the temporal evolution of the particle compositions using EDS during selective etching of Ni by H_2SO_4 at room temperature (Figure 8.4A). While the fcc Ni shells were completely

etched from the CSNPs upon exposure to 1 mM H_2SO_4 within 10 min, the etching of the hcp Ni shells occurred at a significantly slower rate, indicating that the hcp Ni shells in the CSNPs were more stable than their fcc counterparts. The etching rates of the hcp Ni domains in both HDNPs and MBNPs were found to be even slower than that of the hcp Ni shells in CSNPs, suggesting that HDNPs and MBNPs were structurally more stable than CSNPs. The relative stabilities of the Ni domains in various Au@Ni bimetallic heteronanostructures were also assessed by linear sweep voltammetry (LSV) measurements in 1 mM H_2SO_4 electrolyte (Figure 8.4B). The Au@hcp Ni CSNPs exhibited a higher critical potential for Ni dissolution than that of the Au@fcc Ni CSNPs, which was consistent with the chemical etching results. The LSV results also showed that the onset potentials for Ni dissolution from the bimetallic heteronanostructures were all positively shifted with respect to those of monometallic fcc and hcp Ni nanoparticles synthesized in polyols without Au seeds (see the PXRD patterns and TEM images of the monometallic Ni nanoparticles), strongly indicating that the synergy between the Ni and Au domains in the heteronanostructures significantly enhanced resistance of the Ni domains against oxidative etching, a phenomenon previously also observed in other bimetallic nanocrystal systems.[29,33,38] Figures 8.4C-8.4F show the TEM images of various Au@Ni bimetallic heteronanostructures after exposure to 1 mM H_2SO_4 for 30 min. For Au@fcc Ni CSNPs, the Ni shells were completely etched with only the Au cores remained intact, while the hcp Ni in the Au@hcp Ni heteronanostructures was only partially etched to a certain extent, evolving into nanoporous Ni shells or domains attached to Au cores. The relative stability of hcp Ni with respect to fcc Ni was further confirmed by etching experiments performed on monometallic fcc and hcp Ni

nanoparticles. Upon exposure to 1 mM H_2SO_4 for 30 minutes, the monometallic hcp Ni nanoparticles exhibited a partially etched hollow architecture, whereas the monometallic fcc Ni nanoparticles were completely dissolved in the etching solution within 10 minutes.

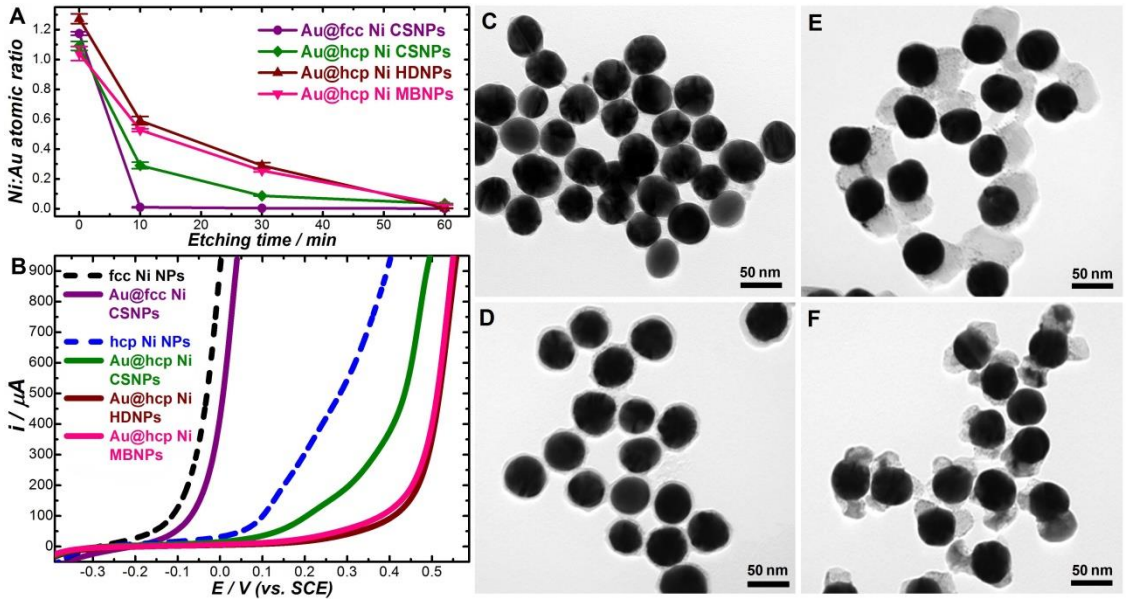

Figure 8.4. **Compositional and structural evolution of Au@Ni heteronanostructures upon selective etching of Ni.** (A) Temporal evolution of Ni/Au atomic ratio after exposure of various Au@Ni heteronanostructures to 1 mM H_2SO_4. The error bars represent the standard deviations of 3 samples. (B) LSV of Au@Ni heteronanostructures and monometallic fcc Ni and hcp Ni NPs in 1 mM H_2SO_4 electrolyte at a potential sweep rate of 50 mV s^{-1}. TEM images of the etched NPs obtained after exposure of (C) Au@fcc Ni CSNPs, (D) Au@hcp Ni CSNPs, (E) Au@hcp Ni HDNPs, and (F) Au@hcp Ni MBNPs to 1 mM H_2SO_4 for 30 min.

In summary, controlled epitaxial growth of fcc and hcp Ni on quasi-spherical fcc Au nanocrystals in polyol solvents enables precise geometry control of various Au-Ni bimetallic heteronanostructures that combine plasmonic Au and magentic Ni in one nanoscale entity. The plasmon resonances of Au nanoparticles are significantly damped upon surface deposition of Ni, causing spectral red-shift of the plasmon resonance frequency as well as weakening and broadening of the plasmon band in the optical extinction spectra, which is in line with previous observations.[7a,9b] The presence of Au,

on the hand, may also introduce interesting modifications to the magnetic properties of Ni. As previously reported, the magnetic characteristics of Au-Ni bimetallic heteronanostructures are sensitively dependent upon the sizes, geometric arrangement, and crystalline phases of the Au and Ni domains.[8a,9b]

8.4 Conclusion

The key findings in this work provide an insightful knowledge framework guiding the rational design of versatile synthetic approaches that extend the nanoscale interfacial heteroepitaxy from lattice-matched to lattice-mismatched bimetallic nanocrystal systems, paving the way toward the rational construction of multimetallic heteronanostructures with further enhanced architectural complexity and compositional diversity. Deliberate geometry control of multimetallic heteronanostructures allows us to further fine-tailor the synergy between multiple constituent domains in one nanoparticle, thereby greatly enhancing our capabilities to fine-tune the optical, electronic, magnetic, and catalytic properties of the multimetallic nanocrystals for specific applications.

8.5 References

(1) Gilroy, K. D.; Ruditskiy, A.; Peng, H. C.; Qin, D.; Xia, Y. N., *Chemical Reviews* **2016**, 116, 10414.

(2) Cortie, M. B.; McDonagh, A. M., *Chemical Reviews* **2011**, 111, 3713.

(3) Weiner, R. G.; Kunz, M. R.; Skrabalak, S. E., *Accounts Chem. Res.* **2015**, 48, 2688.

(4) Carbone, L.; Cozzoli, P. D., *Nano Today* **2010**, 5, 449.

(5) Xia, Y. N.; Xiong, Y. J.; Lim, B.; Skrabalak, S. E., *Angew. Chem.-Int. Edit.* **2009**, 48, 60.

(6) DeSantis, C. J.; Weiner, R. G.; Radmilovic, A.; Bower, M. M.; Skrabalak, S. E., *J.*

Phys. Chem. Lett. **2013**, 4, 3072.

(7) Habas, S. E.; Lee, H.; Radmilovic, V.; Somorjai, G. A.; Yang, P., *Nature Materials* **2007**, 6, 692.

(8) Fan, F. R.; Liu, D. Y.; Wu, Y. F.; Duan, S.; Xie, Z. X.; Jiang, Z. Y.; Tian, Z. Q., *Journal of the American Chemical Society* **2008**, 130, 6949.

(9) Lim, B.; Kobayashi, H.; Yu, T.; Wang, J. G.; Kim, M. J.; Li, Z. Y.; Rycenga, M.; Xia, Y. N., *Journal of the American Chemical Society* **2010**, 132, 2506.

(10) Lim, B.; Wang, J. G.; Camargo, P. H. C.; Jiang, M. J.; Kim, M. J.; Xia, Y. N., *Nano Letters* **2008**, 8, 2535.

(11) Wang, F.; Sun, L. D.; Feng, W.; Chen, H. J.; Yeung, M. H.; Wang, J. F.; Yan, C. H., *Small* **2010**, 6, 2566.

(12) Zhu, C.; Zeng, J.; Tao, J.; Johnson, M. C.; Schmidt-Krey, I.; Blubaugh, L.; Zhu, Y. M.; Gu, Z. Z.; Xia, Y. N., *Journal of the American Chemical Society* **2012**, 134, 15822.

(13) Lu, C. L.; Prasad, K. S.; Wu, H. L.; Ho, J. A. A.; Huang, M. H., *Journal of the American Chemical Society* **2010**, 132, 14546.

(14) Sneed, B. T.; Kuo, C. H.; Brodsky, C. N.; Tsung, C. K., *Journal of the American Chemical Society* **2012**, 134, 18417.

(15) Tsuji, M.; Ogino, M.; Matsunaga, M.; Miyamae, N.; Matsuo, R.; Nishio, M.; Alam, M. J., *Crystal Growth & Design* **2010**, 10, 4085.

(16) Yang, Y.; Liu, J. Y.; Fu, Z. W.; Qin, D., *Journal of the American Chemical Society* **2014**, 136, 8153.

(17) Yu, Y.; Zhang, Q. B.; Liu, B.; Lee, J. Y., *Journal of the American Chemical Society* **2010**, 132, 18258.

(18) Jing, H.; Zhang, Q. F.; Large, N.; Yu, C. M.; Blom, D. A.; Nordlander, P.; Wang, H., *Nano Letters* **2014**, 14, 3674.

(19) Wang, F.; Li, C. H.; Sun, L. D.; Wu, H. S.; Ming, T. A.; Wang, J. F.; Yu, J. C.; Yan, C. H., *Journal of the American Chemical Society* **2011**, 133, 1106.

(20) Gilroy, K. D.; Hughes, R. A.; Neretina, S., *Journal of the American Chemical Society* **2014**, 136, 15337.

(21) Yang, Y.; Wang, W. F.; Li, X. L.; Chen, W.; Fan, N. N.; Zou, C.; Chen, X.; Xu, X. J.; Zhang, L. J.; Huang, S. M., *Chemistry of Materials* **2013**, 25, 34.

(22) Zhang, J. T.; Tang, Y.; Lee, K.; Ouyang, M., *Science* **2010**, 327, 1634.

(23) Ataee-Esfahani, H.; Wang, L.; Nemoto, Y.; Yamauchi, Y., *Chemistry of Materials* **2010**, 22, 6310.

(24) Sobal, N. S.; Ebels, U.; Mohwald, H.; Giersig, M., *J. Phys. Chem. B* **2003**, 107, 7351.

(25) Yan, J. M.; Zhang, X. B.; Akita, T.; Haruta, M.; Xu, Q., *Journal of the American Chemical Society* **2010**, 132, 5326.

(26) Sobal, N. S.; Hilgendorff, M.; Mohwald, H.; Giersig, M.; Spasova, M.; Radetic, T.; Farle, M., *Nano Letters* **2002**, 2, 621.

(27) Chantry, R. L.; Siriwatcharapiboon, W.; Horswell, S. L.; Logsdail, A. J.; Johnston, R. L.; Li, Z. Y., *J. Phys. Chem. C* **2012**, 116, 10312.

(28) Jin, M. S.; Zhang, H.; Wang, J. G.; Zhong, X. L.; Lu, N.; Li, Z. Y.; Xie, Z. X.; Kim, M. J.; Xia, Y. N., *ACS Nano* **2012**, 6, 2566.

(29) Tsuji, M.; Yamaguchi, D.; Matsunaga, M.; Alam, M. J., *Crystal Growth & Design* **2010**, 10, 5129.

(30) Tsuji, M.; Yamaguchi, D.; Matsunaga, M.; Ikedo, K., *Crystal Growth & Design*

2011, 11, 1995.

(31) Huang, L. F.; Shan, A. X.; Li, Z. P.; Chen, C. P.; Wang, R. M., *Crystengcomm* **2013**, 15, 2527.

(32) Zheng, Z.; Ng, Y. H.; Wang, D. W.; Amal, R., *Advanced Materials* **2016**, 28, 9949.

(33) Zhang, H. T.; Ding, J.; Chow, G. M.; Ran, M.; Yi, J. B., *Chemistry of Materials* **2009**, 21, 5222.

(34) Vysakh, A. B.; Lazar, A.; Yadukiran, V.; Singh, A. P.; Vinod, C. P., *Catalysis Science & Technology* **2016**, 6, 708.

(35) Vysakh, A. B.; Babu, C. L.; Vinod, C. P., *J. Phys. Chem. C* **2015**, 119, 8138.

(36) Wang, D. S.; Li, Y. D., *Journal of the American Chemical Society* **2010**, 132, 6280.

(37) She, H. D.; Chen, Y. Z.; Chen, X. Z.; Zhang, K.; Wang, Z. Y.; Peng, D. L., *Journal of Materials Chemistry* **2012**, 22, 2757.

(38) Bharathan, V. A.; Raj, G. K.; Joy, P. A.; Vinod, C. P., *Particle & Particle Systems Characterization* **2014**, 31, 236.

(39) Han, M.; Liu, Q.; He, J. H.; Song, Y.; Xu, Z.; Zhu, J. M., *Advanced Materials* **2007**, 19, 1096.

(40) LaGrow, A. P.; Cheong, S.; Watt, J.; Ingham, B.; Toney, M. F.; Jefferson, D. A.; Tilley, R. D., *Advanced Materials* **2013**, 25, 1552.

(41) Kim, C.; Kim, C.; Lee, K.; Lee, H., *Chemical Communications* **2014**, 50, 6353.

(42) Fan, Z. X.; Zhang, H., *Accounts Chem. Res.* **2016**, 49, 2841.

(43) Fan, Z. X.; Chen, Y.; Zhu, Y. H.; Wang, J.; Li, B.; Zong, Y.; Han, Y.; Zhang, H., *Chem. Sci.* **2017**, 8, 795.

(44) Ye, H. H.; Wang, Q. X.; Catalano, M.; Lu, N.; Vermeylen, J.; Kim, M. J.; Liu, Y. Z.;

Sun, Y. G.; Xia, X. H., *Nano Letters* **2016**, 16, 2812.

(45) Zhao, M.; Figueroa-Cosme, L.; Elnabawy, A. O.; Vara, M.; Yang, X.; Roling, L. T.; Chi, M. F.; Mavrikakis, M.; Xia, Y. N., *Nano Letters* **2016**, 16, 5310.

(46) Zhang, P. N.; Li, Y. J.; Wang, D. Y.; Xia, H. B., *Particle & Particle Systems Characterization* **2016**, 33, 924.

(47) Dong, H.; Chen, Y. C.; Feldmann, C., *Green Chem.* **2015**, 17, 4107.

(48) Venables, J. *Introduction to Surface and Thin Film Processes*; Cambridge University Press: Cambridge, 2000.

(49) Carroll, K. J.; Reveles, J. U.; Shultz, M. D.; Khanna, S. N.; Carpenter, E. E., *J. Phys. Chem. C* **2011**, 115, 2656.

APPENDIX A

PUBLICATIONS RELATED TO THE RESEARCH WORK DESCRIBED IN THIS DISSERTATION

(1) **Guangfang Grace Li**, and Hui. Wang, "Surface Atomic Coordination Matters: Selective Electrocatalytic Activity on Dealloyed Nanosponge Particles", *manuscript in preparation.*

(2) **Guangfang Grace Li**, and Hui. Wang, "Electrocatalytically Active Trimetallic Spongy Nanoparticles with Ultrathin Ligaments", *manuscript in preparation.*

(3) **Guangfang Grace Li**, and Hui. Wang, "Architectural Control of Au-Pt-Cu Trimetallic Hollow Nanostructures by Coupling Galvanic Replacement Reaction with Co-reduction", *manuscript in preparation.*

(4) **Guangfang Grace Li**, and Hui. Wang, "Dealloyed Nanopourous Au catalysts: from Macroscopic Foam to Nanoparticulate Architectures", **2018**, *submitted.*

(5) **Guangfang Grace Li**, Mengqi Sun, Shubham Pandey, Simon R. Phillpot, and Hui Wang, "Galvanic Replacement-Driven Transformations of Atomically Intermixed Bimetallic Nanocrystals: Effects of Compositional Stoichiometry and Structural Ordering", *Langmuir,* **2018***,* 34, 4340-4350.

(6) **Guangfang Grace Li,** Douglas A. Blom, Shubham Pandey, Robert J. Koch, Scott T. Misture,Simon R. Phillpot, and Hui Wang, "Overcoming the Interfacial Lattice Mismatch: Geometry Control of Gold-Nickel Bimetallic Heteronanostructures", *Part. Part. Syst. Charact.* **2017**, 34, 1700361.

(7) **Guangfang Grace Li**, Ye Lin, and Hui Wang, "Residual Silver Remarkably Enhances Electrocatalytic Activity and Durability of Dealloyed Gold Nanosponge Particles", *Nano Lett.* **2016**, 16, 7248-7253.

(8) **Guangfang Grace Li**, Esteban Villarreal, Qingfeng Zhang, Tingting Zheng, Jun-Jie Zhu, and Hui Wang, Controlled Dealloying of Alloy Nanoparticles toward Optimization of Electrocatalysis on Spongy Metallic Nanoframes, *ACS Appl. Mater. Interfaces*, **2016**, 8, 23920-23931.

APPENDIX B

COPYRIGHT PERMISSION

Copyright for Chapter 2

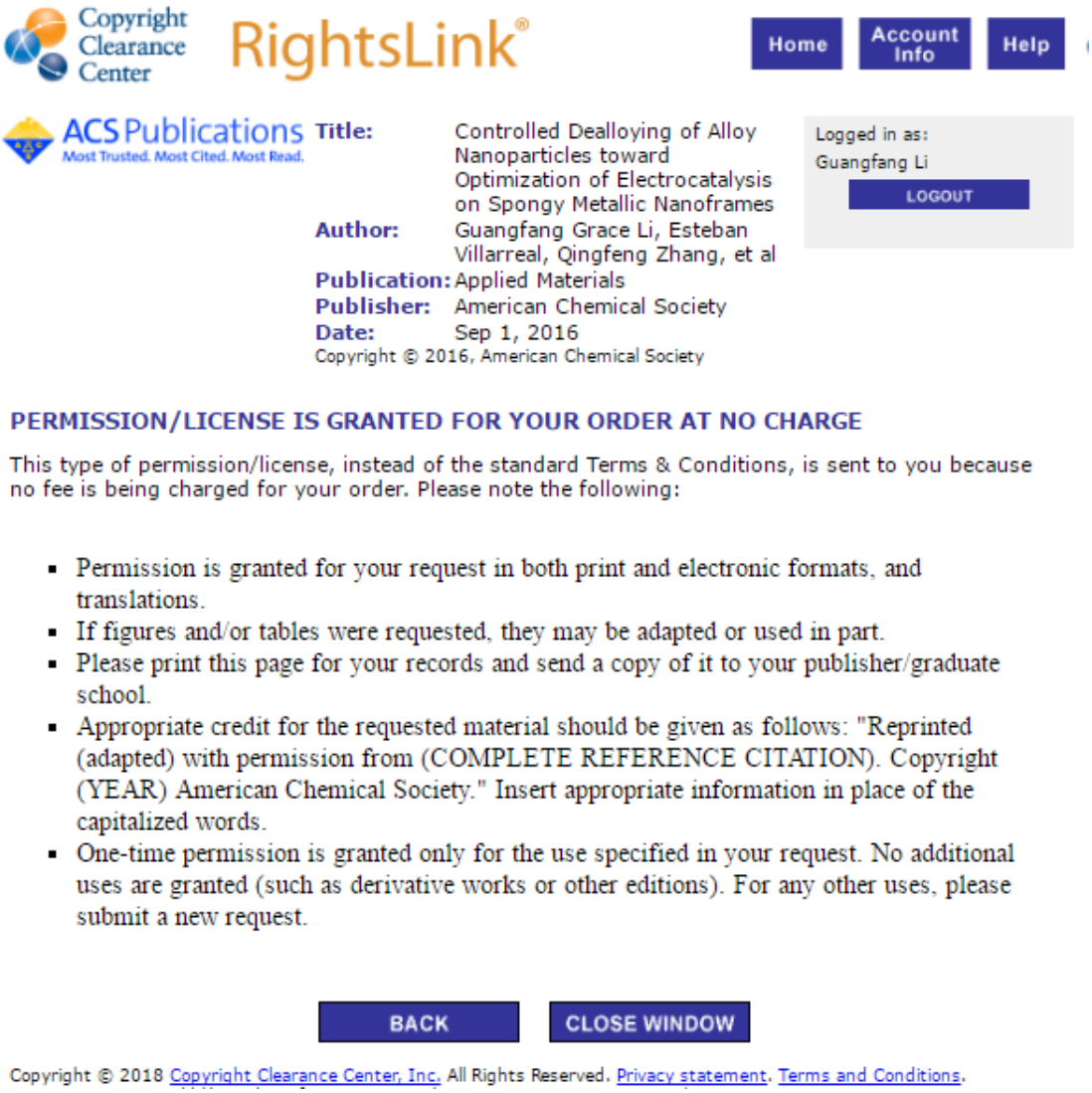

Copyright Clearance Center RightsLink®

Home | Account Info | Help

ACS Publications
Most Trusted. Most Cited. Most Read.

Logged in as:
Guangfang Li
LOGOUT

Title: Controlled Dealloying of Alloy Nanoparticles toward Optimization of Electrocatalysis on Spongy Metallic Nanoframes
Author: Guangfang Grace Li, Esteban Villarreal, Qingfeng Zhang, et al
Publication: Applied Materials
Publisher: American Chemical Society
Date: Sep 1, 2016
Copyright © 2016, American Chemical Society

PERMISSION/LICENSE IS GRANTED FOR YOUR ORDER AT NO CHARGE

This type of permission/license, instead of the standard Terms & Conditions, is sent to you because no fee is being charged for your order. Please note the following:

- Permission is granted for your request in both print and electronic formats, and translations.
- If figures and/or tables were requested, they may be adapted or used in part.
- Please print this page for your records and send a copy of it to your publisher/graduate school.
- Appropriate credit for the requested material should be given as follows: "Reprinted (adapted) with permission from (COMPLETE REFERENCE CITATION). Copyright (YEAR) American Chemical Society." Insert appropriate information in place of the capitalized words.
- One-time permission is granted only for the use specified in your request. No additional uses are granted (such as derivative works or other editions). For any other uses, please submit a new request.

BACK | CLOSE WINDOW

Copyright © 2018 Copyright Clearance Center, Inc. All Rights Reserved. Privacy statement. Terms and Conditions.

Copyright for Chapter 3

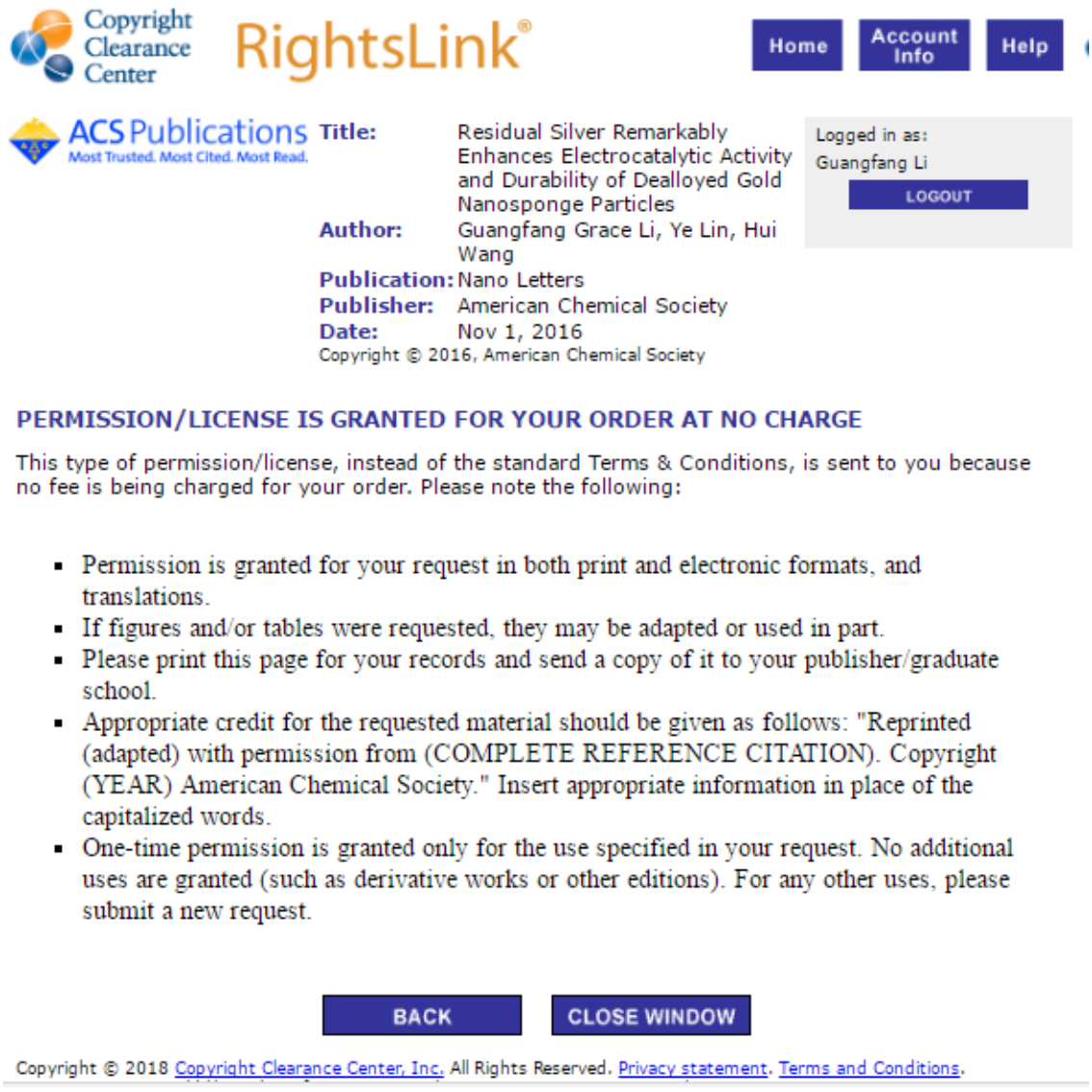

Copyright Clearance Center RightsLink®

Home | Account Info | Help

ACS Publications
Most Trusted. Most Cited. Most Read.

Title: Residual Silver Remarkably Enhances Electrocatalytic Activity and Durability of Dealloyed Gold Nanosponge Particles
Author: Guangfang Grace Li, Ye Lin, Hui Wang
Publication: Nano Letters
Publisher: American Chemical Society
Date: Nov 1, 2016
Copyright © 2016, American Chemical Society

Logged in as:
Guangfang Li
LOGOUT

PERMISSION/LICENSE IS GRANTED FOR YOUR ORDER AT NO CHARGE

This type of permission/license, instead of the standard Terms & Conditions, is sent to you because no fee is being charged for your order. Please note the following:

- Permission is granted for your request in both print and electronic formats, and translations.
- If figures and/or tables were requested, they may be adapted or used in part.
- Please print this page for your records and send a copy of it to your publisher/graduate school.
- Appropriate credit for the requested material should be given as follows: "Reprinted (adapted) with permission from (COMPLETE REFERENCE CITATION). Copyright (YEAR) American Chemical Society." Insert appropriate information in place of the capitalized words.
- One-time permission is granted only for the use specified in your request. No additional uses are granted (such as derivative works or other editions). For any other uses, please submit a new request.

BACK | CLOSE WINDOW

Copyright © 2018 Copyright Clearance Center, Inc. All Rights Reserved. Privacy statement. Terms and Conditions.

Copyright for Chapter 8

Copyright Clearance Center RightsLink®

Home | Account Info | Help

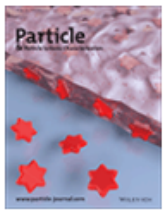

Title: Overcoming the Interfacial Lattice Mismatch: Geometry Control of Gold–Nickel Bimetallic Heteronanostructures
Author: Guangfang Grace Li,Douglas A. Blom,Shubham Pandey,Robert J. Koch,Scott T. Misture,Simon R. Phillpot,Hui Wang
Publication: Particle & Particle Systems Characterization
Publisher: John Wiley and Sons
Date: Dec 27, 2017

Logged in as: Guangfang Li
LOGOUT

Order Completed

Thank you for your order.

This Agreement between Guangfang Li ("You") and John Wiley and Sons ("John Wiley and Sons") consists of your license details and the terms and conditions provided by John Wiley and Sons and Copyright Clearance Center.

Your confirmation email will contain your order number for future reference.

printable details

License Number	4303210520775
License date	Mar 06, 2018
Licensed Content Publisher	John Wiley and Sons
Licensed Content Publication	Particle & Particle Systems Characterization
Licensed Content Title	Overcoming the Interfacial Lattice Mismatch: Geometry Control of Gold–Nickel Bimetallic Heteronanostructures
Licensed Content Author	Guangfang Grace Li,Douglas A. Blom,Shubham Pandey,Robert J. Koch,Scott T. Misture,Simon R. Phillpot,Hui Wang
Licensed Content Date	Dec 27, 2017
Licensed Content Pages	1
Type of use	Dissertation/Thesis
Requestor type	Author of this Wiley article
Format	Print and electronic
Portion	Full article
Will you be translating?	No
Title of your thesis / dissertation	Structural transformations of multimetallic nanoparticles
Expected completion date	Apr 2018
Expected size (number of pages)	260